A dynamic radio view of the Orion Nebula Cluster: Protostellar nonthermal variability at centimeter and millimeter wavelengths

Author:

Jaime VARGAS GONZÁLEZ

Supervised by:

Dr. J. FORBRICH

Dr. M. THOMPSON

Centre for Astrophysics Research

School of Physics, Engineering and Computer Science

University of Hertfordshire

Submitted to the University of Hertfordshire in partial fulfilment of the requirements of the degree of Doctor of Philosophy.

December 2022

Abstract

This thesis contains a comprehensive observational study of the radio time domain of young stars in the search for high-energy (HE) processes. This requires high spatiotemporal-resolution observations and thus the use of the most capable radio interferometers in the world such as the Karl G. Jansky Very Large Array (VLA), Atacama Large Millimeter/submillimeter Array (ALMA) and the Very Long Baseline Array (VLBA).

Young Stellar Objects (YSOs) present high levels of magnetic activity and related HE processes including strong flares that are orders of magnitude more luminous than that of their main-sequence counterparts. Both X-ray and radio wavelength observations provide evidence of these processes. Despite extensive X-ray studies, HE processes are still poorly understood, and only with the improved capabilities of radio facilities in the last decade have we gained access to radio emission associated with HE processes at unprecedented time resolution. YSO radio flaring variability at cm- and mm-wavelengths is associated with nonthermal (gyro-)synchrotron emission from magnetospheric activity with electrons gyrating along magnetic field lines. I present a radio variability study for an unprecedented sample of YSOs at cm- and mm-wavelengths at high spatiotemporal resolution with the VLA, ALMA, and the VLBA. I first present an enlarged census of compact cm-wavelength radio sources towards the Orion Nebula Cluster (ONC) using the VLA. We find evidence of strong variability by up to a factor of five on timescales of minutes to hours towards several sources, and order-of-magnitude variability on a timescale of 4 years in a few sources. These findings lead to a mean time between extreme radio variability events of 2482±1433 h. I also report the discovery of high proper motions from non-stellar radio sources (up to $\sim$373 km s^{-1}). Motivated by the widespread variability found in our VLA study and the few serendipitous discoveries of strong millimetre flares reported to date, I performed the first systematic search for such variability at mm-wavelengths in the ONC using ALMA. This was achieved for a large number of YSOs at high-time resolution. We find widespread mm-wavelength variability including the discovery of an order of magnitude mm-flare from a known YSO. I also present an assessment of systematic effects from interferometric imaging making use of simulated ALMA observations. Finally, I present a follow-up study of a multi-epoch VLBA survey for nonthermal radio emission for a large sample of sources in the ONC where, contrary to the VLA and ALMA data of the ONC, lightcurves can be produced directly from the visibilities allowing us to efficiently generate lightcurves at high-time resolution under given assumptions (unresolved and isolated sources) and allowing us to also explore different Stokes parameters following the same approach.

Declaration

I declare that no part of this work is being submitted concurrently for another award of the University or any other awarding body or institution. This thesis contains a substantial body of work that has not previously been submitted successfully for an award of the University or any other awarding body or institution.

The following parts of this submission have been published previously and/or undertaken as part of a previous degree or research programme:

1. Chapter 2: This has been published as Vargas-González et al., 2021, *Monthly Notices of the Royal Astronomical Society*, **506**, 3169.

2. Chapter 3: This has been published as Vargas-González et al., 2023, *Monthly Notices of the Royal Astronomical Society*, **522**, 56.

Except where indicated otherwise in the submission, the submission is my own work and has not previously been submitted successfully for any award.

Acknowledgements

Contents

List of Figures

List of Tables

List of Abbreviations

AIPS	Astronomical Image Processing System
ALMA	Atacama Large Millimeter/submillimeter Array
AU	Astronomical Unit
BIMA	Berkely-Illinois-Maryland Association
BN/KL	Becklin–Neugebauer/Kleinmann–Low
CARMA	Combined Array for Research in Millimeter-Wave Astronomy
CASA	Common Astronomy Software Application
COUP	Chandra Orion Ultra-deep Project
CTTS	Classical T Tauri Star
DFT	Direct Fourier Transform
ESA	European Space Agency
ESO	European Southern Observatory
FOV	Field of View
FWHM	Full width at half-maximum
GMC	Giant Molecular Clouds
HA	Hour Angle
HPBW	Half-power Beamwidth
HST	Hubble Space Telescope
IR	Infrared
ISM	Interstellar Medium
(J)VLA	(Jansky) Very Large Array
JWST	James Webb Space Telescope
KS	Kolmogorov-Smirnov
LC	Lightcurve

LCP & RCP   Left-hand Circular Polarization & Right-hand Circular Polarization

MJD   Modified Julian Day

MFS   Multi-Frequency Synthesis

MTMFS   Multi-term (Multi Scale) Multi-Frequency Synthesis

NCP   North Celestial Pole

NIR   Near Infrared

NRAO   National Radio Astronomy Observatories

ONC   Orion Nebula Cluster

OMC   Orion Molecular Cloud

ORBS   Orion Radio Burst Source

PROPLYDS   Protoplanetary Disks

RF   Radio frequency

RFI   Radio frequency interference

RMS   Root mean square

SED   Spectral Energy Distribution

SNR   Signal-to-noise ratio

UT   Universal time

UTC   Coordinated universal time

UV   Ultraviolet

VF   Variability Factor

VIRCAM   VISTA Infrared Camera

VISION   VIenna Survey In OrioN

VISTA   Visible and Infrared Survey Telescope for Astronomy

VLBA   Very Long Baseline Array

VLBI   Very-long-baseline interferometry

WTTS   Weak-lined T Tauri Star

YSO   Young Stellar Object

Introduction

The primary goal in star formation research is to understand the whole process of how stars form and evolve. In order to attain this goal both observational and theoretical efforts need to cooperatively advance to establish a more complete theory of stellar evolution. These efforts have been supported by evermore extraordinary technological advancement (upgraded instrumentation, modern telescopes, space-based observatories, wider wavelength coverage, improved observational techniques and computational capabilities). An early and appropriate conception of how stars form (ergo, our own Solar system) was already proposed almost 270 years ago and termed the "nebular hypothesis" describing an orbiting planetary system formed by contraction and flattening of a rotating nebular system (Kant, 1755; de Laplace, 1796) and setting a first approximation towards the modern interpretation of how stars and their disk structures are formed as a consequence of gravitational collapse of a dense molecular cloud core (Shu et al., 1987).

First observations of young stars, even before having been identified as such (e.g., Adams and Pease 1915; Sanford 1920; Joy 1932), have always recalled their distinctive observational characteristics that pointed to the presence of circumstellar material (see also Herbig 1950, 1962). Later on, numerical calculations were used to simulate collapsing protostellar envelopes (Larson, 1969, 1972) and by then, the term "protostar" was already established (Spitzer, 1948). Ever since there was an increased interest for the observation of the early phases of stellar evolution and given the emitting properties of protostars they were called the "Holy Grail" of infrared and submillimeter astronomy (Wynn-Williams, 1982). Theoretical growth was reciprocally followed by technological advancements reflected in our current capability to unveil the early stages of stellar evolution by observing through highly obscured environments within stellar nurseries.

This has been possible with the development of infrared (IR) and radio telescopes that overcome the limitation of optical observations. These limitations are not only due the extinction[1] of optical light by absorption and scattering as it travels through the interstellar medium (ISM) in our Galaxy (optical light is largely absorbed by dust in the ISM, see Trumpler 1930) but mainly because stars that are forming within these stellar nurseries are surrounded by dust that blocks the light they emit. Instead, most of the luminosity of these young systems comes from heating of their dusty envelopes that emit at long wavelengths into the IR and radio range (e.g., Wilking and Lada 1983, Wilking and Lada 1983 and references therein).

An additional limitation pushed this progress further, the Earth's atmosphere. Early observations of sources that were later recognized as protostars were possible with ground-based infrared telescopes (Mendoza V., 1966; Cohen, 1973) but the Earth's atmosphere largely affects the infrared range, in contrast, it is mostly transparent to radio wavelengths. The atmospheric radio window can extent between 0.3 mm and 30 m, subject to observing conditions at different sites mainly defined by altitude and dryness in order to avoid as much as possible the main sources of atmospheric attenuation: water vapor, oxygen, and ozone (e.g. Condon and Ransom 2016; Thompson et al. 2017). Given the atmospheric limitations for infrared observations, further advancements brought the development of space-based telescopes (with the IRAS mission as one of the pioneers; Neugebauer et al. 1984; Rucinski 1985). The progress achieved by observations at long wavelengths (IR and radio range) now allows the study of the youngest protostars (see for example Mendoza V. 1966; Moran et al. 1982 for early IR or radio observations, and also Stutz et al. 2013; Segura-Cox et al. 2020; Tobin et al. 2020 for more recent observations of the youngest protostars with modern facilities). In addition to the extended wavelength coverage, the improved angular resolution and sensitivity achieved by interferometers in the radio/(sub)millimeter and optical/IR regimes also allow us to explore these young protostellar systems in detail revealing complex structures down to size scales comparable to the Solar System (e.g., Encalada et al. 2021; Koumpia et al. 2021; Parker et al. 2022)

---

[1]Starlight can be absorbed and scattered by dust grains in the ISM in our Galaxy (and in other galaxies in general). Absorption of light becomes more efficient for particles with sizes larger than the wavelength of the emitted light while scattering becomes more efficient when the particle's size is comparable to this wavelength. Moreover, the relation between number density (particles per volume unit) and size distribution of dust grains in the ISM is such that extinction is wavelength-dependent and it is indeed stronger at shorter wavelengths (dust extinction first confirmed by Trumpler 1930), although extinction curves depend on the ISM properties which can be different for different galaxies (e.g., Gordon et al. 2003).

or even smaller scales down to a few Astronomical Units (ALMA Partnership et al., 2015; Andrews et al., 2018; van der Marel et al., 2019; Segura-Cox et al., 2020).

From the observational perspective, in order to gather as much evidence as possible to better understand the whole process of stellar evolution, in addition to the examination of a wide range of wavelengths, we need to take into account a range of parameters covering all the evolutionary stages of protostellar systems and the range of features they develop at different physical scales. Most studies have put their focus on the investigation of structures surrounding the central protostar (circumstellar material or protostellar discs), studying their evolution, properties, and its aftermath, planet formation. As a complementary and unique new perspective, taking advantage of the advancements in radio observing capabilities of the last decade, in this thesis I will focus on observables that are directly related to the central protostar itself, particularly its radio emission associated to high-energy processes by exploring the radio time domain in young stars.

The discussion presented in this work will be focused on the low-mass regime that is significantly more numerous than its high-mass counterpart. Despite their relevant influence on the environment, the evolution of high-mass stars (stellar masses $\geq 8\ M_\odot$) is still poorly understood compared to what is known from their low-mass counterparts. This is because high-mass stars tend to form in dense clusters and they rapidly leave their pre-main-sequence phase while still heavily embedded which has made their observation very difficult (McKee and Ostriker, 2007; Zinnecker and Yorke, 2007; Beltrán and de Wit, 2016) not to mention that the typical distance to regions of massive star formation is between 1 and 2 kpc with a few nearby exceptions, compared to sites of low-mass star formation that can be found as close as $\sim 140-150$ pc (Galli et al., 2019).

In the following sections of this chapter I will summarize the main stages in the evolution of low-mass young stars, followed by a brief discussion on the multiwavelength properties in young stars, to then review their radio properties and how this emission can trace high-energy processes in young stars. I will then describe the essential aspects of radio interferometric observations to then introduce the star-forming region explored in this work, the Orion Nebula Cluster (ONC). Motivations, specific objectives and structure of this thesis are described at the end of this chapter.

1.1   Early stages of low-mass stellar evolution

1.1.1   From clouds to protostars: The big picture

There is a well established sequence for the big picture of how low-mass stars form outside the complex processes at every step of the road that are still to be understood. This sequence is mostly, and naturally, based on what we have learnt from our own Galaxy. Stars form within giant molecular clouds (GMCs) in the dense and cold phase of the ISM typically distributed within spiral arms in disk galaxies such as the Milky Way (see an observational review by Blitz and Williams 1999 and both observational and theoretical review by McKee and Ostriker 2007). Molecular clouds consist mostly of molecular gas composed of H_2 followed by He, low abundances of other molecules, and a small fraction of dust ($\sim 1\%$). However, in order to trace the structure of molecular clouds we can not rely in their most abundant component, H_2, since it does not emit in such cold environments[2], instead, molecular clouds are traced using other molecules (the most relevant tracer being carbon monoxide, CO, and its isotopologues), whose transitions can occur at very low temperatures. Comprehensive studies of molecular clouds structures show that GMCs are hierarchical structures far from homogeneous (Williams et al., 2000; Heyer and Dame, 2015; Miville-Deschênes et al., 2017) comprised by filamentary structures in networks connected through sheets (e.g., Hacar et al. 2013 and later reviews on filaments by André et al. 2014; Pineda et al. 2022), dense massive clumps where stellar clusters can form, and smaller dense cores that can collapse into individual stars or small multiple systems (Shu et al., 1987; McKee and Ostriker, 2007; Ballesteros-Paredes et al., 2020).

In this hierarchical chain of structures there is a wide range of size scales, masses, and densities, and while these are not strictly discrete entities they can be categorized within observationally distinct structures relative to their local environment. GMCs, for instance, have sizes of $10-200$ pc with masses of $10^4 - 10^6$ $M_\odot$, low temperatures of $\sim 10-20$ K, and density about 100 cm^{-3} (Miville-Deschênes et al., 2017; Ballesteros-Paredes et al., 2020). Molecular "clumps" (the progenitors of stellar clusters) have mean sizes around

---

[2]H_2 is a homonuclear molecule with symmetric structure which means it has zero dipole moment and ro-vibrational transitions are thus quadripole. Quadruple selection rule requires that rotational quantum number changes by 2, 0, -2 ($\Delta J = 0$, ± 2) which in turns means that the lowest transition allowed is $J = 2 \rightarrow 0$. This requires excitation temperatures $T > 500$ K, significantly above temperatures of cold gas in molecular clouds (Shull and Beckwith, 1982; Sternberg, 1989).
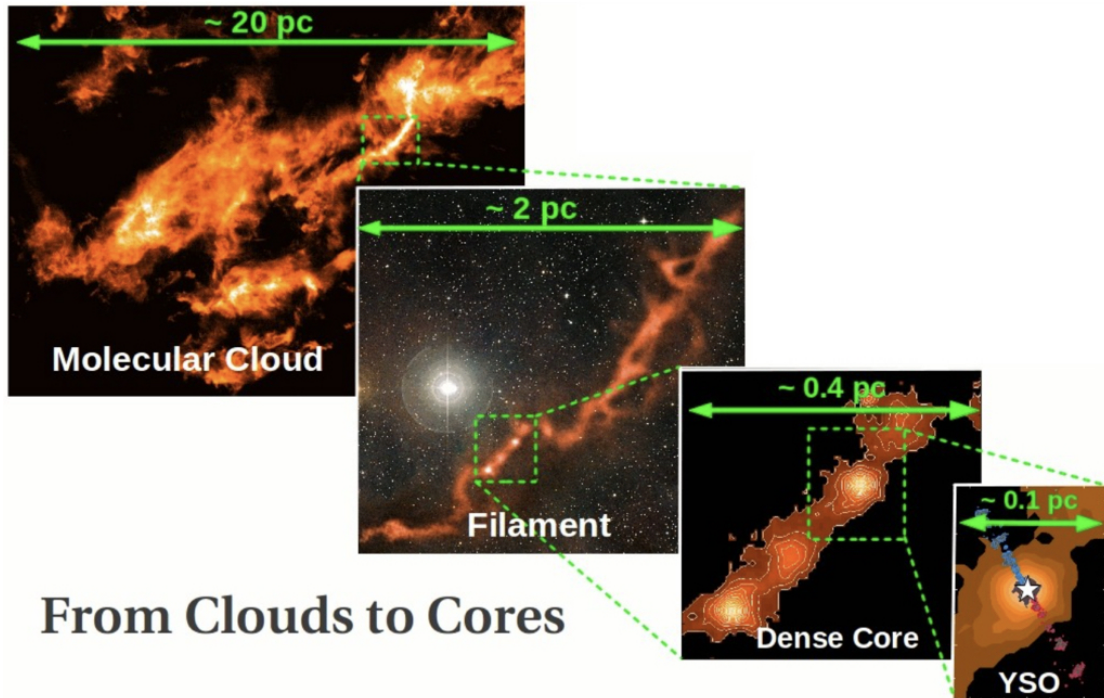
FIGURE 1.1: Dense core formation within molecular clouds (Taurus Molecular Cloud). From left to right, three different spatial scales from several parsecs at molecular cloud scales, with filamentary structure at smaller scales is found hosting dense cores at sub-parsec scales where a central protostar is accumulating mass. Image from A. Hacar lecture in Star and planet formation workshop at ESAC January 2013. Images from: Goldsmith et al. (2008); Hacar et al. (2013); Santiago-García et al. (2009)

1 pc but can be found with sizes up to 10 pc, masses of $10 - 10^3$ M$_\odot$ with a mean mass of ~ 400 M$_\odot$ although extreme cases of $< 10^5$ M$_\odot$, typical temperatures about ~ 16 K but up to 40 K and densities $\sim 10^4$ cm^{-3} (Tan et al., 2013; Urquhart et al., 2018). The smallest in this chain are dense "cores" with sizes $\lesssim 0.1$ pc, masses of $1 - 10$ M$_\odot$ and high densities of $> 10^4$ cm^{-3} (Blitz, 1993; Williams et al., 2000; Miville-Deschênes et al., 2017).

In addition to these structures, filaments have been seen to be ubiquitous in molecular clouds (see Figure 1.1 showing the hierarchical structure of the cloud including its filamentary structure). Filamentary structures in the ISM comprise a wide range of scales from sub-pc filaments within clouds up to kpc-sized structures apparently tracing the spiral structure in the Milky Way (also termed "Galaxy bones", Zucker et al. 2015). Filaments in nearby molecular clouds have lengths < 1 pc, line masses (mass per unit of length) of $5-17$ $M_\odot$ pc^{-1}, median inner widths of 0.1 pc, column densities of $3-9\times10^{21}$ cm^{-2} and temperatures of $14-16$ K. On the other hand, larger scale filaments from Galactic plane surveys (excluding those "Giant molecular filaments" or "Galactic

Bones" studied in Abreu-Vicente et al. 2016; Zucker et al. 2018) have lengths of $5-10$ pc, line masses of $20-200$ $M_\odot$ pc^{-1}, masses of $500-1000$ $M_\odot$, and temperatures of $10-35$ K (Hacar et al., 2022). Within this diversity there is a classification for "filament families" including, for instance, molecular filaments, atomic filaments, dense fibers, striations, hubs, and ridges. Some of these structures are directly associated to the earliest phases of high-mass and cluster formation (see Hacar et al. 2022; Pineda et al. 2022, and reference therein) and in general these coexist and are actually linked to clumps and cores within molecular clouds. In fact, most of the mass of the densest phase in nearby molecular clouds is found in the form of filaments and these contain between 60% to 90% of the star-forming cores (Könyves et al., 2015, 2020).

The sequential course to form a protostar within molecular clouds begins with an unstable cloud overdensity that start to contract. This instabilities can be triggered by shock waves from nearby exploding star or collision between molecular clouds (e.g., Elmegreen 1998; Ballesteros-Paredes et al. 2007). This contraction can derive in such substructures described above. At a cloud core scale, assuming an approximately spherical distribution for simplicity, once it reach a critical mass (Jeans mass − Jeans 1928) gravity overcome internal pressures such as thermal and magnetic pressure and then gravitational collapse of the dense core begins. Initially, the collapsing core is optically thin allowing the energy to escape and thus preventing internal heating (isothermal collapse). The collapse is such that the central density increases faster than the outer regions (inside-out infall − Shu 1977). During this process, the gravitational potential energy is transformed into kinetic energy (infalling gas particles), and in thermal energy due to particle collision. As density also increases, it eventually becomes optically thick and the energy is absorbed by the collapsing system heating up the gas (adiabatic collapse). With increasing temperature, pressure also increases counteracting the effect of gravity and slowing down collapse until a first hydrostatic stellar core (FHSC) is formed (Hayashi, 1966). Further collapse of the surrounding envelope heats up the FHSC leading to its contraction and formation of a protostar that continues to grow its mass by accretion of its surrounding material (accretion disk). Due to conservation of angular momentum the infalling spinning material flattens into a disk and the central protostar is then surrounded by this disk and embedded in an infalling envelope (Shu et al., 1987; Williams et al., 2000; Larson, 2003). In addition to the resulting embedded disk, bipolar outflows and jets appears perpendicular to the disk plane (Bally, 2016; Anglada et al.,

2018) through which angular momentum in transported and removed (Shu et al., 1994; Kölligan and Kuiper, 2018).

The surrounding material in disks and outflows thus are a key element from the observational point of view. Since protostars are deeply embedded not only within the immediate surrounded material but also within the parent molecular cloud, it is impossible to observe them at optical wavelength until they clear up their surroundings. As described earlier in this chapter, most of the emission in protostars comes from their envelopes at long wavelengths (IR and sub-millimeter), but different features can be still observed at a range of wavelengths (see text above). As for the protostellar envelope, it drastically changes throughout its evolution and so does their observed emission. It is depleted by accretion and blown away by the bipolar outflows until the central object eventually becomes optically visible. The observables of this changes mostly in the IR range can be used to describe and classify the evolutionary stages of low-mass protostars. This classification is summarized in the following section.

1.1.2 Low-mass Protostar and YSO Evolutionary Stages

Early classification consisted in three evolutionary classes (I, II, and III) based on the IR excess caused by dusty envelopes and circumstellar disks around YSOs that results in their observed IR spectral energy distribution (SED) in the range between $\lambda = 2.2$ and $\lambda = 100 \ \mu m$ whose shape (slope) is associated to their different evolutionary stages (Lada, 1987). This classifications considers the spectral index (α_{IR}), defined as the slope of the near- to mid-IR SED in $\log_{10} \lambda F_\lambda$ versus $\log_{10} \lambda$, where F_λ is the flux density at a given wavelength λ. This classification was further extended including the Class 0 protostars at a very early stage still deeply embedded and thus really hard to observe requiring longer wavelengths (millimeter/submillimeter) to be detected (Andre et al., 1993). Later on, a new stage was defined and termed "flat-spectrum" class (Greene et al., 1994), that seems to represent a transitional stage in between Classes I and II (e.g., Furlan et al. 2016). These evolutionary stages can be described as follows:

Class 0: A deeply embedded central object in the collapsing phase of a dense cloud core at a very young age of $\lesssim 10^4$ yr (or up to $\lesssim 10^5$ yr, e.g., Dunham et al. 2015) with accretion at a high rate and an optically thick rotating infalling envelope that dominates the mass of the system and makes these objects invisible at optical to near-IR wavelengths.
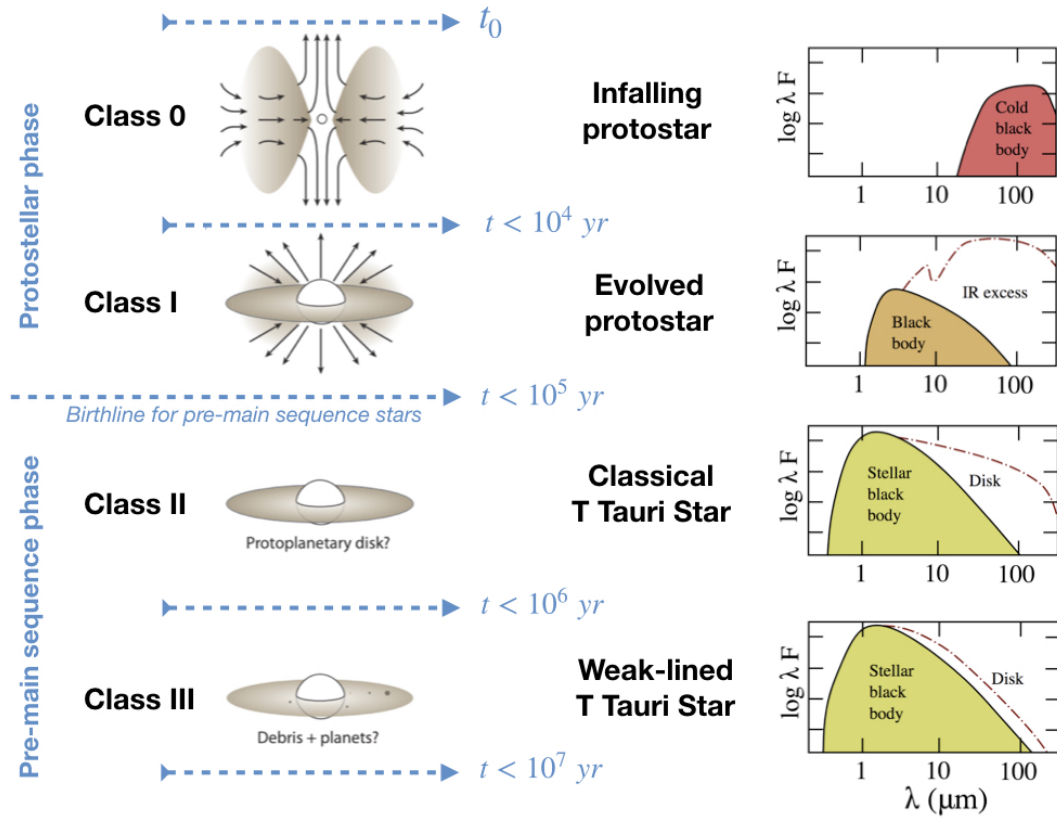
FIGURE 1.2: Schematic illustration of the main stages of low-mass protostellar evolution with their classification based on the shape of their spectral energy distribution (shown on the right-hand side) together with diagrams of their circumstellar environments. Image adapted from Suchitra Narayanan's Astrobites "Protostars to planets - The chemical pathway"[3]) and Vallastro illustration[4].

This infalling envelope, on the other hand, can be detected in the far-IR to millimeter range, although mid-IR emission has been also observed from Class 0 objects during outbursts (e.g., Zakri et al. 2022), and even recent near-IR spectroscopic observations have been able to detect a few spectral features towards this objects (see Laos et al. 2021). Millimeter studies are starting to observationally prove the presence of small circumstellar disks even at this very young protostellar phase (Segura-Cox et al., 2018; Tobin et al., 2020). The SED of these objects resembles that of a black body spectrum (see top row illustration in Figure 1.2) with low bolometric temperature[5] ($T_{bol} \lesssim 70$ K; Chen et al. 1995). The rapid mass accretion at this stage is thought to account for an important fraction of the final star's mass (Fischer et al., 2017). This is accompanied by

---

[3]Astrobites: Protostars to planets - The chemical pathway.
[4]https://commons.wikimedia.org/wiki/User:Vallastro
[5]The effective temperature of a blackbody with the same mean frequency as the protostellar SED (Myers and Ladd, 1993).

the initial development of an embedded disk, together with powerful bipolar outflows and jets perpendicular to the rotating plane.

Class I: At this stage the central object is still embedded with a massive accretion disk and most of the mass from the envelope has already been transferred to both the disk and the central object. These disks have been observed to present a wide range of complex structures that point out to an early onset of planet formation (ALMA Partnership et al., 2015). Class I sources still preserve jets and outflows but these have declined and show wider opening angle as the protostar evolves (Bally, 2016). Protostars can evolve through Class I stage for about $\sim 10^5$ yr (Dunham et al., 2015). They have bolometric temperatures of 70 K$< T_{bol} < 650$ K (Chen et al., 1995). Its SED has a positive spectral index ($0.3 \leq \alpha_{\mathrm{IR}}$; Greene et al. 1994) and what was a blackbody spectrum has now broaden displaying IR excess due to the warm circumstellar material (disk) around the hot central object.

Flat-spectrum: When first introduced by Greene et al. (1994) this class was assigned to those YSOs with uncertain evolutionary status but potentially representing a transitional stage between Class I and II, thus essentially at the birthline transition from protostar to pre-main sequence Class II YSO, however, this has not been yet established. In Großschedl et al. (2019) they find that flat-spectrum sources (from a sample of almost 200 of this sources) are at a younger evolutionary phase compared to Class II sources even if they have already dispersed their envelopes and dense gas. Their SED have a spectral index between $-0.3 \leq \alpha_{\mathrm{IR}} \leq 0.3$ (Greene et al., 1994) and have an associated bolometric temperature of 350 K$< T_{bol} < 650$ K (Evans et al., 2009).

Class II: An advanced stage where the central object is now a pre-main sequence star with most of its mass budget already accreted, has dispersed its envelope and is surrounded by a circumstellar disk. It is now clearly visible with less IR excess in its SED and a negative spectral index ($-1.6 \leq \alpha_{\mathrm{IR}} \leq 0.3$; Greene et al. 1994) and bolometric temperature of 650 K$< T_{bol} < 2800$ K (Chen et al., 1995). This stage is associated to Classical T Tauri Stars (CTTS) and have ages about $\sim 10^6$ yr. T Tauri stars (TTSs) are low-mass pre-main-sequence stars, highly variable with strong emission lines. Sub-classified as CTTSs and Weak-line T Tauri Stars (WTTS, these are associated to Class III sources, see text below) according to their Hα emission line (Herbig and Bell, 1988).

The former have broad and strong Hα emission lines due to higher accretion compared to WTTSs, the latter exhibit narrow and weak Hα emission lines (White and Basri, 2003).

Class III: These pre-main sequence stars have ages around $\sim 10^7$ yr and are already close to the main sequence. Now Their accretion disk is optically thin with and weak emission lines and are associated to Weak-line T Tauri Stars (WTTS). Its almost gone disk leads to a SED with essentially only contribution from the central pre-main sequence star and very little contribution from disk and has typical spectral index values of $\alpha_{\mathrm{IR}} \leq -1.6$ (Greene et al., 1994) and associated bolometric temperatures of 2800 K$< T_{bol}$ (Chen et al., 1995).

This classification based on the observed IR SED can be affected by the viewing angle of the system, for instance, a young embedded protostar expected to have a rising spectrum would result in a flat spectrum if seen "pole-on", or the opposite effect if a Class II object is seen "edge-on" where its SED would then resemble a Class I object. To overcome this observational effect, Robitaille et al. (2006) proposed an alternative classification to adequately describe an "evoluitonary" protostellar sequence based on physical parameters (e.g., envelope density, disk masses, or envelope accretion rate) derived from radiation transfer models of a wide range of YSOs evolutionary stages and stellar masses taking into account the effect of different viewing angles for each model. This classification start with Stage 0 for the earliest phases with a dominant envelope up to Stage III for the latest YSO phases with optically thin disks.

In addition to the main IR properties in YSOs, each stage of protostellar evolution exhibits multiwavelength properties that probes phenomena at different physical scales. For instance, towards the opposite extreme of the electromagnetic spectrum, compared to the above examples (IR and radio range), at shorter wavelength the X-ray emission is associated to magnetic activity in the magnetosphere of young stars (Feigelson and Montmerle, 1999; Preibisch et al., 2005). This phenomenon can also be traced by nonthermal radio emission that is essentially unaffected by extinction (a discussion on radio emission mechanisms is presented in the following subsection - Section 1.2). This emission is (gyro)-synchrotron radiation arising from the electron population gyrating along magnetic field lines in protostellar coronae and vicinities (innermost regions of circumstellar disks). In this context, mildly relativistic electrons can produce gyrosynchrotron radiation detectable at cm-wavelenghts, while electrons at higher energies (MeV)

are responsible for synchrotron radiation observable at millimetre-wavelenghts (Dulk, 1985; Güdel, 2002). At similar wavelengths, cm- and mm-wavelengths, thermal free–free emission can be observed from ionized material at the base of jets and outflows, and also at mm- and submm-wavelengths from protostellar disks usually tracing the dust content. On the other hand, the ultraviolet (UV) range can probe chromospheric emission that is expected to be observable from young stars that have cleared most of their surrounding material making them also visible in the optical range. UV emission is also detected in the inner regions of protoplanetary disks (see for example a recent review by Schneider et al. 2020 and reference therein). Jets and outflows from young stars can be detected in a wide range of wavelengths, with optical jets seen at large scales (up to parsec-scales) while at centimeter radio wavelengths these features are detected on smaller scales nearer the star at the base of jets and outflows (Bally, 2016; Anglada et al., 2018), and even UV observations can also trace jets nearer the star (e.g., Devine et al. 2000).

The YSO classification discussed earlier informs us about how elusive the youngest protostars are for observations during their early infalling phase due to the still low temperatures and highly extincted environments where shorter wavelengths (near- to mid-IR) are no longer significant. Longer wavelengths (submillimeter to centimeter range) are thus an essential tool for the identification of such young protostars (André et al., 2014), beyond the already remarkable value they have for the study of disks and/or jets that are also seen from more evolved protostars (Bally, 2016; Anglada et al., 2018). In the following section I will describe the main properties of the radio emission from low-mass YSOs.

1.2 Radio continuum emission in low-mass Young Stellar Objects

A distinctive property of radio emission that makes it relevant for star formation studies is that it can penetrate high column densities unlike emission at shorter wavelengths. This allows the observation of very young and still deeply embedded sources (such as Class 0 sources, e.g., Andre et al. 1993) and thus giving access to a more complete census of the full population in young star-forming regions. Moreover, together with the X-ray regime, radio emission can also provide information on high-energy processes in young

stars. The X-ray emission, in this context, is thermal emission produced by coronal type activity as a result of heated plasma from magnetic reconnection energy release (Feigelson and Montmerle, 1999; Benz, 2008).

YSO radio continuum emission (spectral line emission is not discussed in this thesis[6]) can originate from different emitting mechanisms, thermal and nonthermal, both proving different physical scales at wavelengths ranging from submillimeter to centimeter range. These mechanisms can also originate simultaneously in the same source. Thermal emission depends on the temperature of the source and it is produced by the motion of charged particles in thermal equilibrium. Thermal motion results in charge acceleration and dipole oscillation generating electromagnetic radiation (conversion of kinetic energy to electromagnetic energy). Contrarily, nonthermal emission does not depend on the temperature of the source, and instead, it is produced by other mechanisms, for example, charged particle acceleration due to the presence of magnetic fields.

The main thermal emission mechanisms that contribute to the emission from YSOs are dust emission and free-free emission (or thermal *Bremsstrahlung*). Dust emission is generated in circumstellar disks around protostars and their surrounding envelope in more embedded sources. Dust grains absorb radiation from the star and re-emit as a non-perfect black body since a small fraction of the radiation is reflected and not absorbed. The spectrum of the thermal dust emission can be described by a modified black body function as:

$$S_\nu \propto \frac{2h\nu^{3+\beta}}{c^2} \frac{1}{exp(h\nu/kT_{\text{dust}})-1} \tag{1.1}$$

Where T_{dust} is the equilibrium temperature of the dust and β is the dust emissivity spectral index, which describes the power-law distribution of dust emissivity as a function of wavelength (e.g., Tibbs et al. 2012). Figure 1.3 shows the modified black body spectrum of the thermal dust emission spectrum for different dust temperatures at a fixed dust emissivity spectral index, where it is observed that the emission of the dust will depend on its temperature.

---

[6]Continuum emission involves a wide-range of particle energies, while line emission corresponds to discrete energies as a result of specific atomic or molecular transitions. Relevant spectral line emission at radio frequencies are radio recombination lines, the 21-cm line of Hydrogen, and MASER emission.
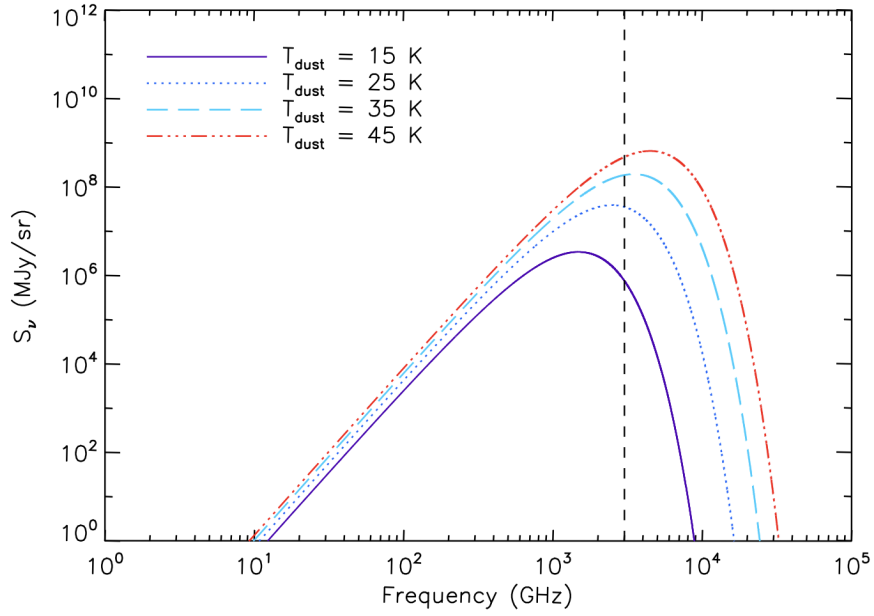
FIGURE 1.3: Modified black body spectrum representing the thermal dust emission for a range of dust temperatures from 15 to 45 K with a fixed dust emissivity spectral index. Image taken from Tibbs et al. (2012).

The thermal free-free emission or thermal Bremsstrahlung, instead, is the result of a charged particle (e.g., electron) accelerating due to the Coulomb field of another charge (e.g., ion or nuclei). While Bremsstrahlung emission refers to the radiation from acceleration of charged particles, there is a distinction between thermal and non-thermal Bremsstrahlung which is due to the population of electrons involved. It is called thermal Bremsstrahlung when the electron population involved is described by a Maxwell-Boltzmann distribution, and nonthermal Bremsstrahlung when the electron population involved is described by a power law distribution. The given name of this emission (free-free) is due to the fact that the electron is always free, before and after the interaction, and it is not captured by the ion. Due to the interaction of the ion and the passing electron, the trajectory of the electron is altered. The deviation of the electron depends on its velocity, and the distance between the electron of charge $-e$, and the ion of charge Ze. This distance is known as the impact parameter, b, whose maximum value is given by $b_{\max} = \nu/\omega$, with ν and ω corresponding to the thermal velocity and plasma frequency, respectively. The $b_{\min}$ value can be approximated to $b_{\min} = 4Ze^2/\pi m\nu^2$.

The free-free emissivity can be expressed as (Rybicki and Lightman, 1986):

$$\epsilon_\nu^{ff} = 6.8 \times 10^{-38} Z^2 n_e n_i T^{-1/2} e^{-h\nu/kT} \overline{g}_{ff} \tag{1.2}$$

where $\overline{g}_{ff}$ corresponds to the velocity averaged Gaunt factor, which is a function of the energy of the electron and the emission frequency (Rybicki and Lightman, 1986), given by:

$$g_{ff} = \frac{\sqrt{3}}{\pi} \, ln\left(\frac{b_{\max}}{b_{\min}}\right) \tag{1.3}$$

For electron population with a Maxwellian distribution of velocities (for thermal free-free emission) we can consider $h\nu_{max} \approx KT$, up to a critical frequency ν_{max} that depends on the electron velocity and impact parameter, $\nu_{max} \approx v/2\pi b$, and thus equation 1.2 will be independent of frequency for $\nu < \nu_{max}$. This results in a nearly flat spectrum at radio frequencies for optically thin sources (see schematic in the bottom curve shown in Figure 1.4), and then an exponentially falling spectrum at higher frequencies.

On the other hand, the nature of nonthermal radio emission is based on the acceleration of charged particles in the presence of a magnetic field. It is caused by electrons gyrating along magnetic field lines at different energy regimes and it is also called gyromagnetic emission. The different energy regimes denote the different particle velocities involved and are usually described in terms of the Lorentz factor $\gamma = 1/\sqrt{1-(v/c)^2}$, where v is particle velocity and c is the speed of light. For $\gamma \sim 1$ it is called non-relativistic regime, but when velocities involved approach the speed of light ($\gamma \gg 1$), it is called ultra-relativistic regime. The three main gyromagnetic emission mechanisms are cyclotron, gyrosynchrotron, and synchrotron. This emission occurs in a magnetic field B with gyrofrequency given by (Güdel, 2002):

$$\nu_c = \frac{eB}{2\pi m_e c} \approx 2.8 \times 10^6 B \; [\text{Hz}] \tag{1.4}$$

where e and m_e are the electron charge and rest mass, respectively, and B the magnetic field strength given in Gauss. For large angles between the electron's velocity vector and the local magnetic field (pitch angle), the spectral power is emitted around a harmonic s with a maximum gyrofrequency given by:

$$\nu_{\max} = s\nu_{c,\text{rel}} \approx \gamma^3 \nu_{c,\text{rel}} \approx 2.8 \times 10^6 B\gamma^2 \; [\text{Hz}] \tag{1.5}$$

TABLE 1.1: Gyromagnetic Emission properties.

Gyromagnetic emission mechanisms (1)	Lorentz factor γ (2)	Harmonic s (3)	Electron energy regime (4)
Cyclotron (gyroresonance)	~ 1	< 10	non-relativistic (typically thermal electrons)
Gyrosynchrotron	$2 \lesssim \gamma \lesssim 3$	$10 - 100$	Mildly relativistic
Synchrotron	$\gamma \gg 1$	> 100	(ultra-)relativistic

where $\nu_{c,\mathrm{rel}} = \nu_c/\gamma$ is the relativistic gyrofrequency. The main mechanism and its properties in terms of γ, s, and energy regime are summarized in Table 1.1.

For cyclotron emission (or gyroresonance emission) the electrons gyrate along magnetic field lines at non-relativistic velocities ($\gamma \sim 1$). It is usually seen as a single spike at the same frequency of the frequency of gyration of the electron in the magnetic field (gyrofrequency). The cyclotron power spectrum is thus a single peak at the gyrofrequency and requires strong magnetic fields to be observable at radio wavelengths. On the other hand, gyrosynchrotron emission is caused by mildly-relativistic electrons ($2 \lesssim \gamma \lesssim 3$, and energies from a few to several tens of keV). Its emission occurs in a wide frequency range (wide range of harmonics of the gyrofrequency - see column 3 in Table 1.1) and has a broad spectra following a power law (see a representative spectra in Figure 1.4). Finally, synchrotron emission is caused by ultra-relativistic electrons ($\gamma \gg 1$) and occurs at a higher number of harmonics of the gyrofrequency ($s > 100$). Its broad continuum emission is described by a power law spectrum proportional to $\nu^{5/2}$ for optically thick low frequencies, and $\nu^{-(\delta-1)/2}$ for optically thin high frequencies, where δ is the power law index of the electron energy distribution. A synchrotron spectrum is represented by the top curve in Figure 1.4.

Observationally, low-mass YSO thermal radio emission originates from free–free (bremsstrahlung) radiation from ionized material while nonthermal radio emission arises from magnetic activity in protostellar coronae and their vicinities (Dulk, 1985; Güdel, 2002). The dominant emission mechanism in YSOs at centimeter-wavelengths is thermal bremsstrahlung (free-free), while at shorter wavelengths (millimeter and sub-millimeter) their radio spectrum is dominated by thermal dust emission (e.g., Rodríguez et al. 2005a; Chandler et al. 2005). On the other hand, nonthermal radio emission can become the main component during strong magnetic events at centimeter and millimeter-wavelengths (Massi et al., 2006; Torres et al., 2012).

Typical physical scales associated to YSO radio emission are as follows:
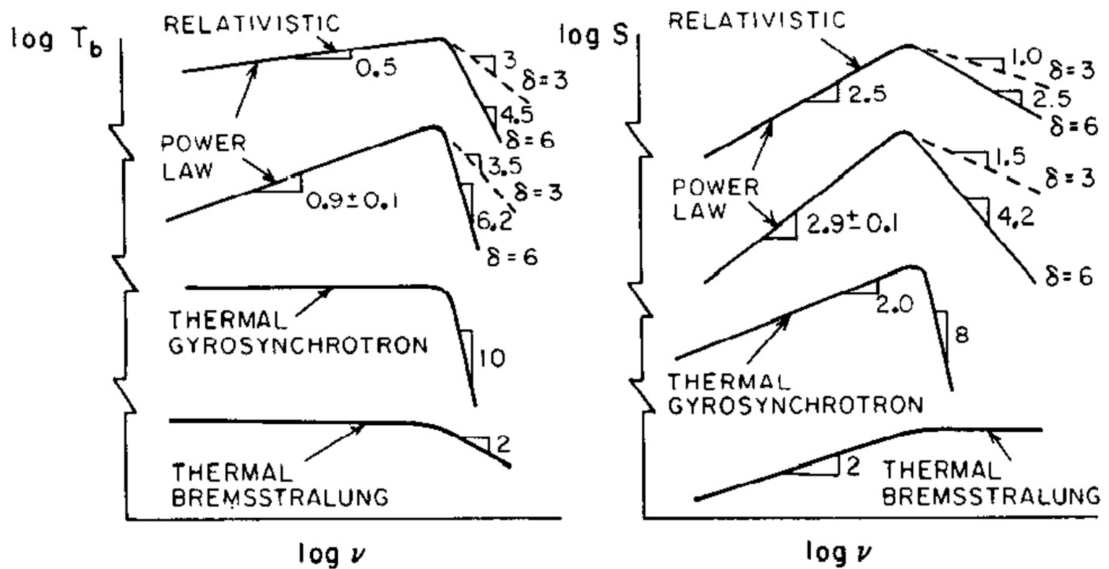
FIGURE 1.4: Schematic of the brightness temperature and flux density spectrum of relevant radio emission mechanisms. The top two curves represent synchrotron and gyrosynchrotron power law spectrum and free-free emission is represented in the bottom curve. Image taken from Dulk (1985).

- Thermal dust emission from envelopes/disks ($\sim 200 - 10000$ AU scales) (see the Disk Substructures at High Angular Resolution Project "DSHARP" − Andrews et al. 2018).

- Thermal bremsstrahlung from the base of partially ionized jets ($\sim$200 AU scales) (Anglada et al., 2018), or externally ionized circumstellar material by the strong radiation field from nearby massive stars ($\sim$200−500 AU scales) (Churchwell et al., 1987; Bally et al., 1998).

- Nonthermal synchrotron emission due to relativistic electrons accelerated in jet shocks ($\sim 10^3 - 10^4$ AU scales) (Osorio et al., 2017).

- Nonthermal (gyro)-synchrotron emission from magnetospheric activity at the smallest scales from magnetic structures linking the central object to the inner disks ($\lesssim$0.5 AU scales; see Figure 1.5) (Dulk, 1985; Feigelson and Montmerle, 1999; Güdel, 2002). This emission together with thermal X-ray emission from rapidly heated gas are both tracing high-energy processes in YSOs (discussed later in the text).

Figure 1.5 shows an illustration of a Class I protostar at three different spatial scales. The left panel shows the collapsing envelope at 10^4 AU scales, the middle panel shows the inner disk and outflow, these are the relevant scales for thermal radio emission from
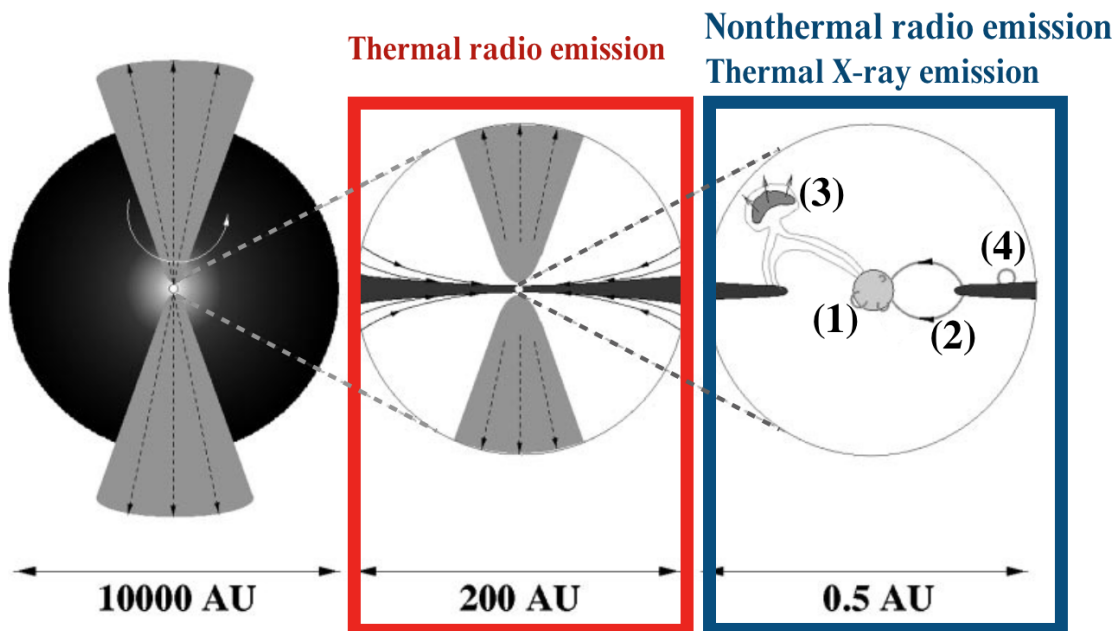
FIGURE 1.5: Schematic illustration of a Class I protostar at three different scales showing its innermost complex magnetic structure. Four magnetic-field configurations (labeled in right panel) that may be responsible for the magnetic activity. Image adapted from Feigelson and Montmerle (1999).

the circumstellar disks and also from ionised material at the base of stellar jets and outflows. Far from the thermal jet at several thousand AU from the central protostar there is also evidence of strong radio knots with negative spectral indices indicative of nonthermal radio jets at centimeter-wavelengths moving at several 10^2 kilometers per second (see Osorio et al. 2017; Anglada et al. 2018 and reference therein). These nonthermal knots are interpreted as strong shocks of the jet against the dense medium surrounding the protostar, and thus the nonthermal emission is likely synchrotron from shock-accelerated relativistic electrons. The right panel in Figure 1.5 shows the innermost scales with a star-disk magnetic interaction region where both thermal X-ray emission and nonthermal radio emission originate from the complex magnetic structure. Four possible magnetic-field configurations are labeled in the right panel, including (1) Solar-type multipolar fields with both footprints rooted in the stellar photosphere, (2) field lines connecting the star to the circumstellar disk at the corotation radius, (3) field lines above the corotation radius where plasmoids filled with X-ray-emitting gas can be ejected away from the disk by reconnection events caused by star-disk differential rotation, and (4) magnetic loops rooted in the disk (Feigelson and Montmerle, 1999).

In order to distinguish between these two mechanisms (thermal and nonthermal) in the observed radio flux of a source, a few diagnostic parameters can be considered. First,

the radio SED of an emitting source can indicate the dominant emission mechanism in terms of the radio SED slope in a log–log plane, this slope is termed spectral index (α), where $S_\nu \propto \nu^\alpha$ for a frequency ν and flux density S_ν, then:

$$\alpha_{radio} = \frac{\partial \log S_\nu}{\partial \log \nu} \qquad (1.6)$$

Thermal radio emission has a positive or flat spectral index, and negative for nonthermal emission. Polarized emission is another constraint to discriminate emission mechanisms. Thermal emission is unpolarized, whereas nonthermal emission is polarized in circular and linear polarization for gyrosynchrotron and synchrotron, respectively(Dulk, 1985; Güdel, 2002). Additionally, brightness temperature[7] (T_b) can also be used to identify nonthermal radio emission. Maximum possible values for thermal free-free emission for frequencies $\nu \gtrsim 1$ GHz are $\leq 10^5$ K (Condon, 1992; Condon and Ransom, 2016) while for nonthermal radio emission this can reach several million kelvin (Andre, 1996; Forbrich et al., 2021). The use of T_b as an observational technique for the observation of nonthermal radio emission will be discussed later in Chapter 4. Finally, rapid variability is also used as a tracer of nonthermal emission as it is associated to magnetic reconnection events that derive in (gyro)-synchrotron radiation at centimeter- or millimeter-wavelengths (Feigelson and Montmerle, 1985; Bower et al., 2003).

Variability in YSOs has been for long an observed property even since early observation when astronomers unknowingly looked at young stars noticing both infrared excess and signs of variability (Joy, 1945). Their variability occurs at a wide range of wavelengths and it can be periodic or stochastic. YSO variability can be associated with:

- Accretion rates: optical/IR/(sub)millimeter on timescales of hours to decades (see a review by Hartmann et al. 2016).

- Geometric changes in the circumstellar disks: optical and mid-infrared (e.g., Cody et al. 2014).

- Hot/cold spots on stellar surfaces: Optical (e.g., (Herbst et al., 1994)).

- Stochastic magnetic interactions between stellar surfaces and inner-disk edges: Optical (e.g., Alencar et al. 2010).

---

[7]Brightness temperature correspond to the temperature that a blackbody would need such that it can emit the same flux density as the observed source at a given frequency.

- Magnetic reconnection events above mentioned: Centimeter/millimeter radio wavelengths and X-ray emission: On timescales of minutes to hours, although the true timescales are still poorly understood since it is suggested that longer timescales variations could be due to a sequence of shorter magnetic events (Feigelson and Montmerle, 1999).

Generally, younger YSOs are more variable (evidence of more time-dependent phenomena and with higher amplitudes for their variability). These are evidently highly variable sources (e.g., Joy 1945 and a more recent review by Cody et al. 2014) and, in the context of rapid radio variability, together with thermal X-ray emission, both are our best tracers of high-energy processes in YSOs (Güdel, 2002; Feigelson and Montmerle, 1999).

The studies presented in this thesis are based on observations towards a nearby massive star-forming region containing both high- and low-mass YSOs (the Orion Nebula Cluster, see Section 1.4 for and overview of this region), although the focus remains on low-mass YSOs. In this regard, radio emission associated with high-mass young stars can be observed from photoionized gas by the embedded massive source in HII regions as thermal free-free emission at centimeter-wavelengths that can be classified as hypercompact HII (HCHII), ultra-compact HII (UCHII), compact HII (CHII), and diffuse HII (Churchwell, 1990, 2002; Kurtz, 2005). Additionally, massive molecular outflows are also seen towards high-mass star forming regions (e.g., Beuther et al. 2005) associated with infrared dark clouds (IRDCs; e.g., Egan et al. 1998). Similar to the thermal jets and nonthermal knots in jets from low-mass YSOs, these can be found in massive YSOs (e.g., Anglada 1996; Reid et al. 1995), as well as nonthermal emission associated to high-energy processes (e.g., Zapata et al. 2006). High-mass young stars also affect nearby young disks resulting in thermal free-free emission in externally photoionized disks (e.g., Garay et al. 1987; Zapata et al. 2004).

In the following section, I will discuss high-energy processes in low-mass YSOs with a main focus on the radio observables that can be used to trace these processes.

1.3 High-energy processes in Young Stellar Objects

High-energy processes are already present at the earliest stages of protostellar evolution as revealed by X-ray and radio observations (Feigelson and Montmerle, 1999). At radio wavelengths, we have already discussed how these processes can be traced by nonthermal emission in the form of (gyro)-synchrotron radiation (electrons gyrating along magnetic field lines in protostellar coronae and innermost regions of circumstellar disks). In this context, mildly relativistic electrons can produce gyrosynchrotron radiation detectable at cm-wavelenghts, while electrons at higher energies (MeV) are responsible for synchrotron radiation into the millimeter range (Dulk, 1985; Güdel, 2002). Despite their related nature, the physical connection between the emission at mm- and cm-wavelengths is just partially understood due to a lack of suitable data and, while a single source may show both simultaneously, there is evidence of millimeter-wavelength solar flares without centimeter counterparts (e.g., Kundu et al. 2000).

Similarly, the heated plasma from magnetic reconnection energy release results in thermal X-ray emission. Extensive work has been done with X-ray data, particularly from observations with the NASA's Chandra X-ray Observatory (Chandra). Observations and modelling of X-ray flare events are interpreted to be produced by rapid magnetic energy release from the outer stellar atmospheres, or accretion and magnetic interaction with circumstellar disks (Hayashi et al., 1996; Favata et al., 2005; Wolk et al., 2005; Güdel et al., 2007; Getman et al., 2008a,b).

Centimeter radio emission from YSOs has been explored in more detail in the last few years due to the improved sensitivity of radio facilities such as the Karl G. Jansky Very Large Array (VLA) and the Very Long Baeeline Array (VLBA) (Rivilla et al., 2015; Forbrich et al., 2016; Sheehan et al., 2016; Tobin et al., 2016; Forbrich et al., 2021), significantly enlarging the number of detected sources compared to studies prior to the upgraded capabilities of, for instance, the VLA[8] (see for example Felli et al. 1993a and Zapata et al. 2004). Recent analysis of deep VLA observations at cm-wavelengths towards hundreds of YSOs in the Orion Nebula Cluster (ONC) revealed intense radio flares with changes in flux density by a factor of 10 in less than 30 min and denominated as extreme radio variability events (Forbrich et al., 2017). These studies comprise a systematic

---

[8]A brief description on these facilities is given later in Section 1.6

search for YSOs variability at cm-wavelengths totaling up to ∼7440 h of cumulative YSO observing time and leading to a mean time between extreme radio variability events of 2482 ± 1433 h. On the other hand, millimeter continuum observations of YSOs are typically used to study the thermal component of circumstellar disks that arises from dust emission assumed to be constant on short timescales. However, a few serendipitous discoveries have shown evidence of strong millimeter flares in YSOs. The first such discovery was a mm-wavelength flare towards a T Tauri star in the ONC (GMR A) as reported in Bower et al. (2003). During these observations using the BIMA array at 86 GHz (∼3 mm) this source became the brightest one in the cluster. This flare was coincidentally complemented with simultaneous X-ray Chandra observations that found strong X-ray activity, starting two days prior to the 3-mm flare.

An additional example of a mm-flare, found towards the T Tauri binary system V773 Tau A, was interpreted to arise from interbinary collisions of coronal structures ("helmet streamers" of one component with the corona of the other) which results in regular flaring activity (Massi et al., 2002, 2006, 2008). Torres et al. (2012) also report gyrosynchrotron emission from the V773 Tau A system becoming brighter near periastron where the detected emission is confined to very compact regions (5–$7R_*$) indicating some interaction between the individual magnetospheres of the components given. A similar interpretation has been proposed for recurring millimeter-wavelength flares in the T Tauri spectroscopic binary system DQ Tau, after the discovery of a strong flare at 3 mm that peaked at almost ∼0.5 Jy. Follow-up observations suggest that these flares come from synchrotron emission due to interacting protostellar magnetospheres near periastron passage (Salter et al., 2008, 2010).

At shorter wavelengths (450 and 850 μm), a submillimeter flare was reported in Mairs et al. (2019) towards the binary T Tauri system JW 566, also in Orion. It was even more luminous than the flares detected in GMR A and DQ Tau, and represents the first coronal YSO flare detected at submillimeter-wavelengths. Together with the few examples of short-timescale mm flares, there are also millimeter variability studies of YSOs on longer timescales and in a different context where thermal dust emission is more relevant and its variability is caused by active mass accretion periods with an impact on timescales of months to years (Liu et al. 2018; Francis et al. 2019 and references therein).

TABLE 1.2: Star Forming complexes within 1 kpc from the Sun

Name	Distance (pc)	References
Taurus	120 to 160	Luhman (2018); Galli et al. (2019); Zucker et al. (2022)
Ophiuchus (ρ Oph)	120 to 140	Cánovas et al. (2019); Grasser et al. (2021)
Corona Australis	150	Galli et al. (2020a); Zucker et al. (2022)
Lupus	160	Galli et al. (2020b)
Perseus	290 to 315	Pavlidou et al. (2021); Zucker et al. (2022)
Orion	290 to 470	Kounkel et al. (2018); Großschedl et al. (2021)
Serpens	380 to 480	Herczeg et al. (2019)
Vela A, C, and D	700	Massi et al. (2019)
North America and Pelican	790	Kuhn et al. (2020)

1.4 Young stellar population in the Orion Nebula Cluster

A large number of star forming regions (SFRs) have been studied in the Solar neighbourhood and beyond (Reipurth, 2008a,b; Kuhn et al., 2019; Zucker et al., 2022) with several located in the main complexes within 1 kpc from the Sun (e.g., Taurus, Rho Ophiuchi, Corona Australis, Lupus, Perseus, Orion, Serpens, part of the Vela Molecular Ridge, North American and Pelican. See Table 1.2) Among these regions and within the Orion complex, the preferred site for observational studies is the Orion Nebula Cluster (ONC), a nearby massive star forming region with thousands of stellar sources in their early stages of evolution (Megeath et al., 2012; Hillenbrand et al., 2013; Großschedl et al., 2018). Figure 1.6 shows a wide field of the Orion A molecular cloud in an optical image overlaid on the Herschel-Planck column density map (Lombardi et al., 2014) highlighting the position of the ONC in red and additionally indicating several objects and star-forming regions throughout cloud complex.

A range of distances have been determined to the ONC throughout the years. Early attempts based on optical radial velocities and proper motions of a few tens of sources yield distances between 380 and 520 pc (Johnson, 1965; Strand, 1958). The accepted distance in the present days is 400 pc based on parallax measurements from optical and radio observations, particularly from *Gaia* mission[9] (Großschedl et al., 2018; Kuhn et al., 2019; Getman et al., 2019) and the NRAO[10] Very Long Baseline Array (VLBA; Menten et al. 2007; Kounkel et al. 2017). The advantages of the ONC over other SFRs, in addition to the fact of being the nearest site of massive star formation, is its convenient

---

[9]Gaia Collaboration et al. (2016); Gaia Collaboration et al. (2021)

[10]The National Radio Astronomy Observatory (NRAO) is operated by Associated Universities, Inc., under a cooperative agreement with the National Science Foundation (NSF).
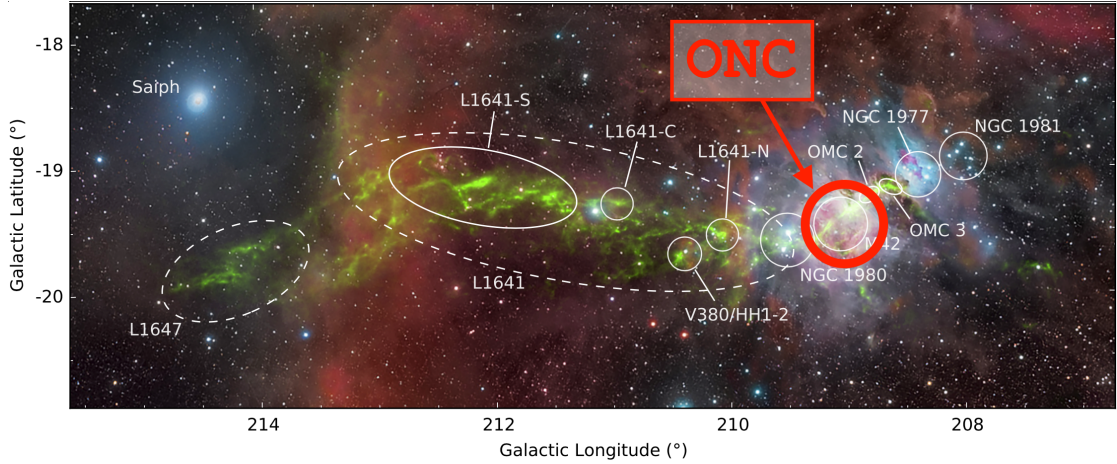
FIGURE 1.6: Optical composite image of the Orion A field (credit: Roberto Bernal Andreo) overlaid on a *Herschel*-Planck column density map from Lombardi et al. (2014) in green. The main regions in the cloud are labeled in white while the ONC is highlighted in red. Image adapted from Meingast et al. (2016).

distance where a large number of young stars can be observed in a smaller projected area on the sky compared to closer regions that become observationally expensive not to mention that these are intrinsically less rich with a lower number of sources.

Given its distinctive attributes, there is a wealth of studies based on the ONC and continuous attempts to describe its stellar population by terms of source distribution, density, evolutionary status and their environment. For instance, Megeath et al. (2016) presented an IR study based on the *Spitzer* Space Telescope Survey of the Orion Molecular clouds. They find that almost 60% of the YSOs found in regions with protostellar surface densities ≥ 10 pc^{-2} are in the ONC. Based on structural properties of the cluster they infer an age of ~2 Myr for the ONC. They find 2821 YSOs in Orion A and 3191 YSOs if including X-ray identified sources. By applying a completeness correction factor (based on the X-ray population) they estimate that there are 4199 YSOs in Orion A.

Earlier studies reported in Hillenbrand and Hartmann (1998), estimated the cluster mass (within 2 pc from the Trapezium) to be ~ 4500 M$_\odot$ which is about twice the stellar mass, as well as the central stellar density to be around 2×10^4 stars pc^{-3} making the ONC the densest nearby cluster. Moreover, the projected geometry of the ONC is elongated resembling also its molecular gas distribution as an additional evidence of its youth. Additional structure parameters were later reported in Hillenbrand et al. (1998), where they find a median stellar mass for the ONC of 0.25 $M_\odot$, a mean radius for low-mass star of 1.8 $R_\odot$, evidence of disks in about 60% and 90% of the population

(disk fraction) been this higher in the inner parts of the cluster (within 0.5 pc) and a total stellar mass in the ONC of about 10^3 $M_\odot$ (Hillenbrand, 1997; Da Rio et al., 2012).

Amongst the X-ray studies mentioned above regarding on high-energy processes, the Chandra Orion Ultra-deep Project (COUP; Getman et al. 2005b) is the deepest X-ray survey of a star forming region (Feigelson et al., 2005; Getman et al., 2005a). COUP monitored the ONC for almost ∼10 days over a $17' \times 17'$ field of view. High-energy processes tracers such as X-ray emission can detect deeply embedded sources that may be strongly affected by the bright nebulosity (e.g., mid-IR). More recently, an updated census of the young stellar population in the Orion A molecular cloud was presented in Großschedl et al. (2019), primarily using the VISTA[11] near-infrared catalogue from the "VIenna Survey In OrioN" (VISION; Meingast et al. 2016) and combined with the extensive archival data including mid- to far-infrared, optical, and also X-ray data. This updated catalogue contains almost 3000 infrared YSO candidates for the whole Orion A cloud, of which about one third are found in the ONC field despite of the large area of the whole cloud complex and the several other regions along the tail and head of the cloud (see 1.6).

Among the most interesting regions in the cluster, at the heart of the ONC, the densest area, hosts the massive Trapezium cluster consisting of the most massive stellar systems. The Trapezium Cluster is the densest part of the ONC within about $2'$ (corresponding to ∼0.3 pc), while the larger ONC extends to about $20'$ (<3 pc) (Hillenbrand et al., 2013). Figure 1.7 shows an optical composite image from the HST of the whole ONC field indicating the Trapezium cluster and its components. The Trapezium hosts one of the youngest and nearest high-mass stars (O5-O7), θ^1 Ori C (also labeled in Figure 1.7), known to be a close binary as reported in Kraus et al. (2007). In this work they traced the orbital motion of the system's components using visual and NIR interferometric spectra and NIR long-baseline inteferometric data. It has a high eccentricity ($e \approx 0.91$) and short-period ($P \approx 10.9$ yrs) orbit. Also in that work, the authors propose a system mass of 48 $M_\odot$ and a distance of 434 pc to the cluster.

Protoplanetary disks (proplyds) surrounding young, low-mass stars in rich young clusters can be affected by the effects of other cluster members (tidal interactions) as well

---

[11]Visible and Infrared Survey Telescope for Astronomy (VISTA, Emerson et al. 2006), a 4-m class telescope operated by the European Southern Observatory (ESO) as part of its Cerro Paranal facilities, mounted with the VISTA Infrared Camera (VIRCAM, Dalton et al. 2006).
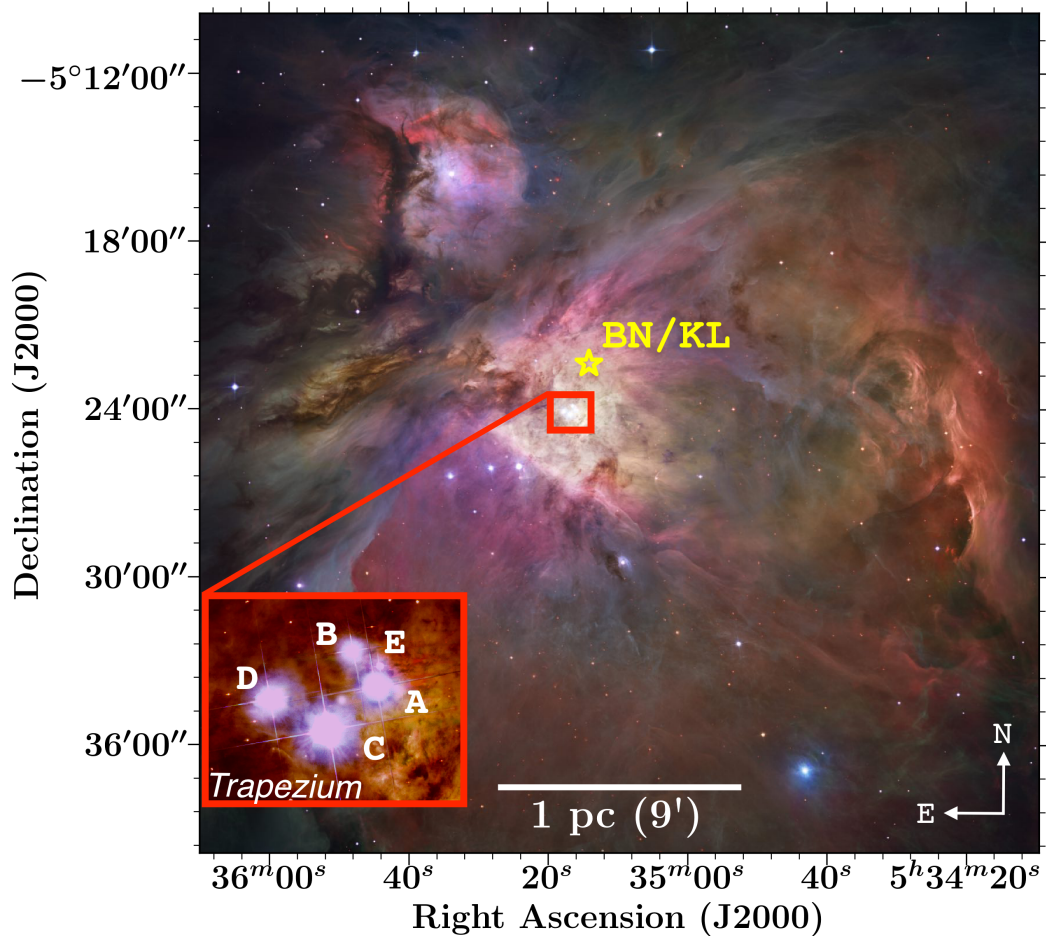
FIGURE 1.7: The Orion Nebula Cluster. The yellow symbol indicates the BN/KL region for reference and the inset shows an enlarged section of the image to highlight the Trapezium cluster indicating in white its main components. The background image is a composite HST image (ACS/WFC) of the Orion Nebula (Credit: NASA, ESA, M. Robberto, and the Hubble Space Telescope Orion Treasury Project Team).

as the UV radiation field from massive stars within the cluster. θ^1 Ori C dominates the ionizing radiation of the ONC and thus is the responsible for the external photoionization of proplyds in the ONC (O'dell et al., 1993; Felli et al., 1993a; O'dell and Wen, 1994), and in turn, this effect can also lead to observable thermal radio emission from the photoionized gas (later discussed in Chapter 2, section 2.3.2).

Another interesting region in the ONC, is the Orion Becklin–Neugebauer/Kleinmann–Low region (BN/KL) (Becklin and Neugebauer, 1967; Kleinmann and Low, 1967). The position of the BN/KL region is also highlighted in Figure 1.7. In this region, an extraordinary outflow arises from the Orion OMC1 cloud core (Zapata et al., 2009; Bally et al., 2011, 2015, 2017, 2020) and also known as "Orion Fingers" (Taylor et al., 1984; Allen and Burton, 1993). The OMC1 outflow has an explosive morphology of molecular material

consequence of the dynamical encounter of stars which were ejected with speeds of a few tens of km/s more than 500 years ago (Bally and Zinnecker, 2005; Rodríguez et al., 2005b). Centimeter radio features associated to the "Orion Fingers" will be discussed in Chapter 2 regarding to their radio proper motions.

Regarding to radio wavelengths observation towards the ONC, the first compact radio detection toward ONC was in the early 80s when Moran et al. (1982, 1983) observed radio continuum emission toward the BN object in the Orion−KL region and it was indeed the first time that a young star was detected at centimeter-wavelengths using the VLA interferometer, then Garay et al. (1987) reported a new catalogue of compact radio sources using VLA at frequencies between 1.5−22.5 GHz. More than a decade later, the already mentioned strong millimeter flare discovered by Bower et al. (2003) (GMR-A T Tauri star) was also accompanied by a strong X-ray flare just ∼ 2 days before the radio detection. A year later, (Zapata et al., 2004) presented a catalogue of 77 compact radio sources with 36 of them showing variability (see also Felli et al. 1993b; Rivilla et al. 2015). Forbrich et al. (2008) reported a strong flare at 22 GHz toward a deeply embedded YSO in the Orion BN/KL region.

Additionally, VLA data has been used to put constraints on the kinematics of the ONC (Gómez et al., 2005, 2008). Multi-epoch VLA observations, prior to its upgrade, spanning almost 29 years have been used in Dzib et al. 2017 to measure the proper motions of the core of the ONC and the BN/KL region. From their results, even when the ONC does not show evidence of expansion, contraction or rotation, there are still interesting objects with peculiar proper motions such as the probable runaway star V 1326 Ori. The fraction of sources detected in this work was limited by the sensitivity provided by the old version of the VLA (88 sources detected), which was significantly improved with its upgraded version as shown in Forbrich et al. (2016) where 556 compact source were detected.

The ONC has been widely studied and it will continue to be the benchmark for star formation research. It will certainly be a suitable target for the upcoming facilities and instrumentation benn developed that will offer extraordinary improvements at a wide range of wavelengths, including the recently commissioned JWST, the new generation of interferometers (ngVLA and SKA − e.g., Isella et al. 2015; Dewdney et al. 2009; or the upcoming receivers for ALMA − Huang et al. 2022), the Giant Magellan Telescope, the

Extremely Large Telescope, etc., that will keep their "eyes" on this inexhaustible source of discoveries.

1.5   Overview of Radio Interferometry

We have seen in the previous section that the ONC has been extensively studied at multiple wavelengths including studies at radio frequencies dated back to late 60s. Early radio continuum observations of the ONC using single-dish telescopes have been used to constraint the extended structure of the ionised gas in the cluster where the integrated continuum flux estimates at centimeter-wavelengths was found to be as bright as $\sim 400 - 470$ Jy (Schraml and Mezger, 1969; Goss and Shaver, 1970), but such observations are not able to resolve the inner structure of the cluster and these are even further to resolve individual sources due to the low resolution obtained with single-dish telescopes ($> 2'$). In order to reach resolutions high enough to disentangle centimeter radio emission associated to individual sources, gigantic dish telescopes would be needed (see discussion below) even for the closest star forming regions, and on top of that, individual sources in the cluster have flux densities orders of magnitude fainter than the bulk emission of the ONC (see Forbrich et al. 2016 and references therein).

An observational leap to achieve high-resolution radio observations able to resolve faint individual sources is accomplished by radio interferometry, technique that is extensively used in the studies presented in this thesis. In this section I will described the fundamentals of this technique.

We really are in a privileged era of radio astronomy not only for the benefits of the extraordinary progress made since its very birth in the early 30s with Karl Jansky's serendipitous discovery of radio signal from the Galactic center (Jansky, 1933; Reber, 1940), but also because we are in the middle of recent technological upgrades and developments such as the next generation interferometers (e.g., Venturi et al. 2020).

The origin of radio interferometry emerges from the limited angular resolution achievable by single dish telescopes, which is proportional to the ratio between the observed wavelength and the antenna diameter, $\theta \propto \lambda/D$, where θ is angular resolution, λ is the wavelengths of the observed radiation, and D is the diameter of the instrument. Radio wavelengths are long enough to require antennas with diameters in the order of

kilometers to achieve arcsecond resolution. This led to the development of interferometry, a technique that combines the coherent signal from a set of small antennas (also denoted as aperture elements) to synthesize a larger aperture in order to achieve a resolution equivalent to that of an antenna of the same size of such synthesized larger aperture. This technique does not obtain a direct image of the observed source, instead it is used to infer the properties of the incident light, and it is able to produce an image representation of the sky brightness at angular resolutions given by the longest separation B between the individual small apertures ($\theta \approx \lambda/B$).

Interferometry is, in principle, based on the interference property of light demonstrated by the Young's double slit experiment[12] (Young, 1804). A radio interferometer, thus measures the interference pattern (or fringe pattern) of the observed electromagnetic wave produced by pairs of apertures. This fringe pattern can be related to the image brightness distribution of the observed source through a Fourier transform (van Cittert-Zernike theorem; van Cittert 1934; Zernike 1938), therefore, an interferometer observes the Fourier transform of an object's brightness pattern on the sky. In the following I will briefly summarize some important concepts for radio interferometry following the definitions from Thompson (1999); Napier (1999); Cornwell et al. (1999); Wilson et al. (2012); and Thompson et al. (2017).

The data obtained from an interferometric observation can be analysed by sets of antenna pairs or two-element interferometer. Figure 1.8 shows an schematic of a two-element interferometer consisting of two antennas collecting the radio waves and pointing at a source in the direction $\hat{s}$ at an angle θ from the baseline vector. The two antennas receive a wavefront signal with a time delay due to the geometric geometric configuration of the observations. This delay is defined by:

$$\tau_g = (\vec{b} \cdot \hat{s})/c \tag{1.7}$$

or in terms of θ by:

$$\tau_g = \vec{b} \cdot \cos\theta \tag{1.8}$$

---

[12]A pair of antennas is analogous to the double-slit experiment where coherent radiation from an emitting point source is diffracted as it pass through two small apertures of diameter "a" separated by distance "d", with $a << d$, generating an interference pattern (fringe pattern with a central peak followed by sidelobes) as the diffracted waves interfere constructively and destructively. The Double-slit equation is given by $m\lambda = d\sin(\theta)$ where constructive points are found for $m = (0, 1, 2, ...)$. θ is the angular spacing between constructive point in the fringe pattern and λ is the wavelength of the emitted radiation.
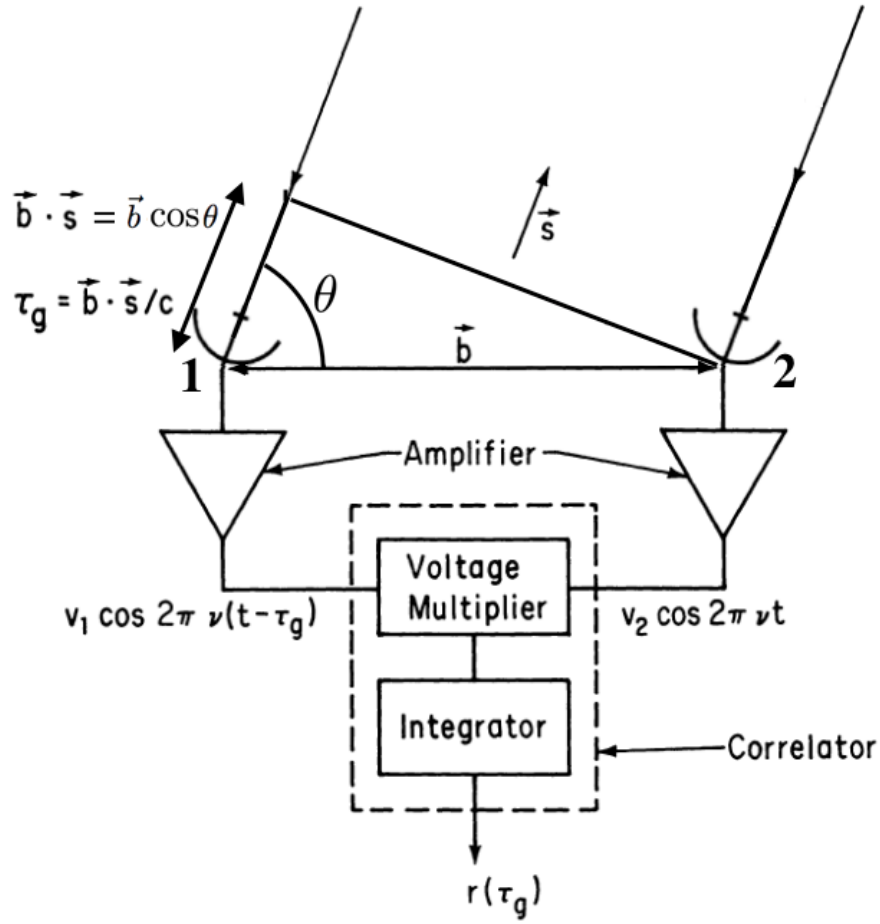
FIGURE 1.8: Simplified schematic diagram of a two-element interferometer. Adapted from Thompson (1999).

where $\vec{b}$ and c are the baseline vector and the speed of light, respectively. Thus, the output voltage from both antennas are the same but delayed by τ_g ("geometrical delay"), and these are defined by:

$$V_1(t) = V \cos{(2\pi\nu t)} \quad \text{and} \quad V_2(t) = V \cos{(2\pi\nu[t - \tau_g])} \tag{1.9}$$

These are combined in the correlator where they are multiplied and time averaged. The correlator response R_C (the C index stands for cosine) is then defined as:

$$R_C = \langle V_1(t) V_2(t) \rangle \qquad = V^2 \cos{(2\pi\nu t)} \cos{(2\pi\nu[t - \tau_g])}$$
$$R_C = \left(\frac{V^2}{2}\right) \cos{(2\pi\nu\tau_g)} \tag{1.10}$$

The first term $\frac{V^2}{2}$ corresponds to the correlator output amplitude and is proportional to flux density of the point source by a factor of $\sqrt{A_1 A_2}$, where A_1 and A_2 are the effective collecting areas of the two antennas. Also, the change in source direction $\hat{s}$ respect to $\vec{b}$ due to Earth's rotation results in a sinusoidal variation in the voltage R_C that is called fringes, whose phase (ϕ_f) is defined by the cosine angle term ($2\pi\nu\tau_g$) in Equation 1.10 and is is called fringe phase. The change in phase as $\vec{s}$ changes (source direction) and taking into account Equation 1.8 and $\nu = c/\lambda$:

$$\phi_f = 2\pi\nu\tau_g \tag{1.11}$$

$$\frac{d\phi_f}{d\theta} = -2\pi \left(\frac{|\vec{b}|\sin\theta}{\lambda} \right) \tag{1.12}$$

Then, for $\Delta\phi_f = 2\pi$ (full period), implies a $\Delta\theta = \lambda/(|\vec{b}|\sin\theta)$, and this is defined as beamwidth:

$$\theta_S \approx \frac{\lambda}{b\sin\theta} \tag{1.13}$$

Similarly as for Equation 1.10 given for a point source, the correlator response for a spatially extended source element $d\Omega$ in the direction of unit vector $\hat{s}$ at a frequency $\nu = c/\lambda$ whose radio brightness is represented by $I_\nu(\hat{s})$, is given by:

$$R_C = \int I_\nu(\hat{s}) \cos(2\pi\nu\vec{b}\cdot\hat{s}/c)d\Omega = \int I_\nu(\hat{s})\cos(2\pi\vec{b}\cdot\hat{s}/\lambda)d\Omega \tag{1.14}$$

This expression corresponds to the symmetric component of $I_\nu(\vec{s})$, but a cosine fringe pattern is "blind" to asymmetric structure, in order to recover the asymmetric component, the sine fringe pattern is needed. This can be recovered by applying a 90 deg phase delay into the output of one of the antennas:

$$R_S = \int I_\nu(\hat{s}) \sin(2\pi\vec{b}\cdot\hat{s}/\lambda)d\Omega \tag{1.15}$$

These definitions set the base to a fundamental function in radio interferometry which is the visibility of a source. It is a construction from two functions and is defined by a complex number whose real and imaginary parts are the cosine and sine response of

the interferometer, respectively, although both R_C and R_S are real functions (Equations 1.14 and 1.15). The complex visibility is thus $V \equiv R_C - iR_S = Ae^{i\phi}$ with and amplitude A and a phase ϕ defined by:

$$A = (R_C^2 + R_S^2)^{1/2} \tag{1.16}$$

$$\phi = \tan^{-1}\left(\frac{R_S}{R_C}\right) \tag{1.17}$$

Thus, the complex visibility V_ν of a source and its sky brightness distribution $I_\nu(\hat{s})$ are related by the Fourier transform (van Cittert-Zernike theorem; van Cittert 1934; Zernike 1938):

$$V_\nu = R_C - iR_S = \int I_\nu(\hat{s})e^{-i2\pi\nu\vec{b}\cdot\hat{s}/c}d\Omega \tag{1.18}$$

Conventionally, this expression is given in (u,v) and (l,m) coordinates. As shown in Figure 1.9, the (u,v) plane represents the projected baselines onto the plane of the sky in the direction of the observed source, where u and v are given in E-W and N-S orientation, respectively, and these are measured in wavelength units ($u = \frac{|\vec{b}|\hat{x}}{\lambda}$ and $v = \frac{|\vec{b}|\hat{y}}{\lambda}$) and also called spatial frequencies. The orthogonal axis to the (u,v)-plane (in the direction of the sky) is denoted as w. On the other hand, the (l,m) coordinates, perpendicular to the phase tracking centre, are described as direction cosines l and m, which are coordinates of source direction vector (E-W and N-S angles on the plane of the sky, respectively). Using this system convention, the 2D Fourier transform of the complex visibility function $V(u,v)$ to obtain the sky brightness distribution $T(l,m)$ is given by:

$$V(u,v) = \int\int T(l,m)\,e^{-2\pi i(ul+vm)}dldm \tag{1.19}$$

$$T(l,m) = \int\int V(u,v)\,e^{2\pi i(ul+vm)}dudv \tag{1.20}$$

In order to obtain a better representation of the sky brightness, a well sampled (u,v) plane is needed by using a large set of antenna pairs. This is also called "aperture
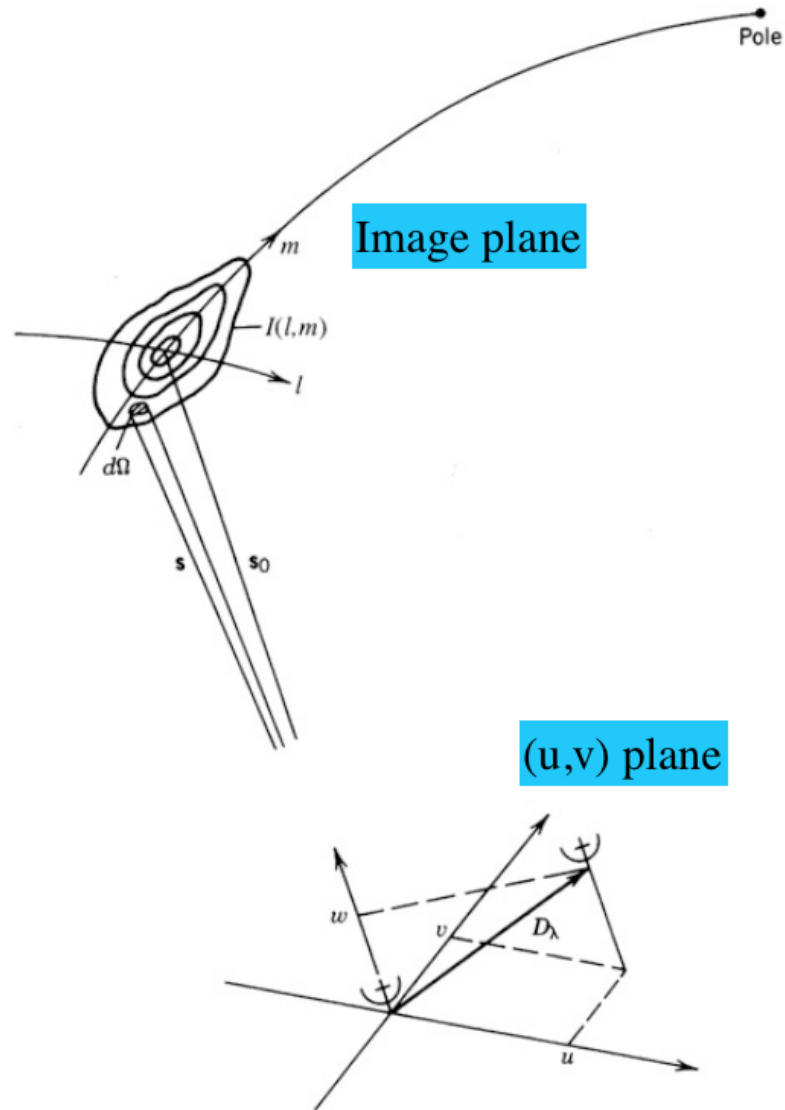
FIGURE 1.9: Geometric relationship between a source under observation $I(l,m)$ and an interferometer or one antenna pair of an array. The antenna baseline vector, measured in wavelengths, has length $|\vec{b}|$ denoted by D_λ in the illustration and has components (u,v,w). Adapted from Thompson et al. (2017).

synthesis" (Ryle, 1975)[13], and in order to further improve this coverage the Earth's rotation is also an advantage in sampling the (u,v) plane over time ("earth rotation synthesis"). Essentially, a good quality image needs a good coverage of the (u,v) plane (a good visibility sampling), however real observations have gaps in the final (u,v) plane coverage since these consist of discrete visibilities rather than a continuous coverage, and this results in a "Dirty Image" given by:

---

[13]Aperture synthesis technique played an important role for the 1974 Nobel Prize in Physics awarded by Martin Ryle. This prize was jointly awarded by M. Ryle and Antony Hewish, this latter by his role on the discovery of pulsars made by Jocelyn Bell Burnell in the late 60s

$$T^D(l,m) = \int\int S(u,v)\,V(u,v)\,e^{2\pi i(ul+vm)}dudv \tag{1.21}$$

where $S(u,v)$ is the sampling function (or weighting function) that is non-zero only for the sampled points of the (u,v) plane. The Fourier transform of the sampling function defines the "dirty beam" (which is the analogue of the point spread function of an optical telescope):

$$B(l,m) = \int\int S(u,v)\,e^{2\pi i(ul+vm)}dudv \tag{1.22}$$

Using the convolution theorem (the convolution of two functions is the product of the Fourier transform of these functions, in other words, the product in one domain is the convolution in the other domain) and Equations 1.20 and 1.22, then the dirty image (Equation 1.21) can be expressed as the true image convolved with the dirty beam as:

$$T^D(l,m) = T(l,m) * B(l,m) \tag{1.23}$$

The dirty image thus contains information of the sky brightness distribution provided only by the sampled visibilities, therefore an image reconstruction technique is required in order to predict the full information, such a technique should consist in a deconvolution of the dirty image to obtain a model of the true sky brightness distribution. The deconvolution process consists on the use of non-linear techniques to extrapolate/interpolate visibility samples into regions not sampled by the (u,v) plane to find a more complete and plausible model of the true $T(l,m)$. There is no unique solution for image reconstruction and different approaches have been proposed, amongst them the most common deconvolution algorithms for image reconstruction are "CLEAN", "Maximum Entropy Method" (MEM), and their variants (a detailed description of these is presented in Cornwell et al. 1999). In the studies presented in this thesis the "CLEAN" algorithm is used which I will briefly describe in the following.

The "CLEAN" algorithm was first presented in Högbom (1974) mainly aimed to overcome the prominent effects of the extended sidelobe patterns of the dirty beam. This approach assumes that the sky brightness distribution can be represented by a collection of point sources in a mostly empty field. The main steps of "CLEAN" are:

- Find the strength and position of the brightest point in the absolute intensity (the maximum peak in the image or in a defined portion of the image called CLEAN window or box).

- Define a factor γ that is a fraction of the peak strength found in the previous step. This factor γ is called loop gain.

- Subtract from the dirty image, at the position of the above peak, the dirty beam multiplied by γ and record into a model the position and magnitude of the point source subtracted which is called a CLEAN component.

- Iterate over these steps until the remaining peaks in the dirty image reach a predefined threshold (usually a factor of the noise level). The result of the consecutive subtractions in the dirty image is called the residuals.

- Define a CLEAN beam consisting of an elliptical Gaussian fitted to the main lobe of the dirty beam, and convolve the model image (all the CLEAN components) with the CLEAN beam.

- Finally add the residual map to generate the "restored image".

Some variations of the standard "CLEAN" method include the Clark and the Cotton-Schwab algorithms, also described in Cornwell et al. (1999). Since the main assumption of CLEAN is based on the superposition of point sources, the reconstruction of extended sources can still be represented by smoothed superposition of point sources. The alternative deconvolution algorithm mentioned above, the MEM algorithm (e.g., Skilling and Bryan 1984) is generally a better approach for extended emission. The radio interferometric dataset from radio facilities such as VLA and ALMA presented in Chapters 2 and 3 have been imaged based on the CLEAN methods, as well as the imaging examples for part of the VLBA dataset presented in Chapter 4. These facilities are briefly described in the following section.

1.6 Interferometric Facilities

The main focus of this thesis is the study of radio emission from large samples of YSOs to analyze their variability. For this purpose, the most versatile and powerful

radio interferometers have been used including the VLA, ALMA, and the VLBA. The wide range of scientific goals achieved by these radio facilities have revolutionised our understanding of the universe, ranging from the study of the most distant galaxies that sheds light on the origin of the universe, to the study of the most nearby protostars in our own Galaxy with unprecedented sensitivity and spatial resolution. Here I will briefly describe these three radio interferometers.

1.6.1 Karl G. Jansky Very Large Array (VLA)

The Karl G. Jansky Very Large Array (VLA) is a radio interferometer operated by the National Radio Astronomy Observatory (NRAO)[14] observing at wavelengths between 0.7 cm and 4 m. The VLA is located on the Plains of San Agustin in New Mexico, northwest Socorro in the United States, at an altitude of about 2,125 m. While its first interferometric observations started as early as 1976, it was fully operational since 1980, and has had an important role in the study of radio emission from YSOs since the very beginning of its operations discovering the first compact cm-radio counterpart of young stars (Moran et al., 1982, 1983). The VLA consists of 28 dish antennas of 25-m diameter each, with 27 of these actively working and one kept as a spare antenna. The 27 active ones are arranged in a Y-shape pattern with one of its arms that can extend up to 18 km and the two other arms up to 21 km. The antennas are mounted on piers and can be transported on railroads to specific positions along these arms that, on a regular schedule, cycles through four different standard configurations, the most extended one has baselines of up to 36 km (A-Configuration), followed by configurations B, C, and D, with maximum baseline lengths of 11, 3.4, and 1 km, respectively. With the most extended A-configuration, the VLA can achieve an angular resolution of 43 milliarcseconds (mas) at 45 GHz (Perley et al., 2011).

The VLA has currently a frequency coverage between 54 MHz and 50 GHz distributed in 10 frequency bands shown in Table 1.3. For this thesis, the C-band with a central wavelength of 6 cm (highlighted in yellow in Table 1.3), has been used in the study presented in Chapter 2.

---

[14]National Radio Astronomy Observatory is a facility of the National Science Foundation operated under cooperative agreement by Associated Universities, Inc.

TABLE 1.3: VLA frequency bands

Band	Nominal Wavelength	Frequency (GHz)
4	4 m	0.054−0.084
P	90 cm	0.240−0.470
L	20 cm	1.0−2.0
S	13 cm	2.0−4.0
C	6 cm	4.0−8.0
X	3 cm	8.0−12.0
Ku	2 cm	12.0−18.0
K	1.3 cm	18.0−26.5
Ka	1 cm	26.5−40.0
Q	7 mm	40.0−50.0

1.6.2 Atacama Large Millimeter/submillimeter Array (ALMA)

Tha Atacama Large Millimeter/submillimeter Array[15] (ALMA) is amongst the forefront interferometric facilities and largest ground-based astronomical observatories in the world. It operates at (sub)millimeter-wavelengths, currently between 0.32 to 3.6 mm and will extend its spectral coverage up to 8.5 mm in the coming years[16]. ALMA is located at an altitude of 5000 m on the Chajnantor plateau in the Atacama desert in northern Chile. This privileged location offers one of the best climatic conditions (clearest and driest regions in the world; Rutllant Costa 1977) that together with its high altitude considerably reduce the impact that the water vapor present in the atmosphere have on the incoming radiation at radio frequencies.

ALMA consists of 66 high-precision dish antennas of two different diameters, 12 and 7 m, and a total collecting area of 6,600 m^2. The main array is composed by 50 antennas of 12-m diameter (called the "12m array") that can be moved between different specific positions (192 antenna sites or "antenna pads") using the Antenna Transporter vehicles to set the array into a compact configuration spanning ∼160 m across or into an extended configuration spanning up to 16 km across. There is also a compact array, the Atacama Compact Array (ACA), composed by 4 antennas of 12-m diameter (the Total Power Array or TP Array) and 12 antennas of 7-m diameter (the "7m array"). The ACA consists of a tight spiral configuration with a small north-south elongation where the

---

[15]ALMA is a partnership of ESO (representing its member states), NSF (USA), and NINS (Japan), together with NRC (Canada), NSC and ASIAA (Taiwan), and KASI (Republic of Korea), in cooperation with the Republic of Chile. The Joint ALMA Observatory is operated by ESO, AUI/NRAO, and NAOJ.

[16]https://www.eso.org/public/teles-instr/alma/receiver-bands/

outer antennas can be moved to set a more elongated configuration to avoid shadowing at low elevations and therefore been able to extend over $30-50$ m (Iguchi et al., 2009).

The most compact array configuration of ALMA can achieve spatial resolutions between $0.5''$ and $4.8''$ for central frequencies of 950 GHz and 110 GHz, respectively. With the most extended array configuration ALMA can achieve spatial resolutions between 2 mas and 43 mas for central frequencies of 230 GHz and 110 GHz, respectively. The current frequency range available in ALMA spans between 84 GHz up to 950 GHz, equivalent to a wavelength range between 3.57 mm down to 0.32 mm. This frequency range is divided into different receiver bands starting with the lowest frequency in Band 3 until the highest one in Band 10 (see Table 1.4). The frequency range will be extended down to 35 GHz with two new bands, Band 1 and 2, that will be available in the coming years. Band 3, highlighted in yellow in Table 1.4, indicates the relevant frequency band used for the study presented in Chapter 3 of this thesis.

TABLE 1.4: ALMA frequency bands

Band	Wavelength (mm)	Frequency (GHz)
1*	$8.57-6.00$	$35-50$
2*	$4.48-3.33$	$67-90$
3	$3.57-2.59$	$84-116$
4	$2.40-1.84$	$125-163$
5	$1.84-1.42$	$163-211$
6	$1.42-1.09$	$211-275$
7	$1.09-0.80$	$275-373$
8	$0.78-0.60$	$385-500$
9	$0.50-0.42$	$602-720$
10	$0.38-0.32$	$787-950$

* ALMA Bands 1 is currently being installed and Band 2 is still in development.

1.6.3 Very Long Baseline Array (VLBA)

The Very Long Baseline Array (VLBA) is a very-long-baseline interferometry (VLBI) array operated by the NRAO and consists of 10 identical antennas of 25 m diameter each observing in a frequency range between 0.3 and 90 GHz (90 cm to 3 mm) serving for both geodetic and astronomical/astrometric observations (Napier et al., 1994; Napier, 1995). The VLBA was the first array fully dedicated to VLBI whose official operations

after being completed started in 1994. The ten antennas are distributed around the United States, with eight of them in continental territory, one in Virgin Islands, and one in Hawaii (see Table 1.5) with the shortest baselines around 200 km and a maximum baseline of 8,600 km. Its frequency coverage and large baselines pose the VLBA as a leading facility for astrometric purposes achieving angular resolutions down to micro-arcseconds. Additionally, the longest baselines make the VLBA sensitive to sources with high brightness temperature particularly relevant for the study of nonthermal radio emission and thus a strong tool for the study of high-energy processes in unresolved YSOs, for example. This will be explained and discussed in Chapter 4.

TABLE 1.5: Location of the 10 VLBA stations/antennas. Adapted from Napier et al. (1994).

Location	N. Latitude (deg min sec)	W. Longitude (deg min sec)	Elevation (m)
St. Croix, VI	17 45 30.57	64 35 02.61	16
Hancock, NH	42 56 00.96	71 59 11.69	309
N. Liberty, IA	41 46 17.03	91 34 26.35	241
Fort Davis, TX	30 38 05.63	103 56 39.13	1615
Los Alamos, NM	35 46 30.33	106 14 42.01	1967
Pie Town, NM	34 18 03.61	108 07 07.24	2371
Kitt Peak, AZ	31 57 22.39	111 36 42.26	1916
Owens Valley, CA	37 13 54.19	118 16 33.98	1207
Brewster, WA	48 07 52.80	119 40 55.34	255
Mauna Kea, HI	19 48 15.85	155 27 28.95	3720

The frequency coverage of VLBA ($0.3-90$ GHz) is arranged in ten frequency band shown in Table 1.6. The study presented in Chapter 4 is based on observations carried out in the C-band (highlighted in yellow in Table 1.6) using a frequency range between 7.068 and 7.324 GHz.

TABLE 1.6: VLBA frequency bands

Band Designations*	Frequency range (GHz)	Central Frequency (GHz)
90 cm (P)	0.312−0.342	0.326
50 cm (UHF)	0.596−0.626	0.611
20 cm (L)	1.35−1.75	1.438
13 cm (S)	2.2−2.4	2.269
6 cm (C)	3.9−7.9	4.993
4 cm (X)	8.0−8.8	8.419
2 cm (Ku)	12.0−15.4	15.363
1 cm (K)	21.7−24.1	22.236
7 mm (Q)	41.0−45.0	43.124
3 mm (W)	80.0−90.0	86.2

* NRAO nomenclature is not exclusive for VLBA, and mostly follows the Institute of Electrical and Electronics Engineers (IEEE) standards with a few exceptions (e.g., bands P and Q).
Different ranges within the 3.9-7.9 GHz receiver highlighted in yellow.

1.7   Motivation and objectives of this work

The improved sensitivity and resolution of the upgraded radio facilities in the last decade that came with wideband receivers is now allowing us to study YSOs and protostars efficiently with hundred of detections in a few hours in nearby SF regions. At the same time, thanks to this improved sensitivity it is possible to detect radio emission from YSOs in a matter of minutes or even in shorter integration times. This exceptional capability sets the beginning of a new era in radio time-domain study of YSO, a key tool for the study of high-energy processes in young stars. Such an interesting research field is additionally relevant for the study of high-energy processes associated to flare-like events that are orders of magnitude more energetic that of the Sun, and thus offering a promising research window to understand the earliest phases in the evolution of our own Solar system. Taking advantage of this capabilities, in this thesis I present the results from an extensive radio variability study of hundreds of compact radio sources comprising a large number of YSOs at centimeter and millimeter-wavelengths.

When it comes to factors that can affect the evolution of protoplanetary disks, the ONC is naturally an ideal laboratory for such studies. For instance, UV radiation from massive stars, particularly from the Trapezium cluster, plays a significant role in the

dispersal of proplyds, however, another relevant factor comes internally from the central object in protostellar systems due to high-energy irradiation. In this latter case, the understanding of high-energy processes in YSOs is crucial to build a complete theory for protoplanetary disk evolution, planet formation and ultimately, planet habitability.

The structure of this thesis is as follows. In Chapter 2, I will present a radio survey at centimeter-wavelength of compact sources in the ONC using the VLA including the study of radio variability, proper motions and multiwavelength properties of the young stellar population in the cluster. In Chapter 3, I present a first systematic survey of millimeter-wavelength flaring variability of YSOs using ALMA. In Chapter 4, a study of time series analysis of nonthermal YSO emission at centimeter-wavelength is presented using VLBA observations. Finally, in Chapter 5, the summary and conclusions are presented including a discussion of the future work.

Centimeter-wavelength radio survey of the Orion Nebula Cluster

2.1 Introduction

The advent of wideband centimeter-wavelength observing capabilities has enabled a new era of stellar radio astronomy, including observations of radio counterparts of YSOs. The study presented in Forbrich et al. (2016), on the search for radio counterparts of YSOs using the NRAO upgraded VLA and pointing for about 30 hours to the heart of the ONC, increased the number of known radio sources in the cluster by a factor of $\sim$7 (detecting 556 compact sources). Other VLA studies also focused in the inner cluster, covering similar areas (within $\sim 6' \times 6'$) usually reaching rms noise levels above 30 μJy bm^{-1} limiting the number of detections from a few tens (prior to the VLA upgrade Churchwell et al. 1987; Garay et al. 1987; Felli et al. 1993b; Zapata et al. 2004) to up to 175 sources (Sheehan et al., 2016). In a larger surveyed area, Kounkel et al. (2014) obtained a shallow map of approximately $1°\!.6 \times 0°\!.4$ around the ONC reporting a total of 165 sources and typical rms noise levels of 60 μJy bm^{-1}.

Additionally, multi-epoch VLA data with its high angular resolution ($0''\!.1$) and astrometric capabilites have been used to constrain the kinematics of the ONC (Gómez et al., 2005; Kounkel et al., 2014; Dzib et al., 2017). The main focus has been on the improvement of proper motion (PM) estimates of the main stellar radio sources in the

Orion BN/KL region in the inner ONC (Becklin and Neugebauer, 1967; Kleinmann and Low, 1967; Gómez et al., 2008; Zapata et al., 2009; Rodríguez et al., 2017, 2020). The PM of these stars supports the scenario where a multiple stellar system experienced a close dynamical interaction resulting in two massive stars (BN source and source I) and at least one low-mass star being ejected at a few tens of km s^{-1} triggering a powerful outflow emerging from the OMC1 cloud core prominently seen at near-infrared wavelengths (Bally et al., 2015). The improved sensitivity of the VLA now enables the detection also of non-stellar emission like that from jets and outflows (Forbrich et al., 2016; Bally et al., 2020), enabling astrometric studies as presented here.

While the deep radio catalogue presented in Forbrich et al. (2016) considerably improved the census of compact radio sources it left open the question of the wider radio population in the ONC, and its interplay with the well-characterized X-ray and infrared populations. The COUP X-ray survey (Getman et al., 2005a) covers a larger area ($\sim 17' \times 17'$) than the single, deep VLA pointing around the same reference center (Forbrich et al., 2016), and we thus conducted a wider survey for radio sources in the ONC which is presented in this work. Six additional pointings surrounding the deep central pointing were obtained at an unprecedented sensitivity in this area and we also repeated the central pointing for comparison (see Figure 2.1).

The new observations discussed here allow us to obtain the largest census to date of radio counterparts to YSOs anywhere, which we can place into the rich multi-wavelength context of the ONC. We additionally make use of radio astrometry in a comparison of the two central pointings, separated by only $\sim$4.15 years, to study fast proper motions in the ONC, which is mainly of interest for non-stellar emission, which otherwise are more difficult to measure while providing valuable additional information for source identification. Finally, we use the excellent sensitivity even on short timescales to continue our study of YSO radio variability, motivated by the findings of extreme variability on short timescales (factor >138 in less than two days and a factor of 10 in less than 30 minutes) in the previous deep ONC pointing (Forbrich et al., 2017).

TABLE 2.1: VLA ONC Observations and main image parameters per pointing.

Pointing	Starting Time (UTC)	Phase center α_{2000}	δ_{2000}	Synthesized beam size (FWHM)	PA (°)	RMS μJy bm^{-1}
1	04 Oct 2016 / 08:42:27	5:35:04.7800	-5:18:00.6700	$0.''33 \times 0.''28$	28	3.4
2	08 Oct 2016 / 11:40:20	5:35:24.1800	-5:18:00.6700	$0.''35 \times 0.''24$	33	3.8
3	17 Oct 2016 / 09:51:32	5:35:33.8800	-5:22:30.5700	$0.''34 \times 0.''24$	24	4.5
4	03 Oct 2016 / 09:35:25	5:34:55.1100	-5:22:30.5700	$0.''35 \times 0.''26$	31	4.3
5	02 Oct 2016 / 12:53:50	5:35:04.7800	-5:26:58.6201	$0.''51 \times 0.''22$	41	5.3
6	16 Oct 2016 / 11:14:20	5:35:24.1800	-5:26:57.6899	$0.''38 \times 0.''24$	35	5.0
Centre	27 Nov 2016 / 04:49:20	5:35:14.4792	-5:22:30.5760	$0.''36 \times 0.''25$	-28	10.2

Note: The light-blue number labels in Figure 2.1 correspond to the pointing numbers in this Table.

2.2 Observations and Data Reduction

The radio data were obtained between October and November 2016 using the NRAO[1]
VLA (project code: 16B-268). Figure 2.1 shows the observational setup which consists of
a central pointing at $(\alpha, \delta)_{J2000} = (5^h35^m14\overset{s}{.}5, -5°22^m30\overset{s}{.}6)$ and six adjacent pointings
observed for about 4 hrs each with the most extended A-configuration array in C-band.
The phase centers and dates of the observations are listed in Table 2.1. The half-power
beamwidth (HPBW) for the low-frequency limit (4288 MHz) is $\sim 10\overset{'}{.}5$ covering a total
area of $\sim 20 \times 20$ arcmin within the collective low-frequency HPBW of all the pointings.
The receivers were in full polarization mode with two basebands of 1 GHz each centred
at 4.8 and 7.3 GHz with a total of 16 spectral windows (8 per baseband) divided into 64
channels of 2 MHz width each. The primary flux density calibrator for all the pointings
was 3C48 and the phase/gain calibrator was J0541-0541 observed every $5-6$ min to
ensure phase stability as in our earlier observations. The light-blue circles in Figure 2.1
represent the HPBW at the low (4288 MHz) and high (7847 MHz) frequency ends of the
bandwidth in dashed and continuous lines ($\sim 10\overset{'}{.}5$ and $\sim 5\overset{'}{.}8$, respectively).

The reduction of the data was performed using the VLA Calibration Pipeline using
the CASA[2] software (release 5.4.1). All pointings except for pointing 5 were reduced with
the automatic processing of the pipeline. Pointing 5 required additional manual selection
of faulty data to be excluded in a small portion of the observation which includes 4
science scans and 1 calibrator scan (equivalent to a 5 min interval). No time or spectral
averaging was applied to any of the different pointings.

The calibrated data were imaged with the TCLEAN task in CASA. All pointings
were imaged to have a size of 8192×8192 pixels with a pixel size of $0\overset{''}{.}1$ as a compromise
between the pixel coverage of the synthesized beam and the final size of the image
in order to cover the largest half-power beamwidth of $\sim 10\overset{'}{.}5$. We used the Stokes
plane I and spectral definition mode 'mfs' (Multi-Frequency Synthesis) that combines
the data from all the selected spectral channels into a single continuum image. The
Hogbom deconvolution algorithm and a Briggs weighting method with a robustness
parameter of 0.5 were used. For the central pointing, an additional set of images was

---

[1]National Radio Astronomy Observatory is a facility of the National Science Foundation operated
under cooperative agreement by Associated Universities, Inc.

[2]Common Astronomy Software Application (McMullin et al., 2007).
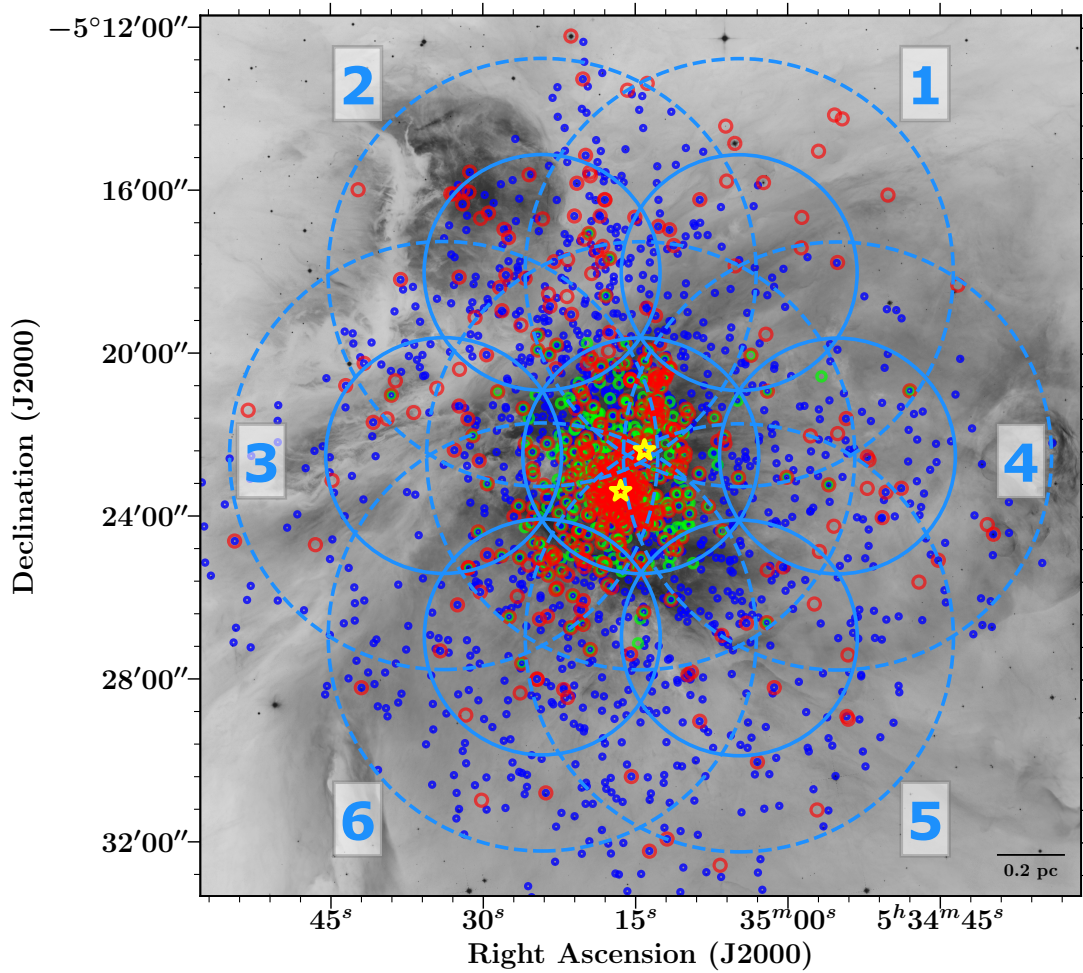
FIGURE 2.1: Observational setup: the central pointing, identical to the pointing position of the observations presented by Forbrich et al. (2016), is surrounded by six additional pointings (listed in Table 2.1) with the same spectral setup in C-band. The light-blue circles indicate the HPBW of each pointing at the low (4288 MHz) and high (7847 MHz) frequency ends of the bandwidth in dashed and continuous lines ($\sim 10'.5$ and $\sim 5'.8$, respectively). Red symbols show the radio sources detected in this work, green symbols indicate radio sources detected in the deep survey (Forbrich et al., 2016), with yellow symbols additionally marking the positions of θ^1 Ori C and the BN object for reference (lower left and upper right, respectively). Blue symbols indicate the positions of X-ray sources from the COUP survey (Getman et al., 2005b). The background image is a HST r-band image (ACS/WFC) of the Orion Nebula (Credit: NASA, ESA, M. Robberto, and the Hubble Space Telescope Orion Treasury Project Team).

created with similar setup but using the 'mtmfs' algorithm (Multi-term Multi-Frequency Synthesis; Rau and Cornwell 2011) with 'nterms=2', generating Taylor-coefficient images corresponding to a continuum intensity and spectral index map. This imaging method used for the central pointing enables a direct comparison with the deep radio observations described in Forbrich et al. (2016). Spatial filtering of the visibility data[3] was applied using baselines of the (u, v) range longer than 100 kλ ($\sim$6 km) to reduce the impact of extended nebular emission on the extraction of point-like sources by filtering out structures greater than $\sim 2''$. This is done by removing the data recorded by pairs of antennas whose baseline is shorter than $\sim$6 km.

The main parameters of the resulting images for each pointing are listed in Table 2.1, including the synthesized beam sizes and noise levels. The synthesized beam sizes are typically around $0''\!.3$ with only a slightly larger major axis of $\sim 0''\!.5$ for pointing 5. The rms noise level, on the other hand, varies considerably throughout the different pointings reaching the highest value in the central pointing due to the complex structure of the inner part of the cluster. All the adjacent pointings have rms noise levels around $3 - 5\,\mu$Jy bm^{-1} reaching the lowest value in pointing 1 in the north-west. The deep observation of the central pointing presented in Forbrich et al. (2016) has a nominal rms noise of $3\,\mu$Jy bm^{-1} being the most sensitive observations of the inner ONC to date at these frequencies. We reached similar rms noise in the outer pointings where most of the crowded area and complex structures lie towards the edges on these images. However, they still represent the most sensitive observations of the ONC to date while similar studies in this region have reported rms noise levels in the range of $25-80\ \mu$Jy bm^{-1} (Zapata et al., 2004; Kounkel et al., 2014; Sheehan et al., 2016). To account for the radial decrease in sensitivity caused by the wideband primary beam response we have applied a primary beam correction factor to each source in our catalogue after imaging the data following the method described in Forbrich et al. (2016). This primary beam correction factor is a function of distance to the pointing center described by a polynomial.

For direct comparison with our earlier results and in order to determine proper motions, while widefield imaging within CASA is preliminary, we have used the standard gridder for our images. Our imaging experiments show that presently available widefield imaging (w-projection method through gridder='wproject') results in standard-gridder

---

[3]Interferometric observations are sensitive to a range of angular scales (θ_{res}) given the range of antenna baselines as $\lambda/B_{max} < \theta_{res} < \lambda/B_{min}$, where B_{min} and B_{max} are the shortest and longest baselines, respectively.

positions in the outer beam (r$>6\overset{'}{.}4$) that can be slightly off by up to $0\overset{''}{.}36$ from the corresponding wproject positions, i.e., up to the size of the synthesized beam, however there is only one source at such a large distance in our catalogue presented in section §2.3.1. At distances $r < 3'$ from the phase center ($\sim$80% of the sources in our catalogue) the offsets found between these two gridders are negligible at $\lesssim 0\overset{''}{.}04$ ($\lesssim$10% the size of the synthesized beam). For even greater distances, the offset rises nonlinearly to about half the synthesized beam size ($0\overset{''}{.}2$) at $r = 5\overset{'}{.}2$, encompassing 97% of our sources. As discussed below, in our paper this has only a minor effect in catalogue cross-matching for a limited number of sources in our catalogue.

The imaging applied in both VLA epochs is identical, except that for the new epoch we have not applied any channel averaging, which is different from the approach in Forbrich et al. (2016). In order to quantify any impact from using these two different approaches we re-imaged the central pointing of the new observations with the same channel averaging used before. The positions in both images are compatible within the uncertainties where even at a large distance from the phase center (r=6$'$) the effect corresponds to a shift of less than 0.5σ ($\sim$22 mas). The impact on flux densities is equally negligible.

2.3   Results

2.3.1   Source Detection and Distribution

The high resolution provided by the A-configuration array together with the additional spatial filtering of the visibility data applied in the imaging process largely mitigated the difficulties of disentangling the compact radio emission from the range of emission size scales over the area due to the complex structure of the Orion Nebula. However, as reported by Forbrich et al. (2016), the use of automated methods for point source extraction leads to a high fraction of spurious detection (up to 50%) on VLA images with the same observational setup towards the ONC. The source detection was thus performed by visual inspection of each individual pointing using the images generated in the multi-frequency synthesis (mfs) spectral mode. The initial source positions in this process were estimated with DAOFIND task in IRAF. This task computes the positions by estimating the point spread function of the source using an elliptical Gaussian approximation within

TABLE 2.2: Source detection per pointing.

Pointing ID	Number of detections		New detections	
	Total	<HPBW[a]	Total	<HPBW[a]
(1)	(2)	(3)	(4)	(5)
1	176	16 (9%)	44 (25%)	14 (8%)
2	214	54 (25%)	72 (34%)	43 (20%)
3	228	31 (14%)	41 (18%)	16 (7%)
4	158	15 (9%)	24 (15%)	9 (6%)
5	151	19 (13%)	26 (17%)	10 (7%)
6	224	56 (25%)	35 (16%)	19 (8%)
Central	272	249 (92%)	22 (8%)	19 (7%)

[a] HPBW at the high frequency end is $5\!\!\!.\!8$ ($r \sim 2\!\!\!.\!9$ from the pointing center).
All the percentages are with respect to column (2).

a given area defined by a box around the source. This first list of detections per pointing corresponds to the input for a source extraction script which uses the IMFIT task in CASA to obtain the final positions, flux densities and additional statistical parameters per source. For each input source we used different box sizes for the fitting ranging from 8 to 30 pixels, applying different offsets from the center of the source to avoid contaminant emission coming from nearby sources. The different outputs for a given source from different box configurations were compared to finally select the measurement with lower uncertainties and measured positions closer to the actual peak pixel, thereby minimising the impact of nearby sources and of complex nebular emission. We also enforced a minimum box size of 10×10 pixels for it to contain at least about ten synthesized beam areas for statistics. To select reliable detections we used a S/N>5 as our detection limit. Compared with a criterion of S/N>3, our adopted limit conservatively accounts for non-Gaussian noise in the inner cluster, which leads to many more sources that would need to be rejected (e.g., compact nebular emission). A 5σ cutoff is also consistent with the most complete radio surveys to date in the ONC field with detection limits between $4.5 - 6\sigma$ (Kounkel et al., 2014; Sheehan et al., 2016; Forbrich et al., 2016).

The final number of sources detected per pointing is listed in column (2) in Table 2.2 and marked in red in Figure 2.1. Column (3) in the table indicates the number of sources within the HPBW (at the high frequency end $\sim 5\!\!\!.\!8$) for each pointing. The maximum number of detections is found in the central pointing with 272 detections (which corresponds to the densest region of the ONC) and the lowest detection count is found in pointing 5.

The total number of detections over the whole area covered by the 7 pointings is 521, without duplicates that are detected in more than one pointing. Since most of the duplicates are isolated sources, those were easily found with a search radius of 1", followed by visual inspection.

Sources detected in several pointings are usually found at different distances from the pointing centers. As noted above, these different detections show minor position shifts. In our catalogue we thus report positions from the closest detection to the phase center, where this corresponding distance is also reported. Partly due to the spatial filtering inherent in our experiment design, focusing on the detection of nonthermal emission with aggressive spatial filtering, most of the sources are unresolved, with only 2% showing a size $\geq$3 times the area of the synthesized beam, and only 8% of the sources larger than twice the synthesized beam. The nominal mean ratio between the integrated to peak flux density in our catalogue is 1.2 ± 0.5. Our catalogue thus only lists peak flux densities.

Our catalogue of 521 sources is listed in Table 2.3 and indicated by red symbols in Figure 2.1. Columns (1) and (2) show the positions in α and δ with their corresponding uncertainties obtained from the fit (IMFIT). Column (3) indicates the source identification number in this catalogue. Columns (4) and (5) indicate the peak flux density (corrected by the primary beam response) and source fitting parameters (major and minor axes, and position angle). Columns (6) and (7) indicate previous designation in the COUP and/or VISION surveys. Column (8) indicates the distance to the stellar system θ^1 Ori C and column (9) indicates the distance to the closest phase center where the reported positions come from. The position uncertainties reported in this catalogue are those given by IMFIT without the addition of minor systematic errors (see above)[4]. These positional uncertainties have median values of 14 and 15 mas in R.A. and decl., respectively. An absolute astrometric accuracy for similar VLA observations (identical to our central pointing) was reported in Forbrich et al. (2016) using five individual epochs resulting in an overall absolute astrometric accuracy of 20-30 mas. An absolute uncertainty in peak flux densities of 5% has been estimated based on systematic variability using a non-variable test-case (source BN; see section §2.3.4). This uncertainty has been added in quadrature with the uncertainties from the 2D-Gaussian fit (IMFIT) already corrected by the primary beam response.

---

[4]We have applied two different and complementary cutoff methods to discuss the proper motion significance in Section §2.3.3.

TABLE 2.3: Catalogue of compact radio sources in the ONC.

$\alpha(2000)$ ($^{\mathrm{h\,m\,s}}$)	$\delta(2000)$ ($^{\circ\,\prime\,\prime\prime}$)	ID	Peak Flux Density (mJy bm^{-1})	Deconvolved Size ^{a} ($\theta_{max} \times \theta_{min}$; PA)	COUP	VISION	Dist. to θ^1 Ori C (arcmin)	rad ^{b} (arcmin)
(1)	(2)	(3)	(4)	(5)	(6)	(7)	(8)	(9)
05:34:39.7603 ± 0.0002	-5:24:25.465 ± 0.003	1	1.422 ± 0.074	$0\rlap{.}''27 \times 0\rlap{.}''17$; 45° ± 5°		05343976-0524254	9.2	4.3
05:34:40.3667 ± 0.0006	-5:24:11.308 ± 0.009	2	0.148 ± 0.011	$0\rlap{.}''21 \times 0\rlap{.}''06$; 64° ± 20°			9.0	4.0
05:34:43.2598 ± 0.0028	-5:18:18.566 ± 0.020	3	0.045 ± 0.009				9.7	5.1
05:34:45.1880 ± 0.0019	-5:25:03.941 ± 0.016	4	0.047 ± 0.006		23	05344519-0525041	8.0	3.6
05:34:47.0976 ± 0.0007	-5:25:36.158 ± 0.017	5	0.063 ± 0.007			05344709-0525363	7.6	3.7
05:34:47.9813 ± 0.0001	-5:20:54.381 ± 0.002	6	0.406 ± 0.021	$0\rlap{.}''16 \times 0\rlap{.}''12$; 117° ± 18°			7.5	2.4
05:34:48.8288 ± 0.0002	-5:23:17.906 ± 0.003	7	0.180 ± 0.010	$0\rlap{.}''09 \times 0\rlap{.}''02$; 49° ± 64°	43	05344883-0523179	6.9	1.8
05:34:50.1332 ± 0.0038	-5:16:06.062 ± 0.020	8	0.040 ± 0.007				9.8	4.1
05:34:50.3353 ± 0.0013	-5:23:23.775 ± 0.028	9	0.019 ± 0.003				6.5	1.5
05:34:50.7098 ± 0.0023	-5:24:01.184 ± 0.016	10	0.020 ± 0.004		57	05345071-0524013	6.4	1.9
05:34:52.0114 ± 0.0002	-5:22:36.387 ± 0.006	11	0.088 ± 0.005			05345201-0522364	6.1	0.8
05:34:52.1746 ± 0.0007	-5:22:31.786 ± 0.017	12	0.027 ± 0.003		67	05345216-0522319	6.1	0.7
05:34:52.1839 ± 0.0011	-5:23:18.237 ± 0.027	13	0.013 ± 0.002				6.0	1.1
05:34:54.0616 ± 0.0025	-5:28:58.287 ± 0.049	14	0.038 ± 0.006				7.9	3.3
05:34:54.0843 ± 0.0034	-5:27:23.612 ± 0.059	15	0.042 ± 0.007				6.9	2.7
05:34:54.1948 ± 0.0022	-5:28:54.243 ± 0.030	16	0.069 ± 0.007		90	05345419-0528543	7.8	3.3
05:34:54.2494 ± 0.0003	-5:21:35.423 ± 0.006	17	0.068 ± 0.005		89	05345425-0521354	5.8	0.9
05:34:54.6354 ± 0.0012	-5:14:13.927 ± 0.023	18	0.042 ± 0.007				10.6	4.6
05:34:55.0949 ± 0.0006	-5:21:57.572 ± 0.010	19	0.041 ± 0.004				5.5	0.6
05:34:55.0981 ± 0.0005	-5:17:45.489 ± 0.009	20	0.076 ± 0.006	$0\rlap{.}''22 \times 0\rlap{.}''16$; 28° ± 65°			7.7	2.4

^{a} As defined by imfit in CASA.

^{b} Distance to closest phase center. Note that the reported positions are from the standard gridder and may be slightly off in the outermost beam areas (see text).

The full catalogue is available in Appendix A in Table A.1.

In this new census of compact radio sources towards the ONC we report 198 new sources not previously reported at these frequencies. This is based on a comparison against the most complete catalogues of compact radio sources made of the ONC and presented in Forbrich et al. (2016); Sheehan et al. (2016); Kounkel et al. (2014); Zapata et al. (2004). The highest fractions of new sources are found in pointings 1 and 2, the northernmost part of the cluster as seen in Figure 2.1.

For a more direct comparison the central pointing was compared against the deep observation presented in Forbrich et al. (2016) which are identical observations apart from the cumulative observing time (∼30 h for the deep obs.). In the same area where they find 556 sources we detect 272. There are 303 sources in the deep catalogue not detected in the central pointing of the new observations (not all the 272 have a counterpart in the deep catalogue) which is expected due to the difference in sensitivity, where a large fraction of faint sources in the deep catalogue are far below the noise level in the new data. However, not all the sources detected in the central pointing of the new and less sensitive observations were detected in the deep data, and indeed there are 19 new sources in the central pointing that should have been clearly detected in the deep data. These are clear targets for variability analysis and are discussed in section §2.3.4.

2.3.2 Multi-wavelength Populations

Our primary goal after revealing the compact radio population in the ONC is the search for radio counterparts to YSOs. They can be detected through both thermal and nonthermal radio emission. While nonthermal emission originates at the smallest scales in the stellar coronae of low-mass young stars, thermal radio emission, in contrast, occurs in a range of larger scales in stellar disks or outflows when it is associated to a stellar source. However, compact sources at these frequencies can also be detected as thermal emission from ionized material not strictly related to a stellar source (Garay et al., 1987; Churchwell et al., 1987; Sheehan et al., 2016; Forbrich et al., 2016). An additional source of contamination comes from extragalactic background sources, even though these have been previously found to be minimal. In the so far deepest catalogue for the inner ONC (Forbrich et al., 2016) it was estimated that ∼97% of the compact radio sources within $r < 1.'6$ are related to the cluster. Here we cover a considerably wider area and while the central region is less prone to present background detections due to the elevated rms

noise caused by the nebula itself, we expect to find faint background radio sources from bright background galaxies in the outer areas, given the high sensitivity. A discussion on the expected number of extragalactic radio sources in the outer areas is presented later on in this section, when discussing Figure 2.5.

In order to approach the nature of the compact radio population we have compared our catalogue against the most complete X-ray and near-infrared (NIR) datasets available for the ONC. The COUP X-ray catalogue reported in Getman et al. (2005a) represents the best reference for YSOs in the ONC. Here, the X-ray emission of young stars is associated to thermal emission from hot plasma in coronal-type activity (e.g., Feigelson and Montmerle, 1999). The observations presented in this work were designed to cover the COUP survey area of $\sim 20' \times 20'$ (blue markers in Figure 2.1 represent the COUP catalogue). The complementary NIR dataset used here is the VISION catalogue reported in Meingast et al. (2016), a survey of the entire Orion A molecular cloud in JHK_S bands. The NIR band is an additional tracer of the young stellar population towards the ONC, since, in general, such X-ray and NIR data are similarly effective at detecting embedded sources (e.g., Ryter, 1996). Any extragalactic background contamination is unlikely where sources are superimposed onto the high extinctions levels of the ONC but at the same time the NIR also picks up foreground sources. Contrary to the X-ray survey, the NIR catalogue is severely affected by bright extended emission of the Orion Nebula in the innermost areas, where it is thus less complete to YSOs.

The angular resolution in COUP and VISION is $< 0\rlap{.}''5$, which is comparable to the typical beam size in our observations. Moreover, the reported positional errors in the COUP survey have a mean value of $0\rlap{.}''1$, with maximum errors of $0\rlap{.}''59$, although, 99% of the sources have positional errors $\leq 0\rlap{.}''5$. On the other hand, the reported astrometric accuracy in the VISION catalogue is ~ 70 mas. Based on these considerations and to additionally account for the smallest nearest-neighbour distances, we have therefore considered a conservative radius of $0\rlap{.}''5$ for the search of counterparts in these surveys. The robustness of this approach is demonstrated when considering that if we increase this search radius to $1''$ the number of correlations with the COUP and VISION surveys would increase by only 5% and 4%, respectively, including unrelated nearest neighbours. Within the area covered in our observations we report 521 radio sources, while the COUP catalogue reports 1616 sources and the VISION catalogue 3558 sources. A total of 275 sources in our catalogue ($\sim 53\%$) have X-ray counterparts which corresponds to only 17%
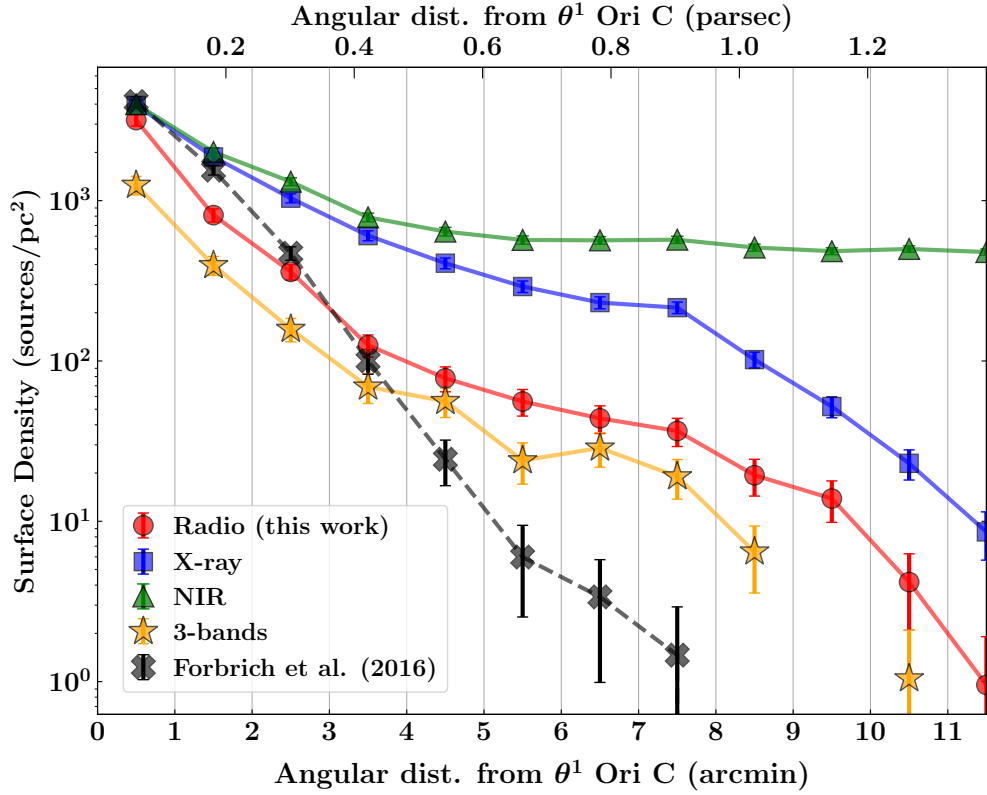
FIGURE 2.2: Azimuthally averaged surface number density as a function of projected distance to θ^1 Ori C for the three different wavelength populations. The VISION, COUP and radio catalogues are indicated by green, blue and red lines, respectively. Sources with detections in all three bands are indicated in orange line, while the dashed black lines indicate the distributions for the deep catalogue from Forbrich et al. (2016). Each data point represent the surface density of sources within annular areas of $1'$ width indicated by vertical lines and the error bars are based on error propagation from counting statistics (Poisson errors).

of the COUP catalogue. On the other hand, 290 radio sources in our catalogue ($\sim$56%) have NIR counterparts, which corresponds to only $\sim$8% of the NIR catalogue within the same area.

Figure 2.2 shows the surface number density of the three wavelength populations as a function of projected distance from θ^1 Ori C, a young and massive stellar system of $\sim$50 $M_\odot$ in the Trapezium cluster at the center of the ONC (Kraus et al., 2007). Our observational setup is actually centered $\sim$1' northwest from θ^1 Ori C towards the BN/KL region to optimize the sensitivity in this complex area while still matching the COUP field of view. Centering our reference on θ^1 Ori C allows us to address any impact that the most massive stars in the center of the cluster have on the radio emission in a multiwavelength context. The overall distributions for the three bands show the densest region in the central cluster ($r < 1'$) with a remarkable correspondence in their total

number of sources equivalent to an average surface density of $(3.7 \pm 0.2) \times 10^3$ sources pc^{-2}. Despite of this similarity, they do not represent the same population and, indeed, at this inner bin their actual correlation, indicated by the orange distribution (population with detections in the three bands), is only one third of their total number of sources. The X-ray and NIR distributions exhibit almost the same profile until $r = 2'$.

The X-ray distribution continuously decreases revealing, in part, the structure of the cluster but also showing the sensitivity limitations in the outer bins. Similarly, the radio distribution continuously decreases, although at a faster rate. Contrary to the deep radio catalogue distribution (dashed black line), our radio catalogue (continuous red line) does not decrease solely due to a sensitivity effect, even though the sensitivity is not constant. The angular distance between the phase centers of adjacent pointings is $\sim 5'$ where the lowest sensitivity occurs at $2'.5$ between each pointing. At this distance, the wideband primary beam correction indicates a flux density correction by 40%, which therefore technically constitutes the maximum variation in sensitivity due to the spacing of our individual pointings. However, we have shown in Forbrich et al. (2016) that at this angular distance from the phase center of the central pointing the image noise is still dominated by the Orion Nebula itself, and the impact on our analysis is thus limited. Under this considerations, the radio distribution seems to reveal the intrinsic structure of the cluster. At larger radii ($r > 4'$) the NIR distribution remains almost constant largely due to the presence of foreground infrared sources in addition to the young stellar population further away from the center of the cluster. Although the COUP distribution may also include contamination, in this case from extragalactic candidates, this is just a small fraction (~ 160) and most of the X-ray sources are likely members of the ONC (Getman et al., 2005a), besides, extragalactic X-ray sources will be affected by foreground extinction in the cloud and thus are unevenly distributed.

In order to assess the correlation between the three main distributions shown in Figure 2.2 (radio/X-ray/NIR) we quantified the different population fractions as a function of projected distance from θ^1 Ori C as shown in Figure 2.3. Since we have shifted our reference center $\sim 1'$ southeast from the actual center of the observations, we have therefore moved the reference frame for this analysis towards the south-east boundary of our radio survey (and COUP given the almost identical coverage). Since the maximum radial coverage in our radio catalogue is $\sim 10'.4$, we are now reaching this boundary at $\sim 9'.4$ south-east from θ^1 Ori C, setting a first limit for our analysis at this
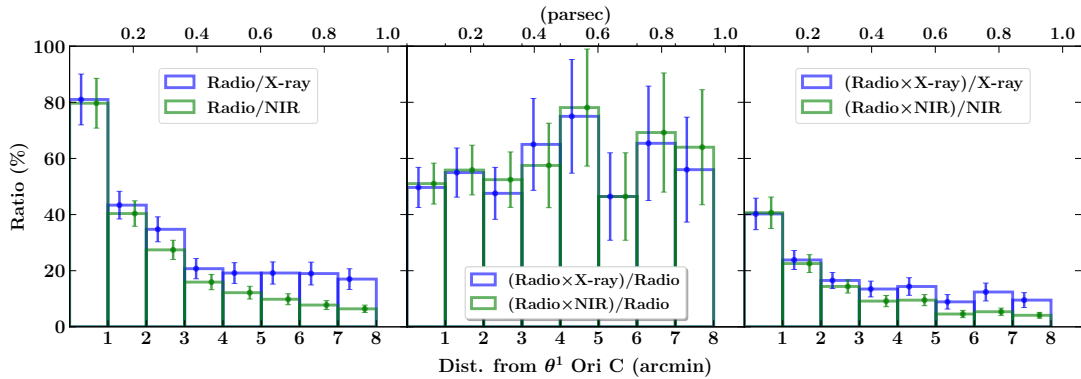
FIGURE 2.3: Detection fractions between the three different populations radio/X-ray/NIR as a function of distance to θ^1 Ori C. The left panel shows the fraction of radio sources over the X-ray (blue) and NIR (green) populations. Central panel shows the X-ray (blue) and NIR (green) detection fraction of radio sources. The right panel shows the radio detection fraction of X-ray sources (blue) and NIR sources (green). The 1σ error bars were derived from counting statistics (Poisson errors).

maximum radius. However, an additional constraint is set to avoid any sensitivity bias for the detection of sources in the boundaries of our radio catalogue (which becomes sensitive to the brightest sources due to the primary beam correction). We have set a radial limit for our analysis to not exceed the midpoint between the HPBW at the low- and high-frequency ends of the bandwidth (dashed and continuous line circles, respectively, in Figure 2.1). This midpoint is reached at $8'$ in the south-east direction, thus we are going to restrict our following analysis to this radius. The left panel in Figure 2.3 indicates the fraction between the total radio distribution shown in Figure 2.2 over the total X-ray and NIR distributions (indicated by blue and green histograms, respectively), without matching individual counterparts. In the central cluster these fractions indicate almost equal numbers of X-ray and NIR sources with radio source numbers lower by $\sim 10-30\%$. These fractions then decrease as expected from their individual distributions in Figure 2.2. Here the radio to NIR fraction (green) decreases at a slightly faster rate due to the more uniform spatial distribution of NIR sources in the field (including foreground sources) compared to the continuously decreasing surface density distribution of radio sources as we go further away from θ^1 Ori C. Interestingly, for projected distances of $r > 3'$, unlike the continuous decrease in the radio to NIR fractions, the radio to X-ray fractions (blue) settles at around $19\pm1\%$ which might indicate how these two populations are tracing a similar structure of the cluster within this radial range.

The middle panel in Figure 2.3 shows the X-ray and NIR detection fraction of radio sources (i.e., X-ray or NIR counterparts to our radio catalogue) indicated by blue

and green histograms, respectively. The overall distributions do not show a significant trend and they are, in effect, compatible with a constant distribution within the errors. Evidently, at larger radii the lower number of radio sources introduces larger uncertainties. A similar comparison is shown in the right panel, but indicating the radio detection fractions of X-ray and NIR sources (i.e., number of X-ray or NIR sources with radio counterparts) in blue and green, respectively. Here, the blue distribution represents our best estimate for the radio detection fraction of YSOs in the ONC and any radial trend with respect to the brightest Trapezium star at the center of the cluster may well provide important information on the underlying emission mechanism dominating at different distances. If YSOs have similar geometries, we would not expect to find any trend here, and the radio to X-ray ratio would instead simply reflect basic YSO properties. However, there is a very clear radial trend suggesting that X-ray sources towards the central part of the cluster are more likely to have a radio counterpart than X-ray sources in the outer areas. This points to a potential impact of the Trapezium on YSO properties in the ONC. One possibility is that circumstellar disks of YSOs (with a central X-ray source) are externally photoionized by the influence of the Trapezium stars (O'dell et al. 1993; Henney and Arthur 1998; Concha-Ramírez et al. 2020 and references therein), leading to the detection of ionized material as thermal free-free radio emission. In this case, as we go further away from the Trapezium, the detection fraction (blue distribution) may become dominated by nonthermal radio emission intrinsic to YSOs. The detection fraction is as high as $40 \pm 6\%$ in the inner bin ($r < 0.12$ pc) and then decreases down to $17 \pm 3\%$ in the third bin ($r < 0.36$ pc). For distances $r > 3'$ (0.36 pc) the radio detection fraction of X-ray sources fluctuates around $11 \pm 2\%$ which might represent a baseline for the detection of nonthermal radio emission from the X-ray emitting YSO population without the influence of nearby young massive stars that would otherwise lead to a constant distribution. In contrast, the radio detection fraction of NIR sources (green) decreases continuously with radial distance, but this is expected since it reflects the fact that the NIR catalogue includes not only cluster members but also sources that are not related to the ONC.

Following the interpretation of the high radio detection fraction of X-ray sources closer to the Trapezium, more likely due to the detection of externally photoionized circumstellar disks, it is expected that the flux distribution of these sources (thermal free-free emission component) decreases with distance from the ionizing source. Figure
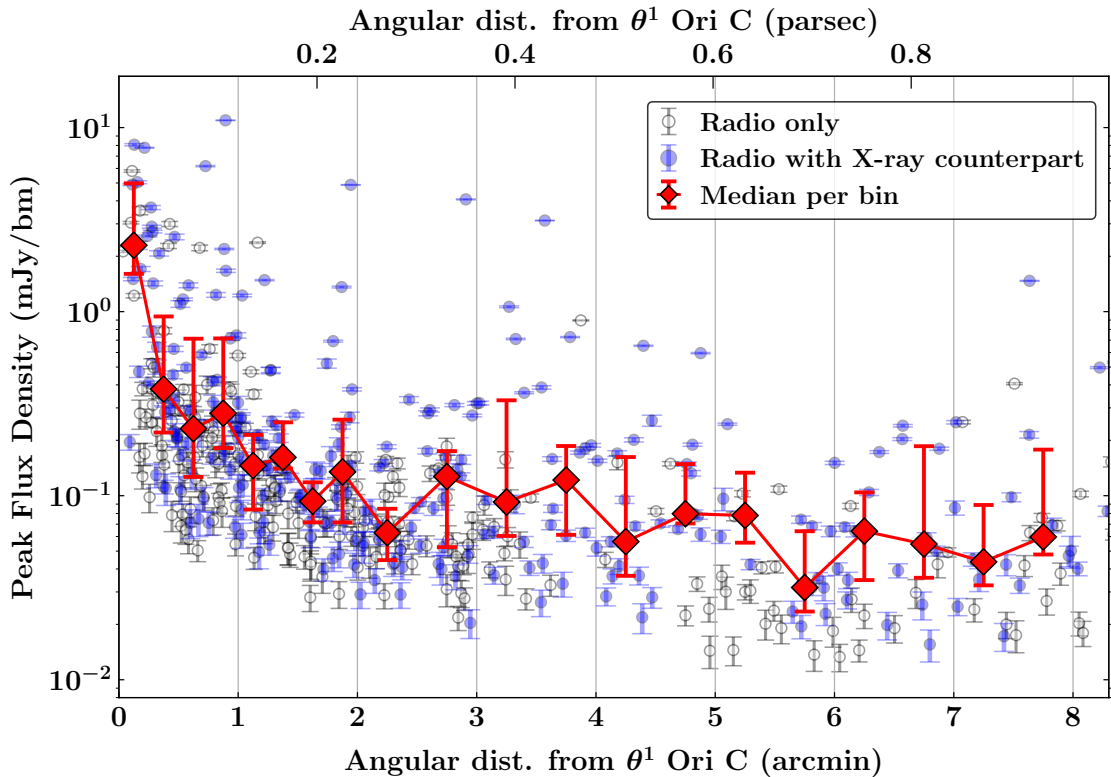
FIGURE 2.4: Peak flux density distribution as a function of projected distance to θ^1 Ori C. Blue symbols indicate sources with X-ray counterparts and grey symbols indicate the remaining sources. Red symbols show the median of the blue distribution per $0\!''\!.25$ bins (for $r < 2'$) and $0\!''\!.5$ bins (for $r > 2'$). The median error bars represent the 25th and 75th percentiles of the data at each bin.

2.4 shows the peak flux density distribution as a function of projected distance to θ^1 Ori C clearly showing higher radio fluxes closer to the Trapezium with a decreasing trend more evident for $r \lesssim 2\!''\!.5$. Possible deviations from this trend are, first, the discrepancy between the projected and actual physical separation to the ionizing source where the actual physical separations could be considerably larger. Second, a fraction of the sources could be intrinsically bright nonthermal radio emitters.

An interesting question prompted by these results concerns the nature of the radio population without X-ray counterparts. On the one hand, towards the center of the cluster most of these sources likely are thermal radio sources including externally photoionized disks, stellar jets and outflows, and also compact emission from the nebula, but towards the outer areas where we do not find a significant influence of the Trapezium stars we would expect a much lower number of these sources. As noted above, while the central area is less prone to background contamination already due to presence of the nebula, this contamination increases in the outer areas. Additionally, there may be a low
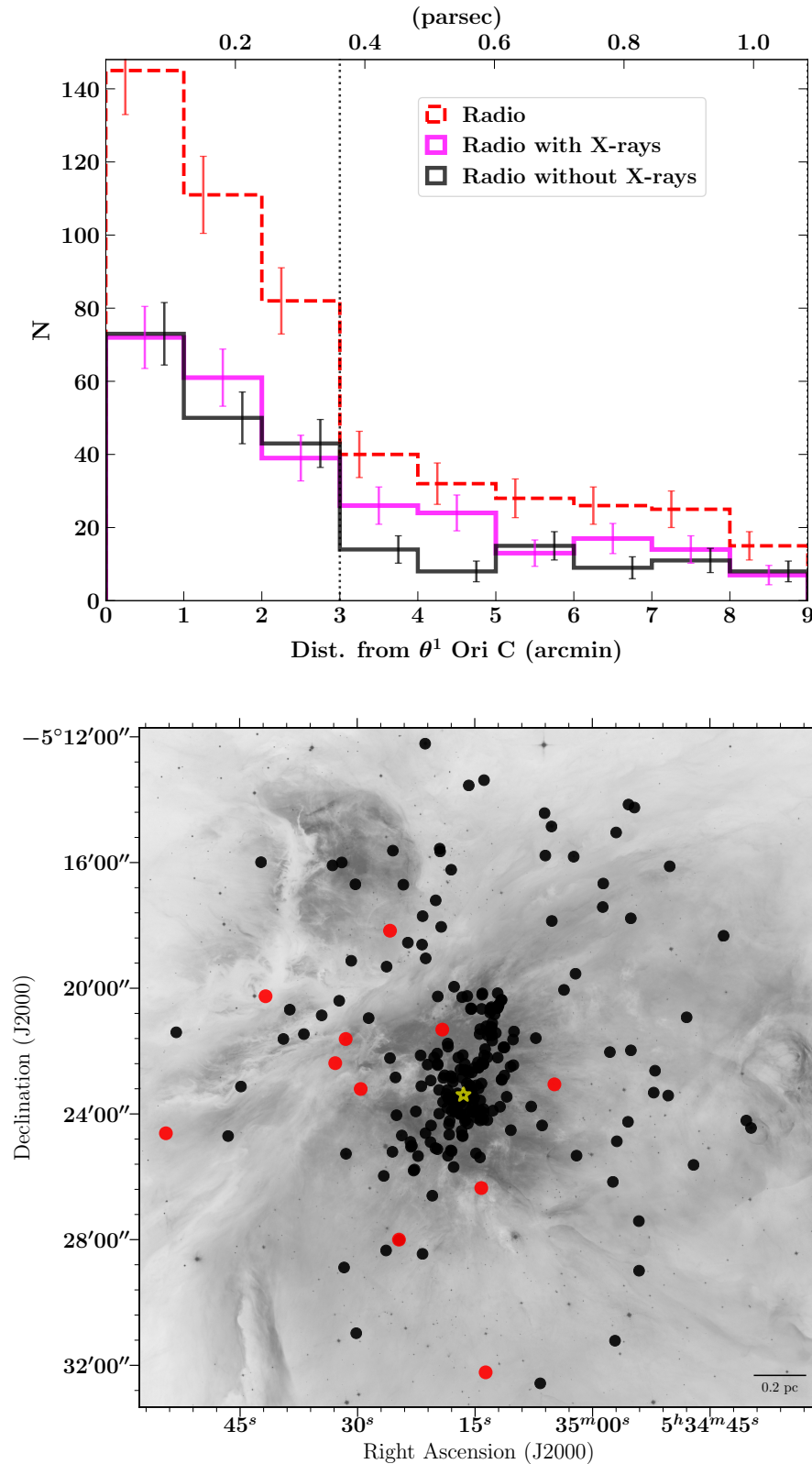
FIGURE 2.5: Top: Radial distribution of sources as a function of projected distance to
θ^1 Ori C. Red dashed line indicate the distribution of radio sources in our catalogue.
Magenta and black lines indicate the distribution of radio sources in our catalogue with
and without X-ray COUP counterparts, respectively. Vertical dotted line indicate the
inner radius of the annular area used to estimate the expected number of extragalactic
sources. Bottom: Spatial distribution of radio sources without X-ray counterpart (black)
and radio sources with X-ray counterpart flagged as extragalactic candidates in the
COUP catalogue (red). The background image is a HST *r*-band image (ACS/WFC) of
the Orion Nebula (Credit: NASA, ESA, M. Robberto, and the Hubble Space Telescope
Orion Treasury Project Team).

number of sources not identified as YSOs if these were not X-ray active at the time of the observations. Indeed, it has been found that X-ray sources with radio counterparts are predominantly sources with high X-ray luminosities and there are even a few cases where nonthermal radio YSOs have no X-ray counterpart at all (Forbrich and Wolk, 2013; Rivilla et al., 2015; Forbrich et al., 2016). The top panel in Figure 2.5 shows the radial distribution of the total radio population, as well as the radio population with and without X-ray counterparts. The radio population without X-ray counterparts peaks in the central area, implying that there is a correlation with the inner cluster and these sources are not only background galaxies that would lead to a constant distribution as we see in the outer area ($> 3'$). In this outer area the distribution of radio sources without X-ray counterparts is evenly spread over the field as indicated by black symbols in the bottom panel of Figure 2.5. In the same bottom panel we included in red symbols the radio sources with X-ray counterparts but flagged as extragalactic candidates in the COUP catalogue. We found only 11 of these sources in our catalogue ($\sim 2\%$) out of 159 extragalactic source candidates in the COUP catalogue, which are evenly spread throughout the whole field (Getman et al., 2005b). In order to assess the possibility to detect extragalactic sources we made use of the work by Fomalont et al. (1991) to estimate the expected number of background sources in a given area above a given flux density threshold. We considered an area between $3' < r < 9'$ excluding the central cluster and where the distribution of radio sources without X-ray counterparts remains nearly constant around 11 ± 3 sources per bin, totaling 65 ± 8 sources. Following the 5σ detection threshold used in our catalogue and an average rms level of 4 μJy bm^{-1} (see Table 2.1) we find an expected number of background sources of $\sim 155 \pm 22$ and therefore extragalactic sources are a reasonable explanation for at least some of the radio sources without X-ray counterparts in the outer areas. In order to further explore the sample of 65 radio sources between $3' < r < 9'$ we have looked into their correlations with NIR and optical wavelengths. 11 sources have NIR counterparts in VISION, 9 sources have optical counterparts in Gaia EDR3 (Gaia Collaboration et al., 2016; Gaia Collaboration et al., 2021), and just 4 sources have counterparts in both bands, however the nature of those remains unknown. On the other hand, 8 sources are associated with the OMC1 outflow discussed later in section §2.3.3, and 4 sources are associated with proplyds found in optical HST data (Ricci et al., 2008), leaving us with 55 unidentified sources in this sample and thus potentially extragalactic candidates.

We have focused our analysis on azimuthally averaged radial trends rather than individual pointings which would require the multi-wavelength distribution of the outer pointings to be similar at a given distance from the reference center. This approach is justified by the fact that we find only limited evidence for significant differences between the individual pointings. In order to quantify these differences we compared their relative multiwavelength distributions using Kolmogorov-Smirnov (KS) tests based on their distribution of radio, X-ray and NIR populations. We used the Venn diagram of these three populations within the inner $r = 2'0$ of each pointing (see Figure 7 in Forbrich et al. (2016)). At this radius there is no overlap between the areas to be compared and, for the radio population, reflects a good compromise between the number of detections and any effect of the primary beam response. Figure 2.6 shows the resulting statistics from the KS test where the values correspond to the 'p-value' (also color-coded by the same parameter). While the majority of the pointings indicate that their multi-wavelengths distributions are essentially the same or comparable (p-value$\sim$1 or p-value$\gtrsim$6), the central pointing clearly proves the most distinct multi-wavelength population distribution against any of the outer pointings. The similarity shown by the outer pointings allows us to assume that there are no indications for significant differences between their multi-wavelength population distributions and therefore we can safely azimuthally average their radial distributions as a function of projected distance to θ^1 Ori C in order to assess the impact that the most massive stars in the inner ONC has in the multi-wavelength radial distribution of the cluster.

Another interesting aspect is the relative fraction of radio sources that have neither X-rays nor NIR counterparts which is significantly lower in the outer fields. This population most likely represents compact radio emission of non-stellar origin. In section §2.3.3, we identify one category of such non-stellar radio emission by employing proper motion measurements, identifying sources associated with the OMC1 outflow.

2.3.3 Proper Motions

In our comparison between the observations presented here and the deep catalogue reported in Forbrich et al. (2016) we were able to implicitly measure the proper motion of 253 sources. This comparison only involves the central pointing in epoch 2016, these are identical observations towards exactly the same phase center and phase-referenced against
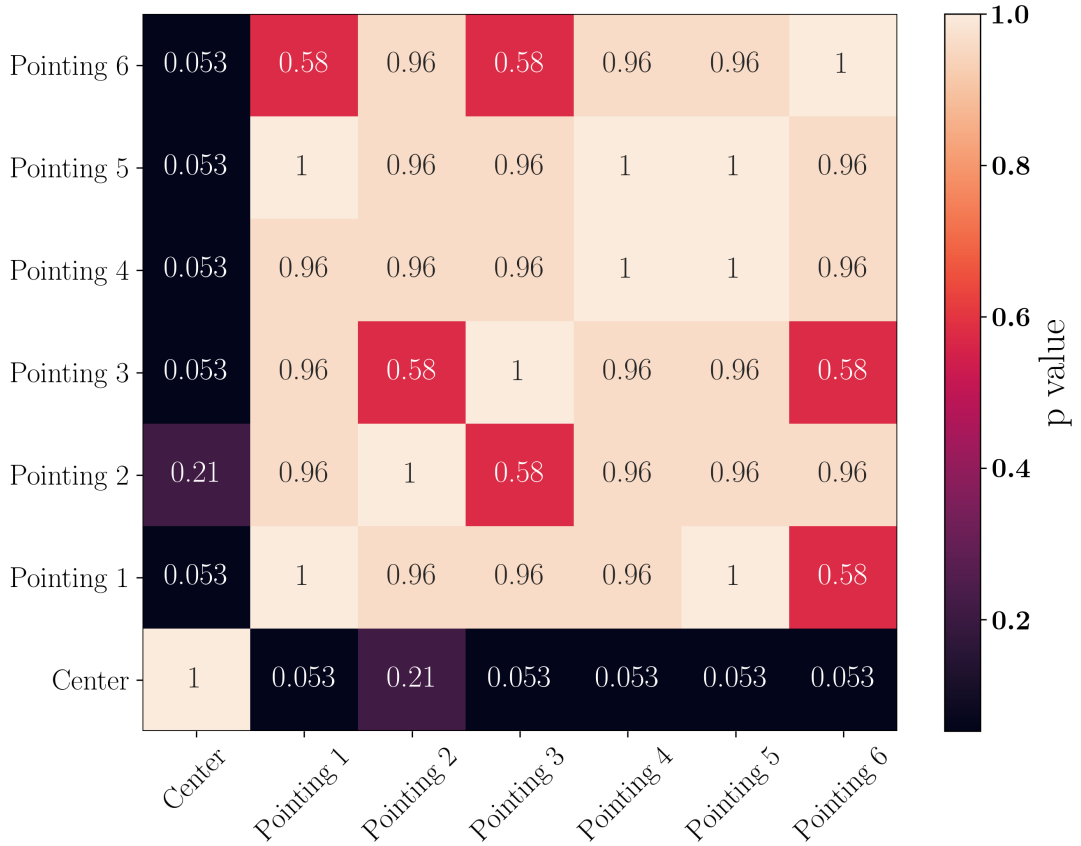
FIGURE 2.6: KS statistics from the comparison between the multi-wavelength population distributions of all the pointings.

the same distant quasar such that this comparison basically represents absolute astrometry. However, we are only covering a time baseline of 4.19 years. The mean position errors in our catalogue are $\sim$20 mas and the estimated astrometric accuracy from the five epochs in Forbrich et al. (2016) is 20-30 mas. In order to detect proper motions above these limits a single source would require a minimum velocity of $\sim$22 km s^{-1}, which is unusual for a stellar source and therefore we did not expect to find significant motions in our sample. Stars with velocities >10 km s^{-1} are considered peculiar sources and above 30 km s^{-1} are already in the runaway regime (Farias et al., 2020; Schoettler et al., 2020). Stellar proper motions in the ONC are typically $\mu_{tot} \lesssim 2$ mas yr^{-1} (4 km s^{-1}) and the mean proper motion of the ONC is $\overline{\mu_\alpha \cos(\delta)} = 1.07 \pm 0.09$ mas yr^{-1} and $\overline{\mu_\delta} = -0.84 \pm 0.16$ mas yr^{-1} (Dzib et al., 2017; Kim et al., 2019). Only a handful number of sources have fast proper motions with $\mu_{tot} \lesssim 30$ mas yr^{-1} (60 km s^{-1}) (Gómez et al., 2005, 2008; Rodríguez et al., 2020) most of them associated to the ejected stars in the BN/KL region (which will be discussed later in this section).

In spite of the above considerations, we surprisingly discover high PMs in our sample

with projected velocities of up to ~ 373 km s^{-1} for a distance of ~ 400 pc to the ONC (Großschedl et al., 2018; Kuhn et al., 2019). In the following analysis, we report absolute PM on the sky. This finding provides an additional and important tool for source identification. Figure 2.7 shows the absolute PM diagram in the $\mu_\alpha \cos(\delta) \times \mu_\delta$ plane for the full sample. Sources with motions above 5σ in at least one direction α or δ are colour coded by their transverse velocity (V_t). It is important to note here that these uncertainties were derived by error propagation from the fitting errors (positional uncertainties) thus these may be underestimated. 48 out of 253 sources fulfil this criterion. The remaining sources are marked in grey. With this first cutoff sources with small uncertainties but still with insignificant PM remain (even with motions above 5σ). An additional cutoff is then applied taking into account the PM dispersion to estimate an intrinsic motion noise in the PM diagram in Figure 2.7. This additional cutoff is described below.

An important caveat to consider in this sample is the fact that not all of the sources represent a stellar counterpart (see §2.3.2) and therefore an unrealistic dispersion might be injected into the central part of the diagram caused by apparent motions of extended sources that can be seen as compact radio emission in form of thermal bremsstrahlung coming from ionized material around young stars, a peak emission in top of a bow shock, for instance. This apparent motion can be caused by fading and brightening events of the same feature in between the two epochs. On the other hand, given the short time separations between the two epochs we are only able to reveal significant motions above a few tens of mas yr^{-1}. However, there is a continuum range of motions spanning from -70 to 60 mas yr^{-1} in α and from -65 to 125 mas yr^{-1} in δ.

In order to determine a realistic PM dispersion we constrained a Gaussian fit for each axis in Figure 2.7 to a sample of sources that (1) are compact, (2) do not lie on a complex or extended emission and (3) do not present a clear motion which is considered as sources with position measurements compatible within 3σ between the two epochs. This selection gives us a dispersion that represents the intrinsic motion noise in the PM diagram due to position uncertainties. This distribution is shown in dark-blue histograms in Figure 2.7 for each axis, together with their Gaussian fit also in dark-blue colour. The full sample distribution is showed in orange histograms. The shaded ellipse represent 5 times the dispersion of the Gaussian fit for each axis in order to exclude ambiguous
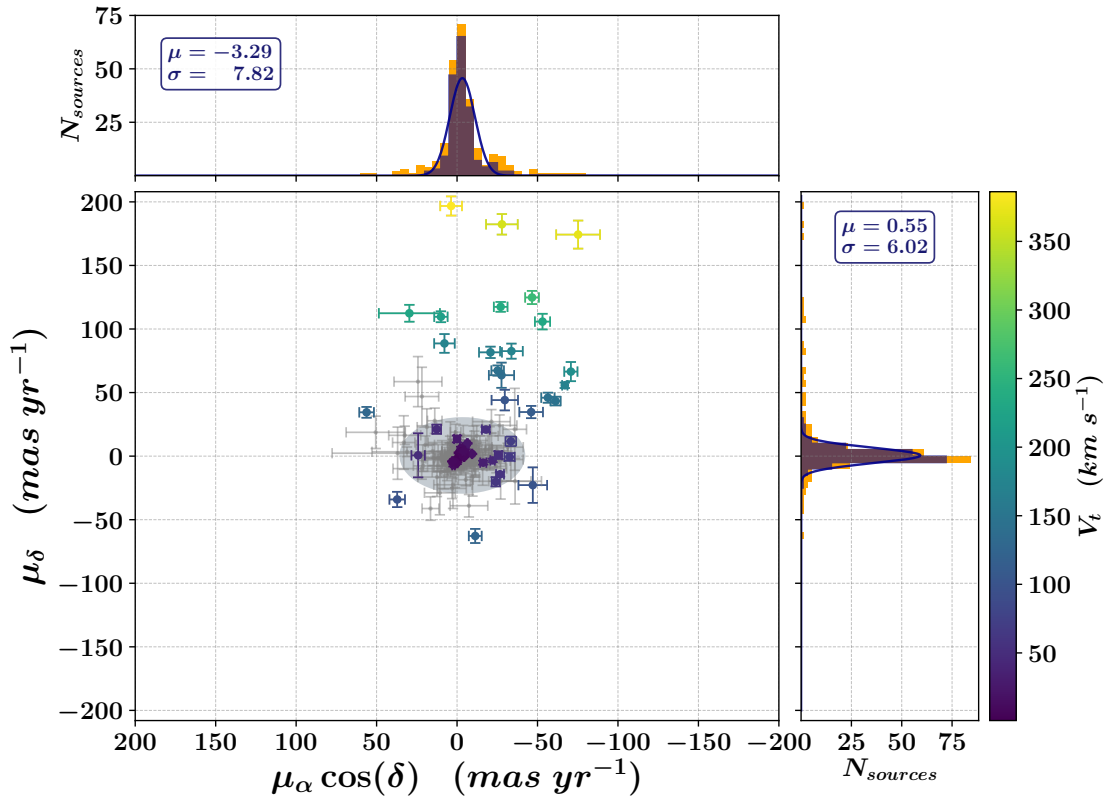
FIGURE 2.7: Absolute proper motions of compact radio sources in the $\mu_\alpha \cos(\delta) \times \mu_\delta$ plane colour coded by their transverse velocity. Sources with motions compatible with zero within 5σ in α and δ are shown in grey. The histogram distributions of motions in α and δ are shown in the top and right panel, respectively, for the full sample (orange) and sub-sample (dark-blue). A Gaussian fit is included for the sub-sample distribution used to define the intrinsic noise elliptical region shown in the diagram.

motions within this area and focus the discussion in the most significant motions after the previous cutoff criteria.

The final sample of significant motions is listed in Table 2.4. Column (1) shows the identification number from the catalogue reported in Table 2.3. Columns (2) and (3) indicate the measured proper motions in α and δ, respectively. Column (4) indicates the total proper motion in the plane of the sky, column (5) the transverse velocity for an adopted distance of 400 pc to the ONC, column (6) the position angle respect to the north celestial pole (NCP), and column (7) indicates the identification number from Forbrich et al. (2016). It consists of 22 sources with transverse velocities in the range of $\sim$95$-$373 km s^{-1} with most of them lying along the "finger" shaped features towards the north and northwest part of the BN/KL outflow from the Orion OMC1 cloud core (Zapata et al., 2009; Bally et al., 2015) and also known as "Orion Fingers" (Taylor et al., 1984; Allen and Burton, 1993). Figure 2.8 shows a high-resolution NIR image towards

TABLE 2.4: Sample of high proper motion in the OMC1 cloud core.

ID	$\mu_\alpha \cos\delta$ (mas yr^{-1})	μ_δ (mas yr^{-1})	μ_{total} (mas yr^{-1})	V_t [a] (km s^{-1})	PA (°)	[FRM2016] [b]
(1)	(2)	(3)	(4)	(5)	(6)	(7)
63	-70.7 ± 4.1	66.5 ± 7.6	97.1 ± 4.5	184.1 ± 8.6	-46.8 ± 2.8	25
78	-56.5 ± 4.1	46.0 ± 4.0	72.8 ± 3.2	138.1 ± 6.0	-50.9 ± 2.5	46
80	-61.2 ± 3.2	43.3 ± 3.4	75.0 ± 2.7	142.2 ± 5.1	-54.7 ± 2.1	48
91	-47.1 ± 8.9	-22.8 ± 14.0	52.3 ± 7.6	99.2 ± 14.4	64.2 ± 10.9	67
94	-53.1 ± 4.7	105.8 ± 6.2	118.4 ± 4.9	224.5 ± 9.3	-26.7 ± 2.0	70
98	-75.2 ± 13.6	174.3 ± 11.0	189.8 ± 8.3	359.9 ± 15.8	-23.4 ± 2.9	74
100	-46.6 ± 4.3	124.8 ± 5.2	133.2 ± 3.63	252.6 ± 6.9	-20.5 ± 1.3	76
101	-25.2 ± 3.9	67.3 ± 4.0	71.9 ± 3.0	136.3 ± 5.6	-20.5 ± 2.3	78
103	-33.8 ± 7.0	82.6 ± 5.9	89.2 ± 4.9	169.2 ± 9.2	-22.3 ± 3.5	81
111	-46.0 ± 7.3	34.7 ± 4.8	57.6 ± 5.5	109.3 ± 10.4	-53.0 ± 4.8	91
119	-29.7 ± 8.2	44.1 ± 8.1	53.1 ± 6.4	100.7 ± 12.2	-33.9 ± 7.1	97
124	-20.8 ± 7.1	81.6 ± 4.5	84.3 ± 3.4	159.7 ± 6.5	-14.3 ± 3.6	103
136	-27.1 ± 4.3	117.4 ± 3.9	120.5 ± 3.3	228.5 ± 6.3	-13.0 ± 1.7	129
153	-27.9 ± 9.8	182.4 ± 8.1	184.5 ± 7.0	349.8 ± 13.3	-8.7 ± 2.6	159
155	3.7 ± 6.8	196.8 ± 7.5	196.8 ± 5.7	373.2 ± 10.8	1.1 ± 1.5	161
157	-27.6 ± 7.9	63.6 ± 9.9	69.4 ± 7.7	131.5 ± 14.6	-23.5 ± 5.4	164
207	10.0 ± 4.1	109.6 ± 4.3	110.1 ± 3.8	208.7 ± 7.2	5.2 ± 1.9	237
208	7.8 ± 6.4	88.7 ± 7.4	89.0 ± 6.5	168.7 ± 12.3	5.4 ± 3.6	238
212	29.6 ± 19.0	112.4 ± 6.6	116.2 ± 7.3	220.4 ± 13.9	14.8 ± 8.7	239
263	56.2 ± 4.5	34.5 ± 4.3	65.9 ± 3.6	125.0 ± 6.7	58.5 ± 3.0	308
372	-11.3 ± 4.0	-62.8 ± 5.6	63.8 ± 4.4	121.0 ± 8.3	10.2 ± 2.8	450
411	37.2 ± 4.8	-34.1 ± 6.0	50.5 ± 5.1	95.6 ± 9.7	-47.5 ± 5.9	495

[a] For an adopted distance of 400 pc to the ONC.
[b] Forbrich et al. (2016).

the OMC1 outflow adapted from Bally et al. (2015) with the broad-band K_s filter in red, the 2.12 μm H$_2$ and 1.64 μm [Fe II] narrow-bands in green and blue, respectively. The OMC1 outflow has an explosive morphology of molecular material consequence of the dynamical encounter of stars which were ejected with speeds of a few tens of km/s more than 500 years ago (Bally and Zinnecker, 2005; Rodríguez et al., 2005b). Most of the material seen in near-IR image in Figure 2.8 seems to have been triggered by this event. This finding proves the sensitivity of these VLA observations to non-stellar radio emission and the utility of proper motions as an additional piece of information in counterpart identification.

The sample of fastest proper motions are indicated in yellow symbols in Figure 2.8. An example of two of the fastest features detected are shown in Figure 2.9. These are the sources 153 and 155 and are the northernmost sources seen in Figure 2.8, with transverse velocities of $V_T = 350 - 373$ km s^{-1} and uncertainties on the order of 13 km s^{-1}. The
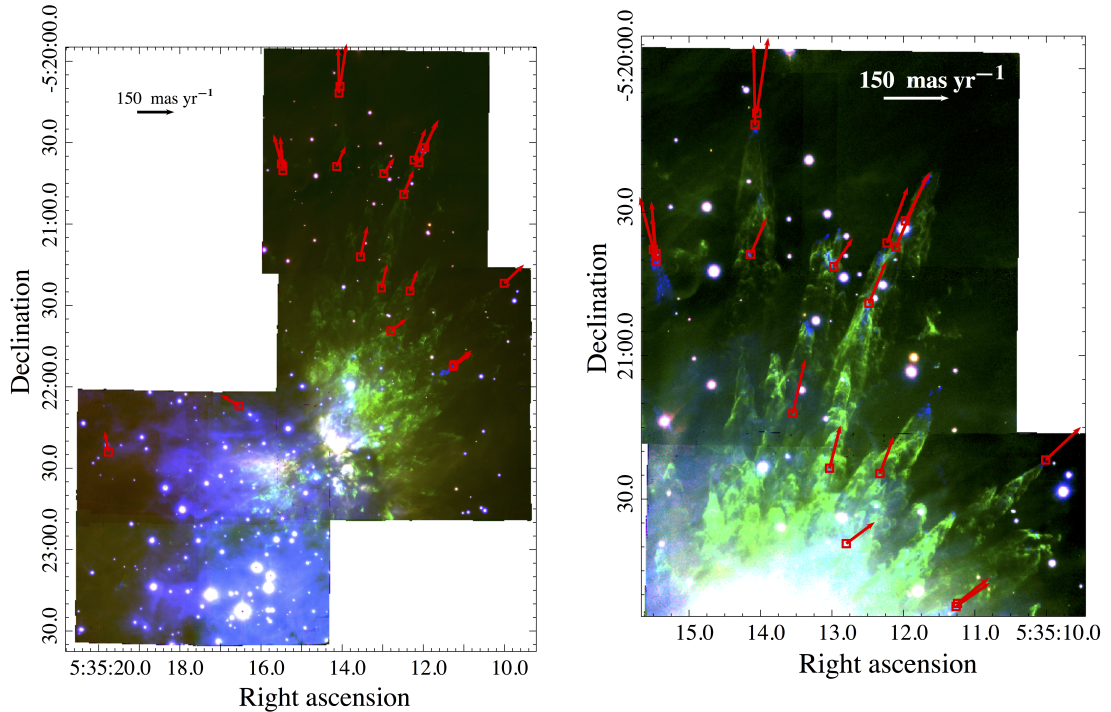
FIGURE 2.8: Color composite image of the GSAOI broad-band K_s filter (red), the 2.12 μm H_2 (green) and 1.64 μm [Fe II] (blue) narrow-band filters towards the OMC1 outflow (Bally et al., 2015). (left) Wide-filed image of the OMC1 outflow. (right) Close-up of the most prominent Orion finger systems in the northernmost field in the left panel (same scale, higher contrast). The positions of sources from the high proper motion sample is indicated with red symbols together with their proper motion vectors.

left panel of Figure 2.9 shows a close-up of Figure 2.8 around the sources 153 and 155 in a slightly larger FOV compared to the right panel FOV (white box) to highlight the larger infrared structure of these features. The right panel shows the VLA detections with the 2016 epoch in white contours of 10 levels between $65 - 140$ μJy bm^{-1} and the background image is the epoch 2012. Also, in the left panel the extrapolated position of both radio sources to the time of the NIR observations are indicated in small white symbols (correspond to the propagated position errors marginally seen in Declination and only visible in RA). These are indicated to elucidate where the radio emission comes from. These features appear to coincide with Fe II emission, perhaps suggestive of free-free radio emission. At this point, however, the emission mechanism remains unclear, not least since the emission is too faint for spectral index analysis.

Additional examples of non-stellar compact radio emission are those associated with the jet-like features around the BN object and shown in Figure 2.10. The radio continuum map corresponds to the 2012 VLA observations from Forbrich et al. (2016) while the white contours in the close-up around BN and the southwest features correspond to the
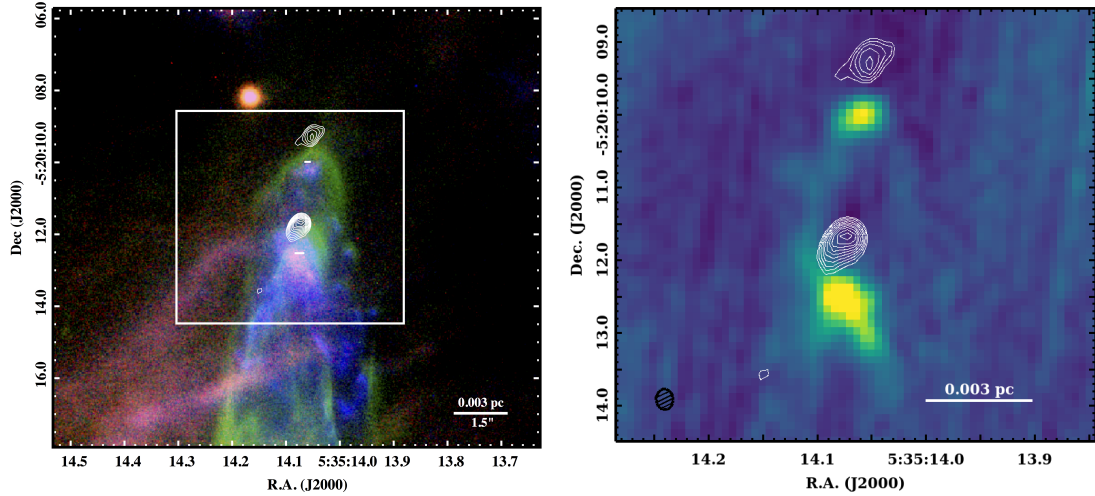
FIGURE 2.9: *(left)* Close-up from Figure 2.8 around the fastest moving sources 153 and 155 (the northernmost in Figure 2.8) highlighting the extended emission features in the NIR. The white box indicates the FOV shown in the right panel. *(right)* Background VLA radio continuum map from epoch 2012 centred around the sources in the left panel showing the VLA 2016 epoch contours in white with 10 levels between $65-140$ μJy bm^{-1}. The synthesized beam size is shown in black in the lower left corner.

2016 VLA observations. These jet-like features are labeled following the discussion in Bally et al. (2020) as E2 and E1 east from BN, and SW1, SW2 and SW3 southwest from BN. The spatial distribution and proper motions of these sources can be interpreted, as further discussed in Bally et al. (2020), to be tracing a low-velocity outflow from BN, although it has been suggested that it may contain a low-luminosity protostar or to be tracing ejected clumps produced by the OMC1 explosion (Dzib et al., 2017; Bally et al., 2020). Both sources SW1 and SW3 are moving away from BN towards the west while E2 is moving away from BN towards the east. The absolute PM of these sources are listed in Table 2.5 also indicating their equivalent transverse velocities for an adopted distance of 400 pc. The source SW1 (Zapata 11; Zapata et al. 2004) was originally reported by Menten and Reid (1995) and its PM have been well constrained on longer timescales using up to 9 VLA epochs ranging from 1985 to 2018 (Dzib et al., 2017; Rodríguez et al., 2020) reporting PM consistent with our measurements. Additionally, Forbrich et al. (2016) reported spectral index measurement for this source with negative value of -0.3 ± 0.09 suggesting nonthermal emission, which has been actually found for YSO jets (see Section 6 in Anglada et al. 2018 and reference therein). Source E1 is not included neither in Forbrich et al. (2016), since it appears as an extended emission in the epoch 2012, nor in the catalogue presented in this work since it is too faint in epoch 2016, however, it is still possible to extract its radio properties in both epochs for the purpose

of the discussion in Bally et al. (2020), although with comparatively high positional uncertainties (55-90 mas in δ and 75-120 mas in α). Interestingly, source E1 and SW2 present motions moving back towards BN, however this may be an apparent motion due to intensity variations of different parts in these features, which also leads to a very high PM for E1. The PM measurements for the sources BN, SW1 (Zapata 11) and E2 (IRc23) are consistent with those reported in Rodríguez et al. (2020).
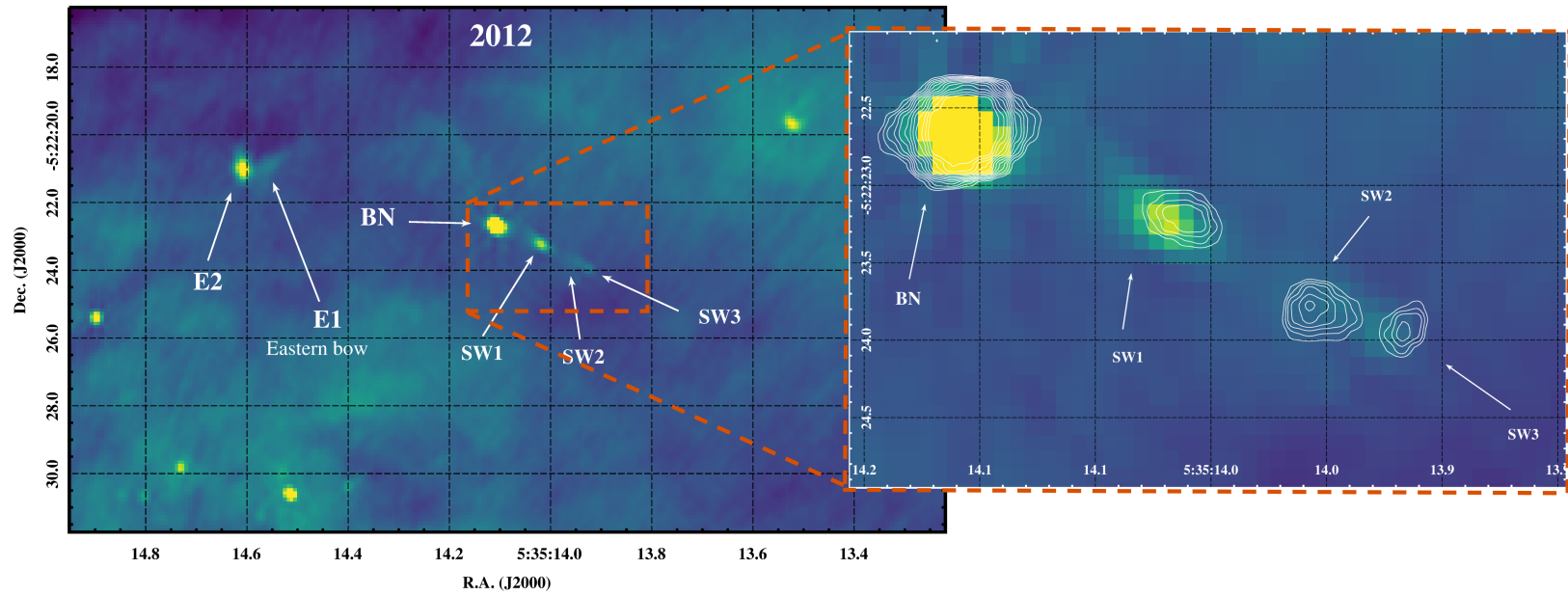
FIGURE 2.10: *(left)* VLA radio continuum map from epoch 2012 centred around the source BN. *(right)* Close-up of the BN source and its jet-like features showing the VLA 2016 epoch contours in white with 12 levels between $0.05 - 0.6$ mJy/beam. The proper motion properties of these sources are listed in Table 2.5.

TABLE 2.5: Absolute Proper Motions of the BN source and the jet-like features around it and shown in Figure 2.10.

Source	α(2000) (h m s)	δ(2000) (° ′ ″)	$\mu_\alpha \cos(\delta)$ (mas yr^{-1})	μ_δ (mas yr^{-1})	V_t (km s^{-1})	P.A. (°)	Source ID [a]	Comments
BN	05:35:14.10681±0.00009	-5:22:22.6396±0.0014	-6.4 ± 0.4	10.1 ± 0.4	22.6 ± 0.7	328 ± 2	156	
SW1	05:35:14.01394±0.00182	-5:22:23.1999±0.0188	-24.7 ± 7.0	4.4 ± 4.0	47.5 ± 12.5	280 ± 9	152	Zapata 11 [b]
SW2	05:35:13.95308±0.00095	-5:22:23.8168±0.0159	21.0 ± 6.2	-7.7 ± 4.3	42.3 ± 8.1	290 ± 8	150	
SW3	05:35:13.91647±0.00069	-5:22:23.9290±0.0155	-33.4 ± 3.3	11.7 ± 3.7	67.1 ± 5.1	289 ± 5	147	
E1 [c]	05:35:14.53241±0.00810	-5:22:20.7142±0.0864	-141.1 ± 48.2	96.5 ± 34.6	324.2 ± 39.5	304 ± 8	—	
E2	05:35:14.61240±0.00067	-5:22:20.9111±0.0136	12.6 ± 2.7	21.2 ± 3.7	46.7 ± 6.0	31 ± 6	177	IRc23 [b]

[a] This work (see Table 2.3).

[b] Source designation in Dzib et al. (2017).

[c] Source properties does not meet the criteria for the catalogues defined by neither Forbrich et al. (2016) (it's a extended emission) nor in this work (it has SNR<5).

2.3.3.1   Peculiar motion of source 117: COUP 510

In the sample of high proper motions there is an intriguing stellar source with apparent fast motion of $\mu_\alpha cos(\delta) = -67.0 \pm 1.7$ mas yr^{-1} and $\mu_\delta = 55.7 \pm 2.2$ mas yr^{-1} equivalent to an unusual stellar transverse velocity of $V_T = 165$ km s^{-1}. It has an X-ray counterpart in the COUP survey (COUP 510) presenting high extinction with hydrogen column density $\log(N_H) = 23.54 \pm 0.06$ cm^{-2} (Getman et al., 2005a) and no detection in the VISION Ks-band thus presenting characteristics of a deeply embedded object. If this corresponds to a genuine linear motion it would be possible to detect its expected X-ray position at the time of the COUP observations back in 2003 by extrapolation, however, in the X-ray COUP images there is no detection at the extrapolated position in 1" around apart from the source COUP 510 and the next closest X-ray source is COUP 533 at $3''\!.1$ away. Therefore a linear motions is not a plausible scenario for this source's motion. We then looked into the VLA archive for high angular resolution multiepoch observations towards this source and found 6 additional observations. These observations have been previously reported by Gómez et al. (2005, 2008), and we followed their data calibration and imaging procedures. The phase centers of these observations are consistent with the one used in this work, except for two observations with offsets of $30''$ (1991.68) and $45''$ (2004.84), which are still smaller than the primary beam size at the observed frequency. The data calibration follows the standard procedure recommended for the pre-upgrade VLA, and the imaging discarded visibilities provided by baselines longer than 100 kλ to diminish the noise caused by the poorly mapped extended emission (for details see Gómez et al. 2008). The positions were corrected to consider the updated position of the phase calibrator. In total, the radio source is detected in 8 epochs above 5σ, with rms noise levels ranging from $3-80$ μJy bm^{-1}, spanning almost 25 years including the epochs 2012 and 2016 used in this work. The main image parameters of these observations are listed in Table 2.6 together with the measured positions of the source.

TABLE 2.6: Multiepoch VLA dataset used for PM measurements of COUP 510.

Epoch	λ (cm)	Synthesized Beam size $(B_{maj} \times B_{min})$	PA (°)	RMS (μJy bm^{-1})	Position [a] $\alpha(2000)$	$\delta(2000)$
1991.68	1.3	$0.''26 \times 0.''25$	-55	80	$12.^{s}9497 \pm 0.^{s}0009$	$54.''8044 \pm 0.''0285$
1994.32	3.6	$0.''22 \times 0.''20$	$+9$	43	$12.^{s}9797 \pm 0.^{s}0007$	$54.''9168 \pm 0.''0205$
1995.55	3.6	$0.''26 \times 0.''22$	$+34$	74	$12.^{s}9648 \pm 0.^{s}0024$	$54.''4929 \pm 0.''0319$
2000.87	3.6	$0.''24 \times 0.''22$	$+3$	45	$12.^{s}9817 \pm 0.^{s}0006$	$54.''9118 \pm 0.''0140$
2004.84	3.6	$0.''22 \times 0.''20$	-6	29	$12.^{s}9814 \pm 0.^{s}0008$	$54.''9668 \pm 0.''0150$
2006.36	3.6	$0.''26 \times 0.''22$	-2	51	$12.^{s}9825 \pm 0.^{s}0009$	$54.''8534 \pm 0.''0285$
2012.75	6	$0.''30 \times 0.''19$	$+30$	3	$12.^{s}9834 \pm 0.^{s}0001$	$54.''9520 \pm 0.''0029$
2016.90	6	$0.''40 \times 0.''28$	-29	33	$12.^{s}9652 \pm 0.^{s}0004$	$54.''7212 \pm 0.''0083$

[a] $\alpha(2000) = 05^{h}35^{m}$; $\delta(2000) = -05°23'$.

Figure 2.11 shows the PM diagram in RA (left) and DEC (right) of the source 117 using the multiepoch observations listed in Table 2.6. We include the additional VLBA observation from 2015 (Forbrich et al., 2021; Dzib et al., 2021). These additional data show that the linear PM estimated only from the two VLA epoch 2012 and 2016 is not representative and may indeed correspond to different components of what seems to be a binary or higher order stellar system. Proper motion measurements for this source have been previously reported in Dzib et al. (2017) using multi-epoch VLA observations with a time baseline of $\sim$29 years. The reported PM in their work are $\mu_{\alpha}cos(\delta) = 1.9 \pm 1.5$ mas yr^{-1} and $\mu_{\delta} = 4.2 \pm 5.6$ mas yr^{-1} which is compatible with a non moving source. The VLBA detection included in this work is compatible with the detection from VLA 2016. What is still intriguing is the fact that in every single observation only one component was detected and never both or more of them at a time, and in four visits with VLBA it was only detected once. Orbital details of this system thus remain unclear.

2.3.4 Radio Variability

The study presented in Forbrich et al. (2017) using the deep VLA observations showed evidence of variability at very short timescales in the range of minutes with a few cases showing changes in flux density by a factor of 10 in less than 30 minutes. Based on these results we re-imaged the central pointing of our data into time slice images of $\sim$ 5 minutes integration time following the procedure described in section §2.2 and then produced light curves for all the 272 sources in the nominal catalogue of the central pointing by extracting their flux information from each of the individual 5-minute images using the methodology described in section §2.3.1. This time resolution also include exactly 3 science scans to ensure an even time on target throughout the time series. It resulted in a total of 41 individual images with a mean rms noise of $29\,\mu$Jy bm^{-1} ranging between $26 - 36\,\mu$Jy bm^{-1}. The first important issue here is the increase in the mean rms noise compared with the averaged $\sim$ 5 h image on where the overall rms noise is $10.24\,\mu$Jy bm^{-1} (see Table 2.1). Regardless of the decrease in sensitivity all the sources were detected in at least one of the individual images, 46% of them were detected in at least half of the 41 images and 22% of them were detected in every single image.
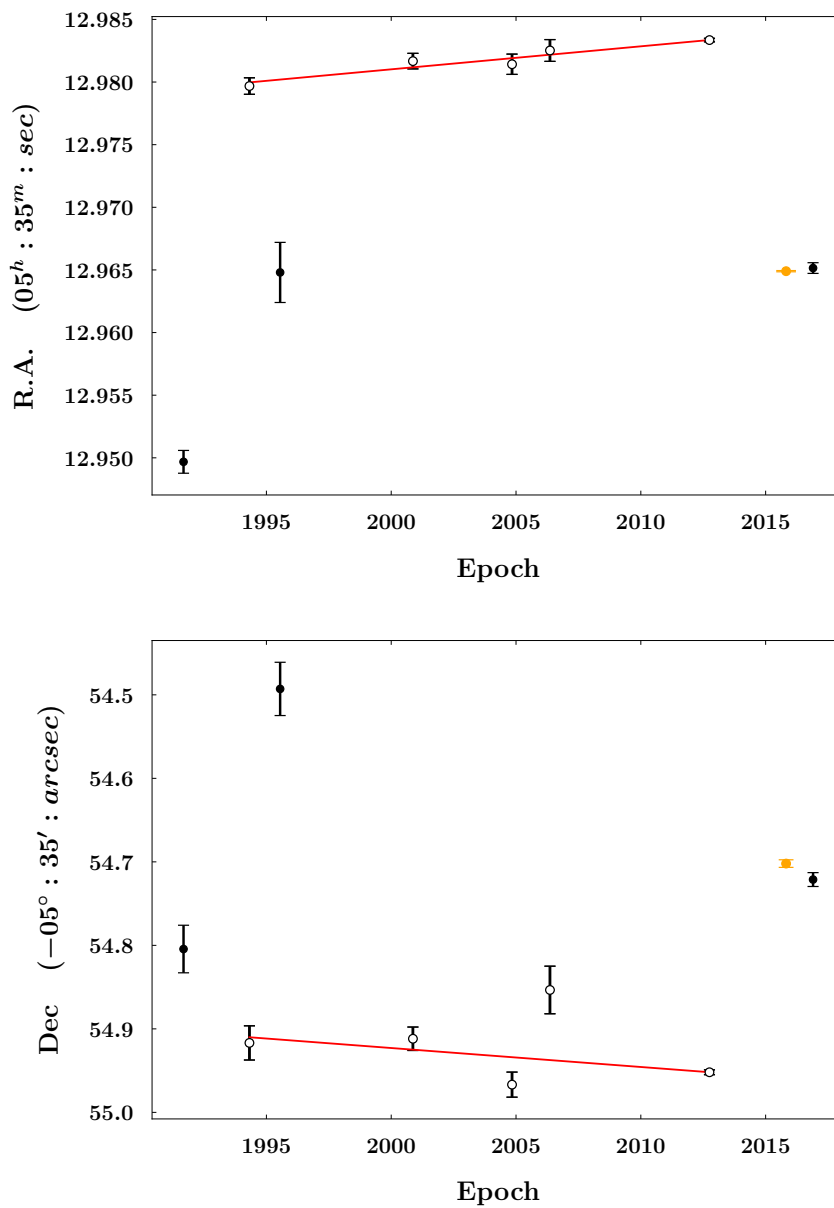
FIGURE 2.11: Proper motions in RA and DEC of the source 117 (COUP 510). VLA observations are indicated in black and the VLBA observation is marked in orange. Open black symbols represent one of the putative components of the system used for the hypothetical least-square fit indicated in red.
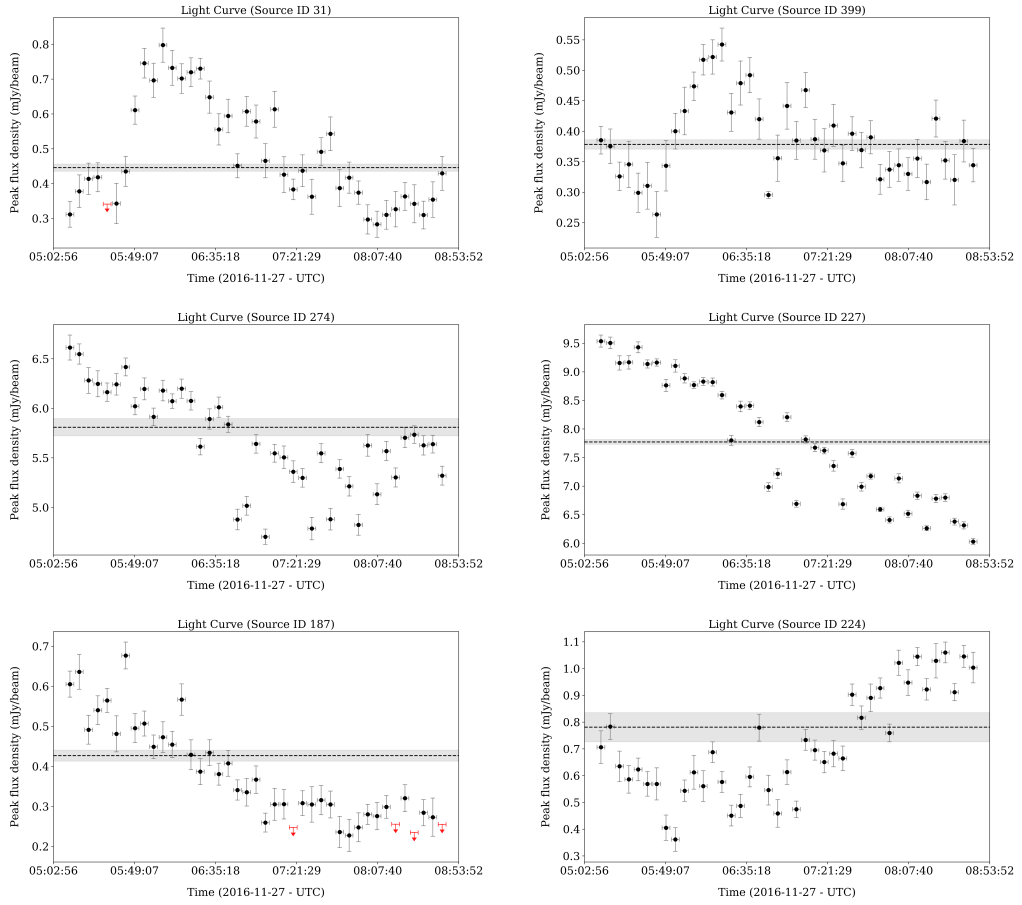
FIGURE 2.12: Radio light curves at 5 minutes time resolution. Detections are indicated in black symbols together with its uncertainties. Red symbols indicate the 5σ upper limits when the source is not detected. The peak flux density from the averaged 5 hrs image is shown by the horizontal dashed black line together with its uncertainty in grey horizontal band. All the measurements are corrected by the primary beam response.

Prior to the quantification of flux variation it was necessary to look at any systematic fluctuation. A very good test-case is the high-mass young stellar object BN, a non-variable thermal radio emitter ([Forbrich et al.,](), [2008](), [2016]()) with a peak flux density in the averaged 5 hrs image of $S_\nu = 2.370 \pm 0.023$ mJy bm^{-1}. Its peak flux density from the light curves has a mean value of $S_\nu = 2.354 \pm 0.007$ mJy bm^{-1} with a relative standard deviation of $\sim 5\%$ (0.127 mJy bm^{-1}). This systematic variation is smaller than the typical value for even just moderate variable sources with relative standard deviation $>20\%$ and therefore it does not impact our results of variability analysis. This measure for the BN source is also consistent with its peak flux density observed in the deep VLA catalogue of $S_\nu = 2.3413 \pm 0.0026$ mJy bm^{-1} which represent a variation of just $0.9 \pm 0.7\%$.

A few examples of light curves are shown in Figure [2.12]() for sources presenting a

small flare-like event and others presenting either increasing or decreasing peak flux density. The peak flux density of a source in the averaged long exposure image evidently does not always represent the overall evolution of its radio emission and there is a clear fluctuation at short timescales of just minutes that even not being extreme events can still be considerably brighter than the averaged peak flux density. Following Forbrich et al. (2017), an extreme variability event refers to a change in flux density by a factor of at least 10 in less than an hour. We define a variability factor VF as the ratio between the maximum and the minimum peak flux density in the timeseries dataset. Although, there is evidence of variability in several sources in the sample, none of them show changes in flux density above a factor of 5 and indeed $\sim$85% have VF<3.

The occurrence rate of extreme radio variability in the ONC has been estimated by Forbrich et al. (2017) based on the deep observations where they found a mean time between these events of 2220$\pm$1280 h ($\sim$ 3 months). The sources involved in this estimate are only sources with X-ray counterpart in the COUP survey assuming that this is the most complete sample of YSOs in the inner ONC. In our sample only 157 out of 272 sources have X-ray counterparts in the COUP survey, and the cumulative radio observing time of these sources is 785 h (5 h on each of the 157 sources) for which we found no extreme variability (not by a factor $\geq$10). However, this result lies within the probabilities of only one such event in a cumulative radio observing time of 2220$\pm$1280 h and yet, our cumulative radio observing time is still below the lower limit of 940 h considering the error. The new cumulative radio observing time adds up to 7445 h including the deep (Forbrich et al., 2016) and the new observation (only the central pointing), it leads to a mean time between extreme radio variability events of 2482$\pm$1433 h. This larger uncertainty compared to the previous estimate is a result of the same number of events we are still considering (3 extreme events from Forbrich et al. 2017).

On the other hand, it is also possible to look for variability on longer timescales by comparing our central pointing against the deep VLA observations. This is a particularly good comparison since these are identical observations and all the sources are affected by the same primary beam response correction due to their equivalent distance to the phase center. In our sample 253 sources are detected in the two datasets. We can measure the variability factor between these two epochs for each source by taking the ratio between their nominal peak flux density from both catalogues. There are two sources presenting a VF>10 at this long timescale and a third one marginally below this limit with a VF of

TABLE 2.7: Main parameters for the sources with highest VF between the two VLA epochs.

Source ID[a]	[FRM2016][b]	VF	S_ν [a] (mJy bm^{-1})	S_ν [b]	Sp. index [b]	COUP	log(N_H) [c] (cm^{-2})
31	4	12.05 ± 1.76	0.446 ± 0.024	0.037 ± 0.005	...	141	21.07 ± 0.03
315	378	10.93 ± 0.56	6.176 ± 0.312	0.565 ± 0.003	0.09±0.01	932	21.17 ± 0.09
179	196	9.40 ± 0.64	0.715 ± 0.039	0.076 ± 0.003	−0.20±0.23	648	21.52 ± 2.26

[a] This work.
[b] Identification number [FRM2016], flux density and spectral index from Forbrich et al. (2016).
[c] Hydrogen column density from Getman et al. (2005a).

TABLE 2.8: Main parameters for the brightest sources in the deep catalogue not detected in the new VLA data.

[FRM2016]	VF	S_ν (mJy bm^{-1})	Sp. index	COUP	log(N_H) (cm^{-2})
(1)	(2)	(3)	(4)	(5)	(6)
422	17.85 ± 0.03	0.676 ± 0.003	1.1 ± 0.1	997	21.60 ± 0.02
515	28.89 ± 0.00	1.188 ± 0.004	1.4 ± 0.1	1232	20.00 ± 0.00

Columns (1), (3), and (4) are identification number, peak flux density, and spectral index, respectively, from Forbrich et al. (2016).
Column (2): VF between the two epochs considering 5 times the local rms in the new observations.
Column (5) and (6) are identification number and Hydrogen column density from Getman et al. (2005a).

9.4±0.6. These three sources have X-ray counterparts in COUP with hydrogen column densities in the range log(N_H) = 21.07 − 21.52 cm^{-2} (Getman et al., 2005a). These parameters are summarized in Table 2.7.

Non-detections in the new observations of previously detected sources are not just due to a difference in sensitivity but potentially also due to variability at least for the brightest sources in the deep observations that should be clearly detected in the new VLA data. There are in total 303 sources in the deep catalogue not detected in the central pointing of the new VLA data. We looked for their positions in the new data and considered 5 times the local rms within a box of 14 pixels (1″4) as upper limits to compare against the peak flux density in the deep catalogue. This allows us to estimate a lower limit for their variability factor. As expected, most of the sources have a VF below 10 and are likely too faint for the new observations, but the are two interesting sources with VF of 18 and 29 listed in Table 2.8. These two sources are indeed in the list of only 13 extremely variable sources in Forbrich et al. (2017). Source [FRM2016] 422 in Forbrich et al. (2017) shows an extreme radio flare on timescales of ∼40 h while

TABLE 2.9: Main parameters for the brightest new detections in the VLA 2016 epoch (S/N≥50).

Source ID	VF [a]	S_ν (mJy bm^{-1})	COUP	$\log(N_H)$ [b] (cm^{-2})
47	2.2	0.31 ± 0.02	260	20.93 ± 0.04
438	1.5	0.69 ± 0.04	1259	21.55 ± 0.05

[a] From the light curves analysis in this work.
[b] Hydrogen column density from Getman et al. (2005a).

source [FRM2016] 515 shows the most extreme variability within just 30 minutes (by a factor of ∼100), also coinciding with an almost simultaneous X-ray flare of similar duration. While source [FRM2016] 422 was also not detected in any of the outer pointings, source [FRM2016] 515 was detected in pointings 3 and 6 with peak flux densities of 0.15±0.01 mJy bm^{-1} and 0.18±0.01 mJy bm^{-1}, respectively, leading to a long term variability with VF∼7 respect to Forbrich et al. (2017), and VF∼5 respect to the central pointing (considering the 5σ upper limit) which were observed with one month difference. Both sources [FRM2016] 422 and [FRM2016] 515 have reported spectral types K8 and O9.5-B2, respectively (Hillenbrand et al., 2013), although for the high-mass star it is noted that the radio emission may be detected from unresolved lower-mass companion.

Finally, another interesting finding concerns the new detections in the central pointing not detected in the previous deep VLA data. There are 19 new detections, 10 of which have X-ray counterparts in the COUP survey. There are 9 sources with S/N>10 and two of them have high S/N of 50 and 82. The main parameters of these two bright new sources are listed in Table 2.9.

2.4 Summary and Conclusions

We have presented a new deep, high-resolution catalogue of compact radio sources towards the ONC at centimeter-wavelengths using the most extended configuration of the VLA. This is the deepest catalogue for the surrounding areas of the ONC reported to date, reaching rms noise levels between $3-5$ μJy bm^{-1} at distances of ∼10.′4 from the center of the cluster, significantly improving the general census of known compact radio sources in the cluster. We detected a total of 521 radio sources above 5σ threshold over an area of ∼20′ × 20′. In this catalogue, 198 sources are new detections not previously reported at these frequencies. The highest stellar surface density occurs in the inner region, and

yet the number of radio sources may still be underestimated due to the difficulty of disentangling small-scale structure of the nebula and stellar point sources.

With our new catalogue, we are sensitive not only to stellar radio emission but also to radio emission originating elsewhere in the ONC, for example in outflows and shocks. It turned out in this regard that even the relatively short time baseline of 4.19 years is sufficient to trace high-velocity proper motions in the ONC, which can be more easily measured with phase-referenced radio than with optical observations. We identify radio sources in the deep 2012 catalogue as co-moving with and thus originating in ejecta of the OMC1 explosion. While we also appear to detect fast proper motions towards stellar sources, those are likely due to insufficiently sampled multiple systems.

We find that the central pointing, also covered in the previous deep survey, contains the majority of ONC radio sources, and interestingly, the surface density of radio sources falls off faster than that of X-ray sources, tracing young stars. This may be due to a surplus of thermal/free-free sources in the inner ONC that are ionized by θ^1 Ori C. Additionally, we find that most ($> 50\%$) radio sources have X-ray counterparts, throughout the area studied here, while only a minority ($< 20\%$) of X-ray sources have radio counterparts. X-ray emission thus remains a poor predictor of radio emission in this sample of young stars. Given the regional differences that we find, this is not simply a sensitivity effect.

Finally, a radio variability analysis for sources in the inner ONC is presented as a follow-up of our previous deep VLA variability study. We produced radio light curves at high time resolution for sources in the central pointing finding changes in flux density by a factor ≤ 5 on timscales of minutes to a few hours thus we do not find extreme variability events. The majority of the sources have detections in the previous deep VLA observations enabling the study of long term variability where we only find two sources with changes in flux density ≥ 10. Based on these two studies we find a mean time between extreme radio variability events of 2482 ± 1433 h.

Millimeter-wavelength flaring variability of Young Stellar Objects: A first systematic survey in the Orion Nebula Cluster

3.1 Introduction

High-energy processes are already present at the earliest stages of protostellar evolution as revealed by X-ray and radio observations (e.g., Feigelson and Montmerle 1999). In the overview presented in Chapter 1, we discussed nonthermal radio emission in the form of (gyro)-synchrotron radiation as a tracer of high-energy processes in YSOs, where mildly relativistic electrons can produce gyrosynchrotron radiation detectable at cm-wavelenghts and electrons at higher energies (MeV) are responsible for synchrotron radiation into the millimeter range (Dulk, 1985; Güdel, 2002). It is thus clear that these two mechanisms are naturally related, however their physical connection has not been fully explored observationally and it seems that these two (millimeter and centimeter emission) do not necessarily coexist simultaneously in a single source (e.g., Kundu et al. 2000). In addition to these emission mechanisms, thermal dust emission arising from circumstellar discs and surrounding envelopes is also an important source of millimetre continuum emission in YSO but this is assumed to be constant on short timescales. In Section 1.3, also in Chapter 1, I also discussed how the improved sensitivity of radio facilities

such as the VLA and VLBA has significantly improved the observation of YSOs at centimeter-wavelengths and, particularly in the context of this thesis, how recent studies have revealed strong and rapid YSO cm-flares (an order of magnitude in less than an hour; Forbrich et al. 2017).

At millimeter-wavelengths, radio continuum observations of YSOs are typically used to study the thermal component of circumstellar disks that arises from dust emission assumed to be constant on short timescales. However, a few serendipitous discoveries have shown evidence of strong millimeter flares in YSOs. The first such discovery was a mm-wavelength flare towards a T Tauri star in the ONC (GMR A) as reported in Bower et al. (2003). A few other mm-flares have been reported towards other YSOs, interestingly, these are all part of binary systems and their flares are interpreted to arise from interbinary collisions of coronal structures near periastron passage (T Tauri binary system V773 Tau A: Massi et al. 2006, 2008 or T Tauri spectroscopic binary system DQ Tau: Salter et al. 2008, 2010). There is also evidence of submillimeter flares in YSOs even more luminous than the flares detected in GMR A and DQ Tau. Mairs et al. (2019) reported the first coronal YSO flare detected at submillimeter-wavelength towards the binary T Tauri system JW 566, also in Orion. Millimeter variability in YSOs has been also studied on longer timescales but with a focus on thermal dust emission where the variability is caused by active mass accretion periods with an impact on timescales of months to years (Liu et al. 2018; Francis et al. 2019 and references therein).

Early estimates for the expected number of radio flares with changes in flux density greater than a factor of 5 in a few hours that can be detected in the Orion nebula at millimeter-wavelengths using ALMA were as high as ∼10-100 flares in short integration times (minutes) for a sensitivity of ∼0.1 mJy and even ∼100-1000 flares for observations with sensitivity of ∼10 μJy (Bower et al., 2003). Similarly, in a more specific frequency range, it has been proposed that with the high sensitivity that ALMA band 3 observations could achieve within just a few hours (on the order of ∼10 μJy) in a small area in the core of the ONC (<30 arcsec) it would be possible to find ∼6 radio flares per day with change in flux density by a factor >2 on timescales of hours to days (Rivilla et al., 2015). However, such sensitivity was not achieved in the ALMA band 3 observations that we are presenting here, which ranges between ∼100 and ∼300 μJy (see section 3.2). Two important elements in the search for flares in such observations are the sensitivity provided by ALMA and the large number of sources in the ONC.

Given the lack of a statistical sample of strong and short-lived millimeter flares we started a first systematic search for such events in YSOs using ALMA, targeting the BN/KL region close to the core of the ONC for a large sample of sources, and observing on short timescales of minutes to days. The use of ALMA is a major benefit for such studies due to the high sensitivity even on very short timescales. Our observations are described in Section 3.2. We then present an assessment of systematic effects for variability measurements using ALMA simulated observations in Section 3.3. Our results on source detection is presented in Section 3.4.1, followed by our variability analysis in Section 3.4.2 including the finding of a strong flare and the overall variability in the sample. We finally present a summary and our conclusions in Section 3.5.

3.2   Observations and Data Reduction

The Kleinmann-Low Nebula, a dense molecular cloud core close to the Becklin-Neugbauer object (herafter BN/KL; Becklin and Neugebauer 1967; Bally et al. 2011) was observed with ALMA during Cycle 5 (program 2017.1.01313.S, PI: J. Forbrich) at 3 mm ($90 - 105$ GHz) on 2017 December 22, 27, and 29. A total of 8 epochs of $\sim$1.2 h each towards a single pointing centred at $\alpha_{\mathrm{J2000}} = 05^{\mathrm{h}}35^{\mathrm{m}}14\overset{s}{.}5$ and $\delta_{\mathrm{J2000}} = -05°22'30\overset{''}{.}6$ were obtained using the array configuration C43-5 with an average of 48 antennas per epoch (12-m array) on baselines of 15-2517 m (see Table 3.1). The longest baselines of this range are particularly relevant to mitigate the extended emission in the Orion Nebula. This phase center position is 1 arcmin NW of θ^1 Ori C, the O7 type star providing most of the photons ionizing the Orion Nebula. In order to prioritize time on source, the observations were carried out in dual-polarization mode recording the XX and YY correlations that allow us to recover the Stokes I intensity maps (Stokes Q is also accessible but insufficient to obtain overall linear polarization without additional calibration). Four continuum spectral windows with bandwidths of 1.875 GHz were used and centred at 90.5, 92.5, 102.5, and 104.5 GHz, each one consisting of 32 channels of 62.5 MHz-width. These spectral windows were chosen to avoid the strong lines of CO and its isotopologues.

TABLE 3.1: ALMA Cycle 5 observation logs.

Epoch #	Starting Time (2017/UTC)	Number of Antennas	Time on Source (h)	Synthesized beam size ^{a} (arcsec^2 ; °)	Sensitivity (1σ rms) (μJy beam^{-1})
(1)	(2)	(3)	(4)	(5)	(6)
1	Dec 22 / 00:37:31	49	1.16	0.41 × 0.24 ; 75	145
2	Dec 22 / 01:58:28	49	1.16	0.35 × 0.25 ; 84	118
3	Dec 22 / 03:19:41	49	1.16	0.32 × 0.25 ; 88	167
4	Dec 22 / 04:40:49	49	1.16	0.34 × 0.25 ; −86	274
5	Dec 27 / 04:55:28	46	1.16	0.36 × 0.24 ; −81	184
6	Dec 29 / 02:52:24	46	1.16	0.32 × 0.24 ; −86	249
7	Dec 29 / 04:13:51	46	1.16	0.34 × 0.24 ; −82	307
8	Dec 29 / 05:35:50	46	1.17	0.44 × 0.23 ; −78	291
—	Concatenated image	—	9.3	0.35 × 0.24 ; −88	42

[Note] The array configuration used for all the observations was C43-5.

^{a} Synthesized beam properties: ($\theta_{\max} \times \theta_{\min}$; PA)

We used the pipeline-calibrated ALMA visibilities processed using the CASA[1] software (release 5.4.1). The initial amplitude and bandpass calibrator was the quasar J0423-0120 and then the phase calibrator was J0529-0519, observed every 3 science scans (every 10 min). The calibrated dataset was imaged with the TCLEAN task in CASA. We used the Stokes plane I and spectral definition mode 'mfs' (Multi-Frequency Synthesis). The Hogbom deconvolution algorithm and a Briggs weighting method[2] with a robustness parameter of 0.5 were used. This robustness value corresponds to the mid-point between "Natural" and "Uniform" weightings, and thus a good compromise between sensitivity and resolution. The image size for all the observations is 2048×2048 pixels with a pixel size of 0.05 arcseconds and the mean synthesized beam size between all the individual maps is 0.36×0.24 arcsec^2, equivalent to physical lengths of $96-144$ au at the distance of the ONC (assumed to be ~ 400 pc; Großschedl et al. 2018; Kuhn et al. 2019). Photometry was extracted from images that were corrected for the primary beam (PB) response following a PB gain level cut-off of 20 per cent (pblim$= 0.2$) and thus masking the image outside a radius of $\sim$0.75 arcmin from the phase centre where the PB gain level reaches 20 per cent due to PB attenuation. The resulting images cover a circular field of view of $\sim$1.5 arcmin in diameter with a half power beam width (HPBW) at the central frequency of $\sim$0.93 arcmin. (see Figure 3.1). In order to further reduce the impact of extended emission on the point-like source extraction process, we applied spatial filtering of the visibility data[3] using baselines of the (u, ν) range longer than 138 kλ ($\sim$414 km) and therefore filtering out structures larger than $\sim$1.5 arcsec, while the largest sources in the field have sizes $\lesssim$1 arcsec (excluding the extended component of the OMC1 hot core). This is done by removing the data recorded by pairs of antennas whose baseline is shorter than the threshold given above. Furthermore, with the angular resolution achieved by our observations and their corresponding physical lengths at the distance of the ONC, we are expecting unresolved emission from protostellar flares, magnetospheres, and even from larger magnetised structures confined within smaller scales than the synthesized beam corresponding to $\sim$100 au (Massi et al., 2008; Salter et al., 2010), while at the same time we are not expecting variability from extended structure (associated with thermal dust emission) on the short timescales studied here of minutes to days.

---

[1]Common Astronomy Software Application (McMullin et al., 2007).

[2]The Briggs method is a visibility weighting strategy that smoothly varies between "Natural" and "Uniform" weighting. Natural weighting results in better sensitivity (lower rms image noise) but poorer resolution. Uniform weighting, instead, results in higher resolution but increased rms image noise.

[3]Same spatial filtering of the visibilities described in Chapter 2 Section 2.2: Longer baselines are sensitive to more compact emission, while shorter baselines are sensitive to more extended emission.

The overall sensitivity ranges between 0.18 and 0.31 mJy beam^{-1} among the different epochs where the highest rms noise levels are found in observations on the same day (29 December). These increased rms noise levels were due to poor weather conditions over the course of the last day of observations and also for epoch 4. The resulting image parameters for all the 1.16-h observations (hereafter "epochs") are summarized in Table 3.1. An additional map with the concatenated data was generated following the same imaging procedure and spatial filtering used for the individual epochs. The improved sensitivity of the concatenated image reaches an rms noise of 0.04 mJy beam^{-1}, corresponding to 36 per cent of the noise levels of the individual epochs where weather conditions were better and 14 per cent of the noise level in the epoch with the worst conditions (epoch 7). This combined image was used as a reference for source detection and to obtain the averaged peak flux densities reported in Table 3.2 and described in the following section. The premise here is that this deep image would yield the best source catalogue as long as many sources have quiescent emission – which is not always the case, as we will see below.

An additional set of images was generated at 20 and 4 minutes time resolution following the same procedure described above and aimed to look at the shorter timescales of the specific flare-like features found in the 1 h light curves described in section 3.4.2. Given the complex emission in this region, such time-sliced imaging and subsequent source fitting was used to obtain source photometry. The 20 minutes time resolution maps were chosen to include exactly 6 continuous science scans from the observations leaving outside only 2 remaining scans at the end of each individual epoch and equivalent to 3 minutes of observation. These 2 scans were then recovered when imaging the 4 minutes time resolution maps. The 20 minutes time resolution maps contain ∼1.3 minutes of time dedicated to calibrations. All these images were used to generate light curves (LCs) at 1-h and 20-min time resolution, leading to 8 and 24 individual images, respectively. The rms noise levels for the 20-min images have values of 290 to 360μJy beam^{-1}. Only 17 images at 4 min time resolution were generated for the time intervals around the flare-like features of the most variable sources. Finally, given the discovery of a strong flare discussed in Section 3.4.2.1, a set of 8-seconds time resolution images were generated only for a time interval of 40 minutes around the strong event following the same imaging procedure already described, resulting in 265 high-time resolution images with typical rms noise levels of ∼1.0 mJy beam^{-1}.
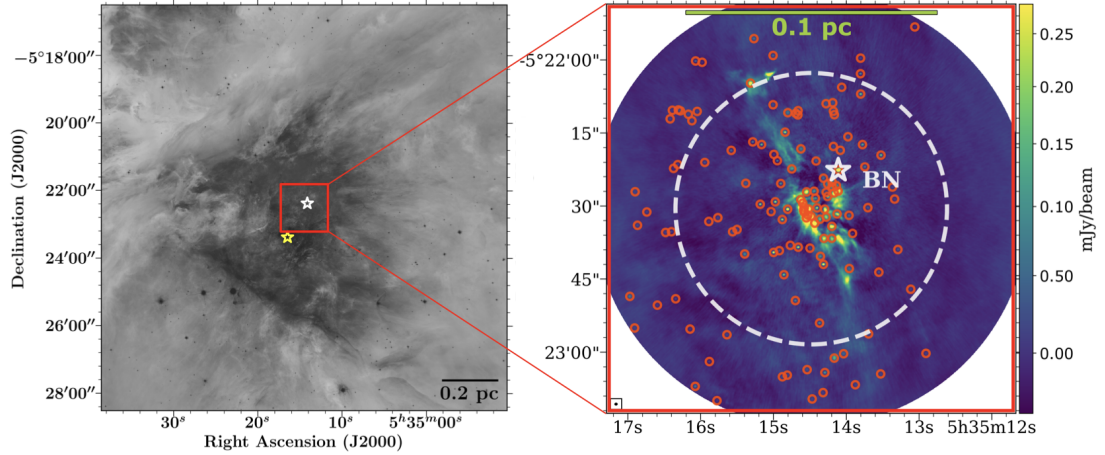
FIGURE 3.1: (left) HST r-band image (ACS/WFC) of the Orion Nebula with a field-of-view of 12×12 arcmin^2 centred at the Orion-KL region (white star symbol) indicating in red the ALMA observed field. The yellow symbol indicates the position of θ^1 Ori C in the Trapezium cluster (Background image credits: NASA, ESA, M. Robberto, and the Hubble Space Telescope Orion Treasury Project Team). (right) ALMA 3 mm continuum map of the Orion-KL region using the concatenated data (8 epochs combined). The white dashed circle indicates the HPBW at the central frequency (∼0.93 arcmin) and the red circles indicate the 133 detected sources ($\geq 5\sigma$). The white star symbol indicates the position of source BN as reference.

3.3 Simulated observations to assess systematic artificial variability in a complex region

Our observations show evidence of widespread YSO millimeter variability on a wide range of timescales from minutes to days, including a strong flare. Our main focus is to characterise the strongest events that we can find in the resulting sample of sources, however this widespread variability extends down to the lowest measurable levels. An assessment of lower variability levels in this observations involves dealing with technical difficulties due to the ubiquitous complex multi-angular scale emission in the ONC on top of its source density which necessarily requires time-sliced imaging of the whole field containing both resolved and unresolved sources and a constantly changing shape and size of the synthesized beam throughout the observations resulting in a variable background. This time-sliced imaging method needs to be applied to re-image the field at any time resolution followed by standard photometry to obtain flux measurements. Due to these complications it is expected that systematic effects will have an impact on flux measurements of unresolved sources and ultimately affecting variability measurements. The opposite scenario would be an isolated and unresolved source on top of a flat

background where instead of time-sliced imaging a direct fit of a point source model to the visibilities would be a suitable method for flux measurements.

In order to quantify the systematic effects described above and to determine what is the minimum level of variability in ONC sources that can be studied using our method we performed an analysis of simulated ALMA observations for a set of artificial, constant sources. Both the simulated observations and the artificial source properties reproduced as closely as possible our actual ALMA observations. These simulations consisted of 300 input images with a single artificial source in each, but using different source properties (brightness and shape) and different background properties as well. We made use of the Simobserve task in CASA to first simulate the visibilities consisting of 7 observations of 1 h integration time each all of them at different hour angles ranging from -5 h to $+1$ h pointing towards the same phase center used in our actual observations as well as the same antenna configuration and reference date of the observations. We then made use of the Simanalyze task to image the simulated visibilities. Finally, flux measurements and variability analysis were performed following the same method used for the analysis of the actual observations.

The artificial sources were 2D Gaussian models with a range of sizes for both major and minor axis equivalent to FWHM between 0.1 and 0.9 arcsec to include completely unresolved, marginally resolved and resolved sources in the experiment. The amplitude of these model sources were set to cover a range of peak flux density between 5 and 100 mJy beam^{-1}. This set of basic parameters resulted in 100 initial artificial sources that were combined with three different background images taken directly from the actual observations using the concatenated data and within the HPBW primary beam. These three background sections of the concatenated image were chosen to represent three arbitrary levels of complexity from standard (largely clear) to highly complex (contaminating extended emission) with rms noise levels ranging between 0.1 and 2.5 mJy beam^{-1}. Each source was located at the center of the three different background images. This resulted in 300 input sky models whose visibilities were simulated for 7 different hour angles (HAs) on the sky and subsequently imaged with Simanalyze with a pixel size of 0.05 arcsec and an image size of 100 pixels per side. This results in a total of 2100 simulated images (seven observations per each of the 300 input sky models).

In order to extract the flux information from each of the 2100 simulated images,

we applied the same method used for source detection in the actual data. Following the source extraction method described in Vargas-González et al. (2021), we obtained flux information using a Gaussian fitting algorithm based on the IMFIT task in CASA that iterates over each input source using different values for fitting area around the source and different offsets from the input position to avoid nearby contamination. The flux measurements were then used to analyze the light curves (LCs) of each source in order to assess the maximum change in peak flux density throughout the 7 observations, hereafter variability factor (VF), and defined as the ratio between the maximum and minimum peak flux density in the LCs. Figure 3.2 shows an example for the resulting analysis and includes the LC of the source in the top left panel and its corresponding maximum change in peak flux density (VF=1.81±0.01). The sky model (shown in the top right panel) corresponds to the input image for the simulation and contains the artificial source combined with one of the three real background images. In this example, this background section of the concatenated data that has an rms noise of 0.5 mJy beam^{-1}, the source model already combined with the background image has a peak flux density of 5.02 ± 0.02 mJy beam^{-1} and an original area of $\sim$0.26 arcsec^2. The resulting simulated observations shown in the middle and bottom panels include the resulting beam in the lower left corner of each map, already highlighting its changes in shape, size and orientation. The areas of these resulting beams are indicated in the bottom-right panel for each observed HA to illustrate how different elevations largely affect the synthesized beam subsequently affecting our final flux density measurements.

As in the example shown in Figure 3.2, the large range of source properties and the different backgrounds used are differently affected by this change in the synthesized beam over the course of the observations, and thus also resulting in a range of artificial variability levels. These artificial variability spans a range of 1.1≤VF≤2.1 and a median value of VF=1.51.

These results represent a conservative and likely overestimated assessment of the maximum systematic VF we could find in our actual observations. This is because we have used a wider range of source properties and also a wider range of elevations than the actual ALMA observations of the ONC comprise, which had a maximum HA coverage between −3h20m and +3h13m, with resulting source elevations between 40° and 72°, these simulations included a HA range of −5h≤HA≤+1h, which results in source elevations between 15° and 72°. If we limit these simulations to −3h20m<HA< +1h, we
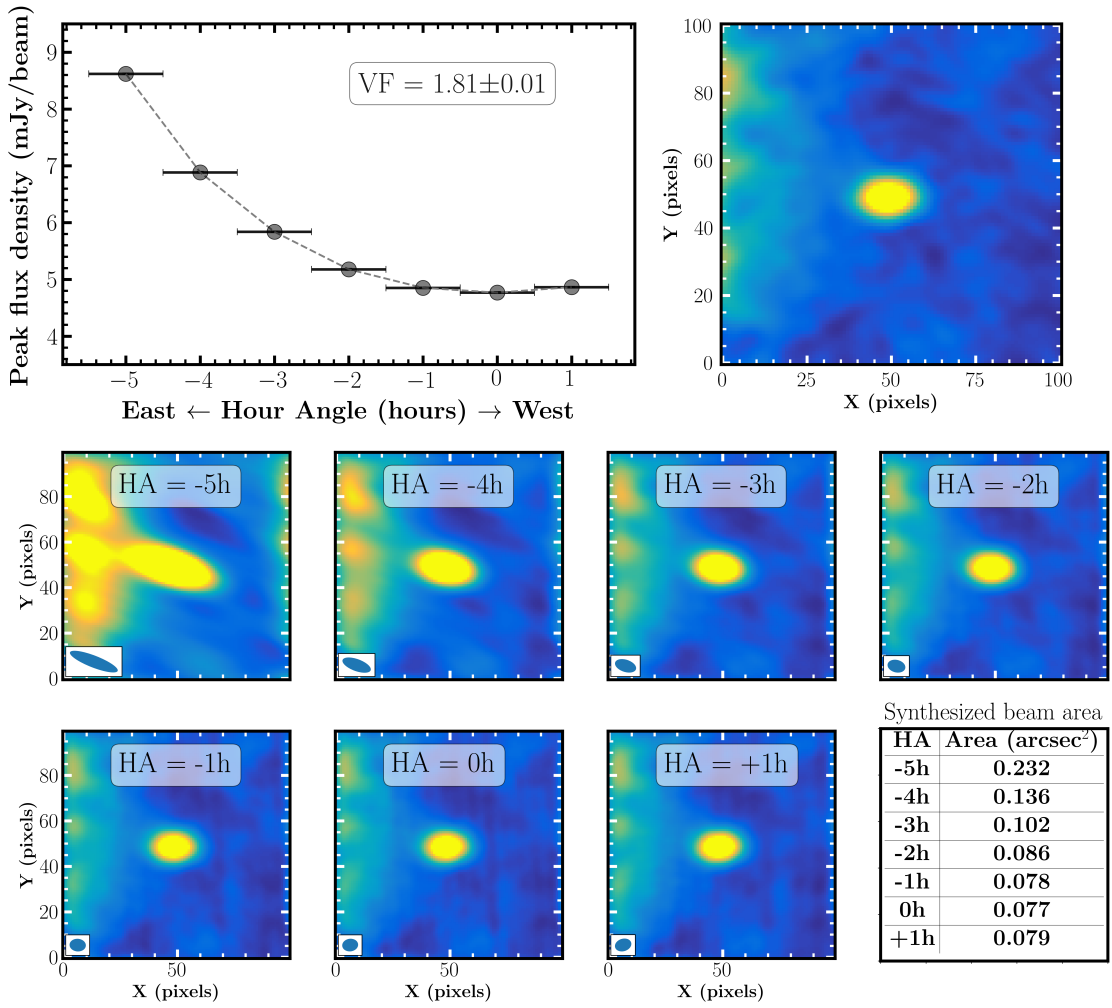
FIGURE 3.2: Simulated constant source and its resulting artificial variability. Left-hand panel in the top row show the resulting LC and VF. Right-hand panel in the top shows the input image containing the artificial source already combined with the background image. The middle and bottom rows show the resulting simulated observations labeled with the corresponding HA and with the resulting synthesized beam indicated in the lower-left corner of each map. The table in the bottom-right panel indicates the synthesized beam area for each observation.

then obtain a maximum systematic variability of VF~1.6. As a compromise between these considerations and the results from the full sample in the simulations, a reasonable cut-off for systematic variability that can affect at least a sample of sources given certain conditions (e.g., source size in combination with a complex background) is VF=2. In these simulations, ~76 per cent of the sources show VF≤2, ~17 per cent show 2.0≤VF≤2.1, and there is a 7 per cent for which it was not possible to obtain a final VF since these were not detected when combined with the most complex background. While sources in our actual ALMA data with VF≤2 may still show real variability, the main focus in our study is to find the strongest events and how often those occur rather than a

detailed study of minor variability. Here, we discuss these highly variable sources as well as important considerations for the study of lower levels of variability for similar datasets. Also, while we have used a wide range of parameters for sources and backgrounds to determine a conservative lower limit in our variability analysis, these do not necessarily comprise the full range of scenarios for every single source in the actual observations and therefore such variability for specific sources would still need visual inspection.

Since the systematic effects relevant here are linked to changes in synthesized beam and in turn this is linked to source elevation, then these systematic effects will generally not occur on arbitrary timescales. An example of this can be seen in the lightcurve shown in Figure 3.2 for which the artificial change in peak flux density smoothly develops with elevation. The only exception would be an adjacent contaminant that would pass through the beam as it rotates throughout the observations. Even in such a scenario the resulting effect would not compromise the detection of a short flare which will have different characteristics.

Beyond these systematic effects, which dominate our analysis, Francis et al. (2020) analyzed the accuracy of ALMA flux calibration and the impact on variability searches, which is particularly relevant for isolated sources with a clean background. They find that with improved calibration strategies the uncertainty can be lowered to a few percent, but this is beyond what can be achieved in our complex target region.

3.4 Results from ALMA observations

3.4.1 Source Detection

Compact source detection methods applied to radio maps towards crowded and complex star-forming regions face a challenge due to contamination from spatially filtered complex extended emission. Even after applying additional spatial filtering, this often remains as uneven noise with occasional spurious point-like emission, and therefore automated source extraction methods typically require significant manual intervention to deal with artifacts. We thus searched for compact sources by visual inspection of the concatenated image followed by an automatic search only on the position of known X-ray sources in the Chandra Orion Ultra-deep Project (COUP; Getman et al., 2005a), known sources

detected at cm-wavelengths with the VLA reported by Forbrich et al. (2016) and Vargas-González et al. (2021), and millimeter sources reported in Friedel and Widicus Weaver (2011), Eisner et al. (2016), and Otter et al. (2021). These catalogues provide an updated and well characterized sample of X-ray and radio sources likely tracing the young stellar population in the Orion BN/KL region. Along with the multiwavelength tracers of young stars, variability itself, particularly at the heart of the OMC1 cloud, would most likely originate from a YSO and it is thus a suitable tool for source identification even for deeply embedded sources inaccessible at other wavelengths, particularly IR and optical, where a strong radio flare would be the only observable tracer in such a case.

From our search in the aforementioned X-ray and radio surveys, within the HPBW primary beam (r<0.47 arcmin from the phase centre) there are 52 COUP sources. Among these X-ray sources, 48 per cent have a counterpart in our catalogue using a search radius of 0.5 arcsec where only two additional nearby X-ray sources could be included with separations ≤0.7 arcsec if applying a search radius of 1 arcsec, one of them COUP 599. This COUP source is not a clear counterpart of source BN and could potentially be just a nearby source or emission from the outflow of BN (Grosso et al., 2005). Similarly, we detect 40 per cent of the 58 VLA sources within the HPBW primary beam (6 cm observations with angular resolutions of ∼0.4 arcsec). Only 4 additional nearby VLA sources (angular separations ≤0.8 arcsec) can be included if extending the search radius from 0.5 arcsec to 1 arcsec (Forbrich et al., 2016; Vargas-González et al., 2021). On the other hand, we detect 89 per cent of the 28 millimeter sources within the HPBW primary beam reported in Friedel and Widicus Weaver (2011) based on 3 mm CARMA observations at different spatial resolutions down to a synthesized beam size of ∼0.5 arcsec. Two of the remaining 3 "non-detected" millimeter sources appear as extended structures (>1.5 arcsec) in our ALMA observations (sources C2 and C30, see Table 1 in Friedel and Widicus Weaver 2011) and are not included in our analysis. We also detect the 4 millimeter sources in the field reported in Eisner et al. (2016) using 1.3 mm ALMA observations with angular resolution of ∼1 arcsec, listed as proplyds and detected in optical and/or near-IR bands (Ricci et al., 2008; Hillenbrand and Carpenter, 2000). Finally, in the ALMA millimeter survey presented in Otter et al. (2021) there are 61 within the HPBW primary beam of which 77 per cent have counterparts in our catalogue within 0.1 arcsec following a search radius of 0.5 arcsec. There are 14 millimeter sources from Otter et al. (2021) not detected in our work that lie within the HPBW primary beam

of our observations. Their reported 3-mm flux measurements are $\leq$0.4 mJy except for two sources with flux measurements of 0.673$\pm$0.010 mJy and 0.850$\pm$0.007 mJy, identified as sources 40 and 38 in their catalogue, the former located $\sim$0.6 arcsec north-west from source BN, where the local rms noise level is $\sim$0.3 mJy beam^{-1} while the latter, located in an empty field with local rms noise of $\sim$0.04 mJy beam^{-1}, would be expected to be clearly detected with S/N>5 if it was a constant source.

We obtained flux information following the source extraction method described in section 3.3 based on a Gaussian fitting algorithm using the IMFIT task in CASA. Due to the presence of noise peaks with S/N levels in the range of $\sim 3-4$, we have enforced a detection threshold of 5σ, leading to a total of 133 sources. We noted a significant improvement for source detection by using the additional spatial filtering of the visibility data allowing a 39 per cent increase in detected sources, amongst these the flaring source discussed in section 3.4.2.1 which is surrounded by complex emission that does not allow to fit a Gaussian component unless applying the additional spatial filtering. The main resulting parameters (position, peak flux densities, and source structure) for the 133 detected sources are listed in Table 3.2 and were obtained from the concatenated data (full catalogue available in the online version). Their variability parameters shown in columns (6) and (7) are described in the following section and were obtained from the time-resolution maps.

All the detected sources are indicated by red symbols in the right panel of Figure 3.1 overlaid on the ALMA 3 mm continuum map from the concatenated data. The continuum map shown in the background in Figure 3.1 was generated without the additional spatial filtering described in section 3.2 for illustrative reasons in order to highlight the complex extended emission particularly in the inner region. The source distribution shows a higher number density towards the eastern side of the cluster with no detections above 5σ in the westernmost area. A similar spatial distribution is found at cm-wavelengths as well as in the X-ray and NIR bands (Forbrich et al., 2016). The lower source density at X-ray and NIR wavelengths can be associated with higher extinction levels, consistent with the higher dust emission towards the western region in the ONC as seen at submillimeter-wavelengths (Di Francesco et al., 2008), while the radio population distribution, essentially unaffected by extinction, is likely tracing the actual YSO distribution with the exception of the intrinsically faint millimeter sources.

The goal of this work is to search for short-term millimeter variability from minutes to days associated with nonthermal radio emission in protostars, and therefore we do not intend to study disk properties here, which have been discussed in detail elsewhere (e.g., Eisner et al. 2016, 2018; Otter et al. 2021). In this context, if the measured flux is dominated by disk emission we will not expect any short-timescale variability, however the resulting flux measurements from insufficiently resolved or totally unresolved sources are likely to be a combination of both the disk component and flares and thus it becomes a relevant concern for disk mass studies. In this regard, while COUP sources in our sample already represent our best tracer of the young stellar population including objects associated with disks, we still searched for counterparts in multiwavelength surveys in Orion as an additional approach to identify the fraction of known protoplanetary disks in our sample and quantify to what extent millimeter flares could potentially dominate such emission towards these sources.

The typical size for circumstellar disks from optical studies within our observed area of the ONC is ∼130 au with just a few larger than 150 au (Vicente and Alves, 2005). The spatial resolution in our observations is equivalent to spatial scales of ∼140 au at the distance of the ONC, and we are therefore looking at unresolved or just marginally resolved protoplanetary disks in the region. We searched for protoplanetary disk counterparts in the literature within 1 arcsec to account for the combined uncertainties between different observations and for the emission scales at optical and/or infrared wavelengths of these systems that could still be associated with a millimeter counterpart within this search radius. Within this field there are 21 out of the 162 protoplanetary disks reported at optical wavelengths in Vicente and Alves (2005) whereas we find 14 mm-counterparts in our catalogue with separations between $0.3 - 0.8$ arcsec. Based on similar observations with the HST, Ricci et al. (2008) reported 29 protoplanetary disks within this field, while we find 16 mm-counterparts in our catalogue with maximum separations of ∼0.5 arcsec. In addition to the four 1.3-mm sources from Eisner et al. (2016) mentioned at the beginning of this section, 24 out of 29 sources detected at 0.85 mm that fall within our observed field are detected in our observations (Eisner et al., 2018). At least ∼25 per cent of well characterized disks are associated with sources in our sample, of which ∼73 per cent of them are already COUP counterparts, and we will also be able to assess any variability associated with these systems. If we include the sample of small protoplanetary disks studied in Otter et al. (2021) there is then a fraction ∼66 per cent of characterized disks

in our sample of which ∼64 per cent are COUP sources.

TABLE 3.2: ALMA 3 mm catalogue: Source properties and variability measurements in the Orion-KL region.

				Deconvolved Size	1 h time resolution		20 min time resolution						
α(2000) (h m s)	δ(2000) (° ′ ″)	ID	Peak Flux Density (mJy bm^{-1})	$\theta_{max} \times \theta_{min}$; P.A. (arcsec^2 ; °)	VF[a]	Timescale (h)	VF[a]	Timescale (h)	COUP	F16[b]	V21[b]	O21[b]	Additional counterpats[c]
(1)	(2)	(3)	(4)	(5)	(6)	(7)	(8)	(9)	(10)	(11)	(12)	(13)	(14)
05:35:12.9031 ± 0.0067	-5:23:00.2701 ± 0.0028	1	0.554 ± 0.020		≤ 2		≤ 2					80	
05:35:13.0633 ± 0.0181	-5:21:53.2754 ± 0.0051	2	0.734 ± 0.037	0.53 × 0.08 ; 102 ± 2	≤ 2		4.9 ± 1	4.1	516			77	
05:35:13.1107 ± 0.0068	-5:22:47.1013 ± 0.0075	3	0.274 ± 0.015		≤ 2		3.0 ± 0.4	1.7	524	107	128		131-247
05:35:13.2887 ± 0.0054	-5:22:38.9703 ± 0.0028	4	0.703 ± 0.023		≤ 2		5.1 ± 0.9	1.7	539			13	
05:35:13.3331 ± 0.0361	-5:22:28.5864 ± 0.0113	5	0.195 ± 0.020		2.4 ↑	4.1	2.6 ± 0.5	169.6					
05:35:13.3655 ± 0.0112	-5:22:26.1496 ± 0.0035	6	0.296 ± 0.017		≤ 2		8.1 ± 1.6	3.1	538	117		36	
05:35:13.5207 ± 0.002	-5:22:19.5594 ± 0.0011	7	2.491 ± 0.027	0.13 × 0.11 ; 79 ± 80	≤ 2		≤ 2		551	127*	135	46	135-220
05:35:13.5242 ± 0.0085	-5:23:04.4708 ± 0.0061	8	0.405 ± 0.024		≤ 2		3.6 ± 0.5	0.4	552			107	HC360
05:35:13.5497 ± 0.0042	-5:22:43.618 ± 0.0027	9	0.624 ± 0.016		≤ 2		2.6 ↑	166.9				7	
05:35:13.6895 ± 0.0066	-5:22:56.2309 ± 0.007	10	0.175 ± 0.013		≤ 2		2.9 ± 0.6	3.1	563			1	
05:35:13.7027 ± 0.0068	-5:22:30.3492 ± 0.0034	11	0.482 ± 0.017		≤ 2		4.4 ± 0.8	169.9	574			29	
05:35:13.7428 ± 0.0031	-5:22:21.9904 ± 0.0017	12	0.955 ± 0.017		≤ 2		4.0 ± 0.5	171.0	573			41	137-222
05:35:13.7756 ± 0.0016	-5:22:17.399 ± 0.0008	13	2.095 ± 0.018	0.13 × 0.03 ; 123 ± 7	≤ 2		≤ 2		572	139		48	
05:35:13.8003 ± 0.0011	-5:22:07.0349 ± 0.0007	14	3.199 ± 0.022	0.12 × 0.04 ; 174 ± 7	≤ 2		≤ 2		579	142	142	59	138-207
05:35:13.8025 ± 0.0051	-5:21:59.6729 ± 0.0028	15	0.802 ± 0.026		≤ 2		3.1 ± 0.3	123.0		140		78	
05:35:13.8032 ± 0.0019	-5:22:02.8587 ± 0.0011	16	2.583 ± 0.030		≤ 2		≤ 2		578			62	
05:35:13.8694 ± 0.0081	-5:23:06.714 ± 0.0039	17	0.345 ± 0.014	0.23 × 0.05 ; 61 ± 12	≤ 2		2.9 ± 0.5	124.3				106	
05:35:13.9099 ± 0.0066	-5:22:35.632 ± 0.0032	18	0.546 ± 0.020		≤ 2		4.3 ± 0.9	119.9	591			16	
05:35:13.9597 ± 0.0249	-5:22:42.8081 ± 0.0186	19	0.263 ± 0.021	0.61 × 0.12 ; 50 ± 5	≤ 2		4.2 ± 0.7	120.6					
05:35:13.9611 ± 0.0135	-5:22:31.9325 ± 0.0073	20	0.479 ± 0.036		2.7 ± 0.5	170.3	4.7 ± 0.7	167.9	590			23	
05:35:13.9733 ± 0.0137	-5:22:15.7734 ± 0.0094	21	0.196 ± 0.025		≤ 2		4.5 ± 0.9	3.1					
05:35:14.0330 ± 0.0064	-5:23:00.3572 ± 0.0038	22	0.594 ± 0.026		2.3 ± 0.2	1.4	3.1 ± 0.5	47.3				81	
05:35:14.0600 ± 0.0195	-5:22:05.6447 ± 0.0094	23	0.268 ± 0.028	0.12 × 0.05 ; 70 ± 37	2.5 ↑	123.0	2.4 ± 0.2	48.3				60	
05:35:14.0820 ± 0.0167	-5:22:18.5331 ± 0.0074	24	0.259 ± 0.028		≤ 2		2.1 ↑	123.0					
05:35:14.1055 ± 0.0005	-5:22:22.6444 ± 0.0002	25	70.991 ± 0.183	0.07 × 0.03 ; 9 ± 9	≤ 2		≤ 2		599	162	156	39	source BN

[a] VF in columns (6) and (8) report values above the systematic threshold discussed in Section 3.3. VF reported as ≤ 2 indicate sources that are either constant or with variability below the systematic threshold. For lower limits an upper arrow symbol is indicated instead of uncertainty values.

[b] Source identificatins for counterparts in: F16 (Forbrich et al., 2016), V21 (Vargas-González et al., 2021), and O21 (Otter et al., 2021). Source from Forbrich et al. (2016) reported as nonthermal centimeter counterpart in the VLBA follow-up (Forbrich et al., 2021) are marked with an asterisk symbol in column (11).

[c] Additional counterparts associated with known circumstellar disks: Ricci et al. (2008); Eisner et al. (2016, 2018); Vicente and Alves (2005); Hillenbrand and Carpenter (2000).

The full catalogue with 133 listed objects is available in Appendix B.

After identifying the fraction of sources associated with well-characterized protostellar systems and a large sample of mm-sources with multiwavelength properties characteristic of young stellar objects we then performed a systematic search for variability based on the 1 h epochs spanning more than a week of observations which we describe in the following section.

3.4.2 Radio Variability

As stated above, we here aim to search for the occurrence rate of the strongest short-term variability. Employing the same source extraction method used on the concatenated data, we search for emission toward all the sources in our catalogue (Table 3.2) in all the observed 1-h epochs. 56 per cent of the sources were detected in all the individual epochs, 90 per cent were detected in at least half of them and every source was detected at least once. While non-detections can be explained by the increased rms noise levels in the individual images of up to 0.3 mJy beam^{-1} compared to the 0.04 mJy beam^{-1} in the concatenated image (see column 6 in Table 3.1), this could still suggest some degree of variability for sources that would only be detected during a flare.

The peak flux measurements from the individual epochs were used to generate the LCs at 1 h time resolution for all the sources as shown for source 74 (the ORBS) in the left-hand panel in Figure 3.3. This LC covers a strong flare discussed in detail in the following section. If no peak above a 5σ detection threshold was found, then three times the local rms noise was used as an upper limit (red symbols in Figure 3.3). The maximum change in peak flux density is defined as VF (see section 3.3). When an upper limit is used as a minimum, then the VF is reported as a lower limit for variability since we are not able to account for the true peak flux density during that minimum. The same criteria were used to generate the LCs at different time resolution as shown in the middle and right-hand panel of Figure 3.3 with LCs at 20- and 4-min time resolution.

3.4.2.1 Strong Flaring source ORBS

Visual inspection of the individual eight epochs (see Table 3.1) for a subset of sources in our catalogue led to the discovery of a flare object identified as source 74 in our catalogue (Table 3.2). It only appears as a very faint source with an average peak flux

density of 0.241 ± 0.022 mJy beam^{-1} in the concatenated image where it is only possible to fit a Gaussian component following the additional spatial filtering of the visibility data described in Section 3.2. Otherwise this source would not be detected, mostly due to complex emission in the surrounding area, the presence of a nearby source within $\sim$0.4 arcsec (source 75 in our catalogue) and its relatively faint average peak flux density. Based on the eight individual 1-h epochs, this source was only detected once, remaining undetected for more than three hours since the start of the observations to then peak at 1.039 ± 0.046 mJy beam^{-1} (S/N$\sim$23) in epoch 4. It remained undetected in the following epochs five days later with an average 3σ upper limit of $\sim$0.4 mJy beam^{-1} (see left-hand panel in Figure 3.3 and the corresponding continuum maps in Figure 3.4 for the individual epochs). This led to a lower limit variability with VF$\sim$4.1 within $\sim$2.7 h against epoch 2. Its LC at 20 min time resolution (see middle panel in Figure 3.3) allows us to further constrain this event to develop in less than an hour with a significantly increased VF$\sim$21$\pm$4 and a peak flux density of 2.562 ± 0.056 mJy beam^{-1}. This source clearly was only detected during this flare which was bright enough to still allow its (faint) detection in the averaged 8-h image.

FIGURE 3.3: Radio LCs of source 74 (ORBS) at 1-h (left-hand panel), 20-min (middle panel), and 4-min (right-hand panel) time resolutions. The middle panel indicates the horizontal axis in arbitrary units representing consecutive epochs with their corresponding time intervals highlighted in red, blue, green, and yellow areas as shown in the left-hand panel. The yellow area indicates the time interval around the flare event then highlighted in the following two panels at higher time resolution. Detections are shown in black with 3σ error bars. Upper limits are indicated in red (three times the local rms noise). The dashed horizontal line represents the averaged peak flux density from the concatenated data with 1σ and 3σ error bands in grey. The dashed background in the 4-min LC spans the time interval shown in Figure 3.5.
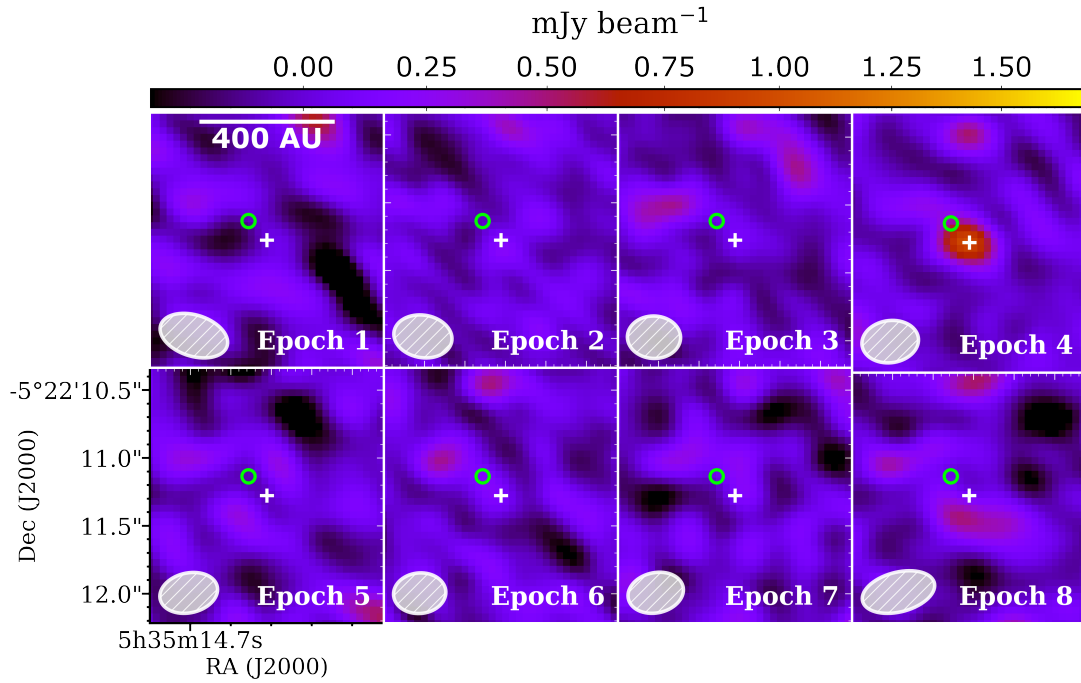
FIGURE 3.4: Continuum maps from the eight individual epochs at 1-h time resolution (listed in Table 3.1) around the position of the flaring source ORBS. The green circles indicate the position of the X-ray source COUP 647 while the white plus symbol indicates the position of the millimeter detection in epoch 4.

Visual inspection of the individual eight epochs (see Table 3.1) for a subset of sources in our catalogue led to the discovery of a flare object identified as source 74 in our catalogue (Table 3.2). It only appears as a very faint source with an average peak flux density of 0.241 ± 0.022 mJy beam^{-1} in the concatenated image where it is only possible to fit a Gaussian component following the additional spatial filtering of the visibility data described in Section 3.2. Otherwise this source would not be detected, mostly due
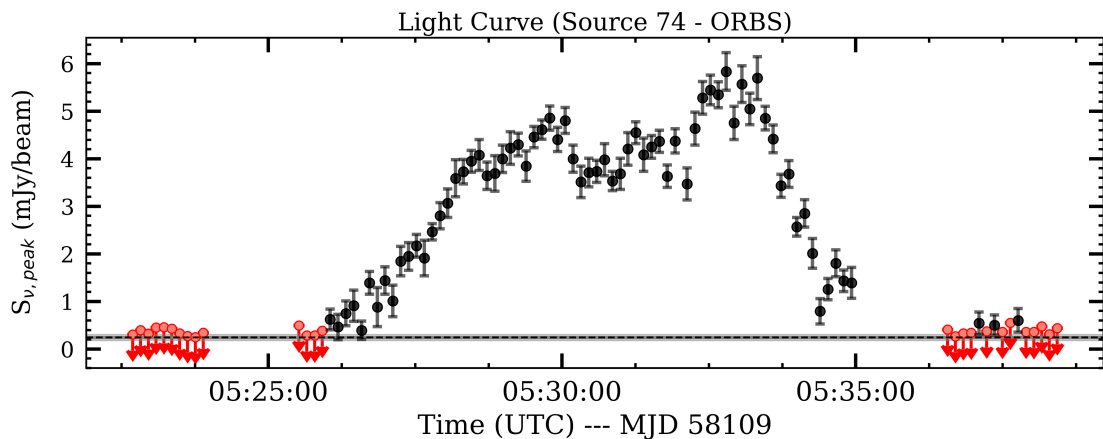
FIGURE 3.5: Radio LC of source ORBS at 8-s time resolution following same symbol notation from Figure 3.3.

to complex emission in the surrounding area, the presence of a nearby source within $\sim$0.4 arcsec (source 75 in our catalogue) and its relatively faint average peak flux density. Based on the eight individual 1-h epochs, this source was only detected once, remaining undetected for more than three hours since the start of the observations to then peak at 1.039 ± 0.046 mJy beam^{-1} (S/N$\sim$23) in epoch 4. It remained undetected in the following epochs five days later with an average 3σ upper limit of $\sim$0.4 mJy beam^{-1} (see left-hand panel in Figure 3.3 and the corresponding continuum maps in Figure 3.4 for the individual epochs). This led to a lower limit variability with VF$\sim$4.1 within $\sim$2.7 h against epoch 2. Its LC at 20 min time resolution (see middle panel in Figure 3.3) allows us to further constrain this event to develop in less than an hour with a significantly increased VF$\sim$21$\pm$4 and a peak flux density of 2.562 ± 0.056 mJy beam^{-1}. This source clearly was only detected during this flare which was bright enough to still allow its (faint) detection in the averaged 8-h image.

Its high S/N even at shorter timescales allows us to constrain the development of this event for which we generated its 4-min and then 8-s time resolution LCs shown in the right-hand panel in Figure 3.3 and separately in Figure 3.5, respectively. The 8-s images span a time interval of 40 min around the flare event, however, the LC in Figure 3.5 is only displaying an interval of $\sim$17 min (96 images in total). Outside this time interval there are no detected peaks above a 5σ threshold.

While at these two time resolutions we are already constraining the brightness of the event with similar peak flux density of 5.159 ± 0.066 mJy beam^{-1} at 4-min time resolution and a maximum of 5.835 ± 0.132 mJy beam^{-1} at 8-s time resolution, it is only at the highest 8-s time resolution that a more detailed substructure in the LC is seen allowing us to constrain the flare duration to $\sim$10 minutes with a rise time of $\sim$4 minutes from the first detection (05:26 UTC) until the first peak corresponding to an order of magnitude change in peak flux density in such a short timescale. However, the presence of several features in the LC may not necessarily correspond to the same event and the flare duration refers to the entire event in the LC which shows a brief decline at 05:30 UTC generating two main peaks, the second one $\sim$7 minutes after the first detection and just $\sim$3 min from the first peak. The second peak is the maximum already mentioned and the first one just slightly fainter at 4.856 ± 0.085 mJy beam^{-1}. Figure 3.6 shows the 8-s time resolution continuum maps at a time frame just prior to the first detection of

the source (left-hand panel) and at the maximum peak (right-hand panel) seen in the LC shown in Figure 3.5 (see caption for details).

After the second peak discussed above, the flux decreases by a factor of ~5 in 2 min when the observations where interrupted to observe the calibrator at around 05:35 UTC. As mentioned above, there are no detections neither before nor after the flare except for the three datapoints at around 05:37:30 UTC that appear to show marginal detections with a signal-to-noise ratio between $6<S/N<7$. This is the most extreme event in the sample showing variability by a factor ≥10 followed by the sources 86 and 87 discussed later in section 3.4.2.2, however these two additional sources show such variability on the opposite extreme on timescales of hours to days.

Based on the flare rise time up to the first peak and its corresponding light travel time, we can estimate an upper limit for the size scale of the emitting region to have a radius r<0.5 au. Following this constraint, the intensity at the first peak would be equivalent to a brightness temperature of 0.5 MK (Güdel, 2002), which in turn represents a lower limit and thus an additional indication for the presence of high-energy particles, nonthermal emission thus being a possibility for the detected radio emission. Since the observation were carried out in dual-polarization mode it is not possible to recover Stokes V information. We imaged Stokes Q intensity maps, instead, but no signal is detected above the rms noise levels at the position of ORBS (note that linear polarization calibration were not obtained during the observations, see Section 3.2). The limited information on Stokes parameters does not allow for a conclusive assessment of neither linear nor circular polarization for the flare emission.

The position of this flare object coincides with a previously reported radio flaring source (within ~0.09 arcsec) referred to as ORBS (Orion radio burst source) detected at cm-wavelengths ($\lambda = 1.3$ cm; $\nu = 22.3$ GHz) with the VLA in *K*-band (Forbrich et al., 2008). During these observations (July 1991) this source showed an order of magnitude increase in its peak flux density in a few hours with a maximum at 47 mJy beam^{-1} with this spectacular event marking the source's first radio detection. The study presented in Forbrich et al. 2008 reports a double radio source at 8.4 GHz (VLA *X*-band) toward this position of which the closest one to the ORBS source (within ~0.11 arcsec) seems to be the south-west component of this double radio source (source SW in Table 2 of Forbrich et al. 2008) while the other component is coincident with the position of another

millimeter source in our catalogue within 0.12 arcsec, source 75, which does not show clear signs of variability at any time resolution (VF≤2). This double radio source, of which the ORBS is the south-west component, had first been detected at 8.4 GHz with the VLA from observations conducted in April 1994 and described in Menten and Reid (1995), see their Figure 4.

While ORBS was detected during a strong X-ray flare later on (COUP 647, Getman et al. 2005b), there are no additional counterparts at neither optical nor infrared wavelengths suggesting that this is a still deeply embedded source. The hydrogen column density derived from its COUP counterpart is $\log(N_H) = 23.51$ which leads to a high visual extinction $A_V \sim 160$ mag (using the conversion $N_H/A_V = 2 \times 10^{21}$ cm^{-2} from Vuong et al. 2003) and thus an additional evidence for not having neither optical nor infrared counterparts. The position of the COUP counterpart is coincident with the position of the flare peak within $\sim$0.17 arcsec and is indicated with a green circle in Figure 3.4. It has been also detected more recently at cm-wavelength with the VLA and VLBA within $\sim$0.02 arcsec and $\sim$0.04 arcsec, respectively (Forbrich et al., 2016; Vargas-González et al., 2021; Dzib et al., 2021). Identified as source 180 in Vargas-González et al. (2021) and source 198 in Forbrich et al. (2016), without significant variability (VF≲2). The VLBA observations consisted of 4 epochs, yet this source was only detected in two of them underlining its highly variable nature along with its non-thermal component. Its apparent large VLBA proper motion suggests this source alone (only the south-west component of the 8.4 GHz double radio source mentioned above) may be a binary system with angular separation of $\sim$4 au at the distance of the ONC. Interestingly, among the few millimeter YSO flares in literature, such as V773 Tau A and DQ Tau, are also multiple systems whose flaring mechanism is thought to be caused by interbinary magnetospheric interaction (Massi et al., 2006; Salter et al., 2008). Moreover, two highly variable sources discussed here (ORBS and source 86) and also reported as nonthermal radio sources in the VLBA observations discussed in Forbrich et al. (2021) are already 50 per cent of the potential binaries in that VLBA sample (Dzib et al., 2021). The upper limit angular size scale for the emitting region derived earlier is $\sim$1.3 mas and thus comparable to the beam size for the unresolved VLBA detection for this source.

Among the 3-mm sources detected by Friedel and Widicus Weaver (2011) using CARMA, source C5 is coincident with the position of source ORBS within 0.2 arcsec. It is reported with a peak flux density of 4.73 ± 0.76 mJy beam^{-1} similar to its values around
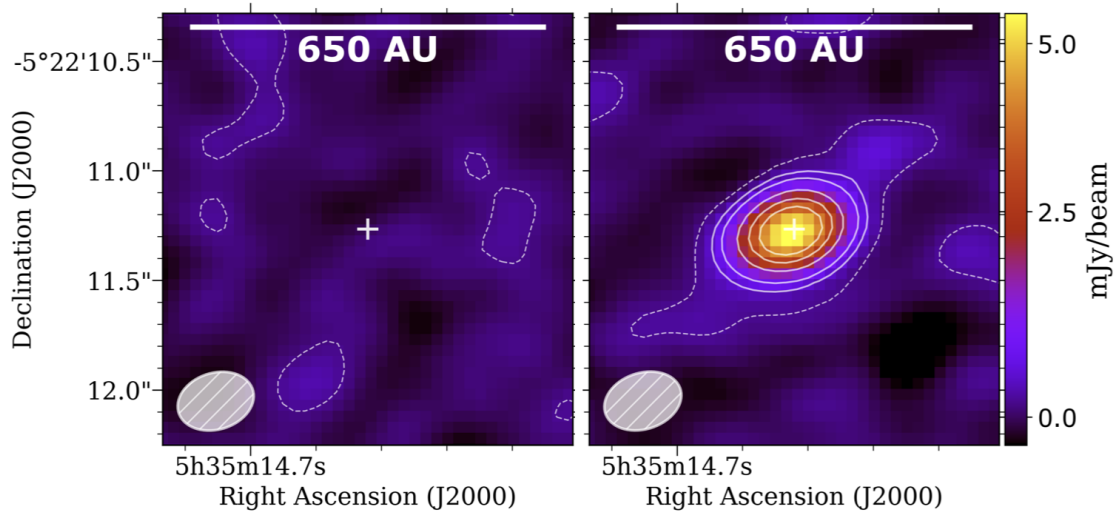
FIGURE 3.6: Continuum maps of the 8-s time resolution images at the position of the flaring source ORBS. The left-hand panel shows a time frame just prior to its first detection at 05:26 UTC (third upper limit after 5:25 UTC in Figure 3.5), and the right-hand panel shows the maximum peak at 05:32:43 UTC. Contour levels are 1σ, 3σ, 5σs, 10σ, 15σ, and 20σ rms levels. The plus symbol indicates the position of the peak from the right panel.

the peak of the flare found here. Remarkably, the peak flux reported in Friedel and Widicus Weaver (2011) comprises several hours of integration between different tracks during 2010, which implies a prolonged bright peak emission (or persisting flares) during those observations. For this flux measurement they used the CARMA A-configuration which resulted in a synthesized beam size of 0.4×0.35 arcsec^2 similar to the typical beam size in our observations. However while we did not resolve ORBS they report it as marginally resolved with a deconvolved source size of 0.4×0.29 arcsec^2.

Source ORBS provides a remarkable example of how radio emission (and X-ray emission as well) during flare events in protostars and YSOs can be significantly more luminous than that of main sequence stellar flares. We can compare the millimeter ORBS flare to the flares of Proxima Cen at 1.3 mm also observed with ALMA (MacGregor et al., 2018, 2021). These were remarkable short-duration ≤ 1 min flares of orders of magnitudes change in peak flux density, representing an analogous flare to those studied here but from a more evolved source (M dwarf with spectral type M5.5V). While the bright Proxima Cen flares peaked at around ~ 100 mJy (the two observed flare peaks in 2017 and 2019), these peaks would have not been detected in our ALMA observations of the ONC, and at ~ 400 pc these peaks would be roughly equivalent to a ~ 1 μJy (with a central frequency at 1.3 mm). On the contrary, the ORBS millimeter flare of ~ 5.5 mJy beam^{-1} would be as

bright as $\sim$500 Jy beam^{-1} at the distance of Proxima Cen (1.3 pc). This translates into absolute radio luminosities of $\sim 2 \times 10^{14}$ and $\sim 1 \times 10^{18}$ ergs s^{-1} Hz^{-1} for Proxima Cen and ORBS flares, respectively. These differences highlight the importance of a continued systematic search for such events in YSOs to better constrain the nature of the radio emission during flares this way provide a significant sample for modelling studies such as those of T-Tauri magnetospheres to model both radio and X-ray emission during flares (Waterfall et al., 2019). Additionally, this finding is also providing a caveat for the study of disk masses, where a case such as ORBS with an averaged peak flux density in the concatenated data completely dominated by a flare would lead to a completely incorrect disk mass estimate. For instance, the ORBS flare would translate into significant change in dust mass since the latter is proportional to the measured flux, $M_{dust} \propto S_\nu$, assuming a fixed dust temperature in disks (see equation 1 in Eisner et al. 2018), and therefore the variability factor of this flare would also mean an order of magnitude difference in the estimated dust mass.

3.4.2.2 Variability factor distribution in Orion-KL

As previously seen, already between the individual 1-h epochs alone we find variability occurring at all the analysed timescales, and even stronger events are accessible at shorter timescales. The resulting VF distributions from the LCs at 1-h and 20-min time resolution are shown in Figure 3.7 in the top and bottom panels, respectively, as a function of the averaged peak flux density from the concatenated data. While there is a spread VF distribution at the two different time resolutions, the distribution from the LCs at shorter timescales reveals significantly greater variability levels of up to a factor of VF$\sim$ 20. This widespread variability occurs at all range of timescales (see insets in Figure 3.7) with the strongest flare displayed by source 74 (ORBS) arising in less than an hour (bottom panel in Figure 3.7). The other two sources with VF$\sim$10 (from the LCs at 20-min time resolution) show such variability on longer timescales of hours to days where a more prolonged flaring state may last longer than the observations (as seen in Figure 3.8).

These differences in the VF distribution when determining variability at different time resolutions are testimony to the interplay between the characteristic timescales of the variability in the sample and the averaged time intervals used to investigate this.
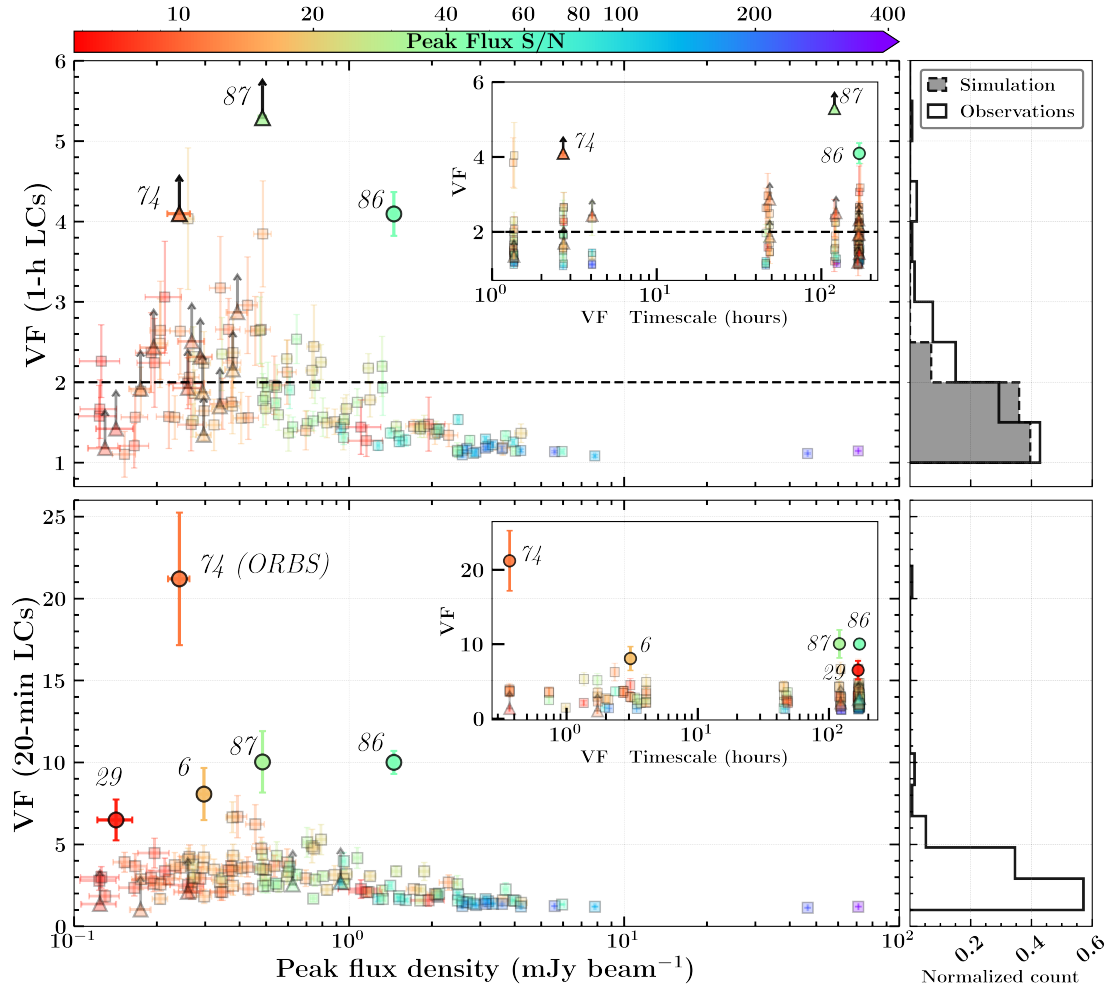
FIGURE 3.7: VF distribution at 1-h (top) and 20-min (bottom) time resolution for the full sample as a function of peak flux density from the concatenated data with 1σ error bars in both axis and color-coded by signal-to-noise ratio of the peak from the concatenated data. Lower limits are indicated by triangles and black arrows. The horizontal dashed line in the top panel indicates the systematic variability cut-off at VF = 2 described in Section 3.3. Sources with VF above this cut-off within 3σ uncertainty and also above the noise distribution shape (see text) are highlighted otherwise are shown with small square symbols and higher transparency levels. The full distribution histograms for both observations and simulations (described in section 3.3) are shown on the right. The insets indicate the VF as a function of timescale for such variability level (time interval between the maximum and minimum in the LCs).

For instance, a short-lived flare would be more evident if imaged or analyzed at a time resolution comparable or shorter than the duration of the event but then its signal would be progressively diluted within the average as longer time intervals are used to determine its brightness. We can see, for example, how short-lived substructures are seen in the LC of source 86 at higher time resolution (red area in the right-hand panel in Figure 3.8) where the lower time resolution LC in the left-hand panel does not show clear evidence of the peak in sub-epoch 7 neither of the sudden increase in sub-epoch 12. A more obvious example was discussed for the ORBS and seen in Figures 3.3 and 3.5 with LCs at different time resolutions showing the strong flare whose true maximum peak flux density significantly increases when measured at the shortest time resolutions and its detection in the concatenated data is only due to its strong short-lived flare.

Given the definition of the VF that is describing relative variability, greater variability levels are displayed predominantly towards lower averaged peak flux densities as seen in Figure 3.7. Sources with averaged peak flux density above ~ 2.0 mJy beam^{-1} are essentially constant and are most likely dominated by dust millimeter emission. Source BN, for example, is a well known thermal centimeter radio source (Forbrich et al., 2008, 2016) and it is thus expected to show no signs of variability on short timescales. This is the brightest millimeter source in our sample (source 25 in Table 3.2) with an averaged peak flux density of 70.991 ± 0.183 mJy beam^{-1} and shows indeed no millimeter variability with VF$\sim$1.1 and VF$\sim$1.2 from the 1-h and 20-min LCs, below our cut-off for potential systematic effects. While 98 per cent of the sources in our catalogue have averaged peak flux density <8 mJy beam^{-1} the only other source with considerably bright peak flux density is the well known Source I (source 61 in our catalogue) which together with source BN are the most massive objects in the Kleinmann–Low (KL) nebula in Orion within a range of $\sim 8-15$ $M_{\odot}$ (Ginsburg et al., 2018; Bally et al., 2020; Wright et al., 2022). Here we report an averaged peak flux density of 46.475 ± 0.190 mJy beam^{-1} for Source I and it is also amongst the most constant sources with VF$\sim$1.1 in both 1-h and 20-min time resolutions LCs.

If we only consider the VF$=2$ threshold discussed in section 3.3, then out of the 133 LCs at 1-h time resolution only $\sim$6 per cent of the sources have VF values above our systematic limit of VF$>$2 within 3σ uncertainty, including those with only upper limits available. As seen in the histograms on the top right-hand panel in Figure 3.7, most of the sources show VF values below the defined cutoff at 1-h time resolution. The

overall VF from the simulations is also shown in grey-filled histogram as reference. On the other hand, at 20-min time resolution, about $\sim$20 per cent of the sample, present VF levels above this defined threshold within 3σ uncertainty, including those with only upper limits available.

Furthermore, the VF distribution shape at the two different time resolution shown in Figure 3.7 also seems to display a systematic effect where a large dispersion is still seen above VF$=2$ and is described by a noise distribution that increases towards lower peak flux densities and peaks at around $S_\nu \sim 0.3-0.4$ mJy beam^{-1} reaching VF$\sim 3-4$ at 1-h time resolution and VF$\sim 5-7$ at 20-min time resolution. This noise distribution shape then decreases towards the faintest sources likely due to a selection bias where the faintest sources were mostly selected by visual inspection of the concatenated image and are located on regions less affected by background noise and therefore these are less likely to display large flux variations caused by noise. This distribution shape is indicated with transparent symbols in Figure 3.7). This effect is thus driven by the VF definition with a larger impact on small flux fluctuations in faint sources with larger uncertainties compared to small flux fluctuations in brighter sources with lower uncertainties (VF$=S_{v,max}/S_{v,min}$ in the source's LC at a given time resolution). However, in our search for relative variability, the main goal is to look for the strongest possible variability in the sample that is well above the relative ALMA flux calibration accuracy (see for example Francis et al. 2020 and references therein). We thus follow the same approach as for the VF$=2$ threshold discussed in section 3.3, where sources below this level, or dispersion envelope in this context, can still be variable but they will be within the noise in the distribution. We thus focus on the largest possible variability in the sample above any systematic effect. With these constraints there are still a few sources clearly above any systematic effect: sources 74 (ORBS), 86, and 87. These three sources are above these effects at both time resolutions and these are discussed individually in the following section, while source ORBS was already discussed in section 3.4.2.1. A few more sources are above these thresholds at 20-min time resolution (e.g., sources 6 and 29, indicated in Figure 3.7) however we will restrict our discussion to those already mentioned that are above these thresholds at both time resolutions.

An additional note associated with the sample of disks that have been characterized at radio wavelengths with 3-mm flux measurements available in Otter et al. (2021), we can compare their flux measurements for those within the HPBW primary beam (47
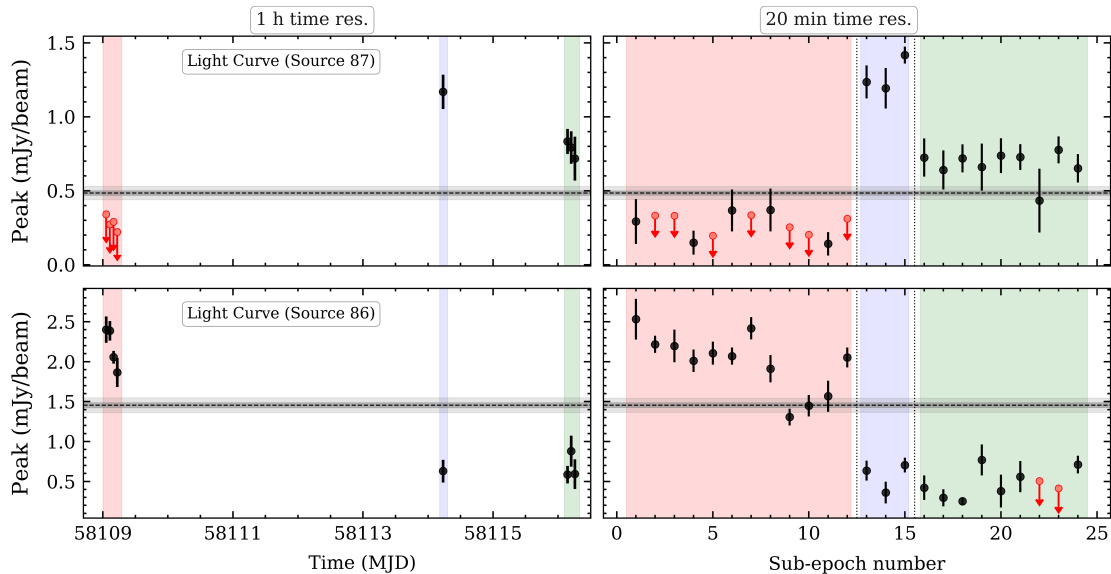
FIGURE 3.8: Radio LCs of the variable sources 86 and 87 at 1-h (left) and 20-min (right) time resolutions. Symbols and colors follows same notation as in Figure 3.3.

sources). 57 per cent of them have flux measurements compatible within 3σ uncertainty, and 19 per cent (9 sources) are not just incompatible within 3σ uncertainty but also show at least 50 per cent difference in flux density where the largest difference is shown by source 86 by a factor of $\sim$3.6 brighter in our observations (using the flux measurement from the concatenated data). This source is among the most variable ones in our sample, and is discussed in the following section together with source 87.

3.4.2.3 Additional highly variable sources

Here we will briefly comment on two additional sources showing the highest variability in the sample after the strong flare earlier discussed. These are the sources 86 and 87 whose largest variability occur on the longer timescales of days with changes in peak flux density by an order of magnitude or greater.

Source 86: With a VF $= 4.1 \pm 0.3$ within 7 days (170.2 h) from its 1-h time resolution LC shown in the bottom left-hand panel in Figure 3.8, this source shows a decreasing brightness in the first hours of observation (first 4 epochs, red are in Figure 3.8) with a maximum peak flux density of 2.401 ± 0.055 mJy beam^{-1} in epoch 1 and a minimum in epoch 6 (first measurement within green area) at 0.586 ± 0.037 mJy beam^{-1}. Interestingly, at shorter timescales, its 20-min time resolution LC illustrates the interplay between the averaged interval and the characteristic timescale of the corresponding variability,

where an evident substructure begins to be temporally resolved revealing three successive peaks at 2.531 ± 0.085, 2.418 ± 0.047, and 2.052 ± 0.042 mJy beam^{-1}, respectively, with the second and third peak rising after 2.1 and 2.7 h from the preceding peak where the maximum change in peak flux density for that interval (red area) occurs between the first and ninth measurement with a VF$\sim$1.9$\pm$0.1.

This source shows an order of magnitude change in peak flux density (VF$\sim$10.0$\pm$0.7) on longer timescales of 7.1 days (171 h) with a maximum at the beginning of the observations (sub-epoch 1) and a minimum within epoch 6 (sub-epoch 18, green band in Figure 3.8). From sub-epoch 13 onward the LC fluctuates around 0.463 mJy beam^{-1} with a standard deviation of 0.166 mJy beam^{-1}. Similarly, this source was also detected at 3 mm continuum observations from September 2017 (Otter et al., 2021; Ginsburg et al., 2018) with a reported flux density of 0.409 ± 0.004 mJy from aperture photometry (see Table 5 in Otter et al. 2021, source 37), which in line with our measurements from sub-epoch 13 onward, may represent a quiescent state of source 86, with the caveat that even such "quiescent state" may still be dominated by flares. An example of this can be illustrated by the seemingly "quiescent state" of source 87 in its 20-min resolution LC starting from sub-epoch 16 onward (top right-hand panel in Figure 3.8, green area) where its peak flux density displays a "quiescent" constant level (except for sub-epoch 22) yet brighter than the first twelve sub-epochs (red area) which are otherwise upper limits mostly.

Source 86 was reviously reported at cm-wavelengths as GMR D in Garay et al. 1987, and more recently in Forbrich et al. 2016, and Vargas-González et al. 2021 with no significant variability (sources [FRM2016] 211 and [VFD2021] 186, respectively). It was reported as a nonthermal radio source in Forbrich et al. 2021 where its VLBA unusual proper motion suggests these are detections of different components among the observations (Dzib et al., 2021) and in such a case source 86 would actually be a close binary system. It also has an X-ray counterpart (COUP 662) with a hydrogen column density $\log(N_H) = 23.22\pm0.03$ leading to a high visual extinction $A_V \sim 80$ mag (using the conversion $N_H/A_V = 2\times10^{21}$ cm^{-2} from Vuong et al. 2003), which supports the fact that neither optical nor IR counterparts have been reported for this source.

Source 87: This source shows the largest variability in the sample at 1 h time resolution with a VF$\sim$5.3 on a timescale of 5 days (120.2 h) and it is indeed just a lower

limit variability since its true radio luminosity remained below detectable levels during the first four epochs where the minimum is reported (as three times the rms noise; top left panel in Figure 3.8). The local rms noise at the minimum (epoch 4) is 0.074 mJy beam^{-1}. The averaged peak flux density of source 87 over the 8 epochs is 0.484$\pm$0.015 mJy beam^{-1}, but peaks at 1.169$\pm$0.039 mJy beam^{-1} in epoch 5 (blue band in Figure 3.8), almost 2.5 times brighter than the averaged peak flux density. If we then look into the 20-min time resolution LC, its peak within epoch 5 increases to 1.417$\pm$0.019 mJy beam^{-1} leading to a variability of an order of magnitude (VF$=10.0\pm1.9$) in 5 days.

This source has been previously detected at cm-wavelengths in Forbrich et al. (2016) and Vargas-González et al. (2021) (source [FRM2016] 212 and [VFD2021] 187, respectively). Source [VFD2021] 187 shows a decrease in peak flux density by a factor of $\sim$ 3 in nearly 2 h as measured from its 5-min time resolution LC of the central pointing presented in Vargas-González et al. 2021. It has an X-ray counterpart in the COUP survey (COUP 670) with a reported spectral type between K4-M0 and a visual extinction $A_V \sim 2.31$ (based on optical and infrared properties from Hillenbrand 1997; Luhman et al. 2000; Lucas et al. 2001) and a near-IR counterpart in the VISION survey (VISION 05351492-0522392; Meingast et al. 2016). Also reported as a nonthermal radio source at cm-wavelengths with the VLBA, where it was only detected in one out of four observed epochs with a 35.1σ significance level (Dzib et al., 2021; Forbrich et al., 2021) pointing out to its extreme variability in the cm-range. Further evidence of its millimeter variability can be inferred from similar ALMA 3mm observations conducted three months prior to our observations where no peak above a 5σ detection threshold is found on images with reported rms noise levels between $0.04-1.0$ mJy beam^{-1} (Otter et al., 2021). According to its IR counterpart in Muench et al. 2002 (source 568, with an angular separation of $\sim$0.14 arsec), Otter et al. 2021 determined a 3mm upper limit a this position of 0.027 mJy (three times the local rms noise).

3.5 Summary and Conclusions

We present ALMA 3mm continuum observations towards the Orion BN/KL region at sub-arcsecond resolution and report the first systematic search for mm-wavelengths flares in YSOs on timescales from minutes to days.

We detect 133 sources within a area of $\sim 1.6 \times 1.6$ arcsec^2 ($\sim 0.2 \times 0.2$ pc^2) and have studied their LCs at different time resolutions. Within this sample, we report the discovery of a strong flare from a known YSOs previously reported as a radio flaring source detected at cm-wavelengths and referred to as ORBS where it showed an order of magnitude change in peak flux density in just a few hours (Forbrich et al., 2008). In our ALMA observations it was only detected in one of the 8 epoch (individual epochs of 1 h each). This single detection and only at this time resolution corresponds to a change in peak flux density by a factor of at least >4 in less than three hours. Further analysis of this flare at high-time resolution of 8-s cadence allowed us to constrain the development of this strong event that had a duration of ~ 10 min with more than an order of magnitude change in peak flux density in ~ 4 min. At this high-time resolution we are also able to resolve a lightcurve substructure at the peak of the event where a double peak is seen at ~ 4.9 and ~ 5.8 mJy beam^{-1} separated by 3 min. This strong millimeter flare from a known YSO is a remarkable evidence of how radio time domain analysis of such dataset is providing us with a new perspective on high-energy irradiation of YSO vicinities, its impact on protoplanetary disks and ultimately on planet formation.

Radio variability analysis for a dataset of this kind towards a complex region such as the ONC necessarily requires time-slicing imaging for flux measurements at different time resolutions. This method entails some uncertainties for lower levels of variability where systematic effects are expected mostly due to the impact that a dynamic shape and size of the synthesized beam throughout the observations has on flux measurements of both resolved sources and/or unresolved sources in a complex region with a variable background. Using simulated observations, we conclude that these systematic effects could produce artificial variability of up to a factor of VF~ 2.

Finally, this study is providing a first look at the capabilities that ALMA offers to the field of radio time-domain studies at high-time resolution in the millimeter range, which also has an impact on the interpretation of averaged millimeter fluxes, such as in the study of disk masses for individual YSOs, particularly since we have demonstrated that strong mm-flares occurs although these seems to be rare events. Additionally, our findings provide strong evidence of the value of both continued radio monitoring of YSOs and the development of even more efficient methods for the analysis of variability in such radio datasets of complex regions at high-time resolution which undoubtedly provides

a unique window to the study of high-energy processes at the earliest phases of stellar evolution.

CHAPTER *4*

Time series analysis of nonthermal YSO emission with the VLBA

4.1 Introduction

As discussed in the previous Chapters on the study of radio variability in low-mass YSOs, these very young systems already show evidence of high-energy processes at such early stages of their evolution (e.g., strong flares at X-ray and radio wavelengths Feigelson and Montmerle 1999). The observed X-ray emission of young stars is associated with thermal emission from hot plasma in coronal type activity, while at radio wavelengths it is associated with thermal free–free emission from ionized material as well as non-thermal (gyro-)synchrotron emission from magnetospheric activity (Dulk, 1985; Güdel, 2002). This latter allows us to trace the high-energy processes in YSOs since it is interpreted to arise from the electron population gyrating along magnetic field lines in protostellar coronae and the innermost regions of circumstellar disks. The higher energy (MeV) electron population will result in synchrotron radiation observable at millimeter wavelengths while mildly relativistic electrons will derive in gyrosynchrotron radiation observed at centimeter wavelengths (Güdel, 2002; White et al., 2011).

Throughout this thesis I have presented a study of radio emission from YSOs in the search for rapid variability at cm- and mm-wavelengths as it represent a very useful approach to disentangle thermal from nonthermal emission with particular interest in the search for nonthermal emission as a tracer of high-energy processes in young stars. In contrast, other tools such as the use of spectral index and polarization have shown to be

a difficult tracer to rely on since these require high S/N ratios to be measured considering that these are a fraction of the total flux that is used to measure variability that in turn it also requires high S/N. An alternative and very useful criterion to distinguish nonthermal radio emission from YSOs is the use of brightness temperature[1] (T_b) whose maximum possible values for thermal free-free emission for frequencies $\nu \gtrsim 1$ GHz are $\leq 10^5$ K (Condon, 1992; Condon and Ransom, 2016) while for nonthermal radio emission this can reach several million kelvins. The observed radio continuum emission from a source can be expressed in terms of its equivalent brightness temperature following the Rayleigh-Jeans approximation in the low-frequency limit ($h\nu \ll kT$). Starting with the brightness defined as:

$$I_\nu = \frac{2\nu^2 k_B T_b}{c^2} \tag{4.1}$$

where k_B, c, ν, and T_b are the Boltzmann constant, speed of light, frequency and the corresponding brightness temperature, respectively. The brightness I_ν can be expresses in terms of the measured flux density S_ν over the beam solid angle Ω as $I_\nu = S_\nu/\Omega$, in turn, the beam solid angle for a Gaussian beam of half-power beam width θ_{HPBW} is $\Omega = \pi \theta_{HPBW}^2/[4\ln(2)]$. Thus, we can use a single factor for all the constant terms and convert into units of mJy, arcseconds, and GHz such that T_b can be expressed as (Condon and Ransom, 2016):

$$T_b = 1.22 \times 10^3 \left(\frac{S_\nu}{\text{mJy}}\right) \left(\frac{\theta_{HPBW}}{\text{arcsec}}\right)^{-2} \left(\frac{\nu}{\text{GHz}}\right)^{-2} \tag{4.2}$$

Therefore, resolution and frequency become relevant parameters for targeted T_b observations. In this context, the Very Long Baseline Interferometry (VLBI) provides baselines of thousands of kilometers achieving high-angular resolution, typically with milliarcsecond beam widths (see Section 1.6.3). For instance, Very Long Baseline Array (VLBA) observation with its longest baseline of $\sim$8600 km at a central frequency of 6 GHz can achieve a resolution of ~ 1 mas, and if we take into account equation 4.2, thus a faint detection of $S_{6GHz} = 0.5$ mJy would have $T_b \approx 10^7$ K, which for unresolved sources this would then represent just a lower limit. This is a key aspect in the context

---

[1]Brightness temperature correspond to the temperature that a blackbody would need such that it can emit the same flux density as the observed source at a given frequency.

of nonthermal radio emission from the coronae of low-mass YSOs[2] which, in addition to its corresponding high-brightness temperature, only extends to sizes of at most a few stellar radii ($< 10^{-2}$ AU for low-mass pre-main sequence stars, e.g., Phillips and Lestrade 1988; Güdel 2002; Massi et al. 2008). Therefore, altogether, the combination of high T_b and compact nature of this emission makes VLBI observations the perfect tool to study compact nonthermal radio emission from low-mass YSOs with its exceptional milliarcsecond high angular resolution and its sensitivity to high-brightness temperatures ideal to filter out thermal emission.

At the same time, the virtue of the VLBI extreme high resolution brings a limitation, a very small field of view. The very long baselines of VLBI observations can derive in fields of view a few orders of magnitude smaller than the primary beam area, and can be just a few arcseconds wide for observations at GHz frequencies due to the effects of time and bandwidth averaging at areas away from the phase center (Bridle and Schwab, 1999). For a VLBA observation at a central frequency of 7.196 GHz, maximum baseline of 8600 km, and typical integration time of 2 s (correlator dump intervals), the useful (undistorted) field of view is around 4.5 arcsec in diameter (Wrobel 1995; see also "Field of View limitations" overview by Bob Campbell[3]). This limitation has been overcome as a result of the multi-phase center technique provided by the Distributed FX (DiFX) software correlator (Deller et al., 2007, 2011) that allows many phase centers (hundreds) in one correlator pass[4] by shifting the phase center of the correlation towards a given position (*uv* shifts) and thus giving access to small fields of view but anywhere in the primary beam area (e.g., Middelberg et al. 2011).

Additionally, VLBA observations can provide polarization information by recording orthogonal polarizations, both left-hand and right-hand circular polarization (LCP and RCP, respectively) whose four possible correlations (RR, LL, RL, LR) can be associated by Fourier transform relations to the Stokes parameters I, Q, U, and V (Cotton, 1993; Roberts et al., 1994). Stokes I represent the total intensity, Stokes Q and U the linear polarized signal, and Stokes V the circular polarized signal. Polarization emission is an

---

[2]There is also evidence of nonthermal radio knots around YSOs tracing strong shocks of their jets against dense material in their surroundings, but these are found far from the central protostar at distances of several thousand AU (Anglada et al., 2018).

[3]http://old.evlbi.org/user_guide/limit.html

[4]The previous VLBA correlator was hardware based and limited to a few number of correlations per observation. This was upgraded to a software-based correlator that significantly increased the number of possible correlations per observation.

important diagnostic of the emission mechanisms in play and an approach to constrain magnetic fields.

In order to selectively study the nonthermal population in the ONC, Forbrich et al. (2021) made use of the NRAO VLBA to observe at 7.196 GHz all the compact radio sources previously identified in the deep VLA observations at similar frequencies (4−8 GHz; Forbrich et al. 2016) plus an additional target from Dzib et al. (2017). About 22% of the sources (123 out of 557) were identified as nonthermal VLBA detections and these do not show a strong correlation with the expected nonthermal population based on in-band spectral indices and extreme variability found in the VLA sample (Forbrich et al., 2017) reinforcing the relevance of VLBA for unbiased nonthermal compact emission surveys. These findings, however, do not rule out the potential nonthermal nature of VLA sources that were not detected in the VLBA observations, since nonthermal radio emission has proved to be highly variable and may well be only intermittently detected during several VLBA epochs, if not just once during a more active state.

In this work we further explore these VLBA observations by presenting a YSO nonthermal radio variability analysis at a wide range of timescales based on the multiepoch observations that span 3 yr and demonstrate the extraordinary advantages that the extreme resolution provided by VLBA observations have over other radio datasets for time series analysis involving crowded regions with complex extended emission. This work is the third of a series of publications and is preceded by a first paper (Paper I, Forbrich et al. 2021) focused on the detection and catalogue definition of the nonthermal population in the ONC within the deep VLA sample of 556 sources (Forbrich et al., 2016) an the additional radio source from Dzib et al. (2017), and a second paper (Paper II, Dzib et al. 2021) focused on the astrometric and proper motions analysis of sources detected in more than one VLBA epoch. The structure of this work is as follows: In section 4.2 we describe the observations and the nominal catalogue, we then present in section 4.3 our preliminary results of the variability between different epochs followed by a description of the methodology used to generate lightcurves at high-time resolution directly from the visibilities for both Stokes I and Stokes V. In section 4.3.4 we compare our method against that based on time-sliced imaging photometry and finally the summary and conclusions are presented in section 4.4.

TABLE 4.1: VLBA observation logs.

Epoch	Project ID	Obs. Date/Time (UT)	Synthesized beam (mas^2 ; °)	Number of Antennas used[a]
(1)	(2)	(3)	(4)	(5)
1	BF117	2015−Oct−26/06:25−14:23	4.7 × 1.6 ; +22.1	8
2	BF123A	2017−Oct−26/06:23−14:21	4.4 × 1.3 ; −17.3	7
3	BF123B	2017−Oct−27/06:19−14:17	4.1 × 1.4 ; −17.8	7
4	BF123C	2018−Oct−26/06:24−14:22	2.8 × 1.2 ; −2.1	10

[Note] Epochs 2, 3, and 4 belong to project BF123 observed in three different segments denoted by A, B, and C in column (2).
[a] More antennas were operational in epochs 2 and 3 but some were flagged during processing (see Forbrich et al. 2021).

4.2   Observations and catalogue description

Four VLBA observations towards the ONC were carried out between 2015 and 2018 using the C-band at a central frequency of 7.196 GHz and an aggregate bandwidth of 256 MHz using dual polarization and a total data rate of 2 Gbps. These observations followed the same pointing position used for the deep VLA observations (Forbrich et al., 2016) centered at $(\alpha, \delta)_{J2000} = (5^h35^m14\overset{s}{.}479, -5°22^m30\overset{s}{.}57)$. The total time on-source per epoch was about 4.7 h interrupted every 2 min to spend 40 s on the phase calibrator (J0541-0541). The observations were obtained on the same day of each year except epoch 3 which was obtained one day after epoch 2 in order to assess variability on a day-timescale. The main information of these observations are shown in Table 4.1. The longest baselines were only available in epoch 4 providing the smallest synthesized beam while for the rest of the observations these resulted more elongated (but still two orders of magnitude smaller than that of the VLA observations) due to either one or two antennas not operational or/and additional antennas flagged during processing (see columns 4 and 5 in Table 4.1). Even for the most affected observations (fewer antennas, thus larger synthesized beams), a faint peak emission of ~ 0.5 mJy beam^{-1} would still have a corresponding $T_b > 10^6$ K (see equation 4.2).

The correlation of all the 557 sources (556 from Forbrich et al. 2016[5] and the additional radio source from Dzib et al. 2017 and associated with the X-ray source COUP 672) was made using the DiFX software correlator (described in Section 4.1). Additional details are described in full in Paper I together with the data reduction which

---

[5]The 556 sources from Forbrich et al. 2016 are identified as [FRM2016] followed by the catalogue number in their paper.

was performed following standard procedures using the NRAO Astronomical Image Processing System (AIPS[6]; Greisen 2003).

The source detection criterion for the nominal catalogue was defined as having at least one detection above a 6.5σ threshold among the 4 epochs. This cutoff was defined in order to reduce the probabilities of false positives due to the presence of noise peaks at the position of a VLA source (see section 3.1 in Paper I). The criterion for a detection in at least one epoch is due to the fact that most of the sources were only detected in one out of the four epochs, pointing to the expected variability from nonthermal YSO emission.

Another important note is the two orders of magnitude superior resolution provided by VLBA over VLA observations, which can result in resolving multiple components for a single VLA source within AU-scales. This is highlighted in the astrometric analysis presented in Paper II and indicated in Table 2 of that work. The authors looked for detections within the imaged fields between ∼40 and ∼400 AU (0.1 and 1 arcsec, respectively) at a resolution of $1-2$ AU (~ 5 mas), at the distance of the ONC. Even at this resolution the radio emission from stellar coronae is expected to be unresolved (Phillips and Lestrade, 1988; Andre et al., 1991), including larger emitting regions, for example those associated to interacting coronae (Massi et al., 2008) or colliding magnetospheres in binary systems (Salter et al., 2010), are also expected to be unresolved.

The nominal catalogue thus consists of 123 detected sources (see Table 2 in Paper I) whose spatial distribution is shown in Figure 4.1 with a few of them apparently corresponding to different components of a single VLA source. Multiple systems are associated to sources [FRM2016] 2, [FRM2016] 177, and [FRM2016] 414 and are indicated with cyan circles in Figure 4.1. Even those not evidently detected as multiple systems could potentially correspond to the detection of a single component of a multiple system. There are few additional sources reported as potential members of a multiple system due to either a large separation from their nominal VLA position (e.g., source [FRM2016] 300) or an unusually large proper motion (e.g., source [FRM2016] 198) as described in Paper II.

In the following sections we will present preliminary results on, first, the inter-epoch variability with a focus on the epochs observed on two consecutive days describing a few

---

[6]http://www.aips.nrao.edu/
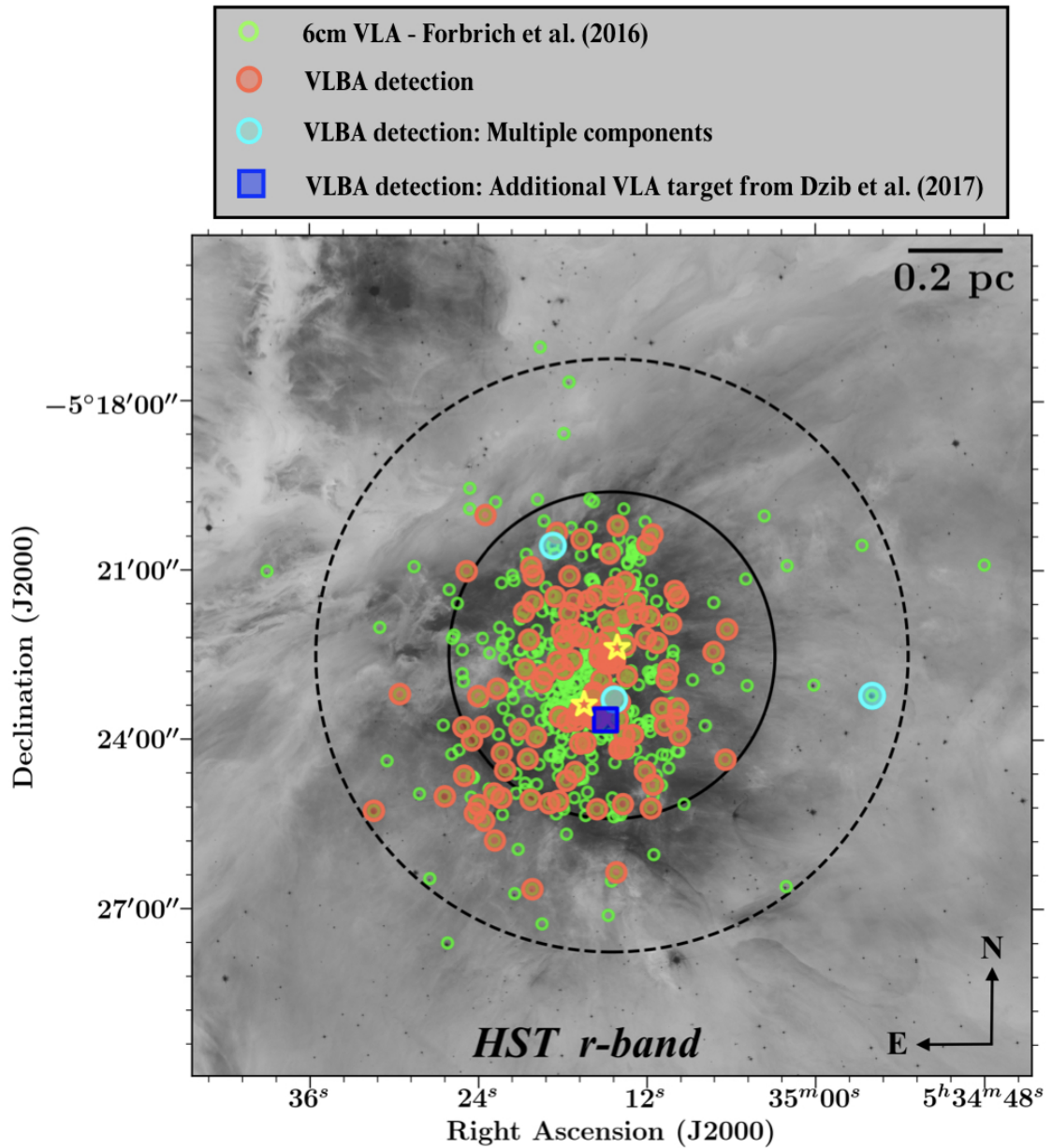
FIGURE 4.1: Source distribution of VLBA and VLA sources. Symbols indicate the VLBA detections (red circles) and the VLA sample (green circles). The cyan circles indicate multiple VLBA destections for a single VLA source. Blue square symbol indicates the position of the additional VLA source reported in Dzib et al. (2017). The yellow star symbols indicate the position of θ^1 Ori C (lower-left) and BN source (upper-right) for reference. The black dashed and continuous circular areas represent the primary beam of the VLA observations at the low- and high-frequency ends of the bandwidth (Forbrich et al., 2016). The background image is a HST *r*-band image (ACS/WFC) of the Orion Nebula (Credit: NASA, ESA, M. Robberto, and the Hubble Space Telescope Orion Treasury Project Team).

examples within the sample. Second, we introduce the method used to obtain high-time resolution lightcurves directly from the visibilities demonstrating first results on a few sources, and third, a brief discussion is presented on the comparison between the method used here to obtain the high-time resolution lightcurves against the time-sliced imaging method.

4.3   Results

4.3.1   Inter-epoch variability: Epochs on two consecutive days

The source detection process from the multiepoch observations described in Paper I already revealed the variable nature of the observed emission with most of the sources been detected with a 6.5σ cutoff (catalogue detection threshold, see Section 4.2) in only one out of the four epochs. In fact, within the observations obtained on two consecutive days (epochs 2 and 3, see Table 4.1) there are sources detected on only one day. In this section we will focus on those sources with evidence of variability within the observations carried out in 2017 on two consecutive days (epochs 2 and 3). This experiment is particularly interesting for the search of rapid nonthermal variability. In order to include additional detections at lower S/N cutoffs we also consider those with S/N>6.0 reported in Paper II that take into account sources whose positions are coincident with the ones reported in the nominal catalogue of Paper I and are clearly detected (S/N>6.5) in at least two out of the four observed epochs. For the measurements that follows, we will use images from each concatenated epoch with sizes of 2048 pixels per side and a pixel scale of 0.05 mas.

With the above consideration, a total of 66 sources were detected in either of the two consecutive days in 2017, including the two components found for source [FRM2016] 414, each of them only detected once and on different days[7]. The component detected on the first day, [FRM2016] 414-1, shows a decrease in peak flux density by at least a factor of ~ 2 within one day (using 3σ local rms upper limit in epoch 3, and thus, a lower limit for this variability), on the other hand, the second component [FRM2016] 414-2 detected in epoch 3 (following this designation from Paper II just from the temporal order they

---

[7]The two components of [FRM2016] 414 were again detected in epoch 4 and one of these was also detected in epoch 1 (see Table 2 in Paper II).

were detected), shows an increase in peak flux density by at least a factor of ~ 3 within one day. This source(s), which is a single VLA source, was also reported as an extremely variable source (an order of magnitude change in peak flux density in about 23 h) in Forbrich et al. (2017) from the variability analysis of the deep VLA observations where 13 sources were reported as extremely variable VLA sources.

Of the 66 sources discussed above, only 12 were detected on both consecutive days. More interestingly, five sources with high S/N (> 10) were detected only once, these are sources [FRM2016] 22, 326, 435, 547, and 557. None of these were reported as extremely variable VLA sources in Forbrich et al. (2017). Source [FRM2016] 22, for example, is only detected on the second of the consecutive days (epoch 3) with a peak flux density of 0.36 ± 0.02 mJy beam^{-1}. Comparing this against its upper limit in epoch 2, this results in an increase in peak flux density by a factor of 5.1 ± 0.3 on timescales ≤ 1 day. Similarly, for sources [FRM2016] 326, 435, 547, and 557, their 1-day lower limit variability are by factors of 3.4, 4.4, 2.7, and 7.5, respectively.

This experiment thus show strong evidence of significant variability on short timescales of one day with lower limits for changes in peak flux density as large as by a factor of 7.5. Moreover, a large fraction ($\sim82\%$) of the sources detected in this experiment did so on only one day. These findings are consistent with the expected variable nature of the YSO nonthermal radio emission and provide just a first look at the variability even before exploring the data at high-time resolution. At the same time, these results emphasize the fact that continuous monitoring is needed to reveal the wide nonthermal population in the targeted sample due to its intrinsic variability where a non-detection is evidently likely to be detected at a different time. In the following section, we will discuss the inter-epoch variability across all four epochs.

4.3.2   Inter-epoch variability: Across all 4 epochs

Our discussion on rapid variability within a day-timescale presented in the previous section clearly illustrates the potential impact on the overall detection rate of sources across epochs. Indeed, as demonstrated in Paper I, only a small fraction of the sources were detected in all four epochs. If we exclude from the nominal catalogue of 123 sources presented in Paper I those sources detected on the combined two epochs from 2017 (epochs 2 and 3), a total of 111 sources are then detected in at least one of the four

epochs. Of these, 78% were detected in only one out of the 4 epochs, 10% were detected in two epochs, 2% were detected in three epochs and 10% were detected in all four epochs. In the following, we will discuss on those cases with detections in all four epochs.

Among the sources detected in all four epochs there are sources known to be part of binary systems (e.g., [FRM2016] 254 and 378) or are thought to belong to multiple systems due to their proper motion results ([FRM2016] 66 and 211) reported in Paper II. Source [FRM2016] 254 is known to belong to the stellar system θ^1 Ori A (Petr-Gotzens and Massi, 2008), however its VLBA detections seems to belong to the same component in all four epochs, and it shows significant variability between epochs particularly epochs 1 and 4 against epochs 2 and 3, displaying flux density 2 to 4 times brighter in the former two cases. This source is also one of the extremely variable VLA sources (Forbrich et al., 2017). The example sources described in this section and its variability are summarized in Table 4.2.

Among the 13 extremely variable VLA sources reported in Forbrich et al. (2017), 7 are VLBA detections ([FRM2016] 53, 98, 189, 254, 319, 515 and the already mentioned source [FRM2016] 414). The most variable source in the VLA deep catalogue is [FRM2016] 515, and it was detected in a single VLBA epoch (epoch 4). The minimum upper limit (3σ local rms) for soure [FRM2016] 515 is found in epoch 3, resulting in a change in flux density by a factor of at least $\sim$2. Another extremely variable VLA source is [FRM2016] 319, detected in all four VLBA epochs. In the VLBA observations, its largest change in flux density is by a factor of $\sim$2.8 between epoch 1 and 4, where its highest S/N detection occurs in epoch 1 with a peak flux density of 0.37$\pm$0.05 mJy beam^{-1}. Its variability between the two consecutive days is by a factor of $\sim$1.9.

Additional examples of sources that are potentially part of multiple systems, according to their proper motions, are sources [FRM2016] 66 and 211 with an inter-epoch variability by a factor of $\sim$2 within a day and a year, respectively. On the other hand, source [FRM2016] 184 (associated to radio source GMR H reported in Garay et al. 1987) also presents unusual proper motions but it is not yet clear if this is due to orbital motions or other reasons, and further analysis is required. In Paper II they found that different positions of source [FRM2016] 184 do not follow a linear motions, with only epoch 2 and 3 (consecutive days) showing consistent positions. The inter-epoch variability for this source shows a maximum change in peak flux density by a factor of $\sim$4.8 between epochs

4 and 1. It has maximum peak of 0.92±0.02 mJy beam^{-1} in epoch 4 and a minimum of 0.19±0.03 mJy beam^{-1} in epoch 1. Its variability between the two consecutive days is by a factor of ∼1.7.

The main results from this preliminary look at inter-epoch variability are, first, the notable evidence of variability in the sample with just comparing the individual epochs. Most of the sources are detected in a single epoch and even in the observations carried out on two consecutive days there is clear signs of variability with examples of bright sources only detected on one of the two days (with a detection threshold of S/N=6.0). Second, an important consideration that should be taken into account when comparing multiepoch flux measurements in similar VLBA observations is that multiple systems can be found even at the very small scales studied here. Different components have been detected towards a single VLA source and only one at a time has been detected in these observations (a single detection in every epoch). The imaged data for the individual epochs allows to constrain the position of the detected peak, and also allows to study proper motions (if the source is detected in more than one epoch) as a useful approach to find potential multiple systems in the sample, which has been also reported in Paper II, providing relevant constraints for our study of inter-epoch variability in distinguishing peaks from different components even at these very small scales.

The overall inter-epoch variability in the sample of sources explored here shows that every source is variable by at least a factor of two on any inter-epoch timescale between one day and 3 years. The maximum change in flux density found on timescales of one day in this sample of sources is by a factor of >7.5 (source [FRM2016] 557) and this corresponds to a lower limit variability, followed by source [FRM2016] 22 with variability by a factor of 5.1±0.3 and source [FRM2016] 435 by a factor of 4.4, also a lower limit variability. The remaining seven sources whose one-day variability was estimated show changes by factors between 2 and 3.4, most of these corresponding to lower limits (due to the non-detection in the other corresponding day). On longer timescales, sources [FRM2016] 184 and 254 show the largest variability by factors of 5 and 4, respectively, within one year. The remaining sources with detections on different years show variability between 2 and 3 on timescales of one to three years. We have not yet explored the inter-epoch variability for the full sample (we have examined 17 sources), but there is virtually no constant source between epochs in the sample explored so far. Within the studied sample there is significant variability with large lower limits. These where found from 1-day time

TABLE 4.2: VLBA inter-epoch notes.

[FRM2016][a]	VF	Timescale for VF	Comments
(1)	(2)	(3)	(4)
22	5.1±0.3	1 day	
184	4.8	3 yr	Unusual proper motion
184	5	1 yr	Unusual proper motion
254	4	1 yr	Binary system (θ^1 Ori A)
319	2.8	3 yr	Detected in all 4 epochs
435	>4.4	1 day	
515	>2	1 yr	Extremely variable VLA source (Forbrich et al., 2017)
557	>7.5	1 day	
66			Multiple system
211			Multiple system
254			Extremely variable VLA source (Forbrich et al., 2017)
378			Binary system

[a] Source identification from Forbrich et al. 2016.
VF: Variability Factor (change in peak flux density).
VF values with no uncertainty correspond to estimated values obtained from the peak pixel of the image at the position of the source in question.

resolution, and therefore, as seen in the preceding studies towards the same observed sample (Forbrich et al., 2016) or observed field (Chapter 2) at similar frequencies, sources that show evidence of variability at an arbitrary (short)timescale, may reveal stronger event at even shorter timescales (hours or few minutes time resolution), and therefore some of the sources reported in this preliminary study may reveal extreme variability at higher time resolution. Those extreme variable sources reported in Forbrich et al. (2017) at similar frequencies using the VLA do not show such variability in our VLBA observations, and those with large upper limits variability in our VLBA observations do not exhibited high-levels of variability in these VLA observations. While it was expected to find variability in this sample of nonthermal sources, the next step is to constraint the rate of inter-epoch variability and the level of this variability for all the 123 sources in the catalogue.

In the following section we will describe the method used to study variability at different time resolutions down to seconds by obtaining flux measurements directly from the visibility data and thus significantly improving the lightcurve generation compared to that of time-sliced imaging for isolated and unresolved point-like sources.

4.3.3   High time-resolution Light curves from the visibilities: Stokes I and V

The multiepoch observations alone have shown the highly variable nature of the emission in this VLBA sample, notably evident from the observations carried out on subsequent days. In the following, we will focus on the use of the Direct Fourier Transform (DFT) of the visibilities as a useful method to study high-time resolution variability with special attention to the exceptional capabilities offered by these VLBA observations that allow us to efficiently produce radio lightcurves in all Stokes parameters for all the sources at any time resolution.

In order to study the flux density time evolution for any source directly from the visibilities we made use of the AIPS program DFTPL (Direct Fourier Transform Plots). The DFTPL[8] method allows us to compute the DFT of the visibilities as a function of time for a specific position in right ascension and declination. DFTPL has the flexibility to define the time interval required and which Stokes parameter to extract. By using this method we are assuming that all the emission in the field comes from the source of interest. DFTPL can be applied on this dataset given the extraordinary high-angular resolution provided by VLBA that on top of allowing to filter out any thermal emission it is also able to produce individual visibility data for very small spatial scales where it is unlikely to find any emission other than from the source in question. Here, we will demonstrate that with the DFTPL applied in our VLBA dataset we can efficiently generate lightcurves at any time resolution down to seconds.

We have already discussed in Section 4.1 the benefits of the VLBA high-angular resolution, proffering the optimal scenario to assume that all the emission in the field is due to the source itself making possible to directly extract flux measurements from the visibilities without dealing with time-expensive imaging procedures and subsequent photometry, as it was necessary for our VLA and ALMA data sets presented in Chapters 2 and 3 where the required conditions conditions are not achieved. In those datasets (VLA and ALMA observations of the ONC), large fields are observed with resolution about ∼0.3 arcsec equivalent to ∼120 AU at the distance of the ONC, where both thermal and nonthermal emission are in play on top of the ubiquitous complex emission in the region. These conditions, as mentioned above, necessarily requires imaging the dataset

---

[8]http://www.aips.nrao.edu/cgi-bin/ZXHLP2.PL?DFTPL
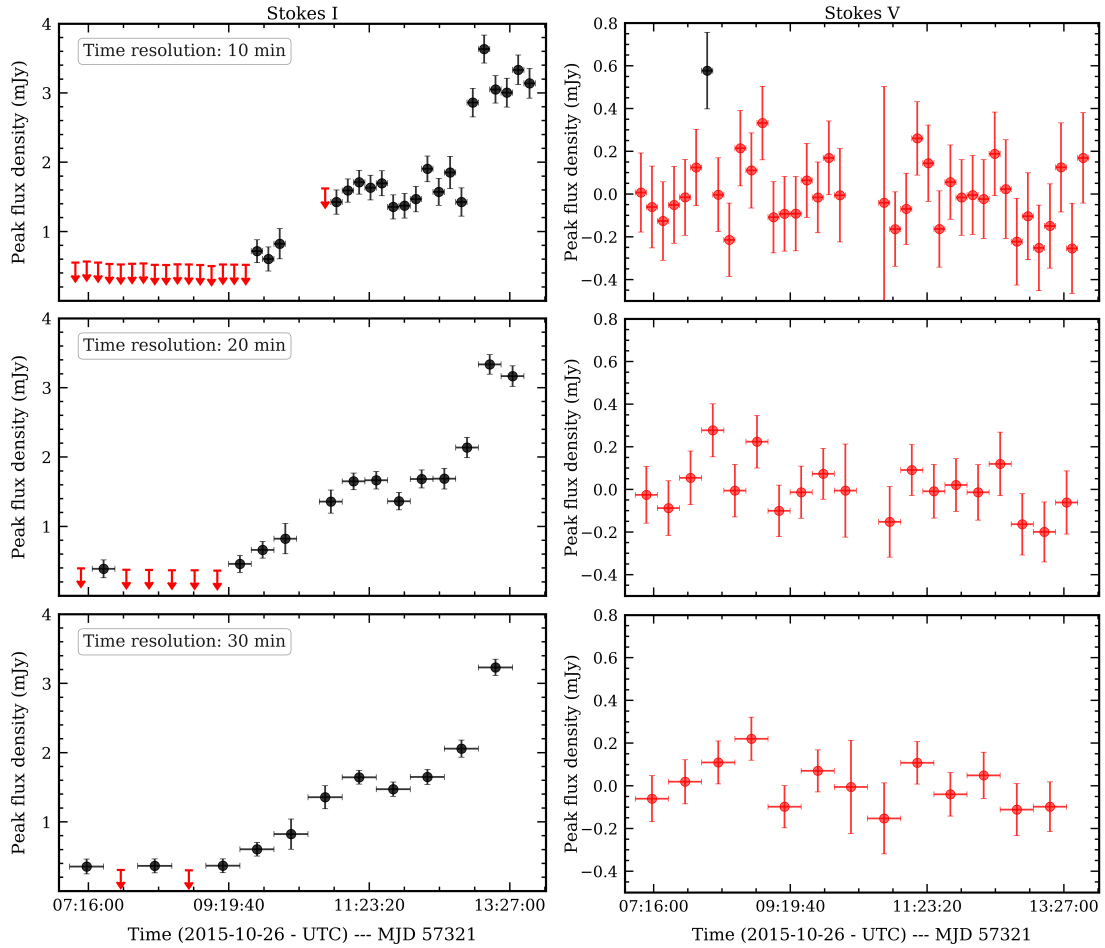
FIGURE 4.2: VLBA radio lighcurves for Stokes I (left) and Stokes V (right) for the same source [FRM2016] 93 obtained with DFTPL at three different time resolutions of 10, 20, and 30 minutes bins. Only detections with S/N≥ 3 are indicated in black symbols, otherwise these are indicated in red for Stokes V, and 3σ rms noise upper limits also indicated in red for Stokes I.

to carefully apply photometry on selected point-like sources (see Section 3.3 in Chapter 3 for a brief description of the difficulties of time-sliced imaging variability analysis of complex regions).

For this experiment, we have selected a couple of sources as examples. These sources were selected after a preliminary analysis of several lightcurves using DFTPL, we then looked for sources that show evidence of variability, but that are not associated to sources in binary or multiple systems and that are bright enough to be detected at short integration times. Figure 4.2 shows the VLBA lightcurves for a single source generated with DFTPL in AIPS for three different time resolution and for both Stokes I and V, although, overall we do not find significant polarization and only upper limits can be provided.

The lightcurves shown in Figure 4.2 correspond to the source [FRM2016] 93, only detected in epoch 1 (see Table 4.1) with a rising flux density. It has an X-ray counterpart in the COUP survey (COUP 504, Getman et al. 2005a) and has been classified as a Class II YSO (Prisinzano et al., 2008). The resulting variability at the different time resolutions slightly changes since both minimum and maximum in the lightcurves change. The variability at 30-min time resolution (bottom panel in Figure 4.2) results in a maximum change in peak flux density by a factor of 11.0 ± 4.0 in 4.5 h. At 20-min time resolution the resulting variability is by a factor of 9.2 ± 3.1 in 4.0 h, and finally, the variability at 10-min time resolution results in a change in peak flux density by a factor of 7.2 ± 2.4 in 4.0 h.

The highest time resolution lightcurve (upper panel in Figure 4.2) shows the brightest peak flux density of 3.6 ± 0.2 mJy beam^{-1} at around 13:04 UTC, compared to the maximum in the other two time resolution lightcurves (3.3 ± 0.1 mJy beam^{-1} and 3.2 ± 0.1 mJy beam^{-1}, at 20- and 30-min time resolution, respectively). Despite that, it shows the lowest variability, although the three variability measurements are compatible within 1σ uncertainty. This is due to the increased rms noise level at shorter integration times (higher time resolution) and the fact that the minimum in the three lightcurves corresponds to upper limits that defined by these rms noise levels. Furthermore, the lightcurves at higher time resolutions can resolve smaller rapid variations that are hidden in the averaged flux at lower time resolutions, for example, the maximum peak around 13:04 UTC at 10-min time resolution seems to be an independent event on top of the increasing flux density and it is not evident in the 30-min time resolution lightcurve where all that time interval is basically a single averaged measurement.

Stokes I lightcurves show highly significant measurements even at the highest time resolution including brief flare-like features with S/N$\sim$20, contrary to Stokes V measurements that all have S/N$<$3 (most of them have S/N$<$1 at any time resolution) except sub-epoch 7 with S/N$\sim$3, and thus the resulting polarization fraction uncertainties are $\geq$90% if we used these S/N$<$1 measurements. Instead, if we consider upper limits Stokes V (3 rms levels), the resulting polarization upper limits are 100% for the first half of the observations and decrease down to 10% to 20% at 30-min and 10-min time resolution, respectively, towards the peak in Stokes I lightcurves around 13:27 UTC. Therefore, no conclusive constraints in polarization can be provided for this source.

Similarly, the 10-min time resolution lightcurves were generated for source [FRM2016] 130 for all the observed epochs in Stokes I and Stokes V as shown in Figure 4.3. This source also has an X-ray counterpart (COUP 554), it has been classified as a YSO with a disk in Megeath et al. (2012) and as a Class I YSO in Großschedl et al. (2019). In this example, there are two main important results, first, the evidence of inter-epoch variability with a clearly increasing flux density across epochs. In the concatenated data of epoch 1, this source shows a S/N∼ 6.7 and then it reaches a S/N∼ 144.7 in the concatenated data of epoch 4. At 10-min time resolution, this source is not detected in epoch 1, and only upper limits are shown in its lightcurve (upper left panel in Figure 4.3), while in epoch 4 it reaches a S/N∼50 in a single measurement at 10-min time resolution. The examples described here are summarized in Table 4.2.

The second relevant result is the evidence of variability on short timescales, more evident in epochs 3 and 4. Starting from the brightest epoch, in epoch 4 the largest change in peak flux density is by a factor of 2.2±0.1 on a timescale of 5.2 h between its maximum of 8.77±0.17 mJy beam^{-1} and minimum of 3.97±0.18 mJy beam^{-1}. In epoch 3, it shows a variability by a factor of 3.0±0.7 in 5 h, and its variability epoch 2, where the minimum peak flux density is an upper limit of 0.55±0.18 mJy beam^{-1} around 11:10 UTC, it shows a lower limit variability by a factor of 2.5±0.9 on a timescale of 1.7 h against the maximum of 1.36±0.22 mJy beam^{-1} at 12:50 UTC. On the other hand, the Stokes V lightcurves shown in the bottom row in Figure 4.3, similar as in the examples shown for source [FRM2016] 93 above, do not exhibit any significant detection and every measurement shows S/N≤ 2 due to the large uncertainties and therefore only upper limits can be provided. This result in polarization upper limits that are particularly high for epochs 1 (100% at all sub-epochs with 50% uncertainty) and epoch 2 (between 40% and 100% with typical uncertainties between 30% and 50%) due to low S/N in both Stokes I and V. In epoch 3, polarization upper limits range between 18% and 70% with typical uncertainties between 10% and 30%. For epoch 4, 7% and 15% with typical uncertainties between 3% and 5%. Therefore, epochs with faint detections do not really provide useful polarization information, but for the brightest epoch (epoch 4) we can report upper limit polarization of ∼20% but no further constraints can be made.

VLBA observations are thus providing exceptional capabilities for variability studies in YSOs allowing us to efficiently produce lightcurves at any time resolution directly from the visibilities using the DFTPL task in AIPS. The use of this method, however,

assumes that all the emission in the field comes from an unresolved and isolated point source. If these conditions are satisfied, then there would be no need to re-image the data several times at different time resolutions to generate lightcurves, instead this imaging process would be a key complementary method to investigate potential sources with interesting properties of true variability or otherwise to identify potential exemptions to the above assumptions, such as the multiple system scenario. Once these are identified, we can thus easily take advantage of the DFTPL method to explore the highest possible time resolution (down to seconds) and study large samples of sources with easy access to all Stokes parameters (when available from the observations). With the DFTPL method we will be thus able to eventually produce the largest sample of VLBA lightcurves of YSOs, at high-time resolution down to seconds for nonthermal radio emission for both Stokes I and V.
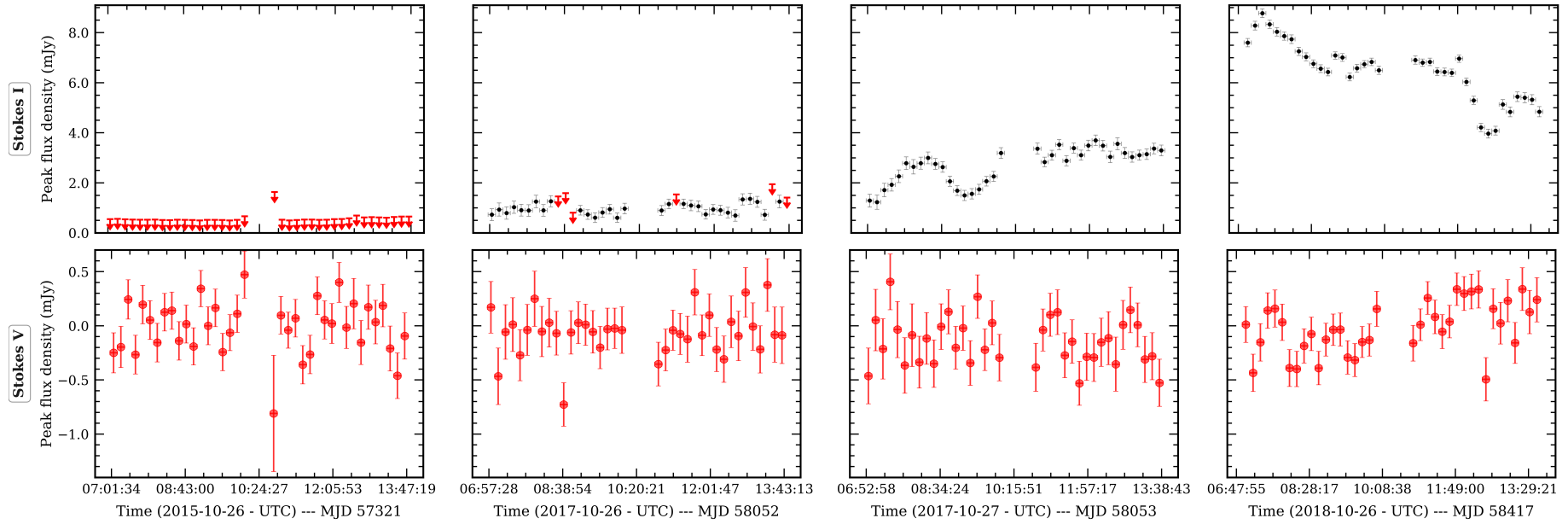
FIGURE 4.3: VLBA radio lighcurves at 10-min time resolution for Stokes I (top row) and Stokes V (bottom row) for the source [FRM2016] 130 obtained with DFTPL for the four observed epochs. Only detections with S/N≥ 3 are indicated in black symbols, otherwise these are indicated in red for Stokes V, and 3σ rms noise upper limits also indicated in red for Stokes I. Both Stokes I and Stokes V lightcurves share the vertical axis scale.

4.3.4 Comparative analysis: DFTPL on visibility data against time-sliced imaging photometry

The use of DFTPL in our VLBA dataset provides a significantly more efficient method to obtain YSO lightcurves compared to that of time-sliced imaging, as long the source in question is unresolved and isolated. Time-sliced imaging is the best approach for variability assessment in datasets such as VLA and ALMA observations towards the ONC presented in Chapters 2 and 3. As noted in the previous section, in the VLBA dataset, the separate visibilities in the direction of each source essentially contain only the emission from the isolated and unresolved source, unlike the scenario for the VLA and ALMA datasets. A potential issue could break this assumption: if any of the observed sources belongs to a multiple system with separations within several AU and two or more of these close components are detected, then we can not assume that all the emission from the visivilities comes from a single source. However, the number of sources that belong to multiple systems in this VLBA sample (and also those that potentially belong to multiple systems) has been constrained in Paper II.

In this section, these two methods (DFTPL and time-sliced imaging) are briefly compared with examples based on the sources described above, [FRM2016] 93 and [FRM2016] 130. For this comparison, we will reproduce their Stokes I lightcurves at 1-h time resolution using the DFTPL task in AIPS and this will be compared against the lightcurves generated from time-sliced imaging with fluxes obtained with the IMFIT task in CASA and applied on the images generated with the IMAGR[9] task in AIPS.

The IMAGR task was applied on the individual visibility datasets of each source to generate Stokes I images at 1-h time resolution using natural weighting, a size of 2048 pixels per side with a pixel size of 0.5 mas and centered on the VLA position of the source (as reported in Forbrich et al. 2016). Since these observations towards the science field were carried out between $07:00-10:00$ (UTC) and $10:48-13:54$ (UTC), we have thus excluded that time interval of 48 minutes in between that does not contain data, resulting in six images of 1-h each, and these will be referred as to sub-epochs. The resulting synthesized beam sizes among the sub-epochs range between 5.5×2.9 mas down to 1.2×1.2 mas, equivalent to linear sizes of 2.2×1.2 AU and 0.5×0.5 AU, respectively (see Section 4.2 and Paper I for imaging details).

---

[9]http://www.aips.nrao.edu/cgi-bin/ZXHLP2.PL?IMAGR
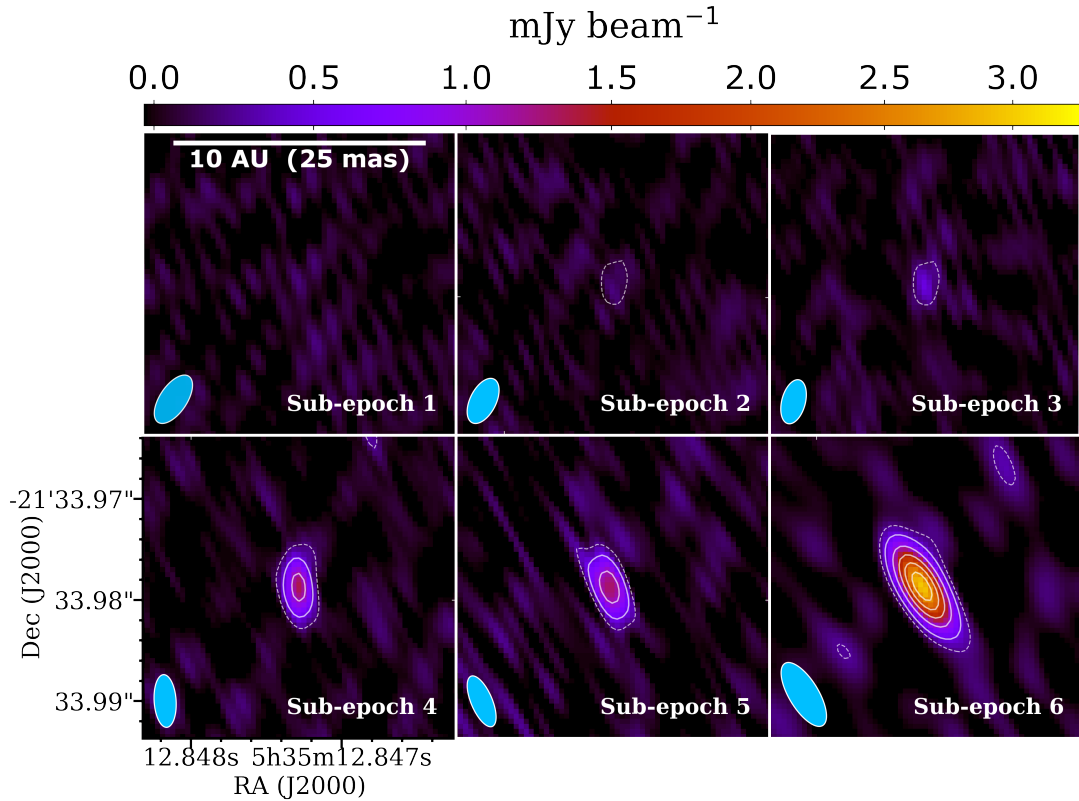
FIGURE 4.4: VLBA continuum maps from the 6 individual 1-h time resolution images generated with IMAGR at the position of the VLA source [FRM2016] 93. Contour levels indicate six levels between 0.48 and 2.89 mJy beam^{-1} spaced by factors of 2 in continuous lines while additionally indicating the 3σ rms levels of each image in dashed lines (see text).

The resulting continuum maps generated with IMAGR are shown in Figure 4.4 (for source [FRM2016] 93), with contour levels indicating six levels between 0.48 and 2.89 mJy beam^{-1} spaced by factors of 2 in continuous lines that correspond to values between 3σ rms levels and peak of the brghtest sub-epoch (sub-epoch 6, in this example) while additionally indicating the 3σ rms levels of each image in dashed lines for reference. The 48-min gap excluded from the imaging, and mentioned above, occurs between sub-epoch 3 and 4 in Figure 4.4. This gap was also considered when generating the lightcurves with the DFTPL task. For each image we employed a 2D-Gaussian fitting with IMFIT within a 200 pixels ($0.''1$) box centred at the peak position of the source. Here, the reference position of the source was obtained from the concatenated data of the observed epoch.

The DFTPL method was applied in the same way as described in section 4.3.3 to generate the lightcurves directly from the visibilities but now using a time interval for each datapoint of 3600 s (1-h time resolution) and for the same time ranges used for the
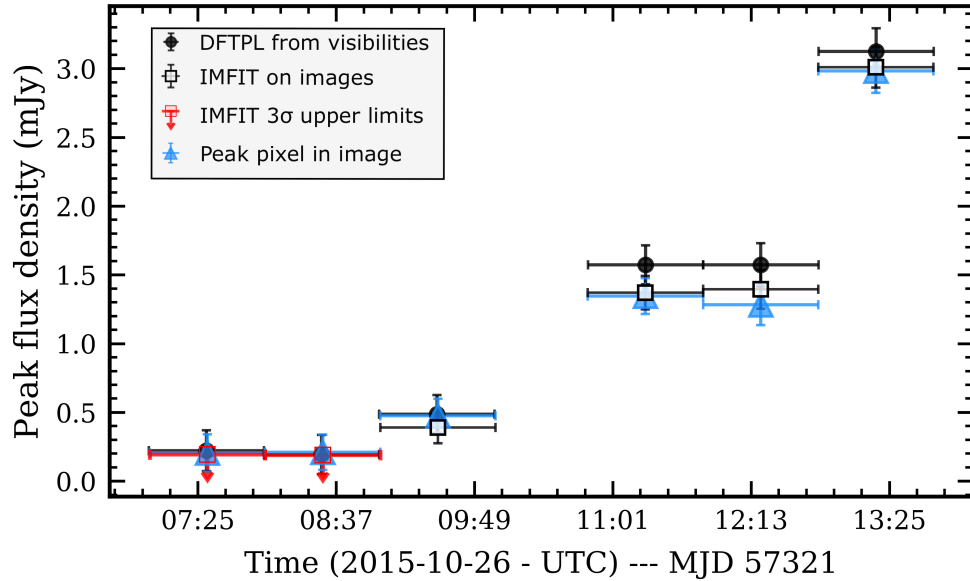
FIGURE 4.5: Radio lightcurves of source [FRM2016] 93 at 1-h time resolution obtained from two different methods: DFTPL from the visibilities (filled black circles) and IMFIT on time-sliced images (open squares). When no peak above S/N≥ 5 is found on the images, an upper limit indicating 3σ local rms level is shown. Time intervals of the measurements are indicated by the horizontal error bars. Vertical error bars represent 2σ uncertainties in peak flux density. The peak pixel value on the images around the position of the source is additionally indicated in the light-blue color lightcurve for comparison. Each datapoint in the lightcurves is refered as to "sub-epoch" in the text.

images shown in Figure 4.4 (first three datapoints from 2015-Oct-26/07:00−10:00 UTC and the remaining three datapoints from 2015-Oct-26/10:48−13:48 UTC). The resulting lightcurves obtained with both DFTPL and IMFIT for source [FRM2016] 93 are shown in Figure 4.5. Both methods agree with their lightcurves compatible at almost every measurement within 1σ uncertainty, except for sub-epochs 4 and 5 that are compatible within 2σ uncertainty, although these uncertainties are likely underestimated since the IMFIT method only includes the 2D-Gaussian fitting errors. The uncertainties reported by the DFTPL method are typically between 5% and 10% higher than the rms noise levels of the corresponding images. A more cautious treatment of the uncertainties would likely result in agreement within 1σ uncertainties at every measurement between these two lightcurves.

The two lightcurves shown in Figure 4.5 are also consistent with the continuum maps shown in Figure 4.4 with a clear increase in peak flux density during the observations. As an additional comparison and in order to confirm that the DFTPL and IMFIT measurements are consistent with the source peak on the images, the peak pixel value at the position of the source is also included in the lightcurve (light-blue triangles) which

is indeed compatible with both DFTPL and IMFIT measurements within 2σ. The uncertainties used for these peak pixel values correspond to the local rms levels in the images. Taking into account the IMFIT lightcurve as well as the continuum maps, there is no detection in either sub-epoch 1 or 2. The mean 3σ rms level between these two sub-epoch images is 0.19 mJy beam^{-1}. It is then detected in sub-epoch 3 with a peak flux density of 0.39±0.06 mJy beam^{-1} to finally reach a maximum peak in sub-epoch 6 at 3.00±0.07 mJy beam^{-1} (IMFIT measurements from the images). This rising IMFIT lightcurve leads to an increase in peak flux density by a factor of >15.8±0.4 in ~4.8 h, and since this source in not detected in the first sub-epochs, this is then a lower limit for this variability.

Similarly, the almost identical DFTPL lightcurve leads to a variability by a factor of 16.1±6.0 on the same timescale. One caveat here is that for the the first two sub-epochs we are taking into account the DFTPL measurements without a S/N threshold and thus the minimum (sub-epoch 2) has low S/N and this cause the variability to have larger uncertainty. In this case, the continuum maps in sub-epochs 1 and 2 shown in Figure 4.4 do not show evidence of a peak but DFTPL still reports the sum flux. These measurements are, however, compatible with the upper limits obtained with IMFIT. Moreover, the reported DFTPL flux for these first two sub-epochs have S/N<3 and thus below the detection threshold defined in Paper I. Therefore, employing the 3σ rms upper limit from DFTPL for the first two sub-epochs, the resulting variability is then also a lower limit with a change in peak flux density by a factor of at least 14.6±0.4 in ~4.8 h, and thus compatible with the variability obtained with IMFIT within 2σ uncertainty.

We have additionally compared DFTPL against IMFIT on source [FRM2016] 130 since it was detected in all four epochs, and thus it allows a comparison throughout all the different observations. However, we will compare these methods in epochs 2, 3, and 4, since the resulting images for epoch 1 (for this source) presents unrecognized imaging artifacts (emission patterns across the image) that will require further analysis to adequately discuss and correct.

In epoch 2, shown in Figures 4.6 (continuum maps) and 4.7 (lightcurves), the source [FRM2016] 130 was detected in every single 1-h sub-epoch using DFTPL with S/N>8.3 (black filled circles in Figure 4.7). However, the time-sliced method shows discrepancies in the resulting flux measurements (black open square symbols). These
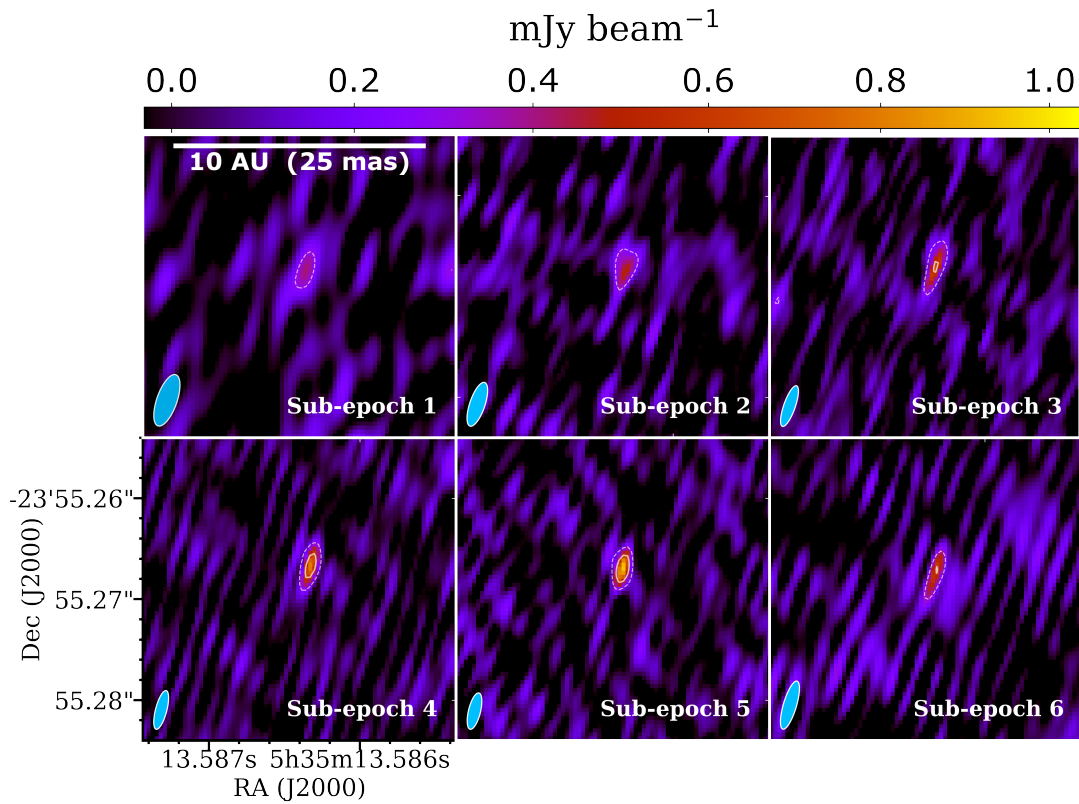
FIGURE 4.6: VLBA continuum maps of source [FRM2016] 130 for epoch 2 (Oct-26-2017). Frames and contours follow same notation described in Figure 4.4.
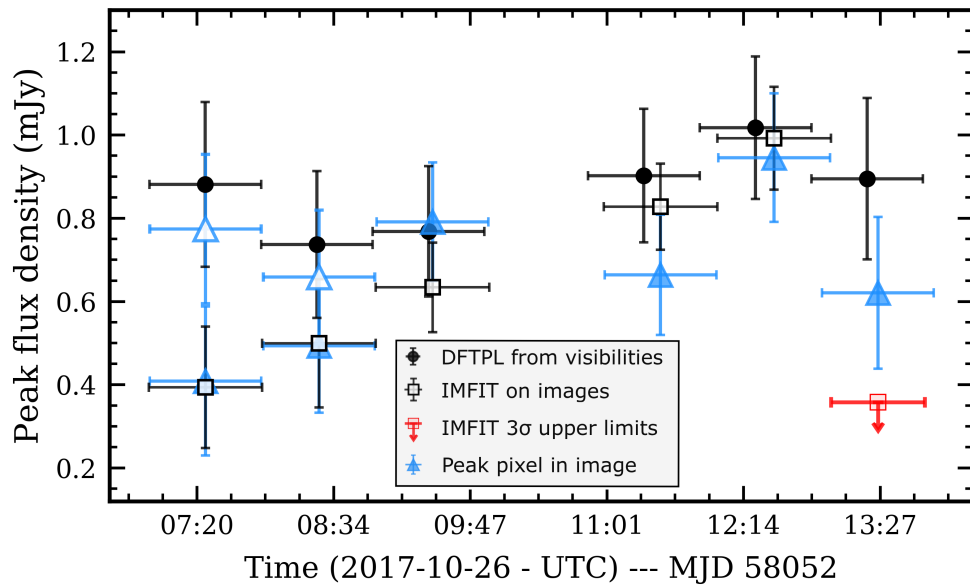
FIGURE 4.7: Radio lightcurves of source [FRM2016] 130 at 1-h time resolution from epoch 2 obtained with DFTPL and IMFIT. Symbols follow same notation of Figure 4.5. A second peak pixel value is included when a nearby source is found on the image (light-blue open triangles). A 3σ upper limit is shown in the last sub-epoch (13:27 UTC) since it was not possible to fit a Gaussian component despite of a peak with S/N$\sim$3 (see text).
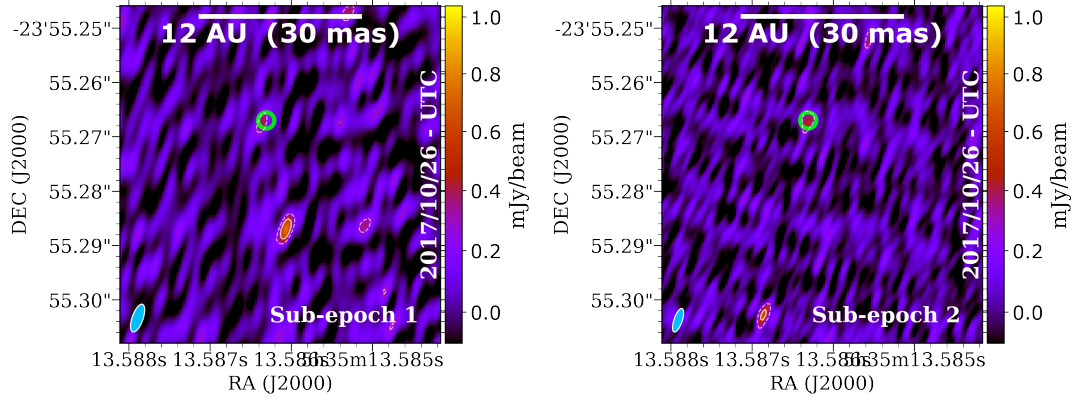
FIGURE 4.8: Continuum map around the position of source [FRM2016] 130 in epoch 2, sub-epoch 1 and 2 re-centred to show the peaks in each image. Green circle indicates the position of source [FRM2016] 130 as reported in Paper II for this epoch.

discrepancies occur in sub-epochs 1, 2, and 6, while for the remaining sub-epochs the flux measurements from the two methods are compatible within 1σ uncertainty. In sub-epochs 1 and 2, the discrepancies show the DFTPL measurements (i.e., the sum flux from the visibilities) brighter than the Gaussian fitting on the images (IMFIT), implying that there is more emission than just that of the central source in both sub-epochs. This is indeed demonstrated with the images shown in Figure 4.8, that corresponds to the two sub-epochs in discussion showing a larger field of view where a nearby peak emission is seen in both images, south-east and south-west of source [FRM2016] 130 in sub-epochs 1 and 2, respectively. In fact, the peak pixel values at the position of these two nearby peaks (shown in light-blue open triangles in Figure 4.7) are compatible with the DFTPL measurements within 1σ uncertainty, while the peak pixel value at the position of [FRM2016] 130 is, as expected, compatible with the peak obtained with IMFIT.

The discrepancy in sub-epoch 6 is due to the fact that the Gaussian fitting fails to extract the true peak value of the source and for that reason we reported a 3σ rms upper limit of 0.36 mJy beam^{-1}. While the IMFIT peak of S/N$\sim$3 is 0.33$\pm$0.11 mJy beam^{-1}, the pixel value at the peak is $\sim$0.62 mJy beam^{-1} (although this peak is still noticeable in the continuum map). Taking into account this peak pixel value in the image and considering the local rms level, this peak is compatible with the DFTPL flux measurement within 1σ uncertainty. Additionally, in this example, in the second half of the data (10:46 UTC onwards) the image time ranges do not exactly match the time ranges defined for DFTPL, and the last image has only $\sim$50 min integration time with the 10-min difference
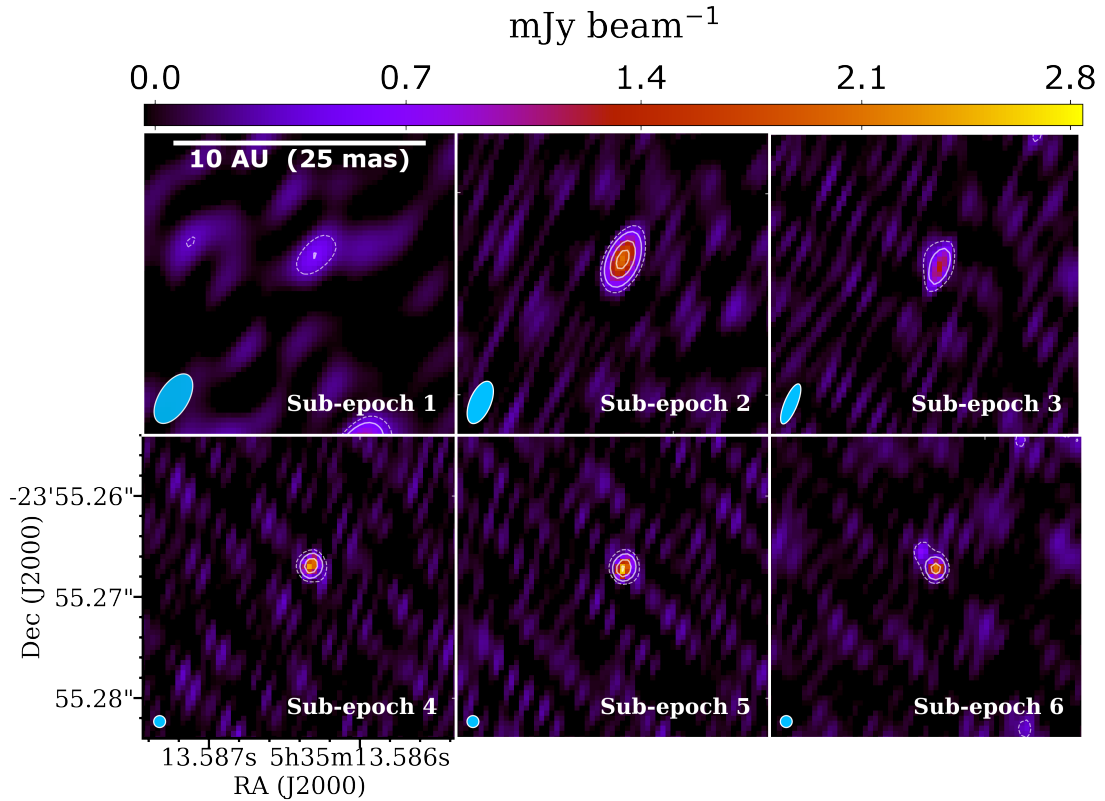
FIGURE 4.9: VLBA continuum maps of source [FRM2016] 130 for epoch 3 (Oct-27-2017). Frames and contours follow same notation described in Figure 4.4.

included in the previous image (image for sub-epoch 5).

The result for this comparison in epoch 3 (Oct-27-2017) shows a systematically brighter lightcurve otherwise showing the same development. DFTPL fluxes are almost systematically 1.3 times brighter than the IMFIT fluxes, except for sub-epoch 1, where nearby peak is found south-west from source [FRM2016] 130, similar as in sub-epoch 1 in epoch 2 (left panel in Figure 4.8). The systematically brighter DFTPL measurements may be due to the fact that this method measures all the emission in the field and thus this factor my represent the remaining emission, i.e., noise, antenna patterns, or the flux from the source itself that has been smeared out making the central peak systematically fainter when imaged and thus a re-examination of the imaging process could help to explain this issue or narrow this difference. The peak at a different position in sub-epoch 1 is shown in Figure 4.9. In the first sub-epoch of source [FRM2016] 130 in epoch 3, there is no peak at the nominal position of this source (as reported in Paper II), although a very faint peak-like emission is barely seen but no bright enough to fit a Gaussian at its position, thus an upper limit (3σ rms) is reported in the corresponding lightcurve shown in Figure 4.10. However, the nearby peak detected 19 mas in south-west direction
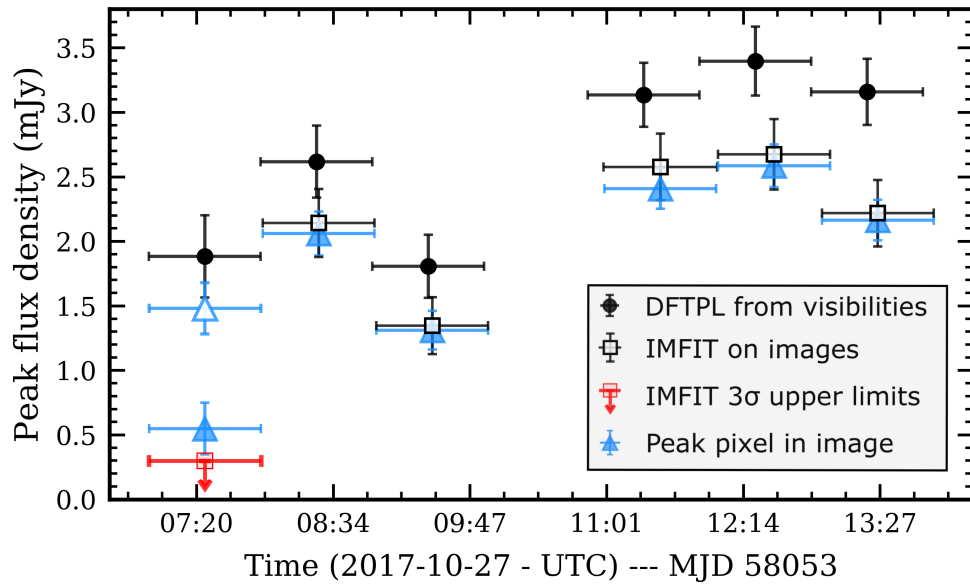
FIGURE 4.10: Radio lightcurves of source [FRM2016] 130 at 1-h time resolution from epoch 3 obtained with DFTPL and IMFIT. Symbols follow same notation of Figure 4.5. A second peak pixel value is included when a nearby source is found on the image (light-blue open triangles).
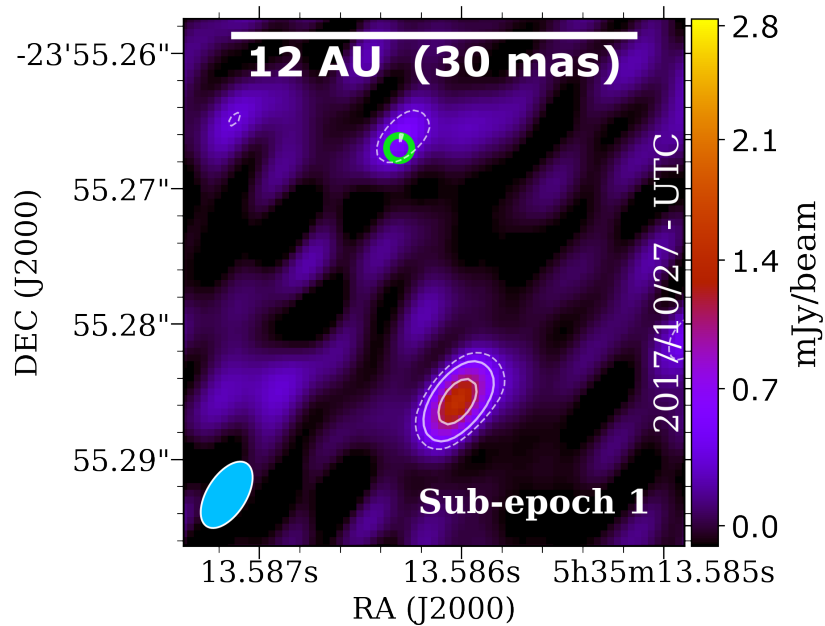
FIGURE 4.11: Continuum map around the position of source [FRM2016] 130 in epoch 3, sub-epoch 1 re-centred to show the intriguing nearby south-west peak. Green circle indicates the position of source [FRM2016] 130 as reported in Paper II for this epoch.
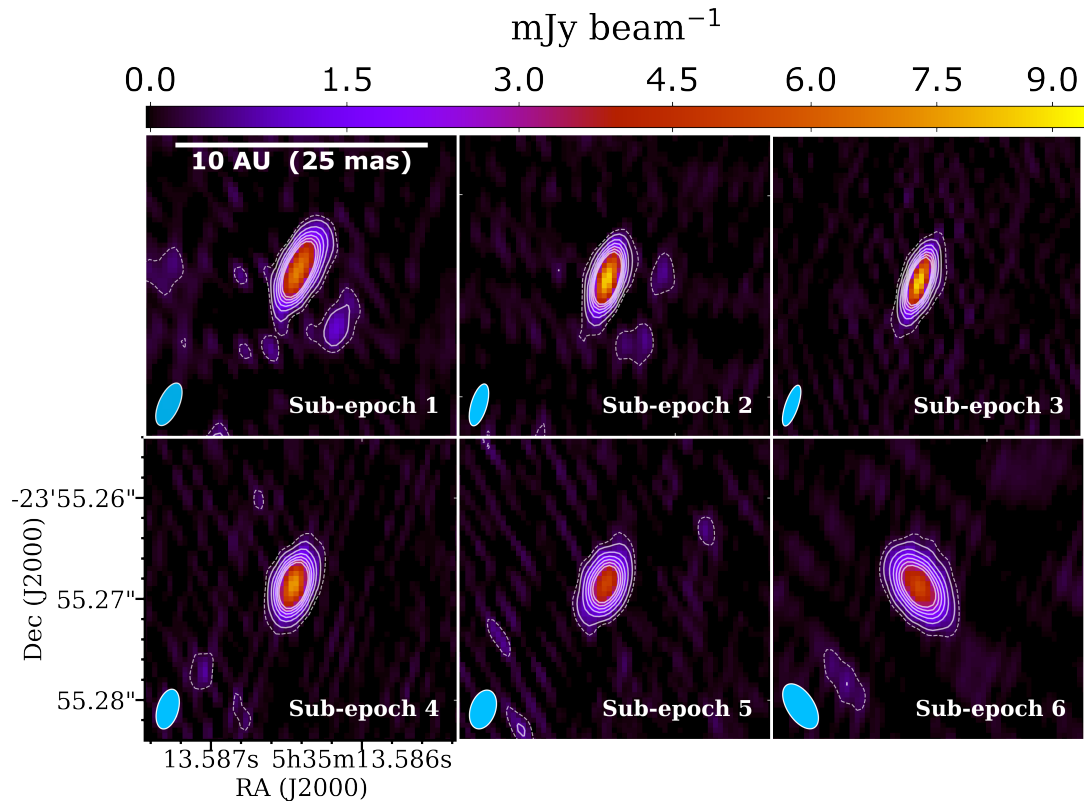
FIGURE 4.12: VLBA continuum maps of source [FRM2016] 130 for epoch 4 (Oct-26-2018). Frames and contours follow same notation described in Figure 4.4

from the nominal source position has a peak flux density of 1.51±0.11 mJy beam, which corresponds to the value reported by DFTPL. In Figure 4.11 this nearby peak is clearly visible with a few synthesized beams separation from the expected position of source [FRM2016] 130. This happens in this sub-epoch and also in two sub-epochs in epoch 2, and these need to be further studied to either discard that this is an imaging issue or to otherwise find plausible explanations for this finding, for instance, a study of the possibility for a short-lived flare nearby the position of source [FRM2016] 130 coincident with a "quiescent" state of this latter or a short flaring companion.

Disregarding sub-epoch 1, the resulting variability (ratio between the maximum and minimum in the lightcurve) from DFTPL and IMFIT for source [FRM2016] 130 in epoch 3 is 1.9±0.1 and 2.0±0.1, respectively, and thus compatible within 1σ uncertainty.

The same comparison was performed in epoch 4, the brightest epoch for source [FRM2016] 130. As seen in Figure 4.12, the source is clearly detected and clearly characterized by the IMFIT lightcurve shown in Figure 4.13, however, only sub-epochs 5 and 6 have compatible measurements between DFTPL and IMFIT, the remaining
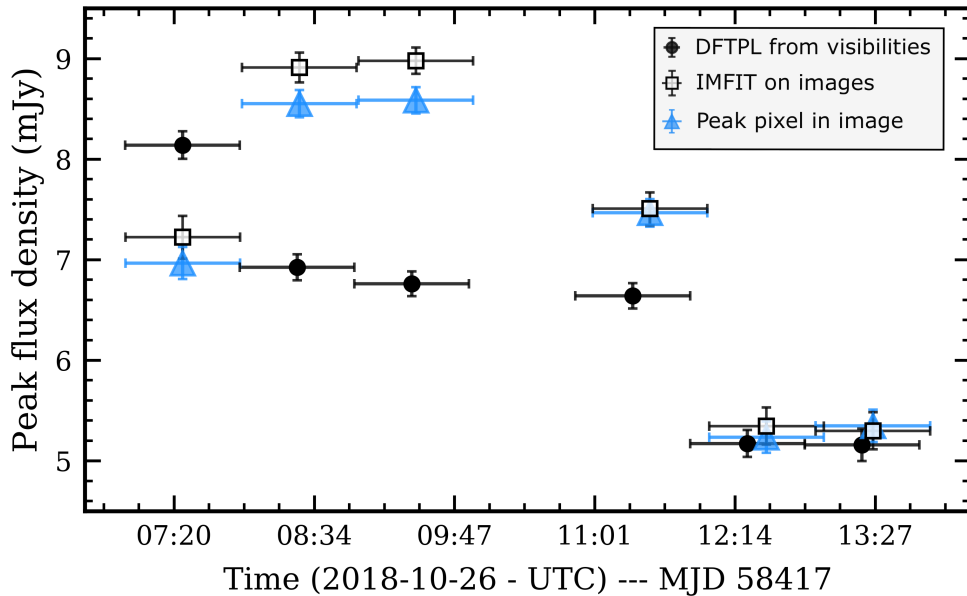
FIGURE 4.13: Radio lightcurves of source [FRM2016] 130 at 1-h time resolution from epoch 4 obtained with DFTPL and IMFIT. Symbols follow same notation of Figure 4.5.

sub-epochs have differences between 12% and 32% in the reported peak flux densities. The reason for these differences are less clear since the lighcurve shapes are also different without following a systematic trend, and the imaged field does not show evidence of nearby compact emission that could lead to the discrepancies, that are more noticeable in sub-epochs 2 and 3. Regardless of these differences, the resulting variability from both methods is still compatible within 2σ uncertainty at similar timescales, with changes in peak flux density by a factor of 1.69±0.03 within 4 h and 1.58±0.03 within 6 h from the IMFIT and DFTPL lightcurves, respectively. For this example, a closer look at the imaging process would be needed in order to constraint these discrepancies by improving the images where negative pixels surrounding the source peak may be causing the 2D-Gaussian fitting to overestimate the true peak flux density, or explorer higher time resolution to constrain any issue in the data within a more specific time interval.

4.4 Summary and conclusions

Following the studies of the four epochs VLBA survey for nonthermal radio emission for a large sample of compact radio sources in the ONC previously identified with the VLA, we now present a follow-up study to discuss a more efficient method for the assessment of nonthermal radio variability in this VLBA sample compared to methods required for

other interferometric datasets (e.g., VLA and ALMA) towards complex regions, such as the ONC. This method consists in obtaining the direct Fourier transform (DFT) directly from the individual visibility datasets of each source, allowing us to generate lightcurves at high-time resolution (down to seconds).

The major advantage of this dataset that makes it possible to directly obtain the flux measurements from the visibilities (using the DFTPL task in AIPS) as an applicable method for variability assessment, is the extraordinary high-angular resolution provided by VLBI that allows to filter out any thermal emission and also provides visibility data towards hundreds of sources at very small spatial scales, where it is very unlikely that any emission would not come from the source in question.

The DFTPL method is presented with some examples of sources with interesting lightcurves in the sample that show clearer evidence of variability, in order to highlight the benefits and prospects of this method. We also present the advantages of this dataset for variability studies compared to that of VLA and ALMA datasets towards the ONC, where the lower resolution, the ubiquitous complex emission in the region, and the high source density necessarily requires time-sliced imaging to obtain lightcurves at a given time resolution.

We additionally present a comparison between the DFTPL method against time-sliced imaging method for the assessment of variability. This comparison shows the advantages of DFTPL to efficiently study flux variability for unresolved and isolated sources in the field. The time-sliced imaging is useful as a complementary tool to identify potential sources where the assumptions required by DFTPL method are not satisfied. We have shown examples where this assumption is satisfied and have demonstrated that the resulting lightcurves from DFTPL and from time-sliced imaging photometry are compatible, while also shown examples where nearby compact emission do not allow us to directly apply DFTPL, leading to incorrect flux measurement and therefore a misinterpretation of the variability of a single source. However, in most of the cases, as already reported in the astrometric study presented in Paper II, multiple systems or potential detection of different components is rarely found and this are also subjects of variability assessments.

Finally, the methodology highlighted in this chapter can also efficiently have access to all Stokes parameters in the same way and under the same assumptions. Here, we

showed examples based in Stokes V in the search for circular polarization. In these examples, there is no significant Stokes V measurements, and only upper limits can be provided. Due to the large uncertainties in Stokes V, the resulting polarization upper limits are very high and also with large uncertainties. Polarization upper limits are better constrained for sub-epochs or measurements with significant Stokes I similar to the example shown in source [FRM2016] 130 in epoch 4, but no conclusive results can be given since these are upper limits. However, these examples illustrate the potential of this dataset to additionally and quickly produce polarization lightcurves.

CHAPTER 5

Summary and future work

5.1 Thesis Summary

Young stars are known to have significantly higher magnetic activity than their more evolved counterparts (i.e. in the main-sequence) with evidence of flares several orders of magnitude more luminous than that of our Sun. From the observational point of view, important progress has been made from the X-ray perspective, but still not much is known about high-energy processes in protostars particularly due to the technological limitations at complementary wavelengths. The improved capabilities of radio interferometers, including the achievement of better sensitivity, allows the observation of radio emission associated with high-energy processes and to study its variability at unprecedented high time resolution.

In this thesis I present comprehensive observational results on the radio time domain of young stars as a unique window to the study of high-energy processes complementing the X-ray perspective. I have used the most capable radio telescopes available for these purposes following their recent technological improvements. The main results of this work are summarized as follows:

- In the first chapter of this thesis I presented a newly enlarged census of the compact radio population towards the ONC using high-sensitivity continuum maps at centimeter-wavelengths over an area of $\sim 20' \times 20'$ obtained with the Karl G. Jansky Very Large Array (VLA) with a mean angular resolution of $0.3''$. This enlarged census complement our previous deep survey of the innermost areas of the ONC, now

covering the field of view of the X-ray Chandra Orion Ultra-deep Project (COUP). This new VLA catalogue contains 521 compact radio sources of which 198 are new detections. Most notably, the radio detection fraction of X-ray sources is higher in the inner cluster and almost constant for $r > 3'$ (0.36 pc) from θ^1 Ori C suggesting a correlation between the radio emission mechanism of these sources and their distance from the most massive stars at the center of the cluster, for example due to increased photoionisation of circumstellar disks. The combination with our previous observations four years prior led to the discovery of fast proper motions of up to $\sim$373 km s^{-1} from faint radio sources associated with ejecta of the OMC1 explosion. Finally, a search for strong radio variability shows evidence of changes in flux density by a factor of $\lesssim$5 within our observations and a few sources with changes by a factor $>$10 on long timescales of a few years.

- Motivated by the results of the systematic search for intense centimeter radio flares in YSOs and by rare findings of strong millimeter-wavelength variability, I present a systematic search for such variability in the ONC using Atacama Large Millimeter/submillimeter Array (ALMA). In this context, mass accretion will also affect the millimeter-wavelength luminosity but typically on longer timescales. Beyond studies of individual YSOs, this characterization of millimeter-wavelength variability with ALMA in the ONC sets first systematic constraints on the occurrence of such variability in a large number of YSOs ($\sim$130). This study shows evidence of a strong YSO millimeter flare of an order of magnitude increase in peak flux density within a few minutes and two additional sources with variability of an order of magnitude on longer timescales of a few days. These findings demonstrate the utility of ALMA monitoring observations and that strong mm-flares occur as rare events and can be characterized at unprecedented high-time resolution. I additionally present an assessment of systematic variability effects caused by the use of time-sliced imaging of a complex region. These are mostly due to the impact of a changing synthesized beam throughout the observations. I made use of simulated observations to reproduce and quantify these systematic effects and set a lower limit for the variability that can be studied using our method in a complex region such as the ONC. All these results demonstrate that the utility of time domain analysis of YSOs extends into the millimeter-wavelength range, potentially interfering with the conversion of observed fluxes into dust masses. This study is thus taking advantage of the ALMA capabilities

with unprecedented sensitivity at mm-wavelengths on short timescales providing a novel perspective on high-energy processes in YSOs complementing extensive VLA and VLBA cm-wavelength observations to much higher energies.

- Finally, I apply a different method for time series analysis, working directly with the visibilities of the multi-epoch survey of nonthermal compact radio sources detected with the VLBA at milliarcsecond resolution. This method (DFTPL) consists in obtaining the flux of a source directly from the individual visibilities (no need of imaging), allowing us to efficiently generate lightcurves at high-time resolution under given assumptions (unresolved and isolated sources). This is possible due to the strong spatial filtering of the dataset that filters out any thermal emission and to the extremely small field of view where nearby compact emission is very unlikely to occur. Such conditions are not met for other interferometric dataset of lower angular resolution such as ALMA or VLA towards regions with complex emission where time-sliced imaging is required for variability analysis. Preliminary results show evidence of variability with changes in peak flux density by a factor of at least 7.5 within 1 day while also evidence of variability on long timescales of a few years, expected due to the nonthermal nature of the emission. A comparison of the DFT method against the time-sliced imaging demonstrates that these are compatible for unresolved and isolated sources (which is generally the case in our sample) and that time-sliced imaging is still a complementary tool for the identification of potential interesting sources where the above assumptions are not satisfied (e.g., potential close companions). In the same way, all Stokes parameters can be explored when available, although we do not find significant Stokes V emission. These results highlight the potential of this dataset to efficiently provide large samples of lightcurves at any time resolution in Stokes I and V.

5.2 Future work

In order to enlarge the sample of radio proper motions (PM) associated to the OMC1 outflow and provide more accurate measurements for the fingertips traced by the H_2 and [Fe II] shocks (see Chapter 2, Section 2.3.3), Recent VLA observations (PI: Jaime Vargas-González; project code: 22A-285) completed a third epoch of the inner ONC repeating the central pointing of our previous observations (Forbrich et al., 2016; Vargas-González et al.,

2021). These observations extend the time baseline from 4 to 10 years and will be used together with the new epoch of the H_2 and [Fe II] observations[1] covering a comparable time baseline of ~ 9 years. This will result in the first nearly simultaneous near-IR and radio kinematic study of the OMC1 outflow with sub-arcsecond resolution covering almost a decade of expansion while additionally providing better constraints on stellar PMs in the cluster. Our analysis so far was limited by the lack of such near-simultaneous IR and VLA observations, limiting our ability to identify IR counterparts of the radio detections in the fast-moving shock structures. This will be remedied in this third epoch, constraining where in the shock structure the radio emission originates. Additionally, these observation will be used to disentangle the nature of the jet-like features near source BN (Bally et al., 2020; Vargas-González et al., 2021), and also confirming the actual direction of the motion of a diffuse radio source in the field (near IRc 23, Dzib et al. 2017). Finally, we will continue our radio variability studies in the ONC, for an unprecedented number of sources. In this way, we will be able to assess long-term variability on the timescale of years, while additionally increasing the chances to find extreme radio events by significantly increasing our total cumulative observing time on YSOs in the ONC.

Additionally, the variability of the outer pointings of the VLA data presented in Chapter 2 has not yet been studied. This was only applied to the central pointing in order to study the variability of the exact same pointing from the deep observation reported in Forbrich et al. (2017), and this way study both short and long timescales for the same field. This was additionally motivated by the simultaneous X-ray observations available the ONC. With the already developed methodology presented in Chapter 2 (Vargas-González et al., 2021) that was also applied to the ALMA data presented in Chapter 3, the variability analysis can be thus extended to the outer VLA pointings.

The statistics of YSO flares at both centimeter and millimeter wavelengths remains as an important goal in the broader picture of high-energy processes in young stars. This motivates the continuous monitoring of nearby star forming regions at these wavelengths. One particular advantage of the radio variability analysis techniques developed in my thesis and scripted for further use, is that it can be functional on both ALMA and VLA continuum observations and can be directly applied on calibrated data to generate time-sliced continuum maps at different time-resolutions. Once the data is imaged, the developed variability analysis code only requires an input catalogue with source positions

---

[1]Gemini GSAOI/GEMS 5-laser AO system, Gemini Program ID: GS-2021B-Q-245, PI: John Bally.

to proceed with source extraction and subsequent production of radio light curves for each input source. Its implementation on existing ALMA and VLA data will significantly increase our statistical sample size of high-time resolution YSOs radio light curves. These methods benefits from the sensitivity capabilities of both facilities making possible to continue our systematic search for strong radio flares on short timescales on a larger sample of nearby star forming regions.

The variability analysis on the ONC reported in Chapter 2 was applied to the central pointing of the VLA observations. These observations were simultaneously observed in X-ray with Chandra and NuSTAR[2]. To further explore previous efforts to characterize the radio-X-ray connection in protostars we plan to search for strong variability in the Chandra and NuSTAR observations in the ONC and search for radio counterparts in our VLA catalogue to generate and analyze simultaneous radio-X-ray light curves.

Finally, a continuation of the analysis presented in Chapter 4 will provide the largest sample of nonthermal YSO lightcurves. Further analysis is needed to complete the search for variability for the full sample. Additionally, some of the imaged examples showed some evidence of nearby compact emission that needs to be investigated in order to discard the possibility of an imaging issue or to otherwise find plausible explanations for this finding and thus study the possibility for a short-lived flare nearby the position of a source (short flaring companion).

---

[2]Chandra Obs. ID: 17735, PI: Hans Guenther ; NuSTAR Obs. ID: 30101101002, PI: Hans Guenther.

Appendix A: Centimeter-wavelength radio survey of the Orion Nebula Cluster

TABLE A.1: Catalogue of compact radio sources in the ONC.

$\alpha(2000)$	$\delta(2000)$	ID	Peak Flux Density	Deconvolved Size [a] $(\theta_{max} \times \theta_{min}$; PA)	COUP	VISION	Dist. to θ^1 Ori C	rad [b]
($^{\mathrm{h\,m\,s}}$)	($^{\circ\,\prime\,\prime\prime}$)		(mJy bm^{-1})	(arcsec^2 ; $^\circ$)			(arcmin)	(arcmin)
(1)	(2)	(3)	(4)	(5)	(6)	(7)	(8)	(9)
05:34:39.76034 ± 0.0002	-5:24:25.4652 ± 0.0029	1	1.422 ± 0.074	0.27× 0.17 ; 45 ± 5		05343976-0524254	9.19	4.27
05:34:40.36673 ± 0.0006	-5:24:11.3077 ± 0.0089	2	0.148 ± 0.011	0.21× 0.06 ; 64 ± 20			9.02	4.04
05:34:43.25981 ± 0.0028	-5:18:18.5661 ± 0.0202	3	0.045 ± 0.009				9.7	5.13
05:34:45.18799 ± 0.0019	-5:25:03.9408 ± 0.0159	4	0.047 ± 0.006		23	05344519-0525041	7.96	3.55
05:34:47.09757 ± 0.0007	-5:25:36.1581 ± 0.0169	5	0.063 ± 0.007			05344709-0525363	7.64	3.68
05:34:47.98129 ± 0.0001	-5:20:54.3807 ± 0.0021	6	0.406 ± 0.021	0.16× 0.12 ; 117± 18			7.51	2.39
05:34:48.82878 ± 0.0002	-5:23:17.9062 ± 0.0031	7	0.18 ± 0.01	0.09× 0.02 ; 49 ± 64	43	05344883-0523179	6.88	1.75
05:34:50.13318 ± 0.0038	-5:16:06.0618 ± 0.0203	8	0.04 ± 0.007				9.8	4.12
05:34:50.33534 ± 0.0013	-5:23:23.7748 ± 0.0276	9	0.019 ± 0.003				6.5	1.48
05:34:50.70982 ± 0.0023	-5:24:01.1836 ± 0.0158	10	0.02 ± 0.004		57	05345071-0524013	6.44	1.87
05:34:52.01143 ± 0.0002	-5:22:36.387 ± 0.0055	11	0.088 ± 0.005			05345201-0522364	6.14	0.78
05:34:52.17461 ± 0.0007	-5:22:31.7862 ± 0.0166	12	0.027 ± 0.003		67	05345216-0522319	6.11	0.73
05:34:52.18385 ± 0.0011	-5:23:18.237 ± 0.0268	13	0.013 ± 0.002				6.04	1.08
05:34:54.06159 ± 0.0025	-5:28:58.2866 ± 0.0487	14	0.038 ± 0.006				7.9	3.33
05:34:54.08431 ± 0.0034	-5:27:23.6121 ± 0.0589	15	0.042 ± 0.007				6.86	2.69
05:34:54.19480 ± 0.0022	-5:28:54.2428 ± 0.0303	16	0.069 ± 0.007		90	05345419-0528543	7.82	3.26
05:34:54.24943 ± 0.0003	-5:21:35.4227 ± 0.0062	17	0.068 ± 0.005		89	05345425-0521354	5.81	0.94
05:34:54.63540 ± 0.0012	-5:14:13.9272 ± 0.0229	18	0.042 ± 0.007				10.64	4.55
05:34:55.09491 ± 0.0006	-5:21:57.5721 ± 0.0104	19	0.041 ± 0.004				5.51	0.55
05:34:55.09811 ± 0.0005	-5:17:45.4892 ± 0.0093	20	0.076 ± 0.006	0.22× 0.16 ; 28 ± 65			7.74	2.42

[a] As defined by imfit in CASA.

[b] Distance to closest phase center. Note that the reported positions are from the standard gridder and may be slightly off in the outermost beam areas (see text).

The full catalogue is available as supplementary material.

TABLE A.1: Continued.

α(2000)	δ(2000)	ID	Peak Flux Density	Deconvolved Size [a] ($\theta_{max} \times \theta_{min}$; PA)	COUP	VISION	Dist. to θ^1 Ori C	rad [b]
($^{\mathrm{h\,m\,s}}$)	($^{\circ\,\prime\,\prime\prime}$)		(mJy bm^{-1})	(arcsec^2 ; $^\circ$)			(arcmin)	(arcmin)
(1)	(2)	(3)	(4)	(5)	(6)	(7)	(8)	(9)
05:34:55.38828 $\pm$ 0.0008	-5:14:08.2473 $\pm$ 0.0127	21	0.106 $\pm$ 0.01	0.19$\times$ 0.14 ; 129$\pm$ 57			10.63	4.52
05:34:55.46975 $\pm$ 0.0037	-5:24:14.0293 $\pm$ 0.0501	22	0.03 $\pm$ 0.005				5.29	3.59
05:34:55.97378 $\pm$ 0.0001	-5:23:13.0321 $\pm$ 0.0022	23	0.245 $\pm$ 0.013		107	05345597-0523130	5.1	0.74
05:34:56.89405 $\pm$ 0.0026	-5:24:51.2505 $\pm$ 0.0380	24	0.03 $\pm$ 0.006				5.09	2.89
05:34:56.96685 $\pm$ 0.0007	-5:15:01.587 $\pm$ 0.0088	25	0.067 $\pm$ 0.006			05345697-0515018	9.66	3.56
05:34:57.13181 $\pm$ 0.0021	-5:31:12.0192 $\pm$ 0.0363	26	0.041 $\pm$ 0.008				9.18	4.63
05:34:57.39476 $\pm$ 0.0019	-5:26:08.6665 $\pm$ 0.0169	27	0.024 $\pm$ 0.003				5.49	2.02
05:34:57.77438 $\pm$ 0.0008	-5:22:00.976 $\pm$ 0.0119	28	0.033 $\pm$ 0.003				4.85	0.83
05:34:58.61685 $\pm$ 0.0003	-5:16:39.1269 $\pm$ 0.0048	29	0.102 $\pm$ 0.006				8.06	2.05
05:34:58.67811 $\pm$ 0.0013	-5:17:23.9968 $\pm$ 0.0237	30	0.02 $\pm$ 0.003	0.08$\times$ 0.02 ; 36 $\pm$ 59		05345868-0517242	7.44	1.64
05:35:00.10929 $\pm$ 0.0008	-5:23:02.053 $\pm$ 0.0202	31	0.028 $\pm$ 0.003		141	05350011-0523019	4.09	1.35
05:35:00.48593 $\pm$ 0.0016	-5:25:14.1136 $\pm$ 0.0437	32	0.022 $\pm$ 0.004		147	05350047-0525143	4.39	2.04
05:35:01.34213 $\pm$ 0.0015	-5:28:11.8962 $\pm$ 0.0186	33	0.035 $\pm$ 0.004		160	05350134-0528118	6.11	1.49
05:35:02.00424 $\pm$ 0.0010	-5:20:55.1289 $\pm$ 0.0146	34	0.037 $\pm$ 0.004		172	05350200-0520551	4.36	2.34
05:35:02.03591 $\pm$ 0.0013	-5:25:18.7794 $\pm$ 0.0288	35	0.045 $\pm$ 0.005				4.08	1.8
05:35:02.07878 $\pm$ 0.0007	-5:26:36.2036 $\pm$ 0.0118	36	0.08 $\pm$ 0.006		173	05350208-0526363	4.82	0.77
05:35:02.15474 $\pm$ 0.0009	-5:19:31.3495 $\pm$ 0.0091	37	0.03 $\pm$ 0.003				5.25	1.65
05:35:02.38438 $\pm$ 0.0003	-5:15:47.9179 $\pm$ 0.0054	38	0.083 $\pm$ 0.005			05350238-0515480	8.35	2.29
05:35:03.00496 $\pm$ 0.0026	-5:30:01.3823 $\pm$ 0.0481	39	0.042 $\pm$ 0.006		188	05350300-0530015	7.44	3.08
05:35:03.62791 $\pm$ 0.0002	-5:20:02.3014 $\pm$ 0.0042	40	0.149 $\pm$ 0.008	0.15$\times$ 0.13 ; 10 $\pm$ 81			4.62	2.05
05:35:04.07781 $\pm$ 0.0010	-5:26:36.9674 $\pm$ 0.0136	41	0.256 $\pm$ 0.022	0.36$\times$ 0.08 ; 60 $\pm$ 12	205	05350406-0526372	4.47	5.01
05:35:04.85665 $\pm$ 0.0001	-5:23:02.6102 $\pm$ 0.0010	42	4.074 $\pm$ 0.205	0.17$\times$ 0.13 ; 76 $\pm$ 8	229		2.91	2.45
05:35:05.18136 $\pm$ 0.0008	-5:17:50.7298 $\pm$ 0.0156	43	0.014 $\pm$ 0.002				6.21	0.19
05:35:05.20982 $\pm$ 0.0002	-5:14:50.2885 $\pm$ 0.0039	44	0.207 $\pm$ 0.012	0.12$\times$ 0.09 ; 51 $\pm$ 73		05350519-0514503	8.99	3.18
05:35:06.00517 $\pm$ 0.0011	-5:15:45.76 $\pm$ 0.0180	45	0.02 $\pm$ 0.003				8.05	2.27

TABLE A.1: Continued.

α(2000)	δ(2000)	ID	Peak Flux Density	Deconvolved Size [a] ($\theta_{max} \times \theta_{min}$; PA)	COUP	VISION	Dist. to θ^1 Ori C	rad [b]
(ʰᵐˢ)	(°′″)		(mJy bm⁻¹)	(arcsec² ; °)			(arcmin)	(arcmin)
(1)	(2)	(3)	(4)	(5)	(6)	(7)	(8)	(9)
05:35:06.10029 ± 0.0003	-5:14:24.8131 ± 0.0045	46	0.188 ± 0.011	0.18× 0.07 ; 77 ± 17		05350610-0514249	9.33	3.61
05:35:06.19131 ± 0.0002	-5:22:12.4737 ± 0.0028	47	0.311 ± 0.017		260	05350617-0522124	2.81	2.08
05:35:06.28289 ± 0.0004	-5:22:02.6506 ± 0.0062	48	0.127 ± 0.009		262	05350628-0522027	2.86	2.09
05:35:06.43060 ± 0.0006	-5:24:21.2035 ± 0.0111	49	0.141 ± 0.009	0.23× 0.07 ; 4 ± 19			2.68	2.66
05:35:06.50172 ± 0.0004	-5:26:54.9408 ± 0.0070	50	0.201 ± 0.011		272	05350650-0526549	4.32	0.43
05:35:06.67956 ± 0.0017	-5:32:33.6369 ± 0.0335	51	0.207 ± 0.027	0.37× 0.21 ; 22 ± 68			9.5	5.6
05:35:06.89008 ± 0.0012	-5:22:09.1505 ± 0.0230	52	0.043 ± 0.007		276	05350688-0522093	2.68	1.92
05:35:07.22432 ± 0.0030	-5:21:34.5279 ± 0.0330	53	0.047 ± 0.009	0.47× 0.15 ; 64 ± 23		05350721-0521344	2.92	2.03
05:35:07.81822 ± 0.0016	-5:23:45.0686 ± 0.1114	54	0.057 ± 0.01				2.18	2.07
05:35:08.65434 ± 0.0015	-5:16:13.1475 ± 0.0246	55	0.017 ± 0.003		319	05350864-0516132	7.42	2.04
05:35:08.68327 ± 0.0008	-5:29:01.5327 ± 0.0119	56	0.064 ± 0.005		323	05350870-0529016	5.97	2.27
05:35:08.73447 ± 0.0021	-5:22:56.6484 ± 0.0230	57	0.042 ± 0.007		322	05350873-0522567	1.97	1.49
05:35:09.49608 ± 0.0004	-5:27:48.9553 ± 0.0069	58	0.149 ± 0.008		335	05350949-0527489	4.76	1.44
05:35:09.66445 ± 0.0011	-5:23:55.5797 ± 0.0269	59	0.164 ± 0.022		338	05350968-0523559	1.78	6.04
05:35:09.76963 ± 0.0004	-5:21:28.3472 ± 0.0074	60	0.093 ± 0.007		342	05350977-0521284	2.53	1.57
05:35:09.76972 ± 0.0004	-5:23:26.8612 ± 0.0099	61	0.082 ± 0.007		343	05350977-0523269	1.67	1.5
05:35:09.83824 ± 0.0005	-5:27:53.1673 ± 0.0083	62	0.132 ± 0.008		349	05350984-0527532	4.8	1.55
05:35:10.00784 ± 0.0007	-5:21:21.8291 ± 0.0218	63	0.054 ± 0.007				2.58	1.6
05:35:10.09748 ± 0.0024	-5:22:26.0837 ± 0.0201	64	0.029 ± 0.005				1.85	1.09
05:35:10.13790 ± 0.0015	-5:21:37.2685 ± 0.0338	65	0.051 ± 0.007				2.36	3.85
05:35:10.14576 ± 0.0009	-5:22:32.6188 ± 0.0153	66	0.071 ± 0.008	0.23× 0.06 ; 62 ± 54	358	05351014-0522327	1.78	1.08
05:35:10.42494 ± 0.0005	-5:24:30.282 ± 0.0104	67	0.113 ± 0.009				1.88	2.24
05:35:10.45978 ± 0.0012	-5:22:28.9968 ± 0.0164	68	0.071 ± 0.012				1.74	5.63
05:35:10.49740 ± 0.0013	-5:22:45.7864 ± 0.0134	69	0.059 ± 0.007		378	05351050-0522455	1.61	1.02
05:35:10.54898 ± 0.0009	-5:22:16.2974 ± 0.0174	70	0.19 ± 0.019	0.29× 0.14 ; 37 ± 29	383	05351053-0522166	1.84	5.45

TABLE A.1: Continued.

α(2000)	δ(2000)	ID	Peak Flux Density	Deconvolved Size [a] $(\theta_{max} \times \theta_{min}$; PA$)$	COUP	VISION	Dist. to θ^1 Ori C	rad [b]
($^{\mathrm{h\,m\,s}}$)	($^{\circ\,\prime\,\prime\prime}$)		(mJy bm^{-1})	(arcsec^2 ; $^\circ$)			(arcmin)	(arcmin)
(1)	(2)	(3)	(4)	(5)	(6)	(7)	(8)	(9)
05:35:10.59031 ± 0.0025	-5:21:56.3242 ± 0.0238	71	0.055 ± 0.008	0.5 × 0.15 ; 68 ± 14	382	05351058-0521562	2.05	1.12
05:35:10.61449 ± 0.0006	-5:22:56.0211 ± 0.0103	72	0.1 ± 0.01		390	05351062-0522560	1.52	1.05
05:35:10.73269 ± 0.0002	-5:23:44.6523 ± 0.0041	73	0.275 ± 0.016		394	05351073-0523446	1.47	1.55
05:35:10.90853 ± 0.0008	-5:22:46.3999 ± 0.0184	74	0.097 ± 0.011		403	05351092-0522464	1.51	0.93
05:35:10.94593 ± 0.0012	-5:24:48.6115 ± 0.0205	75	0.057 ± 0.007	0.24× 0.03 ; 124± 49	404	05351094-0524486	1.98	2.46
05:35:10.94795 ± 0.0014	-5:23:26.6007 ± 0.0191	76	0.15 ± 0.018	0.35× 0.25 ; 79 ± 85		05351093-0523267	1.37	1.28
05:35:11.22293 ± 0.0008	-5:17:20.7713 ± 0.0108	77	0.064 ± 0.006		414	05351121-0517209	6.17	3.29
05:35:11.24280 ± 0.0008	-5:21:51.8335 ± 0.0118	78	0.112 ± 0.012				2.0	1.03
05:35:11.25097 ± 0.0025	-5:22:45.9792 ± 0.0485	79	0.048 ± 0.008	0.7 × 0.11 ; 39 ± 8			1.44	0.84
05:35:11.26239 ± 0.0007	-5:21:52.4773 ± 0.0111	80	0.162 ± 0.014				1.99	1.02
05:35:11.31919 ± 0.0027	-5:24:38.1662 ± 0.0407	81	0.046 ± 0.007	0.32× 0.11 ; 51 ± 12	420	05351131-0524382	1.79	2.85
05:35:11.36128 ± 0.0019	-5:21:52.2172 ± 0.0121	82	0.081 ± 0.014				1.97	5.64
05:35:11.49920 ± 0.0018	-5:26:02.3615 ± 0.0294	83	0.048 ± 0.006		430	05351149-0526023	2.93	1.92
05:35:11.56113 ± 0.0004	-5:24:48.0507 ± 0.0092	84	0.123 ± 0.01		427	05351156-0524481	1.87	2.4
05:35:11.57140 ± 0.0026	-5:22:54.2915 ± 0.0289	85	0.111 ± 0.018	0.47× 0.3 ; 85 ± 39			1.31	0.82
05:35:11.58596 ± 0.0007	-5:20:21.3446 ± 0.0383	86	0.06 ± 0.008				3.26	2.89
05:35:11.61297 ± 0.0031	-5:22:53.282 ± 0.0284	87	0.109 ± 0.021	0.49× 0.16 ; 72 ± 18			1.3	0.81
05:35:11.62647 ± 0.0009	-5:16:57.5613 ± 0.0097	88	0.039 ± 0.004		431	05351163-0516577	6.53	2.0
05:35:11.65501 ± 0.0022	-5:20:21.9893 ± 0.0298	89	0.035 ± 0.007				3.24	3.91
05:35:11.73601 ± 0.0004	-5:23:51.6068 ± 0.0101	90	0.479 ± 0.031	0.4 × 0.24 ; 171± 9	443	05351172-0523517	1.27	1.51
05:35:11.79828 ± 0.0017	-5:23:45.5571 ± 0.0391	91	0.063 ± 0.009	0.61× 0.26 ; 30 ± 13			1.22	1.42
05:35:11.80411 ± 0.0000	-5:21:49.2612 ± 0.0006	92	4.884 ± 0.245	0.08× 0.03 ; 133± 8	450	05351180-0521493	1.94	0.96
05:35:11.90298 ± 0.0007	-5:31:55.1167 ± 0.0107	93	0.663 ± 0.044	0.33× 0.2 ; 56 ± 24	459	05351189-0531552	8.61	5.25
05:35:11.97108 ± 0.0010	-5:20:31.8175 ± 0.0205	94	0.089 ± 0.011				3.06	2.08
05:35:12.00234 ± 0.0010	-5:20:32.3612 ± 0.0221	95	0.065 ± 0.009				3.05	2.06

TABLE A.1: Continued.

$\alpha(2000)$	$\delta(2000)$	ID	Peak Flux Density	Deconvolved Size [a] $(\theta_{max} \times \theta_{min}$; PA)	COUP	VISION	Dist. to θ^1 Ori C	rad [b]
($^{\mathrm{h\,m\,s}}$)	($^{\circ\,\prime\,\prime\prime}$)		(mJy bm^{-1})	(arcsec^2 ; $^{\circ}$)			(arcmin)	(arcmin)
(1)	(2)	(3)	(4)	(5)	(6)	(7)	(8)	(9)
05:35:12.08834 ± 0.0008	-5:22:11.7988 ± 0.0377	96	0.06 ± 0.012				1.61	5.15
05:35:12.09335 ± 0.0011	-5:20:08.7675 ± 0.0205	97	0.028 ± 0.004				3.41	2.81
05:35:12.10538 ± 0.0023	-5:20:37.3143 ± 0.0276	98	0.062 ± 0.011	0.39× 0.18 ; 70 ± 44			2.96	1.98
05:35:12.12902 ± 0.0009	-5:24:33.7831 ± 0.0160	99	0.072 ± 0.008		465	05351212-0524338	1.6	2.14
05:35:12.22954 ± 0.0007	-5:20:36.4416 ± 0.0115	100	0.076 ± 0.007				2.97	1.98
05:35:12.32886 ± 0.0007	-5:21:24.6631 ± 0.0107	101	0.064 ± 0.007				2.22	1.22
05:35:12.39927 ± 0.0038	-5:21:31.6452 ± 0.0207	102	0.083 ± 0.014		476	05351239-0521315	2.11	1.11
05:35:12.48163 ± 0.0014	-5:20:49.0486 ± 0.0185	103	0.098 ± 0.011				2.75	1.76
05:35:12.57513 ± 0.0010	-5:23:01.9775 ± 0.0280	104	0.061 ± 0.01		483	05351257-0523020	1.03	0.71
05:35:12.59834 ± 0.0005	-5:19:45.4586 ± 0.0102	105	0.061 ± 0.005		482	05351260-0519455	3.75	2.61
05:35:12.70988 ± 0.0006	-5:23:53.0147 ± 0.0105	106	0.234 ± 0.018	0.23× 0.2 ; 105± 68			1.06	1.44
05:35:12.73618 ± 0.0002	-5:16:52.6737 ± 0.0024	107	0.203 ± 0.011		490	05351274-0516528	6.57	2.28
05:35:12.77269 ± 0.0009	-5:20:34.8935 ± 0.0480	108	0.02 ± 0.004		492	05351277-0520349	2.95	3.25
05:35:12.77576 ± 0.0004	-5:24:10.6853 ± 0.0071	109	0.19 ± 0.013		496		1.22	1.72
05:35:12.78544 ± 0.0006	-5:21:05.9311 ± 0.0315	110	0.043 ± 0.006				2.46	3.67
05:35:12.79959 ± 0.0017	-5:21:39.3193 ± 0.0145	111	0.06 ± 0.008				1.95	0.95
05:35:12.82263 ± 0.0040	-5:21:29.0799 ± 0.0421	112	0.044 ± 0.009	0.68× 0.12 ; 59 ± 9			2.1	1.1
05:35:12.84832 ± 0.0014	-5:21:33.9827 ± 0.0484	113	0.029 ± 0.005		504	05351285-0521340	2.03	1.03
05:35:12.88254 ± 0.0006	-5:21:13.4276 ± 0.0105	114	0.15 ± 0.013				2.33	1.35
05:35:12.89415 ± 0.0015	-5:20:35.4757 ± 0.0312	115	0.054 ± 0.008				2.93	1.96
05:35:12.92190 ± 0.0021	-5:21:14.5396 ± 0.0230	116	0.043 ± 0.006	0.46× 0.19 ; 110± 22			2.31	1.33
05:35:12.96515 ± 0.0004	-5:23:54.7212 ± 0.0083	117	0.261 ± 0.018	0.18× 0.04 ; 132± 14	510		1.02	1.45
05:35:12.96928 ± 0.0007	-5:23:29.9954 ± 0.0083	118	0.181 ± 0.015		509		0.88	1.06
05:35:12.97336 ± 0.0018	-5:20:41.3807 ± 0.0240	119	0.047 ± 0.009				2.83	1.86
05:35:12.99095 ± 0.0015	-5:20:40.2703 ± 0.0412	120	0.041 ± 0.007	0.43× 0.21 ; 11 ± 41			2.84	3.35

TABLE A.1: Continued.

$\alpha(2000)$	$\delta(2000)$	ID	Peak Flux Density	Deconvolved Size [a] $(\theta_{max} \times \theta_{min}$; PA$)$	COUP	VISION	Dist. to θ^1 Ori C	rad [b]
($^{\mathrm{h\,m\,s}}$)	($^{\circ\,\prime\,\prime\prime}$)		(mJy bm^{-1})	(arcsec^2 ; $^\circ$)			(arcmin)	(arcmin)
(1)	(2)	(3)	(4)	(5)	(6)	(7)	(8)	(9)
05:35:13.00195 ± 0.0005	-5:21:18.9275 ± 0.0060	121	0.157 ± 0.01				2.24	1.25
05:35:13.01146 ± 0.0001	-5:19:04.0758 ± 0.0011	122	0.652 ± 0.033	0.1 × 0.08 ; 140± 52	514	05351301-0519041	4.4	2.31
05:35:13.02026 ± 0.0004	-5:21:17.3848 ± 0.0095	123	0.098 ± 0.008				2.26	1.27
05:35:13.03301 ± 0.0014	-5:21:23.5396 ± 0.0110	124	0.073 ± 0.008				2.16	1.17
05:35:13.04083 ± 0.0002	-5:20:30.1827 ± 0.0039	125	0.317 ± 0.017		515	05351304-0520302	3.0	2.04
05:35:13.04418 ± 0.0045	-5:20:38.3636 ± 0.0396	126	0.03 ± 0.005	0.76× 0.11 ; 116± 8			2.87	1.91
05:35:13.06964 ± 0.0019	-5:20:45.9087 ± 0.0540	127	0.031 ± 0.006	0.46× 0.22 ; 11 ± 72			2.75	3.44
05:35:13.11144 ± 0.0005	-5:22:47.1823 ± 0.0119	128	0.268 ± 0.02	0.33× 0.18 ; 10 ± 17	524	05351310-0522471	1.02	0.44
05:35:13.20851 ± 0.0003	-5:22:54.808 ± 0.0073	129	0.262 ± 0.017	0.1 × 0.01 ; 36 ± 89	530		0.94	0.51
05:35:13.31414 ± 0.0008	-5:23:53.0055 ± 0.0153	130	0.138 ± 0.016		540		0.93	1.4
05:35:13.37543 ± 0.0008	-5:20:51.5088 ± 0.0130	131	0.085 ± 0.008		537	05351337-0520516	2.64	1.67
05:35:13.37719 ± 0.0012	-5:21:29.09 ± 0.0195	132	0.067 ± 0.008	0.32× 0.19 ; 52 ± 64			2.05	1.06
05:35:13.40558 ± 0.0016	-5:22:11.1851 ± 0.0452	133	0.052 ± 0.011				1.42	4.96
05:35:13.40870 ± 0.0002	-5:24:11.1488 ± 0.0050	134	0.471 ± 0.026	0.25× 0.05 ; 5 ± 6			1.11	1.7
05:35:13.52354 ± 0.0008	-5:22:19.6407 ± 0.0102	135	0.253 ± 0.021	0.32× 0.16 ; 71 ± 31	551	05351352-0522196	1.28	0.3
05:35:13.54828 ± 0.0010	-5:21:12.053 ± 0.0132	136	0.127 ± 0.012	0.3 × 0.17 ; 106± 30			2.3	1.33
05:35:13.58564 ± 0.0002	-5:23:55.2518 ± 0.0034	137	1.668 ± 0.09	0.08× 0.07 ; 55 ± 79	554	05351358-0523552	0.9	1.43
05:35:13.61878 ± 0.0017	-5:19:54.8179 ± 0.0228	138	0.026 ± 0.005		561	05351362-0519548	3.54	2.91
05:35:13.63680 ± 0.0017	-5:32:13.0197 ± 0.0292	139	0.125 ± 0.019		568	05351361-0532132	8.86	5.68
05:35:13.69720 ± 0.0026	-5:21:55.541 ± 0.0357	140	0.044 ± 0.009	0.36× 0.29 ; 93 ± 85			1.61	4.7
05:35:13.72388 ± 0.0004	-5:21:35.8508 ± 0.0096	141	0.104 ± 0.008		570	05351372-0521359	1.91	0.93
05:35:13.80684 ± 0.0045	-5:22:07.5091 ± 0.0256	142	0.08 ± 0.014			05351380-0522071	1.42	0.42
05:35:13.82226 ± 0.0014	-5:13:22.0112 ± 0.0272	143	0.064 ± 0.01				10.04	5.16
05:35:13.88208 ± 0.0012	-5:23:57.2014 ± 0.0162	144	0.107 ± 0.011	0.33× 0.22 ; 101± 36			0.86	1.45
05:35:13.89209 ± 0.0003	-5:18:53.1106 ± 0.0070	145	0.071 ± 0.005		586	05351390-0518531	4.54	2.43

$\alpha(2000)$	$\delta(2000)$	ID	Peak Flux Density	Deconvolved Size [a] ($\theta_{max} \times \theta_{min}$; PA)	COUP	VISION	Dist. to θ^1 Ori C	rad [b]
($^{\mathrm{h\,m\,s}}$)	($^{\circ\,\prime\,\prime\prime}$)		(mJy bm^{-1})	(arcsec^2 ; $^{\circ}$)			(arcmin)	(arcmin)
(1)	(2)	(3)	(4)	(5)	(6)	(7)	(8)	(9)
05:35:13.89664 ± 0.0027	-5:23:50.0726 ± 0.0662	146	0.239 ± 0.034	1.0 × 0.25 ; 150± 4			0.78	1.34
05:35:13.91602 ± 0.0007	-5:22:23.9226 ± 0.0119	147	0.132 ± 0.013				1.17	0.18
05:35:13.92701 ± 0.0006	-5:23:20.1065 ± 0.0120	148	0.241 ± 0.022		593	05351392-0523202	0.63	0.84
05:35:13.93490 ± 0.0012	-5:24:09.588 ± 0.0338	149	0.166 ± 0.017	0.6 × 0.1 ; 154± 3			1.0	1.66
05:35:13.95410 ± 0.0009	-5:22:23.8123 ± 0.0100	150	0.166 ± 0.016				1.17	0.17
05:35:13.97080 ± 0.0008	-5:24:09.8147 ± 0.0111	151	0.32 ± 0.031		594		1.0	1.66
05:35:14.01323 ± 0.0018	-5:22:23.2041 ± 0.0153	152	0.138 ± 0.016				1.17	0.17
05:35:14.05272 ± 0.0023	-5:20:09.2714 ± 0.0282	153	0.094 ± 0.014	0.48× 0.21 ; 119± 23			3.28	2.36
05:35:14.07270 ± 0.0026	-5:25:20.3017 ± 0.0401	154	0.053 ± 0.011		604	05351406-0525203	2.05	2.84
05:35:14.07593 ± 0.0013	-5:20:11.7539 ± 0.0211	155	0.157 ± 0.018	0.37× 0.27 ; 131± 72			3.24	2.32
05:35:14.10681 ± 0.0001	-5:22:22.6396 ± 0.0014	156	2.37 ± 0.121				1.16	0.16
05:35:14.13552 ± 0.0016	-5:20:38.7984 ± 0.0309	157	0.054 ± 0.009			05351414-0520388	2.79	1.87
05:35:14.14179 ± 0.0021	-5:23:56.7354 ± 0.0281	158	0.28 ± 0.047		607		0.81	3.82
05:35:14.16360 ± 0.0004	-5:23:01.1134 ± 0.0143	159	2.22 ± 0.136	0.75× 0.31 ; 5 ± 2		05351415-0523011	0.68	0.52
05:35:14.18572 ± 0.0003	-5:26:20.8797 ± 0.0052	160	0.319 ± 0.017		608		3.02	2.42
05:35:14.27449 ± 0.0006	-5:24:24.6726 ± 0.0119	161	0.207 ± 0.017	0.29× 0.04 ; 45 ± 18	616	05351427-0524246	1.17	1.9
05:35:14.28036 ± 0.0034	-5:24:04.9165 ± 0.0600	162	0.178 ± 0.035	0.73× 0.26 ; 41 ± 12			0.89	1.57
05:35:14.28320 ± 0.0022	-5:23:52.9875 ± 0.0352	163	0.402 ± 0.049	0.74× 0.3 ; 135± 7			0.74	1.38
05:35:14.31264 ± 0.0011	-5:24:11.5759 ± 0.0168	164	0.149 ± 0.015	0.26× 0.13 ; 58 ± 59			0.97	3.7
05:35:14.31348 ± 0.0015	-5:21:17.3349 ± 0.0161	165	0.047 ± 0.007				2.16	4.05
05:35:14.32610 ± 0.0056	-5:23:33.7493 ± 0.2524	166	0.065 ± 0.011				0.56	4.19
05:35:14.33520 ± 0.0001	-5:23:17.4139 ± 0.0027	167	1.166 ± 0.061		625		0.54	0.78
05:35:14.35491 ± 0.0003	-5:22:32.8291 ± 0.0099	168	0.743 ± 0.045	0.54× 0.17 ; 24 ± 3	621	05351436-0522327	0.99	0.05
05:35:14.36101 ± 0.0024	-5:25:22.3237 ± 0.0595	169	0.073 ± 0.014	0.6 × 0.22 ; 151± 12		05351434-0525224	2.06	2.86
05:35:14.40423 ± 0.0021	-5:21:26.8258 ± 0.0232	170	0.059 ± 0.012				2.0	4.96

TABLE A.1: Continued.

$\alpha(2000)$	$\delta(2000)$	ID	Peak Flux Density	Deconvolved Size [a] ($\theta_{max} \times \theta_{min}$; PA)	COUP	VISION	Dist. to θ^1 Ori C	rad [b]
($^{\mathrm{h\,m\,s}}$)	($^{\circ\,\prime\,\prime\prime}$)		(mJy bm^{-1})	(arcsec^2 ; $^\circ$)			(arcmin)	(arcmin)
(1)	(2)	(3)	(4)	(5)	(6)	(7)	(8)	(9)
05:35:14.46175 ± 0.0011	-5:25:02.0705 ± 0.0119	171	0.07 ± 0.007		634	05351446-0525020	1.73	3.09
05:35:14.50153 ± 0.0001	-5:22:38.7027 ± 0.0014	172	2.19 ± 0.111		639		0.88	0.14
05:35:14.51608 ± 0.0002	-5:22:30.6233 ± 0.0038	173	0.578 ± 0.033				1.0	0.01
05:35:14.53571 ± 0.0019	-5:23:10.5765 ± 0.0262	174	0.105 ± 0.013	0.55× 0.36 ; 59 ± 25			0.52	0.67
05:35:14.54444 ± 0.0006	-5:23:16.005 ± 0.0107	175	0.213 ± 0.019		640		0.49	0.76
05:35:14.57316 ± 0.0004	-5:22:31.2481 ± 0.0093	176	0.238 ± 0.018				0.98	0.03
05:35:14.61240 ± 0.0007	-5:22:20.9111 ± 0.0136	177	0.356 ± 0.027	0.42× 0.34 ; 167± 34			1.13	0.16
05:35:14.62437 ± 0.0028	-5:23:54.6473 ± 0.0535	178	0.187 ± 0.026	0.93× 0.34 ; 143± 6			0.7	1.4
05:35:14.65535 ± 0.0002	-5:22:33.7357 ± 0.0038	179	0.715 ± 0.039	0.08× 0.01 ; 131± 23	648		0.93	0.07
05:35:14.66482 ± 0.0003	-5:22:11.2796 ± 0.0053	180	0.482 ± 0.029		647		1.27	0.33
05:35:14.72993 ± 0.0013	-5:23:22.909 ± 0.0237	181	0.294 ± 0.037	0.32× 0.29 ; 143± 83	658	05351472-0523229	0.43	0.87
05:35:14.73043 ± 0.0006	-5:22:29.835 ± 0.0125	182	0.224 ± 0.018	0.23× 0.08 ; 148± 22	655	05351472-0522296	0.98	0.06
05:35:14.77875 ± 0.0043	-5:24:06.7784 ± 0.0202	183	0.091 ± 0.013	1.0 × 0.26 ; 96 ± 5			0.84	5.02
05:35:14.80857 ± 0.0006	-5:23:04.7419 ± 0.0102	184	0.29 ± 0.023				0.51	0.58
05:35:14.86832 ± 0.0009	-5:25:14.628 ± 0.0311	185	0.101 ± 0.015	0.3 × 0.07 ; 9 ± 39			1.9	2.74
05:35:14.89892 ± 0.0001	-5:22:25.4098 ± 0.0024	186	1.224 ± 0.064		662		1.03	0.14
05:35:14.91824 ± 0.0003	-5:22:39.2087 ± 0.0056	187	0.427 ± 0.025		670	05351492-0522392	0.82	0.18
05:35:14.93176 ± 0.0006	-5:23:29 ± 0.0118	188	0.351 ± 0.037		671	05351493-0523290	0.39	0.98
05:35:14.94974 ± 0.0009	-5:23:39.2366 ± 0.0143	189	0.33 ± 0.035	0.23× 0.07 ; 65 ± 44	672	05351494-0523393	0.47	1.15
05:35:14.99360 ± 0.0004	-5:21:59.9095 ± 0.0098	190	0.125 ± 0.009		669	05351499-0521599	1.43	0.53
05:35:15.02695 ± 0.0007	-5:22:31.0918 ± 0.0162	191	0.18 ± 0.015	0.38× 0.29 ; 6 ± 41		05351502-0522311	0.93	0.14
05:35:15.05204 ± 0.0017	-5:16:39.2214 ± 0.0226	192	0.026 ± 0.005		677	05351504-0516394	6.74	2.65
05:35:15.07903 ± 0.0013	-5:23:29.0827 ± 0.0610	193	0.187 ± 0.036	0.51× 0.1 ; 7 ± 22			0.36	0.98
05:35:15.15250 ± 0.0025	-5:23:55.972 ± 0.0666	194	0.342 ± 0.059	0.79× 0.29 ; 155± 8			0.64	1.43
05:35:15.20479 ± 0.0011	-5:22:24.028 ± 0.0214	195	0.084 ± 0.011	0.19× 0.16 ; 34 ± 88	688	05351520-0522241	1.03	0.21

$\alpha(2000)$	$\delta(2000)$	ID	Peak Flux Density	Deconvolved Size ^{a} ($\theta_{max} \times \theta_{min}$; PA)	COUP	VISION	Dist. to θ^1 Ori C	rad ^{b}
($^{\mathrm{h\,m\,s}}$)	($^{\circ\,\prime\,\prime\prime}$)		(mJy bm^{-1})	(arcsec^2 ; $^{\circ}$)			(arcmin)	(arcmin)
(1)	(2)	(3)	(4)	(5)	(6)	(7)	(8)	(9)
05:35:15.20948 ± 0.0008	-5:23:18.7327 ± 0.0172	196	0.502 ± 0.051	0.26× 0.17 ; 24 ± 48	690	05351521-0523188	0.32	0.82
05:35:15.25763 ± 0.0021	-5:23:42.3016 ± 0.0235	197	0.256 ± 0.026	0.81× 0.27 ; 57 ± 5			0.44	1.21
05:35:15.26447 ± 0.0005	-5:22:56.8898 ± 0.0133	198	0.166 ± 0.015		689	05351526-0522568	0.53	0.48
05:35:15.27199 ± 0.0039	-5:23:46.9109 ± 0.0926	199	0.323 ± 0.054	1.25× 0.2 ; 148± 4			0.5	5.18
05:35:15.33074 ± 0.0018	-5:22:24.8542 ± 0.0198	200	0.111 ± 0.02		698		1.01	5.03
05:35:15.35688 ± 0.0005	-5:23:21.3527 ± 0.0098	201	0.25 ± 0.021				0.28	0.87
05:35:15.36216 ± 0.0005	-5:23:24.1139 ± 0.0105	202	0.522 ± 0.042	0.11× 0.04 ; 121± 40		05351535-0523241	0.27	0.92
05:35:15.37521 ± 0.0006	-5:22:25.3581 ± 0.0096	203	0.233 ± 0.018	0.19× 0.08 ; 114± 37	699	05351537-0522253	1.0	0.24
05:35:15.39433 ± 0.0009	-5:22:40.0384 ± 0.0096	204	0.628 ± 0.045	0.48× 0.29 ; 77 ± 10		05351539-0522399	0.76	0.28
05:35:15.41954 ± 0.0011	-5:30:23.1229 ± 0.0149	205	0.086 ± 0.009		713	05351541-0530231	7.01	4.06
05:35:15.44281 ± 0.0004	-5:23:45.4493 ± 0.0076	206	0.454 ± 0.032		708	05351544-0523455	0.45	1.27
05:35:15.46105 ± 0.0010	-5:20:38.6401 ± 0.0153	207	0.185 ± 0.022				2.75	1.88
05:35:15.46142 ± 0.0015	-5:20:40.3291 ± 0.0263	208	0.097 ± 0.014		703		2.72	1.85
05:35:15.47052 ± 0.0010	-5:20:39.075 ± 0.0225	209	0.16 ± 0.019	0.26× 0.13 ; 154± 69			2.74	1.87
05:35:15.47059 ± 0.0019	-5:23:14.4021 ± 0.0649	210	0.311 ± 0.051	0.81× 0.36 ; 10 ± 12			0.28	5.66
05:35:15.48365 ± 0.0010	-5:27:22.7369 ± 0.0155	211	0.052 ± 0.006		711	05351547-0527227	4.01	2.2
05:35:15.49887 ± 0.0050	-5:20:37.824 ± 0.0237	212	0.057 ± 0.012	0.69× 0.05 ; 84 ± 10			2.76	1.9
05:35:15.52270 ± 0.0005	-5:23:37.3702 ± 0.0077	213	2.075 ± 0.125	0.46× 0.4 ; 57 ± 41	717	05351552-0523374	0.34	1.14
05:35:15.55304 ± 0.0001	-5:25:14.0604 ± 0.0020	214	1.361 ± 0.07	0.15× 0.08 ; 178± 12	718		1.87	2.74
05:35:15.60183 ± 0.0004	-5:21:26.8559 ± 0.0122	215	0.146 ± 0.011	0.25× 0.04 ; 180± 16	723		1.95	1.1
05:35:15.63561 ± 0.0008	-5:22:56.4158 ± 0.0123	216	0.204 ± 0.022		724	05351564-0522565	0.49	0.52
05:35:15.64682 ± 0.0021	-5:23:10.1663 ± 0.0406	217	0.498 ± 0.062	0.75× 0.31 ; 37 ± 6			0.29	4.35
05:35:15.66630 ± 0.0022	-5:23:55.2344 ± 0.0156	218	0.152 ± 0.021				0.58	1.44
05:35:15.67447 ± 0.0026	-5:23:07.9492 ± 0.0431	219	0.224 ± 0.04	0.54× 0.27 ; 46 ± 29			0.32	4.57
05:35:15.67597 ± 0.0015	-5:23:04.5574 ± 0.0524	220	0.166 ± 0.025	0.68× 0.27 ; 12 ± 13			0.36	0.64

TABLE A.1: Continued.

$\alpha(2000)$	$\delta(2000)$	ID	Peak Flux Density	Deconvolved Size [a] $(\theta_{max} \times \theta_{min}$; PA)	COUP	VISION	Dist. to θ^1 Ori C	rad [b]
(ʰ ᵐ ˢ)	(° ′ ″)		(mJy bm^{-1})	(arcsec^2 ; °)			(arcmin)	(arcmin)
(1)	(2)	(3)	(4)	(5)	(6)	(7)	(8)	(9)
05:35:15.73128 ± 0.0003	-5:23:22.4769 ± 0.0050	221	1.705 ± 0.101	0.22× 0.13 ; 92 ± 19	733		0.18	0.92
05:35:15.76637 ± 0.0010	-5:13:32.1257 ± 0.0156	222	0.093 ± 0.011				9.85	4.94
05:35:15.76694 ± 0.0010	-5:23:38.3933 ± 0.0527	223	0.13 ± 0.02		734	05351576-0523384	0.31	1.18
05:35:15.77266 ± 0.0007	-5:23:09.8399 ± 0.0130	224	0.781 ± 0.067	0.23× 0.13 ; 133± 62	732		0.28	0.73
05:35:15.79780 ± 0.0007	-5:23:26.5255 ± 0.0107	225	3.538 ± 0.252	0.39× 0.36 ; 93 ± 78		05351579-0523265	0.18	0.99
05:35:15.80520 ± 0.0026	-5:22:41.3804 ± 0.0451	226	0.099 ± 0.016	0.66× 0.35 ; 40 ± 16			0.71	5.43
05:35:15.82908 ± 0.0000	-5:23:14.1524 ± 0.0010	227	7.772 ± 0.391	0.13× 0.06 ; 153± 4	745	05351582-0523143	0.21	0.8
05:35:15.84155 ± 0.0002	-5:23:22.4619 ± 0.0033	228	5.052 ± 0.27	0.27× 0.22 ; 77 ± 17	746	05351584-0523224	0.15	0.93
05:35:15.85077 ± 0.0007	-5:23:25.5509 ± 0.0103	229	2.295 ± 0.165	0.38× 0.3 ; 60 ± 59	747		0.16	0.98
05:35:15.88049 ± 0.0008	-5:23:01.9253 ± 0.0152	230	0.337 ± 0.034	0.2 × 0.17 ; 51 ± 73	743	05351588-0523019	0.38	0.63
05:35:15.90587 ± 0.0003	-5:23:37.9617 ± 0.0053	231	1.424 ± 0.083	0.2 × 0.13 ; 41 ± 24	757	05351590-0523380	0.29	1.18
05:35:15.91023 ± 0.0008	-5:24:17.7657 ± 0.0175	232	0.387 ± 0.035	0.35× 0.18 ; 155± 16		05351590-0524178	0.93	1.82
05:35:15.93942 ± 0.0014	-5:22:21.0374 ± 0.0277	233	0.115 ± 0.017	0.33× 0.23 ; 32 ± 75	756	05351594-0522211	1.04	0.4
05:35:15.95304 ± 0.0006	-5:23:49.8235 ± 0.0086	234	2.547 ± 0.156	0.57× 0.47 ; 74 ± 20	758	05351595-0523500	0.47	1.37
05:35:15.97135 ± 0.0009	-5:20:14.2315 ± 0.0137	235	0.068 ± 0.008				3.15	2.3
05:35:16.00028 ± 0.0003	-5:21:09.8364 ± 0.0075	236	0.151 ± 0.01		762	05351600-0521099	2.22	1.4
05:35:16.00307 ± 0.0006	-5:23:52.9711 ± 0.0103	237	1.101 ± 0.072	0.47× 0.33 ; 142± 10	768	05351600-0523529	0.51	1.42
05:35:16.02200 ± 0.0027	-5:23:01.0609 ± 0.0366	238	0.147 ± 0.03	0.41× 0.23 ; 63 ± 47			0.38	4.47
05:35:16.04333 ± 0.0004	-5:19:44.5469 ± 0.0062	239	0.085 ± 0.006		760		3.64	2.66
05:35:16.06920 ± 0.0002	-5:23:24.3657 ± 0.0025	240	3.043 ± 0.16	0.19× 0.1 ; 98 ± 11		05351606-0523243	0.1	0.98
05:35:16.07199 ± 0.0002	-5:23:07.0027 ± 0.0039	241	2.723 ± 0.144	0.35× 0.22 ; 157± 4	766		0.28	0.73
05:35:16.07871 ± 0.0003	-5:23:27.8046 ± 0.0051	242	1.221 ± 0.069	0.28× 0.26 ; 52 ± 71		05351608-0523278	0.13	1.03
05:35:16.09052 ± 0.0018	-5:22:36.3155 ± 0.0130	243	0.206 ± 0.023	0.47× 0.03 ; 96 ± 9			0.78	0.41
05:35:16.09694 ± 0.0014	-5:23:23.0684 ± 0.0160	244	0.196 ± 0.021	0.38× 0.17 ; 104± 21	780	05351611-0523232	0.09	0.96
05:35:16.10786 ± 0.0007	-5:23:14.2505 ± 0.0149	245	0.472 ± 0.041	0.33× 0.21 ; 25 ± 27	779	05351610-0523141	0.17	0.83

α(2000)	δ(2000)	ID	Peak Flux Density	Deconvolved Size ^{a} ($\theta_{max} \times \theta_{min}$; PA)	COUP	VISION	Dist. to θ^1 Ori C	rad ^{b}
($^{\mathrm{h\,m\,s}}$)	($^{\circ\,\prime\,\prime\prime}$)		(mJy bm^{-1})	(arcsec^2 ; $^{\circ}$)			(arcmin)	(arcmin)
(1)	(2)	(3)	(4)	(5)	(6)	(7)	(8)	(9)
05:35:16.11276 ± 0.0008	-5:22:12.527 ± 0.0370	246	0.049 ± 0.01		775	05351611-0522125	1.18	0.5
05:35:16.16424 ± 0.0021	-5:24:10.3355 ± 0.0168	247	0.167 ± 0.017	0.7 × 0.28 ; 103± 7			0.79	1.71
05:35:16.20350 ± 0.0017	-5:21:32.1197 ± 0.0397	248	0.048 ± 0.008	0.42× 0.25 ; 19 ± 80	783	05351619-0521323	1.85	4.05
05:35:16.21692 ± 0.0017	-5:24:56.122 ± 0.0243	249	0.09 ± 0.01	0.55× 0.2 ; 51 ± 8	789	05351620-0524562	1.56	2.83
05:35:16.26677 ± 0.0054	-5:23:41.5395 ± 0.0136	250	0.368 ± 0.036	1.81× 0.22 ; 94 ± 1			0.32	1.26
05:35:16.26730 ± 0.0026	-5:24:12.8278 ± 0.0347	251	0.098 ± 0.018	0.4 × 0.31 ; 96 ± 85			0.83	1.76
05:35:16.28945 ± 0.0001	-5:23:16.5381 ± 0.0024	252	4.904 ± 0.253	0.26× 0.19 ; 136± 7	787	05351629-0523166	0.11	0.89
05:35:16.30174 ± 0.0009	-5:22:23.9692 ± 0.0184	253	0.088 ± 0.011			05351630-0522240	0.98	0.47
05:35:16.30462 ± 0.0010	-5:22:10.2201 ± 0.0165	254	0.072 ± 0.01		784	05351629-0522103	1.21	0.57
05:35:16.31440 ± 0.0008	-5:22:21.5383 ± 0.0152	255	0.158 ± 0.016	0.26× 0.12 ; 50 ± 67	799	05351631-0522215	1.02	0.48
05:35:16.32475 ± 0.0001	-5:23:22.5607 ± 0.0023	256	2.125 ± 0.11	0.15× 0.08 ; 97 ± 13			0.03	0.98
05:35:16.34085 ± 0.0036	-5:24:01.4455 ± 0.0397	257	0.123 ± 0.019	0.74× 0.48 ; 76 ± 46			0.64	4.12
05:35:16.34198 ± 0.0004	-5:22:49.0479 ± 0.0076	258	0.496 ± 0.032	0.22× 0.14 ; 154± 25	800	05351634-0522490	0.56	0.56
05:35:16.37619 ± 0.0017	-5:24:03.3254 ± 0.0230	259	0.221 ± 0.039		801	05351638-0524032	0.67	1.62
05:35:16.39464 ± 0.0021	-5:22:35.3022 ± 0.0204	260	0.224 ± 0.028	0.54× 0.3 ; 93 ± 19			0.79	0.48
05:35:16.41953 ± 0.0015	-5:22:12.1335 ± 0.0153	261	0.063 ± 0.009		806	05351642-0522121	1.18	0.57
05:35:16.47893 ± 0.0012	-5:22:35.4228 ± 0.0158	262	0.321 ± 0.034	0.39× 0.21 ; 69 ± 33	807	05351649-0522351	0.79	0.5
05:35:16.54335 ± 0.0009	-5:22:07.025 ± 0.0132	263	0.105 ± 0.01				1.26	0.65
05:35:16.55384 ± 0.0034	-5:24:41.7724 ± 0.0491	264	0.093 ± 0.014	0.83× 0.21 ; 132± 6			1.32	2.25
05:35:16.59495 ± 0.0005	-5:22:50.3304 ± 0.0095	265	0.378 ± 0.031				0.54	0.62
05:35:16.62104 ± 0.0002	-5:23:16.1157 ± 0.0036	266	1.504 ± 0.082	0.12× 0.09 ; 22 ± 43	820	05351662-0523161	0.12	0.93
05:35:16.62583 ± 0.0007	-5:20:16.348 ± 0.0137	267	0.04 ± 0.004				3.11	2.94
05:35:16.64132 ± 0.0029	-5:24:40.3131 ± 0.0338	268	0.067 ± 0.011	0.56× 0.37 ; 109± 41			1.29	2.96
05:35:16.69130 ± 0.0029	-5:24:31.5038 ± 0.0344	269	0.077 ± 0.013	0.56× 0.25 ; 122± 20			1.15	3.07
05:35:16.75462 ± 0.0002	-5:23:16.4411 ± 0.0026	270	8.07 ± 0.419	0.31× 0.26 ; 108± 12	826		0.13	0.95

TABLE A.1: Continued.

α(2000)	δ(2000)	ID	Peak Flux Density	Deconvolved Size [a] ($\theta_{max} \times \theta_{min}$; PA)	COUP	VISION	Dist. to θ^1 Ori C	rad [b]
(ʰ ᵐ ˢ)	(°′″)		(mJy bm^{-1})	(arcsec^2 ; °)			(arcmin)	(arcmin)
(1)	(2)	(3)	(4)	(5)	(6)	(7)	(8)	(9)
05:35:16.76580 ± 0.0003	-5:24:04.221 ± 0.0051	271	0.583 ± 0.035		828	05351676-0524042	0.69	1.66
05:35:16.77038 ± 0.0002	-5:23:28.077 ± 0.0029	272	2.278 ± 0.12	0.19× 0.1 ; 131± 9	827	05351677-0523280	0.12	1.12
05:35:16.77358 ± 0.0025	-5:23:37.5684 ± 0.0267	273	0.098 ± 0.018	0.39× 0.17 ; 80 ± 30			0.26	4.4
05:35:16.84517 ± 0.0002	-5:23:26.2077 ± 0.0038	274	5.808 ± 0.303	0.47× 0.23 ; 142± 2		05351684-0523261	0.11	1.1
05:35:16.85750 ± 0.0022	-5:22:34.5453 ± 0.0395	275	0.152 ± 0.028	0.46× 0.26 ; 43 ± 36			0.81	0.6
05:35:16.89004 ± 0.0003	-5:23:38.0826 ± 0.0070	276	0.381 ± 0.023	0.21× 0.08 ; 157± 12			0.28	1.27
05:35:16.96420 ± 0.0009	-5:23:33.3567 ± 0.0392	277	0.169 ± 0.025	0.42× 0.09 ; 5 ± 20			0.21	1.22
05:35:16.96442 ± 0.0008	-5:23:34.1715 ± 0.0232	278	0.266 ± 0.032	0.25× 0.07 ; 7 ± 44			0.23	1.23
05:35:16.96559 ± 0.0027	-5:23:59.6795 ± 0.0316	279	0.261 ± 0.046	0.47× 0.31 ; 80 ± 47			0.63	1.61
05:35:16.97189 ± 0.0005	-5:22:48.6515 ± 0.0062	280	1.39 ± 0.081	0.45× 0.36 ; 87 ± 15	844	05351697-0522485	0.58	0.69
05:35:16.97997 ± 0.0005	-5:23:00.9216 ± 0.0106	281	0.285 ± 0.023	0.2 × 0.08 ; 42 ± 52	845	05351698-0523009	0.39	0.8
05:35:16.98236 ± 0.0003	-5:23:36.9793 ± 0.0056	282	3.679 ± 0.206	0.38× 0.36 ; 158± 78	847	05351698-0523370	0.27	1.27
05:35:16.98548 ± 0.0029	-5:23:58.2408 ± 0.0321	283	0.285 ± 0.047	0.56× 0.38 ; 84 ± 33			0.6	1.59
05:35:17.06348 ± 0.0010	-5:23:39.8011 ± 0.0148	284	0.642 ± 0.05	0.51× 0.45 ; 121± 58	856	05351706-0523397	0.32	1.32
05:35:17.06629 ± 0.0001	-5:23:33.9876 ± 0.0019	285	2.576 ± 0.132	0.2 × 0.15 ; 99 ± 11	855	05351706-0523341	0.24	1.24
05:35:17.12199 ± 0.0007	-5:22:11.7702 ± 0.0282	286	0.095 ± 0.013			05351712-0522119	1.2	0.73
05:35:17.12279 ± 0.0028	-5:23:26.5851 ± 0.0378	287	0.28 ± 0.052	0.47× 0.36 ; 114± 92			0.18	5.56
05:35:17.14365 ± 0.0027	-5:23:24.9207 ± 0.0357	288	0.162 ± 0.031	0.45× 0.32 ; 73 ± 83			0.17	1.12
05:35:17.22000 ± 0.0002	-5:21:31.7023 ± 0.0046	289	0.236 ± 0.013		867	05351721-0521317	1.86	1.19
05:35:17.22523 ± 0.0015	-5:23:26.5271 ± 0.0225	290	0.381 ± 0.037	0.58× 0.51 ; 60 ± 399			0.2	1.16
05:35:17.23387 ± 0.0107	-5:23:20.1363 ± 0.0793	291	0.127 ± 0.02	2.12× 0.15 ; 116± 2			0.2	1.08
05:35:17.33267 ± 0.0004	-5:23:41.4166 ± 0.0086	292	0.788 ± 0.05	0.33× 0.16 ; 146± 7		05351733-0523414	0.38	1.38
05:35:17.35309 ± 0.0005	-5:22:35.8905 ± 0.0055	293	1.233 ± 0.072	0.48× 0.27 ; 105± 5	876	05351735-0522357	0.81	0.72
05:35:17.36777 ± 0.0012	-5:25:44.7349 ± 0.0217	294	0.041 ± 0.006		881	05351736-0525447	2.38	2.09
05:35:17.37192 ± 0.0006	-5:23:04.8748 ± 0.0182	295	0.112 ± 0.011		879	05351737-0523049	0.38	0.92

TABLE A.1: Continued.

α(2000)	δ(2000)	ID	Peak Flux Density	Deconvolved Size [a] ($\theta_{max} \times \theta_{min}$; PA)	COUP	VISION	Dist. to θ^1 Ori C	rad [b]
($^{\rm h\,m\,s}$)	($^{\circ\,\prime\,\prime\prime}$)		(mJy bm^{-1})	(arcsec^2 ; $^\circ$)			(arcmin)	(arcmin)
(1)	(2)	(3)	(4)	(5)	(6)	(7)	(8)	(9)
05:35:17.39171 $\pm$ 0.0004	-5:22:03.626 $\pm$ 0.0073	296	0.206 $\pm$ 0.015		874	05351739-0522036	1.34	0.85
05:35:17.39395 $\pm$ 0.0010	-5:24:13.8728 $\pm$ 0.0200	297	0.166 $\pm$ 0.02	0.2 $\times$ 0.17 ; 135$\pm$ 42	887	05351739-0524139	0.88	1.87
05:35:17.41980 $\pm$ 0.0024	-5:23:41.6408 $\pm$ 0.0786	298	0.11 $\pm$ 0.022	0.79$\times$ 0.27 ; 20 $\pm$ 13	886		0.39	1.39
05:35:17.44948 $\pm$ 0.0019	-5:23:54.5917 $\pm$ 0.0442	299	0.058 $\pm$ 0.01	0.45$\times$ 0.28 ; 16 $\pm$ 72			0.58	3.48
05:35:17.46663 $\pm$ 0.0002	-5:23:21.0271 $\pm$ 0.0044	300	0.409 $\pm$ 0.023	0.11$\times$ 0.08 ; 16 $\pm$ 50	885	05351746-0523209	0.25	1.12
05:35:17.48339 $\pm$ 0.0005	-5:22:51.2502 $\pm$ 0.0112	301	0.293 $\pm$ 0.022	0.3 $\times$ 0.22 ; 23 $\pm$ 33	884	05351748-0522513	0.58	0.82
05:35:17.52469 $\pm$ 0.0004	-5:17:40.0673 $\pm$ 0.0064	302	0.074 $\pm$ 0.005		891	05351752-0517401	5.72	1.69
05:35:17.54079 $\pm$ 0.0005	-5:19:28.8665 $\pm$ 0.0082	303	0.063 $\pm$ 0.005		894	05351754-0519289	3.91	2.21
05:35:17.55237 $\pm$ 0.0016	-5:23:54.9403 $\pm$ 0.0242	304	0.085 $\pm$ 0.014			05351754-0523550	0.6	3.46
05:35:17.56256 $\pm$ 0.0002	-5:23:24.8383 $\pm$ 0.0033	305	2.894 $\pm$ 0.154	0.27$\times$ 0.22 ; 108$\pm$ 16	900	05351756-0523249	0.28	1.19
05:35:17.58582 $\pm$ 0.0021	-5:22:56.899 $\pm$ 0.0379	306	0.108 $\pm$ 0.019	0.4 $\times$ 0.31 ; 37 $\pm$ 85	899	05351756-0522568	0.51	0.89
05:35:17.65236 $\pm$ 0.0005	-5:19:56.4451 $\pm$ 0.0087	307	0.097 $\pm$ 0.007	0.19$\times$ 0.03 ; 45 $\pm$ 23			3.45	2.52
05:35:17.65397 $\pm$ 0.0028	-5:22:51.6142 $\pm$ 0.0540	308	0.071 $\pm$ 0.013	0.62$\times$ 0.23 ; 38 $\pm$ 14	906	05351765-0522517	0.6	4.05
05:35:17.67596 $\pm$ 0.0005	-5:23:40.8909 $\pm$ 0.0085	309	2.995 $\pm$ 0.177	0.62$\times$ 0.4 ; 45 $\pm$ 5		05351768-0523410	0.43	1.42
05:35:17.72547 $\pm$ 0.0011	-5:25:40.7572 $\pm$ 0.0261	310	0.06 $\pm$ 0.008	0.37$\times$ 0.2 ; 156$\pm$ 33		05351771-0525408	2.32	2.06
05:35:17.77720 $\pm$ 0.0021	-5:23:42.7077 $\pm$ 0.0277	311	0.223 $\pm$ 0.026	0.68$\times$ 0.29 ; 126$\pm$ 8	912	05351777-0523426	0.47	1.46
05:35:17.82258 $\pm$ 0.0014	-5:22:58.0188 $\pm$ 0.0566	312	0.079 $\pm$ 0.012	0.74$\times$ 0.29 ; 176$\pm$ 10		05351784-0522581	0.53	0.95
05:35:17.82776 $\pm$ 0.0006	-5:22:50.3478 $\pm$ 0.0449	313	0.265 $\pm$ 0.03	0.72$\times$ 0.03 ; 2 $\pm$ 3			0.64	5.82
05:35:17.89861 $\pm$ 0.0002	-5:18:35.0848 $\pm$ 0.0031	314	0.189 $\pm$ 0.01		915	05351789-0518353	4.81	1.67
05:35:17.95230 $\pm$ 0.0001	-5:22:45.4244 $\pm$ 0.0013	315	6.176 $\pm$ 0.312		932	05351794-0522455	0.73	0.9
05:35:17.96994 $\pm$ 0.0008	-5:23:53.4919 $\pm$ 0.0143	316	0.161 $\pm$ 0.014	0.33$\times$ 0.07 ; 132$\pm$ 12			0.63	1.63
05:35:17.97401 $\pm$ 0.0019	-5:25:10.4732 $\pm$ 0.0438	317	0.121 $\pm$ 0.016	0.71$\times$ 0.35 ; 25 $\pm$ 11			1.83	2.36
05:35:17.98479 $\pm$ 0.0006	-5:16:13.8607 $\pm$ 0.0116	318	0.045 $\pm$ 0.004		939	05351799-0516136	7.16	2.35
05:35:18.01644 $\pm$ 0.0009	-5:16:13.1653 $\pm$ 0.0230	319	0.024 $\pm$ 0.004				7.17	2.36
05:35:18.03847 $\pm$ 0.0011	-5:22:05.23 $\pm$ 0.0216	320	0.108 $\pm$ 0.016		942	05351803-0522054	1.35	4.35

TABLE A.1: Continued.

α(2000)	δ(2000)	ID	Peak Flux Density	Deconvolved Size [a] ($\theta_{max} \times \theta_{min}$; PA)	COUP	VISION	Dist. to θ^1 Ori C	rad [b]
(ʰᵐˢ)	(°′″)		(mJy bm⁻¹)	(arcsec² ; °)			(arcmin)	(arcmin)
(1)	(2)	(3)	(4)	(5)	(6)	(7)	(8)	(9)
05:35:18.04723 ± 0.0004	-5:23:30.7056 ± 0.0062	321	2.274 ± 0.135	0.36× 0.29 ; 61 ± 26		05351805-0523308	0.42	1.34
05:35:18.07585 ± 0.0035	-5:24:01.0954 ± 0.0325	322	0.071 ± 0.011	0.65× 0.12 ; 65 ± 10	943	05351807-0524011	0.75	3.31
05:35:18.09045 ± 0.0011	-5:22:47.1099 ± 0.0149	323	0.24 ± 0.023	0.38× 0.21 ; 61 ± 40			0.72	0.94
05:35:18.09074 ± 0.0032	-5:25:09.1058 ± 0.0184	324	0.11 ± 0.016				1.82	2.36
05:35:18.20650 ± 0.0045	-5:23:28.7599 ± 0.0797	325	0.078 ± 0.015	0.93× 0.24 ; 40 ± 6			0.44	3.79
05:35:18.21049 ± 0.0006	-5:17:22.1587 ± 0.0114	326	0.04 ± 0.004		950	05351820-0517220	6.03	1.62
05:35:18.21431 ± 0.0016	-5:23:35.9567 ± 0.0259	327	0.207 ± 0.025	0.49× 0.38 ; 48 ± 62	956	05351820-0523359	0.49	1.43
05:35:18.21916 ± 0.0019	-5:24:12.8236 ± 0.0237	328	0.37 ± 0.039	0.73× 0.26 ; 55 ± 6		05351822-0524129	0.94	1.94
05:35:18.23259 ± 0.0011	-5:17:44.908 ± 0.0209	329	0.023 ± 0.003		951	05351822-0517449	5.65	1.5
05:35:18.24499 ± 0.0003	-5:23:15.596 ± 0.0053	330	0.628 ± 0.038	0.21× 0.12 ; 89 ± 21	955	05351824-0523156	0.46	1.2
05:35:18.28557 ± 0.0009	-5:24:38.9257 ± 0.0223	331	0.105 ± 0.013	0.26× 0.06 ; 26 ± 31		05351829-0524389	1.35	2.34
05:35:18.31845 ± 0.0017	-5:24:19.0263 ± 0.0248	332	0.137 ± 0.018	0.41× 0.34 ; 85 ± 82		05351831-0524189	1.04	2.04
05:35:18.35419 ± 0.0006	-5:24:26.8042 ± 0.0116	333	0.214 ± 0.017	0.18× 0.15 ; 155± 83	967	05351836-0524267	1.17	2.16
05:35:18.37092 ± 0.0006	-5:20:16.3399 ± 0.0156	334	0.037 ± 0.004		962	05351837-0520165	3.14	2.68
05:35:18.37245 ± 0.0000	-5:22:37.42 ± 0.0005	335	10.951 ± 0.549		965	05351836-0522374	0.89	0.98
05:35:18.37495 ± 0.0009	-5:21:43.9752 ± 0.0204	336	0.04 ± 0.006		964	05351837-0521440	1.72	1.24
05:35:18.39228 ± 0.0005	-5:20:20.2597 ± 0.0098	337	0.095 ± 0.007		963	05351839-0520204	3.08	2.74
05:35:18.42895 ± 0.0020	-5:21:50.9952 ± 0.0321	338	0.042 ± 0.008	0.27× 0.18 ; 61 ± 59			1.61	3.9
05:35:18.44173 ± 0.0010	-5:23:29.1625 ± 0.0710	339	0.158 ± 0.026				0.5	3.76
05:35:18.44345 ± 0.0037	-5:25:19.2762 ± 0.0153	340	0.041 ± 0.006			05351844-0525192	2.0	2.17
05:35:18.46298 ± 0.0007	-5:16:37.6252 ± 0.0098	341	0.059 ± 0.005		971	05351846-0516377	6.77	1.99
05:35:18.47281 ± 0.0039	-5:23:13.8029 ± 0.0533	342	0.069 ± 0.014	0.66× 0.27 ; 52 ± 21			0.52	3.99
05:35:18.47560 ± 0.0020	-5:21:45.0252 ± 0.0217	343	0.036 ± 0.007				1.71	3.91
05:35:18.53660 ± 0.0013	-5:23:47.6404 ± 0.0243	344	0.05 ± 0.007	0.21× 0.19 ; 33 ± 31			0.66	3.46
05:35:18.65360 ± 0.0009	-5:23:21.5138 ± 0.0628	345	0.129 ± 0.02				0.55	1.34

TABLE A.1: Continued.

α(2000)	δ(2000)	ID	Peak Flux Density	Deconvolved Size [a] $(\theta_{max} \times \theta_{min}$; PA)	COUP	VISION	Dist. to θ^1 Ori C	rad [b]
(ʰᵐˢ)	(°′″)		(mJy bm^{-1})	(arcsec^2 ; °)			(arcmin)	(arcmin)
(1)	(2)	(3)	(4)	(5)	(6)	(7)	(8)	(9)
05:35:18.66485 ± 0.0007	-5:20:33.7535 ± 0.0073	346	0.157 ± 0.012		985	05351866-0520337	2.87	2.21
05:35:18.67051 ± 0.0011	-5:23:13.922 ± 0.0130	347	0.192 ± 0.019	0.33× 0.18 ; 83 ± 30	986	05351866-0523139	0.57	1.27
05:35:18.71076 ± 0.0012	-5:22:56.6698 ± 0.0402	348	0.096 ± 0.015	0.44× 0.17 ; 163± 23	993	05351870-0522568	0.71	3.8
05:35:18.81015 ± 0.0008	-5:17:29.0609 ± 0.0234	349	0.023 ± 0.003		995	05351880-0517291	5.93	1.44
05:35:18.87719 ± 0.0046	-5:22:45.5198 ± 0.0207	350	0.082 ± 0.016				0.86	5.92
05:35:18.88826 ± 0.0023	-5:23:28.724 ± 0.0206	351	0.133 ± 0.025		1000	05351887-0523287	0.61	3.86
05:35:18.95457 ± 0.0005	-5:22:18.7561 ± 0.0092	352	0.146 ± 0.012		1008	05351895-0522187	1.24	1.13
05:35:19.03771 ± 0.0009	-5:22:50.6089 ± 0.0149	353	0.149 ± 0.017			05351904-0522506	0.84	1.18
05:35:19.06643 ± 0.0008	-5:23:49.5985 ± 0.0120	354	0.419 ± 0.032	0.43× 0.35 ; 61 ± 122	1011	05351906-0523496	0.79	1.74
05:35:19.07205 ± 0.0056	-5:23:36.7664 ± 0.0340	355	0.113 ± 0.017	1.2 × 0.23 ; 71 ± 4			0.69	3.85
05:35:19.12847 ± 0.0027	-5:23:26.9718 ± 0.0250	356	0.075 ± 0.015		1019	05351912-0523271	0.67	3.73
05:35:19.15509 ± 0.0010	-5:21:18.2947 ± 0.0169	357	0.067 ± 0.007		1016		2.18	1.68
05:35:19.29534 ± 0.0009	-5:18:02.248 ± 0.0105	358	0.041 ± 0.004				5.39	1.22
05:35:19.30683 ± 0.0001	-5:20:07.7876 ± 0.0015	359	0.71 ± 0.036		1028	05351930-0520079	3.33	2.44
05:35:19.38237 ± 0.0005	-5:23:06.4456 ± 0.0127	360	0.16 ± 0.014		1029	05351938-0523065	0.78	1.36
05:35:19.42912 ± 0.0015	-5:15:38.2396 ± 0.0248	361	0.027 ± 0.005				7.78	2.65
05:35:19.46015 ± 0.0002	-5:27:16.1783 ± 0.0042	362	0.188 ± 0.01	0.11× 0.06 ; 19 ± 70	1033		3.96	1.21
05:35:19.47903 ± 0.0007	-5:15:32.9305 ± 0.0086	363	0.069 ± 0.006				7.87	2.73
05:35:19.56438 ± 0.0021	-5:23:58.9091 ± 0.0221	364	0.054 ± 0.008	0.37× 0.16 ; 79 ± 34			0.98	3.19
05:35:19.56800 ± 0.0001	-5:17:03.1496 ± 0.0027	365	0.173 ± 0.009		1035	05351956-0517032	6.38	1.5
05:35:19.57400 ± 0.0022	-5:23:13.5396 ± 0.0238	366	0.074 ± 0.013	0.34× 0.09 ; 79 ± 40			0.79	1.46
05:35:19.61106 ± 0.0006	-5:20:01.7232 ± 0.0118	367	0.041 ± 0.004		1041	05351961-0520018	3.44	2.32
05:35:19.62069 ± 0.0016	-5:23:57.245 ± 0.0194	368	0.068 ± 0.01		1044	05351961-0523573	0.97	3.21
05:35:19.66846 ± 0.0036	-5:24:26.5945 ± 0.0405	369	0.159 ± 0.026	0.74× 0.43 ; 115± 25	1045	05351966-0524266	1.33	2.33
05:35:19.73627 ± 0.0007	-5:20:15.1441 ± 0.0123	370	0.049 ± 0.005				3.23	2.5

TABLE A.1: Continued.

α(2000)	δ(2000)	ID	Peak Flux Density	Deconvolved Size [a] ($\theta_{max} \times \theta_{min}$; PA)	COUP	VISION	Dist. to θ^1 Ori C	rad [b]
($^{\mathrm{h\,m\,s}}$)	($^{\circ\,\prime\,\prime\prime}$)		(mJy bm^{-1})	(arcsec^2 ; $^{\circ}$)			(arcmin)	(arcmin)
(1)	(2)	(3)	(4)	(5)	(6)	(7)	(8)	(9)
05:35:19.75603 ± 0.0010	-5:22:26.2309 ± 0.0149	371	0.089 ± 0.011				1.25	1.32
05:35:19.76050 ± 0.0008	-5:22:24.0511 ± 0.0171	372	0.118 ± 0.013	0.14× 0.05 ; 146± 21			1.28	1.32
05:35:19.79251 ± 0.0020	-5:25:06.7561 ± 0.0389	373	0.139 ± 0.028	0.3 × 0.24 ; 168± 84			1.92	6.67
05:35:19.81343 ± 0.0033	-5:22:04.0426 ± 0.0203	374	0.047 ± 0.007	0.63× 0.16 ; 84 ± 10			1.56	1.4
05:35:19.82001 ± 0.0007	-5:22:21.6068 ± 0.0096	375	0.241 ± 0.018	0.32× 0.16 ; 108± 17	1056	05351982-0522216	1.32	1.34
05:35:19.84174 ± 0.0012	-5:24:47.7912 ± 0.0191	376	0.138 ± 0.016	0.3 × 0.25 ; 120± 56	1058	05351984-0524478	1.65	2.42
05:35:19.89148 ± 0.0007	-5:15:08.1046 ± 0.0076	377	0.082 ± 0.007		1053		8.29	3.07
05:35:19.99539 ± 0.0014	-5:17:11.6074 ± 0.0218	378	0.022 ± 0.004				6.25	1.32
05:35:20.04944 ± 0.0033	-5:25:04.6661 ± 0.0378	379	0.085 ± 0.012	0.81× 0.33 ; 57 ± 9			1.92	2.15
05:35:20.05047 ± 0.0007	-5:21:05.9237 ± 0.0155	380	0.067 ± 0.007		1071	05352005-0521059	2.45	1.98
05:35:20.05847 ± 0.0015	-5:25:14.2067 ± 0.0166	381	0.082 ± 0.012		1074	05352005-0525143	2.06	4.39
05:35:20.13885 ± 0.0011	-5:26:04.0312 ± 0.0130	382	0.139 ± 0.012		1086	05352013-0526041	2.84	3.93
05:35:20.15541 ± 0.0009	-5:22:28.2755 ± 0.0124	383	0.165 ± 0.015	0.27× 0.16 ; 76 ± 82	1084	05352015-0522283	1.29	1.41
05:35:20.16318 ± 0.0008	-5:13:15.639 ± 0.0179	384	0.123 ± 0.013	0.26× 0.13 ; 157± 37	1080	05352014-0513156	10.16	4.85
05:35:20.16873 ± 0.0001	-5:26:39.0751 ± 0.0021	385	0.363 ± 0.019		1087	05352016-0526390	3.4	1.05
05:35:20.20429 ± 0.0023	-5:22:11.7649 ± 0.0243	386	0.071 ± 0.013				1.51	1.46
05:35:20.22476 ± 0.0002	-5:20:56.8083 ± 0.0045	387	0.292 ± 0.016	0.12× 0.05 ; 25 ± 34	1090	05352021-0520569	2.61	2.12
05:35:20.28134 ± 0.0008	-5:25:04.0106 ± 0.0157	388	0.266 ± 0.022	0.42× 0.36 ; 167± 47	1091	05352027-0525040	1.94	2.13
05:35:20.35599 ± 0.0006	-5:26:17.4269 ± 0.0077	389	0.062 ± 0.005		1095	05352035-0526174	3.07	1.16
05:35:20.44712 ± 0.0016	-5:26:35.538 ± 0.0133	390	0.055 ± 0.009				3.36	3.92
05:35:20.45400 ± 0.0025	-5:23:29.7175 ± 0.0111	391	0.207 ± 0.02	0.8 × 0.14 ; 93 ± 4	1101	05352045-0523298	1.0	1.79
05:35:20.51723 ± 0.0035	-5:20:52.2758 ± 0.0356	392	0.04 ± 0.008	0.56× 0.2 ; 113± 22	1104	05352052-0520521	2.7	2.22
05:35:20.54118 ± 0.0017	-5:24:20.7578 ± 0.0202	393	0.142 ± 0.02	0.34× 0.17 ; 80 ± 47	1107	05352054-0524209	1.4	2.38
05:35:20.60432 ± 0.0026	-5:24:21.5158 ± 0.0297	394	0.052 ± 0.01				1.42	2.75
05:35:20.63581 ± 0.0013	-5:22:55.5598 ± 0.0233	395	0.046 ± 0.007	0.22× 0.2 ; 72 ± 89		05352063-0522557	1.13	3.32

TABLE A.1: Continued.

$\alpha(2000)$	$\delta(2000)$	ID	Peak Flux Density	Deconvolved Size ^{a} ($\theta_{max} \times \theta_{min}$; PA)	COUP	VISION	Dist. to θ^1 Ori C	rad ^{b}
($^{h\,m\,s}$)	($^{\circ\,\prime\,\prime\prime}$)		(mJy bm^{-1})	(arcsec^2 ; $^\circ$)			(arcmin)	(arcmin)
(1)	(2)	(3)	(4)	(5)	(6)	(7)	(8)	(9)
05:35:20.64330 ± 0.0010	-5:22:45.5442 ± 0.0116	396	0.1 ± 0.01		1110	05352064-0522455	1.21	1.55
05:35:20.66215 ± 0.0009	-5:24:46.5621 ± 0.0212	397	0.523 ± 0.04	0.75× 0.32 ; 29 ± 3	1112		1.74	2.35
05:35:20.66854 ± 0.0010	-5:24:53.233 ± 0.0402	398	0.095 ± 0.012	0.58× 0.1 ; 163± 10			1.83	2.25
05:35:20.72386 ± 0.0002	-5:21:44.3214 ± 0.0031	399	0.378 ± 0.02		1116	05352072-0521443	1.95	1.73
05:35:20.75375 ± 0.0000	-5:15:49.2224 ± 0.0008	400	1.47 ± 0.074	0.09× 0.09 ; 33 ± 76	1114	05352075-0515492	7.64	2.35
05:35:20.84778 ± 0.0011	-5:21:21.3857 ± 0.0206	401	0.043 ± 0.007		1120	05352083-0521216	2.3	3.44
05:35:20.99702 ± 0.0005	-5:16:37.4721 ± 0.0081	402	0.05 ± 0.004		1127	05352099-0516376	6.85	1.6
05:35:21.03181 ± 0.0012	-5:22:25.2326 ± 0.0201	403	0.092 ± 0.013	0.18× 0.09 ; 98 ± 70		05352103-0522250	1.49	1.63
05:35:21.04783 ± 0.0001	-5:23:48.9691 ± 0.0014	404	1.483 ± 0.075	0.12× 0.07 ; 139± 12	1130	05352104-0523490	1.22	2.09
05:35:21.16473 ± 0.0023	-5:25:56.9376 ± 0.0182	405	0.036 ± 0.006		1139	05352116-0525569	2.82	1.26
05:35:21.24514 ± 0.0011	-5:22:59.4722 ± 0.0116	406	0.14 ± 0.013	0.32× 0.1 ; 89 ± 19	1141	05352124-0522595	1.25	1.75
05:35:21.27526 ± 0.0003	-5:19:02.3847 ± 0.0059	407	0.082 ± 0.005			05352127-0519025	4.5	1.26
05:35:21.31520 ± 0.0048	-5:24:36.1532 ± 0.0355	408	0.072 ± 0.013	0.84× 0.28 ; 105± 17			1.72	4.75
05:35:21.33054 ± 0.0007	-5:12:12.4251 ± 0.0116	409	0.394 ± 0.032	0.26× 0.22 ; 55 ± 74		05352131-0512127	11.24	5.85
05:35:21.39442 ± 0.0000	-5:26:44.0491 ± 0.0007	410	3.126 ± 0.157		1151	05352139-0526440	3.57	0.73
05:35:21.51435 ± 0.0012	-5:23:16.7895 ± 0.0231	411	0.054 ± 0.007	0.32× 0.07 ; 44 ± 31	1155	05352150-0523166	1.26	1.91
05:35:21.66158 ± 0.0003	-5:25:26.4838 ± 0.0066	412	0.333 ± 0.021	0.14× 0.09 ; 167± 84	1161	05352166-0525265	2.43	3.43
05:35:21.66402 ± 0.0016	-5:17:41.8133 ± 0.0197	413	0.014 ± 0.003				5.83	0.7
05:35:21.69831 ± 0.0003	-5:28:26.6991 ± 0.0074	414	0.102 ± 0.007				5.23	1.61
05:35:21.73758 ± 0.0019	-5:18:36.1429 ± 0.0322	415	0.014 ± 0.003				4.96	0.85
05:35:21.76954 ± 0.0006	-5:23:39.2929 ± 0.0107	416	0.15 ± 0.013	0.17× 0.09 ; 75 ± 78	1167	05352177-0523392	1.35	2.15
05:35:21.84258 ± 0.0008	-5:23:06.4399 ± 0.0113	417	0.14 ± 0.013	0.26× 0.06 ; 70 ± 40		05352185-0523065	1.37	1.93
05:35:21.92655 ± 0.0019	-5:22:07.7148 ± 0.0157	418	0.06 ± 0.01				1.85	4.87
05:35:22.08053 ± 0.0020	-5:28:15.0946 ± 0.0253	419	0.096 ± 0.014		1186	05352206-0528153	5.07	4.49
05:35:22.08882 ± 0.0039	-5:24:32.7749 ± 0.0269	420	0.098 ± 0.017	0.64× 0.16 ; 77 ± 13	1184	05352209-0524328	1.82	2.47

TABLE A.1: Continued.

α(2000)	δ(2000)	ID	Peak Flux Density	Deconvolved Size [a] ($\theta_{max} \times \theta_{min}$; PA)	COUP	VISION	Dist. to θ^1 Ori C	rad [b]
($^{\mathrm{h\,m\,s}}$)	($^{\circ\,\prime\,\prime\prime}$)		(mJy bm^{-1})	(arcsec^2 ; $^\circ$)			(arcmin)	(arcmin)
(1)	(2)	(3)	(4)	(5)	(6)	(7)	(8)	(9)
05:35:22.12174 ± 0.0011	-5:22:34.0149 ± 0.0149	421	0.112 ± 0.013		1191	05352211-0522341	1.63	1.9
05:35:22.26794 ± 0.0019	-5:25:19.9153 ± 0.0149	422	0.058 ± 0.007	0.46× 0.05 ; 103± 12			2.43	1.7
05:35:22.32539 ± 0.0011	-5:24:14.2375 ± 0.0179	423	0.136 ± 0.015	0.33× 0.21 ; 55 ± 84	1205	05352232-0524142	1.69	2.61
05:35:22.54446 ± 0.0038	-5:23:54.7275 ± 0.0220	424	0.028 ± 0.005	0.61× 0.13 ; 87 ± 14		05352254-0523547	1.6	3.08
05:35:22.72000 ± 0.0010	-5:25:45.6918 ± 0.0346	425	0.022 ± 0.003				2.84	1.25
05:35:22.74320 ± 0.0001	-5:19:47.8132 ± 0.0030	426	0.181 ± 0.01		1224	05352274-0519479	3.91	1.82
05:35:22.82570 ± 0.0006	-5:20:22.6426 ± 0.0098	427	0.056 ± 0.005		1229	05352282-0520227	3.4	2.39
05:35:22.83588 ± 0.0013	-5:25:47.6009 ± 0.0178	428	0.042 ± 0.005	0.23× 0.02 ; 72 ± 23		05352283-0525476	2.89	1.22
05:35:22.87937 ± 0.0003	-5:24:57.5705 ± 0.0044	429	0.185 ± 0.01	0.16× 0.05 ; 63 ± 15	1232	05352289-0524578	2.25	2.03
05:35:22.99627 ± 0.0005	-5:17:44.9053 ± 0.0098	430	0.036 ± 0.003		1234	05352300-0517450	5.86	0.39
05:35:23.05060 ± 0.0011	-5:25:00.2394 ± 0.0159	431	0.063 ± 0.006	0.28× 0.1 ; 61 ± 27			2.31	1.98
05:35:23.16145 ± 0.0011	-5:25:02.2462 ± 0.0134	432	0.07 ± 0.007	0.28× 0.07 ; 90 ± 26			2.35	1.94
05:35:23.23568 ± 0.0007	-5:24:52.8063 ± 0.0118	433	0.072 ± 0.007				2.26	2.09
05:35:23.39674 ± 0.0003	-5:18:50.6194 ± 0.0061	434	0.077 ± 0.005		1248	05352339-0518506	4.85	0.85
05:35:23.49621 ± 0.0001	-5:20:01.631 ± 0.0012	435	0.728 ± 0.037	0.12× 0.07 ; 14 ± 10	1249	05352349-0520017	3.78	2.02
05:35:23.54701 ± 0.0011	-5:18:32.3982 ± 0.0202	436	0.014 ± 0.003				5.15	0.55
05:35:23.60166 ± 0.0012	-5:25:26.4919 ± 0.0169	437	0.053 ± 0.006	0.27× 0.17 ; 106± 89	1262	05352359-0525264	2.72	1.53
05:35:23.65590 ± 0.0001	-5:23:31.9181 ± 0.0019	438	0.692 ± 0.036		1259	05352366-0523319	1.8	2.5
05:35:23.66038 ± 0.0012	-5:26:27.0223 ± 0.0192	439	0.043 ± 0.005	0.24× 0.11 ; 123± 42	1263	05352366-0526270	3.55	0.53
05:35:23.68753 ± 0.0023	-5:22:12.6436 ± 0.0145	440	0.035 ± 0.006		1258	05352368-0522127	2.15	2.55
05:35:23.83818 ± 0.0005	-5:30:47.3717 ± 0.0069	441	0.214 ± 0.014		1269	05352383-0530474	7.63	3.83
05:35:23.98585 ± 0.0004	-5:25:09.8692 ± 0.0058	442	0.175 ± 0.011	0.2 × 0.12 ; 107± 39	1275	05352398-0525098	2.59	1.8
05:35:24.02300 ± 0.0024	-5:23:14.0033 ± 0.0282	443	0.072 ± 0.011	0.46× 0.27 ; 110± 42	1276	05352403-0523138	1.89	2.49
05:35:24.12570 ± 0.0004	-5:16:41.8142 ± 0.0082	444	0.049 ± 0.004				6.95	1.31
05:35:24.26127 ± 0.0005	-5:25:18.7032 ± 0.0086	445	0.164 ± 0.011	0.23× 0.21 ; 109± 87	1281	05352426-0525187	2.74	1.65

TABLE A.1: Continued.

α(2000)	δ(2000)	ID	Peak Flux Density	Deconvolved Size ^{a} ($\theta_{max} \times \theta_{min}$; PA)	COUP	VISION	Dist. to θ^1 Ori C	rad ^{b}
($^{\mathrm{h\,m\,s}}$)	($^{\circ\,\prime\,\prime\prime}$)		(mJy bm^{-1})	(arcsec^2 ; $^\circ$)			(arcmin)	(arcmin)
(1)	(2)	(3)	(4)	(5)	(6)	(7)	(8)	(9)
05:35:24.33852 $\pm$ 0.0027	-5:24:40.6852 $\pm$ 0.0793	446	0.111 $\pm$ 0.013	1.56$\times$ 0.23 ; 153$\pm$ 2			2.35	3.21
05:35:24.45596 $\pm$ 0.0017	-5:26:31.5316 $\pm$ 0.0312	447	0.033 $\pm$ 0.005	0.32$\times$ 0.26 ; 146$\pm$ 76	1291	05352446-0526314	3.72	0.44
05:35:24.51755 $\pm$ 0.0004	-5:25:01.5447 $\pm$ 0.0054	448	0.281 $\pm$ 0.017	0.25$\times$ 0.16 ; 86 $\pm$ 19	1293	05352451-0525015	2.59	1.94
05:35:24.59986 $\pm$ 0.0004	-5:19:33.2591 $\pm$ 0.0077	449	0.068 $\pm$ 0.005		1296	05352460-0519333	4.33	1.55
05:35:24.60917 $\pm$ 0.0002	-5:19:55.0036 $\pm$ 0.0034	450	0.155 $\pm$ 0.008	0.11$\times$ 0.07 ; 28 $\pm$ 57	1297	05352461-0519551	4.01	1.91
05:35:24.68304 $\pm$ 0.0016	-5:28:00.2158 $\pm$ 0.0274	451	0.036 $\pm$ 0.006	0.19$\times$ 0.09 ; 56 $\pm$ 30			5.06	1.05
05:35:24.70109 $\pm$ 0.0008	-5:27:59.5574 $\pm$ 0.0220	452	0.06 $\pm$ 0.006		1304	05352470-0527595	5.05	1.04
05:35:25.01170 $\pm$ 0.0027	-5:24:01.9885 $\pm$ 0.0469	453	0.029 $\pm$ 0.005	0.68$\times$ 0.32 ; 42 $\pm$ 14			2.23	2.68
05:35:25.03728 $\pm$ 0.0007	-5:24:38.4106 $\pm$ 0.0120	454	0.086 $\pm$ 0.007	0.25$\times$ 0.16 ; 55 $\pm$ 66	1313	05352503-0524384	2.48	2.33
05:35:25.06471 $\pm$ 0.0007	-5:22:58.4862 $\pm$ 0.0133	455	0.059 $\pm$ 0.006	0.15$\times$ 0.02 ; 54 $\pm$ 27	1309	05352506-0522585	2.18	2.24
05:35:25.08949 $\pm$ 0.0003	-5:23:46.7508 $\pm$ 0.0061	456	0.142 $\pm$ 0.009		1311	05352508-0523467	2.18	2.53
05:35:25.12790 $\pm$ 0.0019	-5:22:25.1758 $\pm$ 0.0246	457	0.029 $\pm$ 0.005	0.34$\times$ 0.12 ; 116$\pm$ 39	1314	05352513-0522252	2.36	2.18
05:35:25.13640 $\pm$ 0.0013	-5:22:49.7587 $\pm$ 0.1212	458	0.101 $\pm$ 0.017	1.32$\times$ 0.18 ; 2 $\pm$ 4			2.23	4.14
05:35:25.38039 $\pm$ 0.0011	-5:24:11.4324 $\pm$ 0.0155	459	0.051 $\pm$ 0.006		1323	05352537-0524114	2.36	2.7
05:35:25.45619 $\pm$ 0.0043	-5:15:36.7933 $\pm$ 0.1452	460	0.018 $\pm$ 0.003				8.08	2.42
05:35:25.53513 $\pm$ 0.0013	-5:25:11.844 $\pm$ 0.0256	461	0.028 $\pm$ 0.004			05352553-0525118	2.9	1.8
05:35:25.84255 $\pm$ 0.0019	-5:22:12.9376 $\pm$ 0.0310	462	0.132 $\pm$ 0.014	0.79$\times$ 0.29 ; 137$\pm$ 5			2.61	2.02
05:35:25.84667 $\pm$ 0.0015	-5:18:09.4453 $\pm$ 0.0207	463	0.02 $\pm$ 0.003		1337		5.72	0.44
05:35:26.06344 $\pm$ 0.0007	-5:21:20.949 $\pm$ 0.0106	464	0.063 $\pm$ 0.006		1341	05352606-0521210	3.14	2.27
05:35:26.20629 $\pm$ 0.0001	-5:27:36.7513 $\pm$ 0.0014	465	0.595 $\pm$ 0.03		1350	05352620-0527367	4.88	0.82
05:35:26.26606 $\pm$ 0.0009	-5:19:18.2956 $\pm$ 0.0198	466	0.022 $\pm$ 0.003				4.75	1.39
05:35:26.35521 $\pm$ 0.0004	-5:28:20.2183 $\pm$ 0.0068	467	0.109 $\pm$ 0.007				5.53	1.48
05:35:26.39947 $\pm$ 0.0002	-5:25:00.6931 $\pm$ 0.0030	468	0.273 $\pm$ 0.014		1360	05352639-0525007	2.96	2.03
05:35:26.49693 $\pm$ 0.0009	-5:23:44.9455 $\pm$ 0.0131	469	0.053 $\pm$ 0.005		1359	05352649-0523450	2.52	3.26
05:35:26.64056 $\pm$ 0.0016	-5:25:57.9142 $\pm$ 0.0304	470	0.033 $\pm$ 0.005			05352664-0525579	3.62	1.17

TABLE A.1: Continued.

α(2000)	δ(2000)	ID	Peak Flux Density	Deconvolved Size [a] ($\theta_{max} \times \theta_{min}$; PA)	COUP	VISION	Dist. to θ^1 Ori C	rad [b]
($^{\rm h\,m\,s}$)	($^{\circ\,\prime\,\prime\prime}$)		(mJy bm^{-1})	(arcsec^2 ; $^\circ$)			(arcmin)	(arcmin)
(1)	(2)	(3)	(4)	(5)	(6)	(7)	(8)	(9)
05:35:26.96527 ± 0.0003	-5:24:00.3423 ± 0.0055	471	0.134 ± 0.008		1372	05352697-0524005	2.69	2.28
05:35:27.44237 ± 0.0006	-5:26:28.2188 ± 0.0117	472	0.056 ± 0.005		1384	05352744-0526281	4.12	0.95
05:35:27.47649 ± 0.0013	-5:17:09.5124 ± 0.0527	473	0.016 ± 0.003		1382	05352747-0517099	6.8	1.18
05:35:27.74154 ± 0.0002	-5:18:04.581 ± 0.0030	474	0.151 ± 0.008		1391	05352774-0518046	6.0	0.89
05:35:27.93097 ± 0.0009	-5:16:57.2504 ± 0.0151	475	0.025 ± 0.003		1400	05352793-0516572	7.03	1.41
05:35:28.12735 ± 0.0004	-5:18:57.1198 ± 0.0118	476	0.042 ± 0.003		1405	05352813-0518572	5.3	1.36
05:35:28.18812 ± 0.0012	-5:24:58.0385 ± 0.0355	477	0.09 ± 0.011	0.54× 0.28 ; 177± 19	1409	05352820-0524581	3.32	2.23
05:35:28.35716 ± 0.0006	-5:18:23.0277 ± 0.0134	478	0.032 ± 0.003		1411	05352835-0518231	5.81	1.1
05:35:28.55829 ± 0.0000	-5:20:56.6358 ± 0.0010	479	0.896 ± 0.045	0.12× 0.09 ; 84 ± 12			3.87	2.05
05:35:29.45961 ± 0.0006	-5:16:33.3052 ± 0.0185	480	0.033 ± 0.004		1424	05352946-0516334	7.55	1.96
05:35:29.58446 ± 0.0004	-5:24:56.8683 ± 0.0106	481	0.069 ± 0.005		1429	05352958-0524569	3.62	2.66
05:35:29.58846 ± 0.0001	-5:23:12.1422 ± 0.0017	482	1.063 ± 0.054	0.22× 0.14 ; 99 ± 6	1428		3.27	1.27
05:35:29.65014 ± 0.0003	-5:20:02.1009 ± 0.0066	483	0.066 ± 0.004		1430	05352965-0520021	4.69	2.44
05:35:30.16791 ± 0.0007	-5:30:58.2647 ± 0.0099	484	0.153 ± 0.012	0.19× 0.06 ; 94 ± 40		05353015-0530584	8.32	4.28
05:35:30.23908 ± 0.0026	-5:16:41.1361 ± 0.0433	485	0.017 ± 0.004	0.37× 0.07 ; 46 ± 72			7.52	2.01
05:35:30.28053 ± 0.0005	-5:25:51.653 ± 0.0079	486	0.095 ± 0.006		1438	05353028-0525516	4.24	1.88
05:35:30.38071 ± 0.0002	-5:22:38.0854 ± 0.0035	487	0.387 ± 0.021		1439	05353038-0522381	3.54	0.88
05:35:30.49148 ± 0.0002	-5:24:23.0709 ± 0.0049	488	0.158 ± 0.009	0.13× 0.02 ; 22 ± 27	1443	05353049-0524231	3.63	2.06
05:35:30.77798 ± 0.0017	-5:19:07.1786 ± 0.0176	489	0.019 ± 0.004				5.55	1.98
05:35:30.99752 ± 0.0002	-5:22:01.3558 ± 0.0029	490	0.171 ± 0.009		1456	05353100-0522013	3.86	0.87
05:35:31.30085 ± 0.0001	-5:15:32.9086 ± 0.0027	491	0.343 ± 0.018	0.13× 0.12 ; 51 ± 84	1462	05353129-0515331	8.66	3.03
05:35:31.36825 ± 0.0001	-5:16:02.4897 ± 0.0019	492	0.497 ± 0.025	0.17× 0.08 ; 56 ± 7	1468	05353136-0516026	8.22	2.66
05:35:31.43549 ± 0.0003	-5:25:16.2619 ± 0.0069	493	0.17 ± 0.01		1473	05353143-0525162	4.18	2.47
05:35:31.46223 ± 0.0010	-5:25:15.6582 ± 0.0201	494	0.152 ± 0.015				4.18	2.49
05:35:31.49133 ± 0.0009	-5:21:36.5142 ± 0.0133	495	0.037 ± 0.004		1471	05353149-0521365	4.14	1.08

TABLE A.1: Continued.

α(2000)	δ(2000)	ID	Peak Flux Density	Deconvolved Size ^{a} ($\theta_{max} \times \theta_{min}$; PA)	COUP	VISION	Dist. to θ^1 Ori C	rad ^{b}
($^{\mathrm{h\,m\,s}}$)	($^{\circ\,\prime\,\prime\prime}$)		(mJy bm^{-1})	(arcsec^2 ; $^\circ$)			(arcmin)	(arcmin)
(1)	(2)	(3)	(4)	(5)	(6)	(7)	(8)	(9)
05:35:31.71562 $\pm$ 0.0015	-5:28:52.8219 $\pm$ 0.0342	496	0.03 $\pm$ 0.006	0.22$\times$ 0.11 ; 158$\pm$ 77			6.68	2.68
05:35:31.97916 $\pm$ 0.0005	-5:15:59.4867 $\pm$ 0.0097	497	0.062 $\pm$ 0.005			05353197-0515596	8.34	2.8
05:35:31.99956 $\pm$ 0.0009	-5:16:19.9705 $\pm$ 0.0165	498	0.04 $\pm$ 0.004		1485	05353199-0516201	8.04	2.57
05:35:32.31345 $\pm$ 0.0013	-5:20:23.557 $\pm$ 0.0224	499	0.024 $\pm$ 0.004	0.17$\times$ 0.04 ; 111$\pm$ 45		05353232-0520237	4.95	2.15
05:35:32.34690 $\pm$ 0.0001	-5:18:07.7945 $\pm$ 0.0025	500	0.24 $\pm$ 0.013	0.09$\times$ 0.05 ; 10 $\pm$ 54	1487	05353234-0518078	6.57	2.04
05:35:32.35321 $\pm$ 0.0015	-5:21:17.6481 $\pm$ 0.0187	501	0.028 $\pm$ 0.004		1488	05353235-0521177	4.47	1.27
05:35:32.52441 $\pm$ 0.0007	-5:26:10.5103 $\pm$ 0.0119	502	0.062 $\pm$ 0.006		1492	05353252-0526104	4.88	2.22
05:35:32.83004 $\pm$ 0.0017	-5:22:22.5612 $\pm$ 0.0203	503	0.041 $\pm$ 0.005		1498		4.2	0.29
05:35:32.91821 $\pm$ 0.0001	-5:16:05.129 $\pm$ 0.0018	504	0.531 $\pm$ 0.027	0.08$\times$ 0.03 ; 109$\pm$ 85	1500	05353291-0516052	8.37	2.91
05:35:33.15723 $\pm$ 0.0017	-5:16:05.0714 $\pm$ 0.0800	505	0.057 $\pm$ 0.01	0.8 $\times$ 0.12 ; 13 $\pm$ 6			8.4	2.95
05:35:34.22103 $\pm$ 0.0012	-5:27:18.3368 $\pm$ 0.0311	506	0.032 $\pm$ 0.005		1511	05353422-0527184	5.91	2.52
05:35:34.55220 $\pm$ 0.0004	-5:20:51.4421 $\pm$ 0.0068	507	0.077 $\pm$ 0.006				5.16	1.66
05:35:36.82600 $\pm$ 0.0012	-5:21:27.3056 $\pm$ 0.0320	508	0.02 $\pm$ 0.004				5.42	1.28
05:35:38.11268 $\pm$ 0.0005	-5:18:11.2802 $\pm$ 0.0086	509	0.098 $\pm$ 0.007	0.13$\times$ 0.01 ; 68 $\pm$ 29	1544	05353811-0518113	7.48	3.47
05:35:38.62641 $\pm$ 0.0011	-5:20:40.6296 $\pm$ 0.0229	510	0.027 $\pm$ 0.004			05353862-0520405	6.14	2.18
05:35:39.01601 $\pm$ 0.0004	-5:21:01.7726 $\pm$ 0.0079	511	0.068 $\pm$ 0.005		1550	05353901-0521017	6.09	1.96
05:35:39.44309 $\pm$ 0.0011	-5:21:36.6132 $\pm$ 0.0421	512	0.018 $\pm$ 0.004				5.99	1.65
05:35:40.81032 $\pm$ 0.0003	-5:21:41.8302 $\pm$ 0.0058	513	0.104 $\pm$ 0.007		1561	05354081-0521418	6.29	1.91
05:35:41.70043 $\pm$ 0.0002	-5:20:14.8649 $\pm$ 0.0030	514	0.251 $\pm$ 0.014		1565	05354170-0520149	7.02	2.98
05:35:41.99864 $\pm$ 0.0018	-5:28:12.7096 $\pm$ 0.0385	515	0.05 $\pm$ 0.01	0.22$\times$ 0.15 ; 178$\pm$ 57	1568	05354197-0528128	7.98	4.61
05:35:42.28144 $\pm$ 0.0003	-5:15:59.1479 $\pm$ 0.0050	516	1.985 $\pm$ 0.113	0.34$\times$ 0.21 ; 59 $\pm$ 8		05354227-0515594	9.8	4.94
05:35:43.51319 $\pm$ 0.0008	-5:20:47.7067 $\pm$ 0.0222	517	0.035 $\pm$ 0.005		1579	05354351-0520477	7.21	2.95
05:35:44.86521 $\pm$ 0.0002	-5:23:07.4706 $\pm$ 0.0038	518	0.251 $\pm$ 0.014	0.13$\times$ 0.08 ; 16 $\pm$ 60			7.07	2.8
05:35:46.50727 $\pm$ 0.0008	-5:24:42.0877 $\pm$ 0.0237	519	0.042 $\pm$ 0.006				7.59	3.83
05:35:53.11730 $\pm$ 0.0007	-5:21:24.1136 $\pm$ 0.0099	520	0.181 $\pm$ 0.015	0.28$\times$ 0.05 ; 66 $\pm$ 14			9.34	4.91
05:35:54.46292 $\pm$ 0.0003	-5:24:36.8632 $\pm$ 0.0042	521	3.09 $\pm$ 0.169	0.32$\times$ 0.29 ; 104$\pm$ 51	1609		9.54	5.54

Appendix B: ALMA 3 mm catalogue of compact sources in the Orion-KL region

TABLE B.1: ALMA 3 mm catalogue: Source properties and variability measurements in the Orion-KL region.

α(2000) (h m s)	δ(2000) (° ′ ″)	ID	Peak Flux Density (mJy bm⁻¹)	Deconvolved Size θ$_{max}$ × θ$_{min}$; P.A. (arcsec² ; °)	1 h time resolution VF[a]	Timescale (h)	20 min time resolution VF[a]	Timescale (h)	COUP	F16[b]	V21[b]	O21[b]	Additional counterparts[c]
(1)	(2)	(3)	(4)	(5)	(6)	(7)	(8)	(9)	(10)	(11)	(12)	(13)	(14)
05:35:12.9031 ± 0.0067	-5:23:00.2701 ± 0.0028	1	0.554 ± 0.020		≤ 2		≤ 2					80	
05:35:13.0633 ± 0.0181	-5:21:53.2754 ± 0.0051	2	0.734 ± 0.037	0.53 × 0.08 ; 102 ± 2	≤ 2		4.9 ± 1	4.1	516			77	
05:35:13.1107 ± 0.0068	-5:22:47.1013 ± 0.0075	3	0.274 ± 0.015		≤ 2		3.0 ± 0.4	1.7	524	107	128		131-247
05:35:13.2887 ± 0.0054	-5:22:38.9703 ± 0.0028	4	0.703 ± 0.023		≤ 2		5.1 ± 0.9	1.7	539			13	
05:35:13.3331 ± 0.0361	-5:22:28.5864 ± 0.0113	5	0.195 ± 0.020		2.4 ↑	4.1	2.6 ± 0.5	169.6					
05:35:13.3655 ± 0.0112	-5:22:26.1496 ± 0.0035	6	0.296 ± 0.017		≤ 2		8.1 ± 1.6	3.1	538	117		36	
05:35:13.5207 ± 0.002	-5:22:19.5594 ± 0.0011	7	2.491 ± 0.027	0.13 × 0.11 ; 79 ± 80	≤ 2		≤ 2		551	127*	135	46	135-220
05:35:13.5242 ± 0.0085	-5:23:04.4708 ± 0.0061	8	0.405 ± 0.024		≤ 2		3.6 ± 0.5	0.4	552			107	HC360
05:35:13.5497 ± 0.0042	-5:22:43.618 ± 0.0027	9	0.624 ± 0.016		≤ 2		2.6 ↑	166.9				7	
05:35:13.6895 ± 0.0066	-5:22:56.2309 ± 0.007	10	0.175 ± 0.013		≤ 2		2.9 ± 0.6	3.1	563			1	
05:35:13.7027 ± 0.0068	-5:22:30.3492 ± 0.0034	11	0.482 ± 0.017		≤ 2		4.4 ± 0.8	169.9	574			29	
05:35:13.7428 ± 0.0031	-5:22:21.9904 ± 0.0017	12	0.955 ± 0.017		≤ 2		4.0 ± 0.5	171.0	573			41	137-222
05:35:13.7756 ± 0.0016	-5:22:17.399 ± 0.0008	13	2.095 ± 0.018	0.13 × 0.03 ; 123 ± 7	≤ 2		≤ 2		572	139		48	
05:35:13.8003 ± 0.0011	-5:22:07.0349 ± 0.0007	14	3.199 ± 0.022	0.12 × 0.04 ; 174 ± 7	≤ 2		≤ 2		579	142	142	59	138-207
05:35:13.8025 ± 0.0051	-5:21:59.6729 ± 0.0028	15	0.802 ± 0.026		≤ 2		3.1 ± 0.3	123.0		140		78	
05:35:13.8032 ± 0.0019	-5:22:02.8587 ± 0.0011	16	2.583 ± 0.030		≤ 2		≤ 2		578			62	
05:35:13.8694 ± 0.0081	-5:23:06.714 ± 0.0039	17	0.345 ± 0.014	0.23 × 0.05 ; 61 ± 12	≤ 2		2.9 ± 0.5	124.3				106	
05:35:13.9099 ± 0.0066	-5:22:35.632 ± 0.0032	18	0.546 ± 0.020		≤ 2		4.3 ± 0.9	119.9	591			16	
05:35:13.9597 ± 0.0249	-5:22:42.8081 ± 0.0186	19	0.263 ± 0.021	0.61 × 0.12 ; 50 ± 5	≤ 2		4.2 ± 0.7	120.6					
05:35:13.9611 ± 0.0135	-5:22:31.9325 ± 0.0073	20	0.479 ± 0.036		2.7 ± 0.5	170.3	4.7 ± 0.7	167.9	590			23	
05:35:13.9733 ± 0.0137	-5:22:15.7734 ± 0.0094	21	0.196 ± 0.025		≤ 2		4.5 ± 0.9	3.1					
05:35:14.0330 ± 0.0064	-5:23:00.3572 ± 0.0038	22	0.594 ± 0.026		2.3 ± 0.2	1.4	3.1 ± 0.5	47.3				81	
05:35:14.0600 ± 0.0195	-5:22:05.6447 ± 0.0094	23	0.268 ± 0.028	0.12 × 0.05 ; 70 ± 37	2.5 ↑	123.0	2.4 ± 0.2	48.3				60	
05:35:14.0820 ± 0.0167	-5:22:18.5331 ± 0.0074	24	0.259 ± 0.028		≤ 2		2.1 ↑	123.0					
05:35:14.1055 ± 0.0005	-5:22:22.6444 ± 0.0002	25	70.991 ± 0.183	0.07 × 0.03 ; 9 ± 9	≤ 2		≤ 2		599	162	156	39	source BN

[a] VF in columns (6) and (8) report values above the systematic threshold discussed in Section 3.3. VF reported as ≤ 2 indicate sources that are either constant or with variability below the systematic threshold. For lower limits an upper arrow symbol is indicated instead of uncertainty values.

[b] Source identifications for counterparts in: F16 (Forbrich et al., 2016), V21 (Vargas-González et al., 2021), and O21 (Otter et al., 2021). Source from Forbrich et al. (2016) reported as nonthermal centimeter counterpart in the VLBA follow-up (Forbrich et al., 2021) are marked with an asterisk symbol in column (11).

[c] Additional counterparts associated with known circumstellar disks: Ricci et al. (2008); Eisner et al. (2016, 2018); Vicente and Alves (2005) Hillenbrand and Carpenter (2000).

TABLE B.1: Continued.

				Deconvolved Size	1 h time resolution		20 min time resolution						
$\alpha(2000)$ (h m s)	$\delta(2000)$ (° ′ ″)	ID	Peak Flux Density (mJy bm^{-1})	$\theta_{\max} \times \theta_{\min}$; P.A. (arcsec^2 ; °)	VF[a]	Timescale (h)	VF[a]	Timescale (h)	COUP	F16[b]	V21[b]	O21[b]	Additional counterpats[c]
(1)	(2)	(3)	(4)	(5)	(6)	(7)	(8)	(9)	(10)	(11)	(12)	(13)	(14)
05:35:14.1080 ± 0.0261	-5:22:26.9292 ± 0.0134	26	1.719 ± 0.106		≤ 2		2.3 ± 0.1	49.0					
05:35:14.1242 ± 0.0096	-5:22:31.6324 ± 0.0042	27	1.814 ± 0.067	0.37 × 0.10 ; 68 ± 5	≤ 2		≤ 2						
05:35:14.1319 ± 0.0281	-5:22:25.8623 ± 0.0268	28	0.535 ± 0.048	0.75 × 0.17 ; 43 ± 4	≤ 2		3.7 ± 0.7	2.7					
05:35:14.1642 ± 0.0135	-5:22:11.2622 ± 0.0142	29	0.142 ± 0.021		≤ 2		6.5 ± 1.2	167.2					
05:35:14.1656 ± 0.0052	-5:23:01.2915 ± 0.0225	30	1.318 ± 0.046	1.23 × 0.16 ; 174 ± 1	≤ 2		≤ 2			166	159		142-301
05:35:14.1678 ± 0.008	-5:22:27.3331 ± 0.008	31	1.816 ± 0.082	0.34 × 0.22 ; 168 ± 21	≤ 2		2.2 ± 0.1	45.6					
05:35:14.1740 ± 0.0077	-5:22:17.7767 ± 0.0096	32	0.221 ± 0.021		≤ 2		2.9 ± 0.3	123.0					
05:35:14.1767 ± 0.0066	-5:22:10.5702 ± 0.0145	33	0.206 ± 0.013		≤ 2		≤ 2						
05:35:14.1835 ± 0.0096	-5:22:08.872 ± 0.0355	34	0.123 ± 0.019		≤ 2		2.8 ± 0.6	166.2					
05:35:14.1922 ± 0.0533	-5:22:25.0681 ± 0.0394	35	0.214 ± 0.031	0.78 × 0.16 ; 52 ± 7	3.1 ± 0.7	170.3	3.4 ± 0.8	4.1					
05:35:14.1934 ± 0.0119	-5:22:26.0864 ± 0.0132	36	0.830 ± 0.043	0.58 × 0.18 ; 145 ± 4	≤ 2		≤ 2						
05:35:14.1964 ± 0.0152	-5:22:34.1877 ± 0.0053	37	2.075 ± 0.081	0.68 × 0.26 ; 99 ± 2	≤ 2		≤ 2						
05:35:14.1973 ± 0.0066	-5:22:36.6957 ± 0.015	38	0.978 ± 0.047		≤ 2		3.2 ± 0.4	45.6					
05:35:14.2563 ± 0.0018	-5:22:28.0589 ± 0.001	39	3.952 ± 0.042		≤ 2		≤ 2					34	
05:35:14.2565 ± 0.0163	-5:22:25.4689 ± 0.0219	40	0.430 ± 0.036	0.54 × 0.11 ; 27 ± 6	≤ 2		≤ 2						
05:35:14.2726 ± 0.0069	-5:22:27.1866 ± 0.0065	41	0.498 ± 0.026		≤ 2		3.5 ± 0.6	171.3				35	
05:35:14.2756 ± 0.0102	-5:22:09.027 ± 0.0442	42	0.166 ± 0.020		≤ 2		≤ 2						
05:35:14.2775 ± 0.0127	-5:22:32.3286 ± 0.0115	43	0.953 ± 0.046	0.59 × 0.31 ; 43 ± 6	≤ 2		2.9 ± 0.5	167.9					
05:35:14.2915 ± 0.0107	-5:22:30.6887 ± 0.0181	44	1.191 ± 0.059	0.72 × 0.06 ; 25 ± 2	≤ 2		3.1 ± 0.2	169.6					
05:35:14.2926 ± 0.0011	-5:23:04.2034 ± 0.0006	45	2.892 ± 0.018	0.11 × 0.06 ; 136 ± 9	≤ 2		≤ 2		614			82	HC361
05:35:14.3070 ± 0.0081	-5:22:36.6826 ± 0.0055	46	1.484 ± 0.057	0.32 × 0.22 ; 128 ± 16	≤ 2		3.4 ± 0.3	170.3		170			
05:35:14.3115 ± 0.0115	-5:22:24.3307 ± 0.0089	47	0.485 ± 0.034		3.8 ± 0.7	1.3	3.5 ± 0.7	0.7					
05:35:14.3119 ± 0.0008	-5:22:42.0101 ± 0.0004	48	5.584 ± 0.024	0.08 × 0.02 ; 163 ± 9	≤ 2		≤ 2					9	
05:35:14.3138 ± 0.0634	-5:23:08.3116 ± 0.0081	49	0.259 ± 0.036		≤ 2		2.5 ± 0.4	47.7	624			85	HC345
05:35:14.3545 ± 0.014	-5:22:40.3893 ± 0.0055	50	0.695 ± 0.048		≤ 2		2.9 ± 0.5	171.2				10	

TABLE B.1: Continued.

α(2000) (ʰᵐˢ)	δ(2000) (°′″)	ID	Peak Flux Density (mJy bm⁻¹)	Deconvolved Size $\theta_{\max} \times \theta_{\min}$; P.A. (arcsec² ; °)	1 h time resolution VF[a]	Timescale (h)	20 min time resolution VF[a]	Timescale (h)	COUP	F16[b]	V21[b]	O21[b]	Additional counterpats[c]
(1)	(2)	(3)	(4)	(5)	(6)	(7)	(8)	(9)	(10)	(11)	(12)	(13)	(14)
05:35:14.3589 ± 0.006	-5:22:32.7333 ± 0.0043	51	1.176 ± 0.050		≤ 2		≤ 2		621	178	168	21	
05:35:14.3664 ± 0.0024	-5:22:54.056 ± 0.0012	52	1.606 ± 0.021	0.11 × 0.03 ; 48± 16	≤ 2		≤ 2		623			3	HC399
05:35:14.3993 ± 0.0041	-5:22:30.4126 ± 0.0018	53	2.746 ± 0.063		≤ 2		≤ 2		628	180		28	
05:35:14.4142 ± 0.0092	-5:22:20.7929 ± 0.0103	54	0.456 ± 0.036		2.6 ± 0.4	47.3	6.2 ± 1.2	2.3					
05:35:14.4219 ± 0.014	-5:22:28.3925 ± 0.0053	55	0.744 ± 0.039	0.37 × 0.16 ; 91± 5	≤ 2		4.8 ± 0.4	172.0				64	
05:35:14.4291 ± 0.0054	-5:22:33.5108 ± 0.0033	56	4.019 ± 0.102	0.31 × 0.15 ; 125± 7	≤ 2		≤ 2					18	
05:35:14.4389 ± 0.0103	-5:22:26.9933 ± 0.0086	57	0.791 ± 0.036	0.45 × 0.17 ; 136± 6	2.3 ± 0.2	123	5.3 ± 0.9	1.4					
05:35:14.4633 ± 0.0106	-5:23:09.5972 ± 0.0082	58	0.296 ± 0.017		≤ 2		4.2 ± 0.7	45.6					
05:35:14.4773 ± 0.0127	-5:22:32.1249 ± 0.0153	59	2.050 ± 0.125	0.54 × 0.30 ; 156± 9	≤ 2		≤ 2						
05:35:14.5010 ± 0.0121	-5:22:38.6743 ± 0.0083	60	0.392 ± 0.032		2.9 ↑	48.7	6.7 ± 1.3	168.2	639	184	172	14	
05:35:14.5174 ± 0.0007	-5:22:30.6221 ± 0.0004	61	46.475 ± 0.190	0.16 × 0.02 ; 146± 2	≤ 2		≤ 2			185	173	26	
05:35:14.5269 ± 0.0172	-5:22:31.7713 ± 0.0263	62	1.157 ± 0.159		≤ 2		≤ 2						
05:35:14.5351 ± 0.0174	-5:23:03.609 ± 0.0076	63	0.340 ± 0.029		3.2 ± 0.6	173.0	≤ 2					83	HC364
05:35:14.5395 ± 0.0066	-5:22:27.153 ± 0.0081	64	1.071 ± 0.032	0.57 × 0.38 ; 165± 6	≤ 2		4.2 ± 0.6	169.6					
05:35:14.5495 ± 0.0319	-5:22:32.433 ± 0.0107	65	1.104 ± 0.192		≤ 2		≤ 2						
05:35:14.5715 ± 0.0143	-5:22:30.4249 ± 0.0393	66	1.944 ± 0.274		≤ 2		≤ 2						
05:35:14.5766 ± 0.0118	-5:22:31.288 ± 0.007	67	3.618 ± 0.214	0.26 × 0.09 ; 51± 18	≤ 2		≤ 2			191	176	24	
05:35:14.5839 ± 0.0094	-5:22:30.8851 ± 0.0086	68	4.217 ± 0.213	0.33 × 0.24 ; 162± 33	≤ 2		≤ 2						
05:35:14.5898 ± 0.0328	-5:22:29.431 ± 0.0163	69	2.301 ± 0.176	0.75 × 0.11 ; 117± 3	≤ 2		2.7 ± 0.5	124.7					
05:35:14.6189 ± 0.0157	-5:22:28.7245 ± 0.0066	70	1.876 ± 0.083	0.64 × 0.30 ; 99± 3	≤ 2		3.4 ± 0.6	172.3					
05:35:14.6253 ± 0.0122	-5:22:18.2723 ± 0.0099	71	0.377 ± 0.021	0.41 × 0.25 ; 43± 15	≤ 2		6.7 ± 0.9	123.0					
05:35:14.6580 ± 0.001	-5:22:38.4977 ± 0.0004	72	3.594 ± 0.018	0.17 × 0.02 ; 105± 2	≤ 2		≤ 2			200		15	HC756/7
05:35:14.6589 ± 0.0128	-5:22:10.4433 ± 0.0064	73	0.373 ± 0.029		≤ 2		3.7 ± 0.7	2.7				56	
05:35:14.6621 ± 0.0097	-5:22:11.277 ± 0.0164	74	0.241 ± 0.022		4.1 ↑	2.7	21.2± 4	0.4	647	198	180		
05:35:14.6908 ± 0.0307	-5:22:10.9992 ± 0.0057	75	0.346 ± 0.033		≤ 2		≤ 2			201		53	

TABLE B.1: Continued.

				Deconvolved Size	1 h time resolution		20 min time resolution						
α(2000) ($^{\mathrm{h\,m\,s}}$)	δ(2000) ($^{\circ\,\prime\,\prime\prime}$)	ID	Peak Flux Density (mJy bm^{-1})	$\theta_{\max} \times \theta_{\min}$; P.A. (arcsec^2 ; $^\circ$)	VF[a]	Timescale (h)	VF[a]	Timescale (h)	COUP	F16[b]	V21[b]	O21[b]	Additional counterpats[c]
(1)	(2)	(3)	(4)	(5)	(6)	(7)	(8)	(9)	(10)	(11)	(12)	(13)	(14)
05:35:14.6977 ± 0.002	-5:22:49.4271 ± 0.0009	76	1.276 ± 0.014		≤ 2		≤ 2		657			4	HC411
05:35:14.7444 ± 0.0081	-5:22:22.4051 ± 0.0032	77	0.644 ± 0.017	0.43 × 0.05 ; 111± 2	2.5 ± 0.3	2.7	3.2 ± 0.3	172.0					
05:35:14.7641 ± 0.0169	-5:22:38.0788 ± 0.0091	78	0.243 ± 0.019		2.6 ± 0.5	45.9	3.6 ± 0.7	167.2	656			69	
05:35:14.8019 ± 0.0137	-5:22:10.8722 ± 0.013	79	0.376 ± 0.027	0.37 × 0.24 ; 156± 28	≤ 2		3.4 ± 0.7	170.3					
05:35:14.8034 ± 0.0013	-5:22:30.687 ± 0.0007	80	7.825 ± 0.056	0.09 × 0.03 ; 140± 14	≤ 2		≤ 2			206		27	
05:35:14.8064 ± 0.0165	-5:23:04.7366 ± 0.0057	81	0.339 ± 0.020	0.38 × 0.07 ; 105± 6	≤ 2		2.7 ± 0.5	2.0		207	184		
05:35:14.8384 ± 0.0012	-5:22:14.8507 ± 0.0006	82	3.324 ± 0.022	0.10 × 0.06 ; 74± 14	≤ 2		≤ 2			208		51	
05:35:14.8552 ± 0.0011	-5:22:44.1362 ± 0.0006	83	2.578 ± 0.015		≤ 2		≤ 2					6	HC771
05:35:14.8760 ± 0.0046	-5:23:05.072 ± 0.0032	84	0.506 ± 0.015		≤ 2		2.5 ± 0.4	170.6	664			84	HC714
05:35:14.8771 ± 0.001	-5:22:32.7857 ± 0.0005	85	2.680 ± 0.015	0.11 × 0.05 ; 61± 7	≤ 2		≤ 2					20	
05:35:14.8988 ± 0.0037	-5:22:25.4168 ± 0.0017	86	1.454 ± 0.030		4.1 ± 0.3	170.2	10.0± 0.7	171.0	662	211	186	37	
05:35:14.9173 ± 0.0041	-5:22:39.2064 ± 0.0034	87	0.484 ± 0.015		5.3 ↑	120.2	10.0± 1.9	120.6	670	212	187		
05:35:14.9452 ± 0.0026	-5:22:20.712 ± 0.0015	88	1.411 ± 0.022		≤ 2		2.5 ± 0.2	173.0				44	
05:35:14.9740 ± 0.0016	-5:22:29.1649 ± 0.0008	89	3.132 ± 0.027	0.11 × 0.06 ; 124± 14	≤ 2		≤ 2					32	
05:35:14.9916 ± 0.0181	-5:22:19.4644 ± 0.0168	90	0.191 ± 0.022	0.25 × 0.09 ; 10± 60	≤ 2		3.0 ± 0.5	119.9					
05:35:14.9965 ± 0.0011	-5:22:39.5676 ± 0.0006	91	4.215 ± 0.027		≤ 2		≤ 2					12	
05:35:15.0043 ± 0.0041	-5:21:59.1175 ± 0.0021	92	1.324 ± 0.031	0.06 × 0.04 ; 175± 78	≤ 2		≤ 2		669		190	72	
05:35:15.0061 ± 0.0103	-5:22:09.1992 ± 0.0084	93	0.260 ± 0.014		4.0 ± 0.9	1.4	4.1 ± 0.7	168.5					
05:35:15.0283 ± 0.016	-5:22:31.1197 ± 0.0072	94	0.364 ± 0.035		2.7 ± 0.4	2.7	3.4 ± 0.6	2.7		216	191	65	150-231
05:35:15.1622 ± 0.0016	-5:22:17.3881 ± 0.0008	95	2.836 ± 0.025	0.06 × 0.01 ; 61± 38	≤ 2		≤ 2		680	219		49	
05:35:15.1804 ± 0.0008	-5:22:29.6564 ± 0.0004	96	3.135 ± 0.015	0.08 × 0.01 ; 157± 10	≤ 2		≤ 2		681			31	
05:35:15.2666 ± 0.0038	-5:21:55.6694 ± 0.0017	97	1.518 ± 0.029		≤ 2		≤ 2		687			73	
05:35:15.2826 ± 0.0018	-5:22:16.849 ± 0.001	98	1.521 ± 0.016		≤ 2		≤ 2					50	
05:35:15.3129 ± 0.0029	-5:22:04.7802 ± 0.0019	99	5.950 ± 0.096	0.20 × 0.15 ; 41± 16	≤ 2		≤ 2			224		61	
05:35:15.3770 ± 0.0139	-5:22:25.3742 ± 0.0048	100	0.323 ± 0.019	0.25 × 0.01 ; 89± 11	≤ 2		3.5 ± 0.6	1.7	699	231	203		

TABLE B.1: Continued.

$\alpha(2000)$ ($^{\mathrm{h\,m\,s}}$)	$\delta(2000)$ ($^{\circ\,\prime\,\prime\prime}$)	ID	Peak Flux Density (mJy bm^{-1})	Deconvolved Size $\theta_{\max} \times \theta_{\min}$; P.A. (arcsec^2 ; $^\circ$)	1 h time resolution VF[a]	Timescale (h)	20 min time resolution VF[a]	Timescale (h)	COUP	F16[b]	V21[b]	O21[b]	Additional counterpats[c]
(1)	(2)	(3)	(4)	(5)	(6)	(7)	(8)	(9)	(10)	(11)	(12)	(13)	(14)
05:35:15.3945 ± 0.0119	-5:22:39.8713 ± 0.0054	101	0.887 ± 0.048	0.26 × 0.12 ; 75± 18	≤ 2		3.1 ± 0.6	167.2		233	204	11	154-240
05:35:15.5009 ± 0.0217	-5:22:34.834 ± 0.0124	102	0.153 ± 0.014	0.37 × 0.18 ; 119± 22	≤ 2		3.9 ± 0.6	167.6					
05:35:15.5602 ± 0.0317	-5:22:35.2513 ± 0.0131	103	0.124 ± 0.018		≤ 2		≤ 2						
05:35:15.5789 ± 0.0017	-5:22:18.5825 ± 0.0008	104	0.932 ± 0.008	0.12 × 0.08 ; 75± 14	≤ 2		2.7 ↑	171.6	715			47	
05:35:15.6392 ± 0.0111	-5:22:56.4422 ± 0.0049	105	0.294 ± 0.018		≤ 2		3.6 ± 0.6	170.3	724	244	216	127	HC389
05:35:15.7632 ± 0.0075	-5:22:32.4123 ± 0.0048	106	0.272 ± 0.013		≤ 2		3.0 ± 0.5	167.9				22	
05:35:15.7712 ± 0.0105	-5:23:09.8898 ± 0.0077	107	0.596 ± 0.044		≤ 2		3.9 ± 0.8	0.4	732	250	224		
05:35:15.8795 ± 0.0051	-5:23:01.9503 ± 0.0029	108	0.961 ± 0.030		≤ 2		2.6 ± 0.2	4.1	743	259	230	87	HC370
05:35:15.8865 ± 0.0127	-5:22:33.1881 ± 0.005	109	0.232 ± 0.016		≤ 2		3.7 ± 0.8	0.4	741			19	HC447
05:35:15.9419 ± 0.0028	-5:22:21.0764 ± 0.0017	110	0.608 ± 0.011		≤ 2		3.6 ± 0.6	2.4	756	263	233	43	159-221
05:35:15.9778 ± 0.0048	-5:22:00.527 ± 0.0029	111	0.475 ± 0.016		2.6 ± 0.4	2.7	3.5 ± 0.6	48.7	755			74	
05:35:16.0467 ± 0.0158	-5:22:10.6157 ± 0.006	112	0.206 ± 0.017		≤ 2		2.6 ± 0.4	173.3				54	
05:35:16.0686 ± 0.0031	-5:22:00.2536 ± 0.0016	113	2.484 ± 0.042		≤ 2		≤ 2					75	
05:35:16.0742 ± 0.0029	-5:23:07.1125 ± 0.0045	114	3.707 ± 0.074	0.42 × 0.08 ; 169± 2	≤ 2		≤ 2		766	272	241	88	161-307
05:35:16.1190 ± 0.0227	-5:22:12.5161 ± 0.0046	115	0.175 ± 0.015		≤ 2		≤ 2		775	280	246		
05:35:16.1428 ± 0.0185	-5:22:55.2909 ± 0.0113	116	0.267 ± 0.027		≤ 2		≤ 2		777			93	HC393
05:35:16.1696 ± 0.0256	-5:22:11.192 ± 0.0056	117	0.288 ± 0.028		2.3 ↑	168.9	2.9 ± 0.7	3.1				52	
05:35:16.2784 ± 0.0105	-5:22:10.4753 ± 0.0049	118	0.378 ± 0.023		2.2 ↑	168.9	≤ 2		784			55	163-210
05:35:16.3024 ± 0.0144	-5:22:10.3078 ± 0.0077	119	0.297 ± 0.020		≤ 2		≤ 2			291	254	57	
05:35:16.3122 ± 0.0049	-5:22:21.5149 ± 0.0019	120	0.542 ± 0.012		≤ 2		2.6 ± 0.3	173.0	799	294	255	42	163-222
05:35:16.3421 ± 0.0054	-5:22:49.0894 ± 0.0029	121	0.741 ± 0.021	0.20 × 0.11 ; 121± 16	≤ 2		≤ 2		800	296	258	5	163-249
05:35:16.3736 ± 0.032	-5:22:22.31 ± 0.0054	122	0.167 ± 0.018		≤ 2		3.7 ± 0.8	0.4				122	
05:35:16.3893 ± 0.0354	-5:22:10.408 ± 0.0205	123	0.126 ± 0.020		≤ 2		3.0 ± 0.6	166.2					
05:35:16.4000 ± 0.0073	-5:22:35.3044 ± 0.0034	124	0.602 ± 0.023		≤ 2		3.3 ± 0.6	172.0		301	260	17	
05:35:16.4186 ± 0.0079	-5:22:12.1306 ± 0.0029	125	0.496 ± 0.019		≤ 2		2.8 ± 0.5	3.3	806	303	261	101	

TABLE B.1: Continued.

				Deconvolved Size	1 h time resolution		20 min time resolution						
α(2000) (h m s)	δ(2000) (° ′ ″)	ID	Peak Flux Density (mJy bm^{-1})	$\theta_{max} \times \theta_{min}$; P.A. (arcsec^2 ; °)	VF[a]	Timescale (h)	VF[a]	Timescale (h)	COUP	F16[b]	V21[b]	O21[b]	Additional counterpats[c]
(1)	(2)	(3)	(4)	(5)	(6)	(7)	(8)	(9)	(10)	(11)	(12)	(13)	(14)
05:35:16.4813 ± 0.0117	-5:22:35.4552 ± 0.006	126	0.270 ± 0.013	0.38 × 0.16 ; 64± 7	≤ 2		3.8 ± 0.7	4.1	807	306	262		
05:35:16.5922 ± 0.0108	-5:22:50.3664 ± 0.0045	127	0.379 ± 0.021		≤ 2		4.3 ± 0.7	45.2		311	265	95	166-250
05:35:16.7374 ± 0.0056	-5:22:31.2518 ± 0.0023	128	0.486 ± 0.014		≤ 2		2.5 ± 0.4	0.7	825			108	167-231
05:35:16.8670 ± 0.0058	-5:22:33.9816 ± 0.0031	129	0.750 ± 0.024		≤ 2		2.8 ± 0.4	173.3		323	275	100	
05:35:16.8979 ± 0.0213	-5:22:27.0950 ± 0.0106	130	0.130 ± 0.016		≤ 2		≤ 2						
05:35:16.9046 ± 0.0146	-5:22:55.0208 ± 0.0064	131	0.428 ± 0.035		3.0 ± 0.6	47.3	3.6 ± 0.6	0.7				94	HC397
05:35:16.9711 ± 0.004	-5:22:48.561 ± 0.0027	132	2.123 ± 0.042	0.28 × 0.23 ; 56± 16	≤ 2		≤ 2		844	330	280	96	170-249
05:35:17.3538 ± 0.0061	-5:22:35.7777 ± 0.0045	133	2.475 ± 0.076	0.30 × 0.23 ; 43± 18	≤ 2		2.6 ± 0.5	3.5	876	347	293	99	173-236

Bibliography

Abreu-Vicente, J., Ragan, S., Kainulainen, J., et al., 2016. Giant molecular filaments in the Milky Way. II. The fourth Galactic quadrant. *A&A*, 590:A131.

Adams, W.S. and Pease, F.G., 1915. The Spectrum of T Tauri. *PASP*, 27(159):133.

Alencar, S.H.P., Teixeira, P.S., Guimarães, M.M., et al., 2010. Accretion dynamics and disk evolution in NGC 2264: a study based on CoRoT photometric observations. *A&A*, 519:A88.

Allen, D.A. and Burton, M.G., 1993. Explosive ejection of matter associated with star formation in the Orion nebula. *Nature*, 363(6424):54.

ALMA Partnership, Brogan, C.L., Pérez, L.M., et al., 2015. The 2014 ALMA Long Baseline Campaign: First Results from High Angular Resolution Observations toward the HL Tau Region. *ApJ*, 808(1):L3.

Andre, P., 1996. Radio Emission as a Probe of Large-Scale Magnetic Structures Around Young Stellar Objects. In A.R. Taylor and J.M. Paredes, editors, *Radio Emission from the Stars and the Sun*, volume 93 of *Astronomical Society of the Pacific Conference Series*, pages 273–284.

André, P., Di Francesco, J., Ward-Thompson, D., et al., 2014. From Filamentary Networks to Dense Cores in Molecular Clouds: Toward a New Paradigm for Star Formation. In H. Beuther, R.S. Klessen, C.P. Dullemond, and T. Henning, editors, *Protostars and Planets VI*, page 27.

Andre, P., Phillips, R.B., Lestrade, J.F., et al., 1991. Direct VLBI Detection of the Magnetosphere Surrounding the Young Star S1 in rho Ophiuchi. *ApJ*, 376:630.

Andre, P., Ward-Thompson, D., and Barsony, M., 1993. Submillimeter Continuum Observations of rho Ophiuchi A: The Candidate Protostar VLA 1623 and Prestellar Clumps. *ApJ*, 406:122.

Andrews, S.M., Huang, J., Pérez, L.M., et al., 2018. The Disk Substructures at High Angular Resolution Project (DSHARP). I. Motivation, Sample, Calibration, and Overview. *ApJ*, 869(2):L41.

Anglada, G., 1996. Radio Jets in Young Stellar Objects. In A.R. Taylor and J.M. Paredes, editors, *Radio Emission from the Stars and the Sun*, volume 93 of *Astronomical Society of the Pacific Conference Series*, pages 3–14.

Anglada, G., Rodríguez, L.F., and Carrasco-González, C., 2018. Radio jets from young stellar objects. *A&ARv*, 26(1):3.

Ballesteros-Paredes, J., André, P., Hennebelle, P., et al., 2020. From Diffuse Gas to Dense Molecular Cloud Cores. *Space Sci. Rev.*, 216(5):76.

Ballesteros-Paredes, J., Klessen, R.S., Mac Low, M.M., et al., 2007. Molecular Cloud Turbulence and Star Formation. In B. Reipurth, D. Jewitt, and K. Keil, editors, *Protostars and Planets V*, page 63.

Bally, J., 2016. Protostellar Outflows. *Annual Review of Astronomy and Astrophysics*, 54:491.

Bally, J., Cunningham, N.J., Moeckel, N., et al., 2011. Explosive Outflows Powered by the Decay of Non-hierarchical Multiple Systems of Massive Stars: Orion BN/KL. *ApJ*, 727(2):113.

Bally, J., Ginsburg, A., Arce, H., et al., 2017. The ALMA View of the OMC1 Explosion in Orion. *ApJ*, 837(1):60.

Bally, J., Ginsburg, A., Forbrich, J., et al., 2020. The Orion Protostellar Explosion and Runaway Stars Revisited: Stellar Masses, Disk Retention, and an Outflow from the BecklinNeugebauer Object. *ApJ*, 889(2):178.

Bally, J., Ginsburg, A., Silvia, D., et al., 2015. The Orion fingers: Near-IR adaptive optics imaging of an explosive protostellar outflow. *A&A*, 579:A130.

Bally, J., Sutherland, R.S., Devine, D., et al., 1998. Externally Illuminated Young Stellar Environments in the Orion Nebula: Hubble Space Telescope Planetary Camera and Ultraviolet Observations. *AJ*, 116(1):293.

Bally, J. and Zinnecker, H., 2005. The Birth of High-Mass Stars: Accretion and/or Mergers? *AJ*, 129(5):2281.

Becklin, E.E. and Neugebauer, G., 1967. Observations of an Infrared Star in the Orion Nebula. *ApJ*, 147:799.

Beltrán, M.T. and de Wit, W.J., 2016. Accretion disks in luminous young stellar objects. *A&ARv*, 24:6.

Benz, A.O., 2008. Flare Observations. *Living Reviews in Solar Physics*, 5(1):1.

Beuther, H., Sridharan, T.K., and Saito, M., 2005. Caught in the Act: The Onset of Massive Star Formation. *ApJ*, 634(2):L185.

Blitz, L., 1993. Giant Molecular Clouds. In E.H. Levy and J.I. Lunine, editors, *Protostars and Planets III*, page 125.

Blitz, L. and Williams, J.P., 1999. Molecular Clouds (a review). *arXiv e-prints*, astro-ph/9903382.

Bower, G.C., Plambeck, R.L., Bolatto, A., et al., 2003. A Giant Outburst at Millimeter Wavelengths in the Orion Nebula. *ApJ*, 598:1140.

Bridle, A.H. and Schwab, F.R., 1999. Bandwidth and Time-Average Smearing. In G.B. Taylor, C.L. Carilli, and R.A. Perley, editors, *Synthesis Imaging in Radio Astronomy II*, volume 180 of *Astronomical Society of the Pacific Conference Series*, page 371.

Cánovas, H., Cantero, C., Cieza, L., et al., 2019. Census of ρ Ophiuchi candidate members from Gaia Data Release 2. *A&A*, 626:A80.

Chandler, C.J., Brogan, C.L., Shirley, Y.L., et al., 2005. IRAS 16293-2422: Proper Motions, Jet Precession, the Hot Core, and the Unambiguous Detection of Infall. *ApJ*, 632(1):371.

Chen, H., Myers, P.C., Ladd, E.F., et al., 1995. Bolometric Temperature and Young Stars in the Taurus and Ophiuchus Complexes. *ApJ*, 445:377.

Churchwell, E., 1990. Ultracompact HII regions: the impact of newly formed massive stars on their environment. *A&ARv*, 2(2):79.

Churchwell, E., 2002. Ultra-Compact HII Regions and Massive Star Formation. *Annual Review of Astronomy and Astrophysics*, 40:27.

Churchwell, E., Felli, M., Wood, D.O.S., et al., 1987. Solar system-sized condensations in the Orion Nebula. *ApJ*, 321:516.

Cody, A.M., Stauffer, J., Baglin, A., et al., 2014. CSI 2264: Simultaneous Optical and Infrared Light Curves of Young Disk-bearing Stars in NGC 2264 with CoRoT and Spitzer—Evidence for Multiple Origins of Variability. *AJ*, 147(4):82.

Cohen, M., 1973. Infra-red observations of young stars - I. Stars in young clusters. *MNRAS*, 161:85.

Concha-Ramírez, F., Wilhelm, M.J.C., Portegies Zwart, S., et al., 2020. Effects of stellar density on the photoevaporation of circumstellar discs. *MNRAS*.

Condon, J.J., 1992. Radio emission from normal galaxies. *Annual Review of Astronomy and Astrophysics*, 30:575.

Condon, J.J. and Ransom, S.M., 2016. *Essential Radio Astronomy*.

Cornwell, T., Braun, R., and Briggs, D.S., 1999. Deconvolution. In G.B. Taylor, C.L. Carilli, and R.A. Perley, editors, *Synthesis Imaging in Radio Astronomy II*, volume 180 of *Astronomical Society of the Pacific Conference Series*, page 151.

Cotton, W.D., 1993. Calibration and Imaging OG Polarization Sensitive Very Long Baseline Interferometer Observations. *AJ*, 106:1241.

Da Rio, N., Robberto, M., Hillenbrand, L.A., et al., 2012. The Initial Mass Function of the Orion Nebula Cluster across the H-burning Limit. *ApJ*, 748(1):14.

Dalton, G.B., Caldwell, M., Ward, A.K., et al., 2006. The VISTA infrared camera. In I.S. McLean and M. Iye, editors, *Society of Photo-Optical Instrumentation Engineers (SPIE) Conference Series*, volume 6269 of *Society of Photo-Optical Instrumentation Engineers (SPIE) Conference Series*, page 62690X.

de Laplace, P.S., 1796. *Exposition du système du monde*.

Deller, A.T., Brisken, W.F., Phillips, C.J., et al., 2011. DiFX-2: A More Flexible, Efficient, Robust, and Powerful Software Correlator. *PASP*, 123(901):275.

Deller, A.T., Tingay, S.J., Bailes, M., et al., 2007. DiFX: A Software Correlator for Very Long Baseline Interferometry Using Multiprocessor Computing Environments. *PASP*, 119(853):318.

Devine, D., Grady, C.A., Kimble, R.A., et al., 2000. A Lyα Bright Jet from a Herbig AE Star. *ApJ*, 542(2):L115.

Dewdney, P.E., Hall, P.J., Schilizzi, R.T., et al., 2009. The Square Kilometre Array. *IEEE Proceedings*, 97(8):1482.

Di Francesco, J., Johnstone, D., Kirk, H., et al., 2008. The SCUBA Legacy Catalogues: Submillimeter-Continuum Objects Detected by SCUBA. *ApJ*, 175:277.

Dulk, G.A., 1985. Radio emission from the sun and stars. *Annual Review of Astronomy and Astrophysics*, 23:169.

Dunham, M.M., Allen, L.E., Evans, Neal J., I., et al., 2015. Young Stellar Objects in the Gould Belt. *ApJ*, 220(1):11.

Dzib, S.A., Forbrich, J., Reid, M.J., et al., 2021. A VLBA Survey of Radio Stars in the Orion Nebula Cluster. II. Astrometry. *ApJ*, 906(1):24.

Dzib, S.A., Loinard, L., Rodríguez, L.F., et al., 2017. Radio Measurements of the Stellar Proper Motions in the Core of the Orion Nebula Cluster. *ApJ*, 834(2):139.

Egan, M.P., Shipman, R.F., Price, S.D., et al., 1998. A Population of Cold Cores in the Galactic Plane. *ApJ*, 494(2):L199.

Eisner, J.A., Arce, H.G., Ballering, N.P., et al., 2018. Protoplanetary Disk Properties in the Orion Nebula Cluster: Initial Results from Deep, High-resolution ALMA Observations. *ApJ*, 860(1):77.

Eisner, J.A., Bally, J.M., Ginsburg, A., et al., 2016. Protoplanetary Disks in the Orion OMC1 Region Imaged with ALMA. *ApJ*, 826(1):16.

Elmegreen, B.G., 1998. Observations and Theory of Dynamical Triggers for Star Formation. In C.E. Woodward, J.M. Shull, and J. Thronson Harley A., editors, *Origins*, volume 148 of *Astronomical Society of the Pacific Conference Series*, page 150.

Emerson, J., McPherson, A., and Sutherland, W., 2006. Visible and Infrared Survey Telescope for Astronomy: Progress Report. *The Messenger*, 126:41.

Encalada, F.J., Looney, L.W., Tobin, J.J., et al., 2021. 870 μm Dust Continuum of the Youngest Protostars in Ophiuchus. *ApJ*, 913(2):149.

Evans, Neal J., I., Dunham, M.M., Jørgensen, J.K., et al., 2009. The Spitzer c2d Legacy Results: Star-Formation Rates and Efficiencies; Evolution and Lifetimes. *ApJ*, 181(2):321.

Farias, J.P., Tan, J.C., and Eyer, L., 2020. Hunting for Runaways from the Orion Nebula Cluster. *ApJ*, 900(1):14.

Favata, F., Flaccomio, E., Reale, F., et al., 2005. Bright X-Ray Flares in Orion Young Stars from COUP: Evidence for Star-Disk Magnetic Fields? *ApJ*, 160(2):469.

Feigelson, E.D., Getman, K., Townsley, L., et al., 2005. Global X-Ray Properties of the Orion Nebula Region. *ApJ*, 160(2):379.

Feigelson, E.D. and Montmerle, T., 1985. An extremely variable radio star in the rho Ophiuchi cloud. *ApJ*, 289:L19.

Feigelson, E.D. and Montmerle, T., 1999. High-Energy Processes in Young Stellar Objects. *Annual Review of Astronomy and Astrophysics*, 37:363.

Felli, M., Churchwell, E., Wilson, T.L., et al., 1993a. The radio continuum morphology of the Orion Nebula - From 10 arcmin to 0.1 arcsec Resolution. *A&A Supp.*, 98:137.

Felli, M., Taylor, G.B., Catarzi, M., et al., 1993b. The Orion Radio Zoo Revisited - Source Variability. *A&A Supp.*, 101:127.

Fischer, W.J., Megeath, S.T., Furlan, E., et al., 2017. The Herschel Orion Protostar Survey: Luminosity and Envelope Evolution. *ApJ*, 840(2):69.

Fomalont, E.B., Windhorst, R.A., Kristian, J.A., et al., 1991. The micro-Jansky radio source population at 5 GHz. *AJ*, 102:1258.

Forbrich, J., Dzib, S.A., Reid, M.J., et al., 2021. A VLBA Survey of Radio Stars in the Orion Nebula Cluster. I. The Nonthermal Radio Population. *ApJ*, 906(1):23.

Forbrich, J., Menten, K.M., and Reid, M.J., 2008. A 1.3 cm wavelength radio flare from a deeply embedded source in the Orion BN/KL region. *A&A*, 477:267.

Forbrich, J., Reid, M.J., Menten, K.M., et al., 2017. Extreme Radio Flares and Associated X-Ray Variability from Young Stellar Objects in the Orion Nebula Cluster. *ApJ*, 844(2):109.

Forbrich, J., Rivilla, V.M., Menten, K.M., et al., 2016. The Population of Compact Radio Sources in the Orion Nebula Cluster. *ApJ*, 822:93.

Forbrich, J. and Wolk, S.J., 2013. On the radio-X-ray connection in young stellar objects in the Orion nebula cluster. *A&A*, 551:A56.

Francis, L., Johnstone, D., Dunham, M.M., et al., 2019. Identifying Variability in Deeply Embedded Protostars with ALMA and CARMA. *ApJ*, 871(2):149.

Francis, L., Johnstone, D., Herczeg, G., et al., 2020. On the Accuracy of the ALMA Flux Calibration in the Time Domain and across Spectral Windows. *AJ*, 160(6):270.

Friedel, D.N. and Widicus Weaver, S.L., 2011. A High Spatial Resolution Study of the λ = 3 mm Continuum of Orion-KL. *ApJ*, 742(2):64.

Furlan, E., Fischer, W.J., Ali, B., et al., 2016. The Herschel Orion Protostar Survey: Spectral Energy Distributions and Fits Using a Grid of Protostellar Models. *ApJ*, 224(1):5.

Gaia Collaboration, Brown, A.G.A., Vallenari, A., et al., 2021. Gaia Early Data Release 3. Summary of the contents and survey properties. *A&A*, 649:A1.

Gaia Collaboration et al., 2016. The Gaia mission. *A&A*, 595:A1.

Galli, P.A.B., Bouy, H., Olivares, J., et al., 2020a. Corona-Australis DANCe. I. Revisiting the census of stars with Gaia-DR2 data. *A&A*, 634:A98.

Galli, P.A.B., Bouy, H., Olivares, J., et al., 2020b. Lupus DANCe. Census of stars and 6D structure with Gaia-DR2 data. *A&A*, 643:A148.

Galli, P.A.B., Loinard, L., Bouy, H., et al., 2019. Structure and kinematics of the Taurus star-forming region from Gaia-DR2 and VLBI astrometry. *A&A*, 630:A137.

Garay, G., Moran, J.M., and Reid, M.J., 1987. Compact continuum radio sources in the Orion Nebula. *ApJ*, 314:535.

Getman, K.V., Feigelson, E.D., Broos, P.S., et al., 2008a. X-Ray Flares in Orion Young Stars. I. Flare Characteristics. *ApJ*, 688:418-436.

Getman, K.V., Feigelson, E.D., Grosso, N., et al., 2005a. Membership of the Orion Nebula Population from the Chandra Orion Ultradeep Project. *ApJ*, 160:353.

Getman, K.V., Feigelson, E.D., Kuhn, M.A., et al., 2019. Gaia stellar kinematics in the head of the Orion A cloud: runaway stellar groups and gravitational infall. *MNRAS*, 487(3):2977.

Getman, K.V., Feigelson, E.D., Micela, G., et al., 2008b. X-Ray Flares in Orion Young Stars. II. Flares, Magnetospheres, and Protoplanetary Disks. *ApJ*, 688:437-455.

Getman, K.V., Flaccomio, E., Broos, P.S., et al., 2005b. Chandra Orion Ultradeep Project: Observations and Source Lists. *ApJ*, 160:319.

Ginsburg, A., Bally, J., Goddi, C., et al., 2018. A Keplerian Disk around Orion SrCI, a ~ 15 M $_\odot$ YSO. *ApJ*, 860(2):119.

Goldsmith, P.F., Heyer, M., Narayanan, G., et al., 2008. Large-Scale Structure of the Molecular Gas in Taurus Revealed by High Linear Dynamic Range Spectral Line Mapping. *ApJ*, 680(1):428.

Gómez, L., RodrÍguez, L.F., Loinard, L., et al., 2005. Dynamical Decay of a Massive Multiple System in Orion KL? *ApJ*, 635(2):1166.

Gómez, L., Rodríguez, L.F., Loinard, L., et al., 2008. Monitoring the Large Proper Motions of Radio Sources in the Orion BN/KL Region. *ApJ*, 685:333.

Gordon, K.D., Clayton, G.C., Misselt, K.A., et al., 2003. A Quantitative Comparison of the Small Magellanic Cloud, Large Magellanic Cloud, and Milky Way Ultraviolet to Near-Infrared Extinction Curves. *ApJ*, 594(1):279.

Goss, W.M. and Shaver, P.A., 1970. Galactic Radio Sources I: High Resolution 5000 MHz observations. *Australian Journal of Physics Astrophysical Supplement*, 14:1.

Grasser, N., Ratzenböck, S., Alves, J., et al., 2021. The ρ Ophiuchi region revisited with Gaia EDR3. Two young populations, new members, and old impostors. *A&A*, 652:A2.

Greene, T.P., Wilking, B.A., Andre, P., et al., 1994. Further Mid-Infrared Study of the rho Ophiuchi Cloud Young Stellar Population: Luminosities and Masses of Pre–Main-Sequence Stars. *ApJ*, 434:614.

Greisen, E.W., 2003. AIPS, the VLA, and the VLBA. In A. Heck, editor, *Information Handling in Astronomy - Historical Vistas*, volume 285 of *Astrophysics and Space Science Library*, page 109.

Grosso, N., Feigelson, E.D., Getman, K.V., et al., 2005. Chandra Orion Ultradeep Project Census of X-Ray Stars in the BN-KL and OMC-1S Regions. *ApJ*, 160(2):530.

Großschedl, J.E., Alves, J., Meingast, S., et al., 2018. 3D shape of Orion A from Gaia DR2. *A&A*, 619:A106.

Großschedl, J.E., Alves, J., Meingast, S., et al., 2021. 3D dynamics of the Orion cloud complex. Discovery of coherent radial gas motions at the 100-pc scale. *A&A*, 647:A91.

Großschedl, J.E., Alves, J., Teixeira, P.S., et al., 2019. VISION - Vienna survey in Orion. III. Young stellar objects in Orion A. *A&A*, 622:A149.

Güdel, M., 2002. Stellar Radio Astronomy: Probing Stellar Atmospheres from Protostars to Giants. *Annual Review of Astronomy and Astrophysics*, 40:217.

Güdel, M., Briggs, K.R., Arzner, K., et al., 2007. The XMM-Newton extended survey of the Taurus molecular cloud (XEST). *A&A*, 468(2):353.

Hacar, A., Clark, S., Heitsch, F., et al., 2022. Initial Conditions for Star Formation: A Physical Description of the Filamentary ISM. *arXiv e-prints*, arXiv:2203.09562.

Hacar, A., Tafalla, M., Kauffmann, J., et al., 2013. Cores, filaments, and bundles: hierarchical core formation in the L1495/B213 Taurus region. *A&A*, 554:A55.

Hartmann, L., Herczeg, G., and Calvet, N., 2016. Accretion onto Pre-Main-Sequence Stars. *Annual Review of Astronomy and Astrophysics*, 54:135.

Hayashi, C., 1966. Evolution of Protostars. *Annual Review of Astronomy and Astrophysics*, 4:171.

Hayashi, M.R., Shibata, K., and Matsumoto, R., 1996. X-Ray Flares and Mass Outflows Driven by Magnetic Interaction between a Protostar and Its Surrounding Disk. *ApJ*, 468:L37.

Henney, W.J. and Arthur, S.J., 1998. Modeling the Brightness Profiles of the Orion Proplyds. *AJ*, 116(1):322.

Herbig, G.H., 1950. The Spectrum of the Nebulosity Surrounding T Tauri. *ApJ*, 111:11.

Herbig, G.H., 1962. The Properties and Problems of T Tauri Stars and Related Objects. *Advances in Astronomy and Astrophysics*, 1:47.

Herbig, G.H. and Bell, K.R., 1988. *Third Catalog of Emission-Line Stars of the Orion Population : 3 : 1988*.

Herbst, W., Herbst, D.K., Grossman, E.J., et al., 1994. Catalogue of UBVRI Photometry of T Tauri Stars and Analysis of the Causes of Their Variability. *AJ*, 108:1906.

Herczeg, G.J., Kuhn, M.A., Zhou, X., et al., 2019. An Initial Overview of the Extent and Structure of Recent Star Formation within the Serpens Molecular Cloud Using Gaia Data Release 2. *ApJ*, 878(2):111.

Heyer, M. and Dame, T.M., 2015. Molecular Clouds in the Milky Way. *Annual Review of Astronomy and Astrophysics*, 53:583.

Hillenbrand, L.A., 1997. On the Stellar Population and Star-Forming History of the Orion Nebula Cluster. *AJ*, 113:1733.

Hillenbrand, L.A. and Carpenter, J.M., 2000. Constraints on the Stellar/Substellar Mass Function in the Inner Orion Nebula Cluster. *ApJ*, 540(1):236.

Hillenbrand, L.A. and Hartmann, L.W., 1998. A Preliminary Study of the Orion Nebula Cluster Structure and Dynamics. *ApJ*, 492(2):540.

Hillenbrand, L.A., Hoffer, A.S., and Herczeg, G.J., 2013. An Enhanced Spectroscopic Census of the Orion Nebula Cluster. *AJ*, 146:85.

Hillenbrand, L.A., Strom, S.E., Calvet, N., et al., 1998. Circumstellar Disks in the Orion Nebula Cluster. *AJ*, 116(4):1816.

Högbom, J.A., 1974. Aperture Synthesis with a Non-Regular Distribution of Interferometer Baselines. *A&A Supp.*, 15:417.

Huang, Y.D., Hwang, Y.J., Chiong, C.C., et al., 2022. ALMA Band-1 (35-50GHz) receiver: first light, performance, and road to completion. In J. Zmuidzinas and J.R. Gao, editors, *Millimeter, Submillimeter, and Far-Infrared Detectors and Instrumentation for Astronomy XI*, volume 12190 of *Society of Photo-Optical Instrumentation Engineers (SPIE) Conference Series*, page 121900K.

Iguchi, S., Morita, K.I., Sugimoto, M., et al., 2009. The Atacama Compact Array (ACA). *PASJ*, 61(1):1.

Isella, A., Hull, C.L.H., Moullet, A., et al., 2015. Next Generation Very Large Array Memo No. 6, Science Working Group 1: The Cradle of Life. *arXiv e-prints*, arXiv:1510.06444.

Jansky, K.G., 1933. Radio Waves from Outside the Solar System. *Nature*, 132(3323):66.

Jeans, J.H., 1928. *Astronomy and cosmogony*.

Johnson, H.M., 1965. The Spectra and Radial Velocities of Stars in the Orion Nebula Cluster. *ApJ*, 142:964.

Joy, A.H., 1932. Notes on the Spectra of Certain Variable Stars. *PASP*, 44(262):385.

Joy, A.H., 1945. T Tauri Variable Stars. *ApJ*, 102:168.

Kant, I., 1755. *Allgemeine Naturgeschichte und Theorie des Himmels*.

Kim, D., Lu, J.R., Konopacky, Q., et al., 2019. Stellar Proper Motions in the Orion Nebula Cluster. *AJ*, 157(3):109.

Kleinmann, D.E. and Low, F.J., 1967. Discovery of an Infrared Nebula in Orion. *ApJ*, 149:L1.

Kölligan, A. and Kuiper, R., 2018. Jets and outflows of massive protostars. From cloud collapse to jet launching and cloud dispersal. *A&A*, 620:A182.

Könyves, V., André, P., Arzoumanian, D., et al., 2020. Properties of the dense core population in Orion B as seen by the Herschel Gould Belt survey. *A&A*, 635:A34.

Könyves, V., André, P., Men'shchikov, A., et al., 2015. A census of dense cores in the Aquila cloud complex: SPIRE/PACS observations from the Herschel Gould Belt survey. *A&A*, 584:A91.

Koumpia, E., de Wit, W.J., Oudmaijer, R.D., et al., 2021. The first interferometric survey of massive YSOs in the K-band. Hot dust, ionised gas, and binarity at au scales. *A&A*, 654:A109.

Kounkel, M., Covey, K., Suárez, G., et al., 2018. The APOGEE-2 Survey of the Orion Star-forming Complex. II. Six-dimensional Structure. *AJ*, 156(3):84.

Kounkel, M., Hartmann, L., Loinard, L., et al., 2014. The Gould's Belt Very Large Array Survey. III. The Orion Region. *ApJ*, 790:49.

Kounkel, M., Hartmann, L., Loinard, L., et al., 2017. The Gould's Belt Distances Survey (GOBELINS) II. Distances and Structure toward the Orion Molecular Clouds. *ApJ*, 834(2):142.

Kraus, S., Balega, Y.Y., Berger, J.P., et al., 2007. Visual/infrared interferometry of Orion Trapezium stars: preliminary dynamical orbit and aperture synthesis imaging of the θ^1 Orionis C system. *A&A*, 466(2):649.

Kuhn, M.A., Hillenbrand, L.A., Carpenter, J.M., et al., 2020. The Formation of a Stellar Association in the NGC 7000/IC 5070 Complex: Results from Kinematic Analysis of Stars and Gas. *ApJ*, 899(2):128.

Kuhn, M.A., Hillenbrand, L.A., Sills, A., et al., 2019. Kinematics in Young Star Clusters and Associations with Gaia DR2. *ApJ*, 870(1):32.

Kundu, M.R., White, S.M., Shibasaki, K., et al., 2000. Nonthermal Flare Emission from MEV-Energy Electrons at 17, 34, and 86 GHZ. *ApJ*, 545(2):1084.

Kurtz, S., 2005. Hypercompact HII regions. In R. Cesaroni, M. Felli, E. Churchwell, and M. Walmsley, editors, *Massive Star Birth: A Crossroads of Astrophysics*, volume 227, pages 111–119.

Lada, C.J., 1987. Star formation: from OB associations to protostars. In M. Peimbert and J. Jugaku, editors, *Star Forming Regions*, volume 115, page 1.

Laos, S., Greene, T.P., Najita, J.R., et al., 2021. The Near-stellar Environment of Class 0 Protostars: A First Look with Near-infrared Spectroscopy. *ApJ*, 921(2):110.

Larson, R.B., 1969. Numerical calculations of the dynamics of collapsing proto-star. *MNRAS*, 145:271.

Larson, R.B., 1972. The evolution of spherical protostars with masses 0.25 M_solar to 10 M_solar. *MNRAS*, 157:121.

Larson, R.B., 2003. The physics of star formation. *Reports on Progress in Physics*, 66(10):1651.

Liu, H.B., Dunham, M.M., Pascucci, I., et al., 2018. A 1.3 mm SMA survey of 29 variable young stellar objects. *A&A*, 612:A54.

Lombardi, M., Bouy, H., Alves, J., et al., 2014. Herschel-Planck dust optical-depth and column-density maps. I. Method description and results for Orion. *A&A*, 566:A45.

Lucas, P.W., Roche, P.F., Allard, F., et al., 2001. Infrared spectroscopy of substellar objects in Orion. *MNRAS*, 326(2):695.

Luhman, K.L., 2018. The Stellar Membership of the Taurus Star-forming Region. *AJ*, 156(6):271.

Luhman, K.L., Rieke, G.H., Young, E.T., et al., 2000. The Initial Mass Function of Low-Mass Stars and Brown Dwarfs in Young Clusters. *ApJ*, 540(2):1016.

MacGregor, M.A., Weinberger, A.J., Loyd, R.O.P., et al., 2021. Discovery of an Extremely Short Duration Flare from Proxima Centauri Using Millimeter through Far-ultraviolet Observations. *ApJ*, 911(2):L25.

MacGregor, M.A., Weinberger, A.J., Wilner, D.J., et al., 2018. Detection of a Millimeter Flare from Proxima Centauri. *ApJ*, 855(1):L2.

Mairs, S., Lalchand, B., Bower, G.C., et al., 2019. The JCMT Transient Survey: An Extraordinary Submillimeter Flare in the T Tauri Binary System JW 566. *ApJ*, 871(1):72.

Massi, F., Weiss, A., Elia, D., et al., 2019. Dense cores and star formation in the giant molecular cloud Vela C. *A&A*, 628:A110.

Massi, M., Forbrich, J., Menten, K.M., et al., 2006. Synchrotron emission from the T Tauri binary system V773 Tauri A. *A&A*, 453:959.

Massi, M., Menten, K., and Neidhöfer, J., 2002. Periodic radio flaring on the T Tauri star V 773 Tauri. *A&A*, 382:152.

Massi, M., Ros, E., Menten, K.M., et al., 2008. Interacting coronae of two T Tauri stars: first observational evidence for solar-like helmet streamers. *A&A*, 480(2):489.

McKee, C.F. and Ostriker, E.C., 2007. Theory of Star Formation. *Annual Review of Astronomy and Astrophysics*, 45(1):565.

McMullin, J.P., Waters, B., Schiebel, D., et al., 2007. CASA Architecture and Applications. In R.A. Shaw, F. Hill, and D.J. Bell, editors, *Astronomical Data Analysis Software and Systems XVI*, volume 376 of *Astronomical Society of the Pacific Conference Series*, page 127.

Megeath, S.T., Gutermuth, R., Muzerolle, J., et al., 2012. The Spitzer Space Telescope Survey of the Orion A and B Molecular Clouds. I. A Census of Dusty Young Stellar Objects and a Study of Their Mid-infrared Variability. *AJ*, 144(6):192.

Megeath, S.T., Gutermuth, R., Muzerolle, J., et al., 2016. The Spitzer Space Telescope Survey of the Orion A and B Molecular Clouds. II. The Spatial Distribution and Demographics of Dusty Young Stellar Objects. *AJ*, 151(1):5.

Meingast, S., Alves, J., Mardones, D., et al., 2016. VISION - Vienna survey in Orion. I. VISTA Orion A Survey. *A&A*, 587:A153.

Mendoza V., E.E., 1966. Infrared Photometry of T Tauri Stars and Related Objects. *ApJ*, 143:1010.

Menten, K.M. and Reid, M.J., 1995. What is powering the Orion Kleinmann-low infrared nebula. *ApJ*, 445:L157.

Menten, K.M., Reid, M.J., Forbrich, J., et al., 2007. The distance to the Orion Nebula. *A&A*, 474:515.

Middelberg, E., Deller, A., Morgan, J., et al., 2011. Wide-field VLBA observations of the Chandra deep field South. *A&A*, 526:A74.

Miville-Deschênes, M.A., Murray, N., and Lee, E.J., 2017. Physical Properties of Molecular Clouds for the Entire Milky Way Disk. *ApJ*, 834(1):57.

Moran, J.M., Garay, G., Reid, M.J., et al., 1982. Compact continuum radio sources in the Orion Nebula. *Annals of the New York Academy of Sciences*, 395:204.

Moran, J.M., Garay, G., Reid, M.J., et al., 1983. Detection of radio emission from the Becklin-Neugebauer object. *ApJ*, 271:L31.

Muench, A.A., Lada, E.A., Lada, C.J., et al., 2002. The Luminosity and Mass Function of the Trapezium Cluster: From B Stars to the Deuterium-burning Limit. *ApJ*, 573(1):366.

Myers, P.C. and Ladd, E.F., 1993. Bolometric Temperatures of Young Stellar Objects. *ApJ*, 413:L47.

Napier, P.J., 1995. VLBA Design. In J.A. Zensus, P.J. Diamond, and P.J. Napier, editors, *Very Long Baseline Interferometry and the VLBA*, volume 82 of *Astronomical Society of the Pacific Conference Series*, page 59.

Napier, P.J., 1999. The Primary Antenna Elements. In G.B. Taylor, C.L. Carilli, and R.A. Perley, editors, *Synthesis Imaging in Radio Astronomy II*, volume 180 of *Astronomical Society of the Pacific Conference Series*, page 37.

Napier, P.J., Bagri, D.S., Clark, B.G., et al., 1994. The Very Long Baseline Array. *IEEE Proceedings*, 82(5):658.

Neugebauer, G., Habing, H.J., van Duinen, R., et al., 1984. The Infrared Astronomical Satellite (IRAS) mission. *ApJ*, 278:L1.

O'dell, C.R. and Wen, Z., 1994. Postrefurbishment Mission Hubble Space Telescope Images of the Core of the Orion Nebula: Proplyds, Herbig-Haro Objects, and Measurements of a Circumstellar Disk. *ApJ*, 436:194.

O'dell, C.R., Wen, Z., and Hu, X., 1993. Discovery of New Objects in the Orion Nebula on HST Images: Shocks, Compact Sources, and Protoplanetary Disks. *ApJ*, 410:696.

Osorio, M., Díaz-Rodríguez, A.K., Anglada, G., et al., 2017. Star Formation Under the Outflow: The Discovery of a Non-thermal Jet from OMC-2 FIR 3 and Its Relationship to the Deeply Embedded FIR 4 Protostar. *ApJ*, 840(1):36.

Otter, J., Ginsburg, A., Ballering, N.P., et al., 2021. Small Protoplanetary Disks in the Orion Nebula Cluster and OMC1 with ALMA. *arXiv e-prints*, arXiv:2109.14592.

Parker, R., Ward-Thompson, D., and Kirk, J., 2022. Taxonomy of protoplanetary discs observed with ALMA. *MNRAS*, 511(2):2453.

Pavlidou, T., Scholz, A., and Teixeira, P.S., 2021. The substructure of the Perseus star-forming region: a survey with Gaia DR2. *MNRAS*, 503(3):3232.

Perley, R.A., Chandler, C.J., Butler, B.J., et al., 2011. The Expanded Very Large Array: A New Telescope for New Science. *ApJ*, 739(1):L1.

Petr-Gotzens, M.G. and Massi, M., 2008. The Triple System θ^1 Orionis A in the Heart of the Orion Trapezium Cluster. In S. Hubrig, M. Petr-Gotzens, and A. Tokovinin, editors, *Multiple Stars Across the H-R Diagram*, page 281.

Phillips, R.B. and Lestrade, J.F., 1988. Compact non-thermal radio emission from B-peculiar stars. *Nature*, 334(6180):329.

Pineda, J.E., Arzoumanian, D., André, P., et al., 2022. From Bubbles and Filaments to Cores and Disks: Gas Gathering and Growth of Structure Leading to the Formation of Stellar Systems. *arXiv e-prints*, arXiv:2205.03935.

Preibisch, T., Kim, Y.C., Favata, F., et al., 2005. The Origin of T Tauri X-Ray Emission: New Insights from the Chandra Orion Ultradeep Project. *ApJ*, 160(2):401.

Prisinzano, L., Micela, G., Flaccomio, E., et al., 2008. X-Ray Properties of Protostars in the Orion Nebula. *ApJ*, 677:401-424.

Rau, U. and Cornwell, T.J., 2011. A multi-scale multi-frequency deconvolution algorithm for synthesis imaging in radio interferometry. *A&A*, 532:A71.

Reber, G., 1940. Notes: Cosmic Static. *ApJ*, 91:621.

Reid, M.J., Argon, A.L., Masson, C.R., et al., 1995. Synchrotron Emission from the H 2O Maser Source in W3(OH). *ApJ*, 443:238.

Reipurth, B., 2008a. *Handbook of Star Forming Regions, Volume I: The Northern Sky*, volume 4.

Reipurth, B., 2008b. *Handbook of Star Forming Regions, Volume II: The Southern Sky*, volume 5.

Ricci, L., Robberto, M., and Soderblom, D.R., 2008. The Hubble Space Telescope/Advanced Camera for Surveys Atlas of Protoplanetary Disks in the Great Orion Nebula. *AJ*, 136:2136.

Rivilla, V.M., Chandler, C.J., Sanz-Forcada, J., et al., 2015. Short- and Long-Term Radio Variability of Young Stars in The Orion Nebula Cluster and Molecular Cloud. *ApJ*, 808:146.

Roberts, D.H., Wardle, J.F.C., and Brown, L.F., 1994. Linear Polarization Radio Imaging at Milliarcsecond Resolution. *ApJ*, 427:718.

Robitaille, T.P., Whitney, B.A., Indebetouw, R., et al., 2006. Interpreting Spectral Energy Distributions from Young Stellar Objects. I. A Grid of 200,000 YSO Model SEDs. *ApJ*, 167(2):256.

Rodríguez, L.F., Dzib, S.A., Loinard, L., et al., 2017. The Proper Motions of the Double Radio Source n in the Orion BN/KL Region. *ApJ*, 834(2):140.

Rodríguez, L.F., Dzib, S.A., Zapata, L., et al., 2020. Proper Motions of the Radio Source Orion MR, Formerly Known as Orion n, and New Sources with Large Proper Motions in Orion BN/KL. *ApJ*, 892(2):82.

Rodríguez, L.F., Loinard, L., D'Alessio, P., et al., 2005a. IRAS 16293-2422B: A Compact, Possibly Isolated Protoplanetary Disk in a Class 0 Object. *ApJ*, 621(2):L133.

Rodríguez, L.F., Poveda, A., Lizano, S., et al., 2005b. Proper Motions of the BN Object and the Radio Source I in Orion: Where and When Did the BN Object Become a Runaway Star? *ApJ*, 627(1):L65.

Rucinski, S.M., 1985. IRAS observations of T Tauri and post-T Tauri stars. *AJ*, 90:2321.

Rutllant Costa, J., 1977. *O the Extreme Aridity of Coastal and Atacama Deserts in Northern Chile.* Ph.D. thesis, University of Wisconsin, Madison.

Rybicki, G.B. and Lightman, A.P., 1986. *Radiative Processes in Astrophysics.*

Ryle, M., 1975. Radio Telescopes of Large Resolving Power. *Science*, 188(4193):1071.

Ryter, C.E., 1996. Interstellar Extinction from Infrared to X-Rays: an Overview. *Ap&SS*, 236(2):285.

Salter, D.M., Hogerheijde, M.R., and Blake, G.A., 2008. Captured at millimeter wavelengths: a flare from the classical T Tauri star DQ Tauri. *A&A*, 492:L21.

Salter, D.M., Kóspál, Á., Getman, K.V., et al., 2010. Recurring millimeter flares as evidence for star-star magnetic reconnection events in the DQ Tauri PMS binary system. *A&A*, 521:A32.

Sanford, R.F., 1920. The Spectrum of T Tauri. *PASP*, 32(185):59.

Santiago-García, J., Tafalla, M., Johnstone, D., et al., 2009. Shells, jets, and internal working surfaces in the molecular outflow from IRAS 04166+2706. *A&A*, 495(1):169.

Schneider, P.C., Günther, H.M., and France, K., 2020. The UV Perspective of Low-Mass Star Formation. *Galaxies*, 8(1):27.

Schoettler, C., de Bruijne, J., Vaher, E., et al., 2020. Runaway and walkaway stars from the ONC with Gaia DR2. *MNRAS*, 495(3):3104.

Schraml, J. and Mezger, P.G., 1969. Galactic H II Regions.IV. 1.95-CM Observations with High Angular Resolution and High Positional Accuracy. *ApJ*, 156:269.

Segura-Cox, D.M., Looney, L.W., Tobin, J.J., et al., 2018. The VLA Nascent Disk and Multiplicity Survey of Perseus Protostars (VANDAM). V. 18 Candidate Disks around Class 0 and I Protostars in the Perseus Molecular Cloud. *ApJ*, 866(2):161.

Segura-Cox, D.M., Schmiedeke, A., Pineda, J.E., et al., 2020. Four annular structures in a protostellar disk less than 500,000 years old. *Nature*, 586(7828):228.

Sheehan, P.D., Eisner, J.A., Mann, R.K., et al., 2016. A VLA Survey for Faint Compact Radio Sources in the Orion Nebula Cluster. *ApJ*, 831(2):155.

Shu, F., Najita, J., Ostriker, E., et al., 1994. Magnetocentrifugally Driven Flows from Young Stars and Disks. I. A Generalized Model. *ApJ*, 429:781.

Shu, F.H., 1977. Self-similar collapse of isothermal spheres and star formation. *ApJ*, 214:488.

Shu, F.H., Adams, F.C., and Lizano, S., 1987. Star formation in molecular clouds: observation and theory. *Annual Review of Astronomy and Astrophysics*, 25:23.

Shull, J.M. and Beckwith, S., 1982. Interstellar molecular hydrogen. *Annual Review of Astronomy and Astrophysics*, 20:163.

Skilling, J. and Bryan, R.K., 1984. Maximum Entropy Image Reconstruction - General Algorithm. *MNRAS*, 211:111.

Spitzer, Lyman, J., 1948. The Formation of Cosmic Clouds. In *Harvard Observatory Monographs*, volume 7, page 87.

Sternberg, A., 1989. The excitation of molecular hydrogen and its significance. In E. Böhm-Vitense, editor, *Infrared Spectroscopy in Astronomy*, page 269.

Strand, K.A., 1958. Stellar Motions in the Orion Nebula Cluster. *ApJ*, 128:14.

Stutz, A.M., Tobin, J.J., Stanke, T., et al., 2013. A Herschel and APEX Census of the Reddest Sources in Orion: Searching for the Youngest Protostars. *ApJ*, 767(1):36.

Tan, J.C., Shaske, S.N., and Van Loo, S., 2013. Molecular Clouds: Internal Properties, Turbulence, Star Formation and Feedback. In T. Wong and J. Ott, editors, *Molecular Gas, Dust, and Star Formation in Galaxies*, volume 292, pages 19–28.

Taylor, K.N.R., Storey, J.W.V., Sandell, G., et al., 1984. Molecular hydrogen jets from the Orion nebula. *Nature*, 311(5983):236.

Thompson, A.R., 1999. Fundamentals of Radio Interferometry. In G.B. Taylor, C.L. Carilli, and R.A. Perley, editors, *Synthesis Imaging in Radio Astronomy II*, volume 180 of *Astronomical Society of the Pacific Conference Series*, page 11.

Thompson, A.R., Moran, J.M., and Swenson, George W., J., 2017. *Interferometry and Synthesis in Radio Astronomy, 3rd Edition*.

Tibbs, C.T., Paladini, R., and Dickinson, C., 2012. On the Limitations of the Anomalous Microwave Emission Emissivity. *Advances in Astronomy*, 2012:124931.

Tobin, J.J., Looney, L.W., Li, Z.Y., et al., 2016. The VLA Nascent Disk and Multiplicity Survey of Perseus Protostars (VANDAM). II. Multiplicity of Protostars in the Perseus Molecular Cloud. *ApJ*, 818(1):73.

Tobin, J.J., Sheehan, P.D., Megeath, S.T., et al., 2020. The VLA/ALMA Nascent Disk and Multiplicity (VANDAM) Survey of Orion Protostars. II. A Statistical Characterization of Class 0 and Class I Protostellar Disks. *ApJ*, 890(2):130.

Torres, R.M., Loinard, L., Mioduszewski, A.J., et al., 2012. VLBA Determination of the Distance to nearby Star-forming Regions. V. Dynamical Mass, Distance, and Radio Structure of V773 Tau A. *ApJ*, 747(1):18.

Trumpler, R.J., 1930. Absorption of Light in the Galactic System. *PASP*, 42(248):214.

Urquhart, J.S., König, C., Giannetti, A., et al., 2018. ATLASGAL - properties of a complete sample of Galactic clumps. *MNRAS*, 473(1):1059.

van Cittert, P.H., 1934. Die Wahrscheinliche Schwingungsverteilung in Einer von Einer Lichtquelle Direkt Oder Mittels Einer Linse Beleuchteten Ebene. *Physica*, 1(1):201.

van der Marel, N., Dong, R., di Francesco, J., et al., 2019. Protoplanetary Disk Rings and Gaps across Ages and Luminosities. *ApJ*, 872(1):112.

Vargas-González, J., Forbrich, J., Dzib, S.A., et al., 2021. From downtown to the outskirts: a radio survey of the Orion Nebula Cluster. *MNRAS*, 506(3):3169.

Venturi, T., Paragi, Z., Lindqvist, M., et al., 2020. VLBI20-30: a scientific roadmap for the next decade – The future of the European VLBI Network. *arXiv e-prints*, arXiv:2007.02347.

Vicente, S.M. and Alves, J., 2005. Size distribution of circumstellar disks in the Trapezium cluster. *A&A*, 441(1):195.

Vuong, M.H., Montmerle, T., Grosso, N., et al., 2003. Determination of the gas-to-dust ratio in nearby dense clouds using X-ray absorption measurements. *A&A*, 408:581.

Waterfall, C.O.G., Browning, P.K., Fuller, G.A., et al., 2019. Modelling the radio and X-ray emission from T-Tauri flares. *MNRAS*, 483(1):917.

White, R.J. and Basri, G., 2003. Very Low Mass Stars and Brown Dwarfs in Taurus-Auriga. *ApJ*, 582(2):1109.

White, S.M., Benz, A.O., Christe, S., et al., 2011. The Relationship Between Solar Radio and Hard X-ray Emission. *Space Sci. Rev.*, 159(1-4):225.

Wilking, B.A. and Lada, C.J., 1983. The discovery of new embedded sources in the centrally condensed coreof the rho Ophiuchi dark cloud : the formation of a bound cluster ? *ApJ*, 274:698.

Williams, J.P., Blitz, L., and McKee, C.F., 2000. The Structure and Evolution of Molecular Clouds: from Clumps to Cores to the IMF. In V. Mannings, A.P. Boss, and S.S. Russell, editors, *Protostars and Planets IV*, page 97.

Wilson, T.L., Rohlfs, K., and Huttemeister, S., 2012. *Tools of Radio Astronomy, 5th edition*.

Wolk, S.J., Harnden, Jr., F.R., Flaccomio, E., et al., 2005. Stellar Activity on the Young Suns of Orion: COUP Observations of K5-7 Pre-Main-Sequence Stars. *ApJ*, 160:423.

Wright, M., Bally, J., Hirota, T., et al., 2022. Structure of the Source I Disk in Orion-KL. *ApJ*, 924(2):107.

Wrobel, J.M., 1995. VLBI Observing Strategies. In J.A. Zensus, P.J. Diamond, and P.J. Napier, editors, *Very Long Baseline Interferometry and the VLBA*, volume 82 of *Astronomical Society of the Pacific Conference Series*, page 411.

Wynn-Williams, C.G., 1982. The search for infrared protostars. *Annual Review of Astronomy and Astrophysics*, 20:587.

Young, T., 1804. The Bakerian Lecture: Experiments and Calculations Relative to Physical Optics. *Philosophical Transactions of the Royal Society of London Series I*, 94:1.

Zakri, W., Megeath, S.T., Fischer, W.J., et al., 2022. The Rate, Amplitude, and Duration of Outbursts from Class 0 Protostars in Orion. *ApJ*, 924(2):L23.

Zapata, L.A., Rodríguez, L.F., Ho, P.T.P., et al., 2006. In Search of Circumstellar Disks around Young Massive Stars. *AJ*, 131(2):939.

Zapata, L.A., Rodríguez, L.F., Kurtz, S.E., et al., 2004. Compact Radio Sources in Orion: New Detections, Time Variability, and Objects in OMC-1S. *AJ*, 127:2252.

Zapata, L.A., Schmid-Burgk, J., Ho, P.T.P., et al., 2009. Explosive Disintegration of a Massive Young Stellar System in Orion. *ApJ*, 704(1):L45.

Zernike, F., 1938. The concept of degree of coherence and its application to optical problems. *Physica*, 5(8):785.

Zinnecker, H. and Yorke, H.W., 2007. Toward Understanding Massive Star Formation. *Annual Review of Astronomy and Astrophysics*, 45(1):481.

Zucker, C., Battersby, C., and Goodman, A., 2015. The Skeleton of the Milky Way. *ApJ*, 815(1):23.

Zucker, C., Battersby, C., and Goodman, A., 2018. Physical Properties of Large-scale Galactic Filaments. *ApJ*, 864(2):153.

Zucker, C., Goodman, A.A., Alves, J., et al., 2022. Star formation near the Sun is driven by expansion of the Local Bubble. *Nature*, 601(7893):334.